CHALLENGES AND SOLUTIONS IN SAMPLE PREPARATION FOR HIGH-RESOLUTION CRYO-ELECTRON MICROSCOPY

EDITED BY: Felix Weis, Rebecca F. Thompson and Arjen J. Jakobi

PUBLISHED IN: Frontiers in Molecular Biosciences

frontiers Research Topics

frontiers

ISSN 1664-8714
ISBN 978-2-83250-860-2
DOI 10.3389/978-2-83250-860-2

About Frontiers

Frontiers is more than just an open-access publisher of scholarly articles: it is a pioneering approach to the world of academia, radically improving the way scholarly research is managed. The grand vision of Frontiers is a world where all people have an equal opportunity to seek, share and generate knowledge. Frontiers provides immediate and permanent online open access to all its publications, but this alone is not enough to realize our grand goals.

Frontiers Journal Series

The Frontiers Journal Series is a multi-tier and interdisciplinary set of open-access, online journals, promising a paradigm shift from the current review, selection and dissemination processes in academic publishing. All Frontiers journals are driven by researchers for researchers; therefore, they constitute a service to the scholarly community. At the same time, the Frontiers Journal Series operates on a revolutionary invention, the tiered publishing system, initially addressing specific communities of scholars, and gradually climbing up to broader public understanding, thus serving the interests of the lay society, too.

Dedication to Quality

Each Frontiers article is a landmark of the highest quality, thanks to genuinely collaborative interactions between authors and review editors, who include some of the world's best academicians. Research must be certified by peers before entering a stream of knowledge that may eventually reach the public - and shape society; therefore, Frontiers only applies the most rigorous and unbiased reviews.
Frontiers revolutionizes research publishing by freely delivering the most outstanding research, evaluated with no bias from both the academic and social point of view. By applying the most advanced information technologies, Frontiers is catapulting scholarly publishing into a new generation.

What are Frontiers Research Topics?

Frontiers Research Topics are very popular trademarks of the Frontiers Journals Series: they are collections of at least ten articles, all centered on a particular subject. With their unique mix of varied contributions from Original Research to Review Articles, Frontiers Research Topics unify the most influential researchers, the latest key findings and historical advances in a hot research area! Find out more on how to host your own Frontiers Research Topic or contribute to one as an author by contacting the Frontiers Editorial Office: frontiersin.org/about/contact

CHALLENGES AND SOLUTIONS IN SAMPLE PREPARATION FOR HIGH-RESOLUTION CRYO-ELECTRON MICROSCOPY

Topic Editors:
Felix Weis, European Molecular Biology Laboratory Heidelberg, Germany
Rebecca F. Thompson, University of Leeds, United Kingdom
Arjen J. Jakobi, Delft University of Technology, Netherlands

Citation: Weis, F., Thompson, R. F., Jakobi, A. J., eds. (2022). Challenges and Solutions in Sample Preparation for High-Resolution Cryo-Electron Microscopy. Lausanne: Frontiers Media SA. doi: 10.3389/978-2-83250-860-2

Table of Contents

frontiers | Frontiers in Molecular Biosciences

PERSPECTIVE
published: 26 April 2022
doi: 10.3389/fmolb.2022.864829

Perspective: Biochemical and Physical Constraints Associated With Preparing Thin Specimens for Single-Particle Cryo-EM

Bong-Gyoon Han[1], *Max Armstrong*[1,2], *Daniel A. Fletcher*[2,3,4] *and Robert M. Glaeser*[1]*

[1]Lawrence Berkeley National Laboratory, University of California, Berkeley, Berkeley, CA, United States, [2]Department of Bioengineering, University of California, Berkeley, Berkeley, CA, United States, [3]Biological Systems and Engineering Division, Lawrence Berkeley National Laboratory, University of California, Berkeley, Berkeley, CA, United States, [4]Chan Zuckerberg Biohub, San Francisco, CA, United States

While many aspects of single-particle electron cryo-microscopy (cryo-EM) of biological macromolecules have reached a sophisticated level of development, this is not yet the case when it comes to preparing thin samples on specimen grids. As a result, there currently is considerable interest in achieving better control of both the sample thickness and the amount of area that is useful, but this is only one aspect in which improvement is needed. This Perspective addresses the further need to prevent the macromolecular particles from making contact with the air-water interface, something that can result in preferential orientation and even structural disruption of macromolecular particles. This unwanted contact can occur either as the result of free diffusion of particles during the interval between application, thinning and vitrification of the remaining buffer, or—when particles have been immobilized—by the film of buffer becoming too thin prior to vitrification. An opportunity now exists to apply theoretical and practical insights from the fields of thin-film physical chemistry and interfacial science, in an effort to bring cryo-EM sample preparation to a level of sophistication that is comparable to that of current data collection and analysis.

Keywords: cryo-EM, sample thickness, air-water interface, axisymmetric draining, affininity grids

OPEN ACCESS

Edited by:
Rebecca F. Thompson, University of Leeds, United Kingdom

Reviewed by:
Edoardo D'Imprima, European Molecular Biology Laboratory (EMBL) Heidelberg, Germany

***Correspondence:**
Robert M. Glaeser
rmglaeser@lbl.gov

Specialty section:
This article was submitted to Structural Biology, a section of the journal Frontiers in Molecular Biosciences

Received: *28 January 2022*
Accepted: *25 March 2022*
Published: *26 April 2022*

Citation:
Han B-G, Armstrong M, Fletcher DA and Glaeser RM (2022) Perspective: Biochemical and Physical Constraints Associated With Preparing Thin Specimens for Single-Particle Cryo-EM. Front. Mol. Biosci. 9:864829. doi: 10.3389/fmolb.2022.864829

INTRODUCTION

Although high-resolution electron cryo-microscopy (cryo-EM) of purified biological macromolecules (Glaeser et al., 2021) has become a successful and mature method, preparing the required thin, vitrified samples often remains a major challenge. Efforts have been under way for some time to improve the way in which samples are thinned before they are vitrified, as has recently been reviewed by Weissenberger et al. (2021). Nevertheless, the classic goal of embedding particles within free-standing films of buffer, as depicted in the cartoon shown as Figure 2 of (Glaeser, 2021), appears to be rarely achieved. Instead, the desired encapsulation of biological macromolecules within vitrified buffer is generally thwarted by rapid diffusion of proteins to the air-water interface (AWI), often followed by formation of a sacrificial, denatured-protein monolayer (Han and Glaeser, 2021). While subsequent adsorption of additional particles to such sacrificial monolayers may still result in an acceptable outcome, it often does not, and better alternatives are generally needed.

Interaction of proteins with the AWI was considered to be a potential hazard in the early days of cryo-EM sample preparation—see section 6.6 of (Dubochet et al., 1988). Indeed, attempts were made at that time to develop some type of electron-transparent slide and coverslip that might be suitable for use in cryo-EM. Exploratory directions of work included sandwiching samples between thin, hydrophilic support films (Taylor and Glaeser, 1973; Taylor and Glaeser, 1976) and the use of fatty-acid monolayers as a conformal coverslip (Hayward et al., 1978; Chang et al., 1985a; Chang et al., 1985b).

Nevertheless, the simplicity and the success of blotting a holey support film with filter paper initially caused such concerns to be put aside.

The issue was reopened, however, in a retrospective of cryo-EM sample preparation—see Figure 5 in (Taylor and Glaeser, 2008). Awareness then continued to grow that the challenges encountered when preparing samples on grids were due to interaction with the AWI, rather than to how the sample was isolated. Perhaps the foremost indication was that the number of particles seen in images was often either more than, or fewer than, what would be expected from the known sample concentration and the thickness of the sample (Vinothkumar and Henderson, 2016). Finally, after cryo-tomography demonstrated that nearly all types of biological macromolecules were adsorbed to the AWI (Noble et al., 2018; D'Imprima et al., 2019; Fan et al., 2019), the problem again began to be discussed more widely in the literature (Drulyte et al., 2018; Carragher et al., 2019; Klebl et al., 2020). It now is widely acknowledged that avoiding interaction with the AWI remains one of the most important challenges still to be solved for single-particle cryo-EM.

This Perspective focuses on the strategy of immobilizing particles onto the surface of a thin support film, preferably followed by washing off unbound particles with buffer, and then removing all but a suitably thin layer of the wash-buffer. Other potential strategies for avoiding interaction with the AWI, which are not reviewed here for lack of space, include 1) thinning and then vitrifying samples so quickly that adsorption to the AWI does not have time to occur; 2) sandwiching samples between structure-friendly, electron-transparent windows, in effect confining particles between some type of electron-transparent "slide and coverslip" (Frederik et al., 1989); and 3) milling or sectioning thin samples from bulk-frozen material.

More specifically, this Perspective addresses two issues that remain relevant after macromolecules have been immobilized onto the surface of a grid. The first of these is the fact that immobilization does nothing that might reduce the unwanted variation in ice thickness that is produced by traditional blotting with filter paper. Second, although immobilization prevents diffusion of particles to the AWI, it does nothing to prevent the AWI from still touching the particles, should the thickness of buffer become comparable to, or less than, the size of the bound particles themselves.

IMMOBILIZATION OF PARTICLES CAN BE AN EFFECTIVE WAY TO AVOID INITIAL CONTACT WITH THE AWI

Some macromolecules will hit and perhaps adsorb to the AWI, even while the drop of sample is initially forming at the tip of the pipette, because particles that are within 100 nm of a newly formed aqueous surface will diffuse to the AWI within a ms or less (Taylor and Glaeser, 2008; Naydenova and Russo, 2017). Something similar is expected to happen when protein solutions wet the surface of a dip pen, and subsequently the grid surface, a system that is roughly equivalent to the glass rod historically used to quantitatively deliver denatured protein to the surface of a Langmuir trough (Trurnit, 1960). In addition, diffusion will deliver particles to the fresh AWI that then spans the exposed side of ~micrometer-sized, open holes of the holey carbon grid. In other words, the AWI on the underside (i.e., back) of the grid is just as much of a hazard to proteins as is the larger, continuous surface over the top of the deposited sample.

As mentioned in the Introduction, one alternative is to bind samples onto the surfaces of support films. Furthermore, excess sample might be washed from such grids, depending about the binding affinity, the intent being to remove proteins adsorbed to the AWI at the top of the applied sample. There are, in fact, many ways in which biological macromolecules can be immobilized at solid-liquid interfaces in a structure-friendly way, as is known from the field of biochemical chromatography. Grids that are intended to immobilize biological macromolecules in a structure-friendly way are therefore referred to here as being "affinity grids", a terminology that is meant to be taken figuratively rather than literally.

At the same time, there are also many types of solid substrates that are not always structure friendly, as has been reviewed briefly in the Discussion section of (Joppe et al., 2020). Thus, as is summarized in **Table 1**, adsorption onto solid surfaces such as glow-discharge treated carbon film or graphene oxide may produce favorable results for some proteins, while adsorption of other proteins to the same substrates results in preferred orientation or even severe particle damage. It therefore seems likely that the same, specimen-dependent outcome will prove to be true for adsorption of proteins onto the silicon nitride windows of microfluidic EM grids (Huber et al., 2022).

A large number of alternatives have already been investigated for making affinity grids, as is summarized in **Table 1**. Some of those strategies have already given high-resolution results, even when using samples that previously resisted preparation with standard approaches (D'Imprima et al., 2019; Gillies et al., 2021; Kasinath et al., 2021; Lahiri et al., 2019; Sauer et al., 2021; Wang et al., 2020). While all such affinity grids have attractive features, the most appealing may be ones with high binding affinities, so that—as mentioned above—grids can be washed without eluting the immobilized particles. Furthermore, it is essential that there be little risk that the chosen immobilization strategy results in preferred orientation of particles. The point being made here is that many effective strategies are already available for making affinity grids, and it is certainly welcome if more of them can be developed.

NEW VITRIFICATION STRATEGIES SHOULD BE CONSIDERED WHEN PARTICLES ARE IMMOBILIZED ONTO AFFINITY GRIDS

As previously indicated, one can blot affinity grids with filter paper in the traditional way, but the usual, unsatisfactory features

TABLE 1 | Representative examples of different types of affinity grids used for cryo-EM sample preparation, and the current status of results that have been obtained.

Type of support film	Expected features Risk of damage or preferred orientation	Binding strength	Results Selected references
Glow-discharge treated carbon film	• Although the surface is polar, some types of particles may still be damaged upon binding and other types may still show preferred orientation	• Particle -dependent; varies from weak to strong	• Although this may the first thing to try if sample preparation proves to be challenging, and numerous high-resolution structures have been obtained with such support films, evaporated carbon contributes a level of structural noise that may be undesirable, especially for small particles
Functionalized carbon film	• Provides improved specificity with which particles are bound; risk of preferred orientation remains possible	• Usually intermediate in strength	• Methods of functionalization include nonspecific pre-binding of antibodies (Yu et al., 2016) and designed chemical modification of the surface (Llaguno et al., 2014)
Graphene oxide	• Although the surface is polar, some types of particles may still be damaged upon binding and others may still show preferred orientation	• Usually intermediate in strength	• Although many high-resolution structures have been obtained with graphene oxide, there is a trade-off between covering a high percentage of holes and limiting the number of graphene oxide flakes that lie over individual holes
Functionalized graphene or graphene oxide	• While both ionic binding and chemically specific binding has been achieved, there also still remains a risk of damage or preferred orientation unless the surface is further passivated, for example by additional functionalization with polyethylene glycol	• Binding varies from weak to intermediate	• Physisorption of aromatic groups that bear ionizable groups; high resolution achieved for fatty acid synthase (D'Imprima et al., 2019) • Covalent modification with Ni-NTA functional groups; high resolution achieved for streptavidin (Liu et al., 2019) • Covalent functionalization of components of the Spy/SpyCatcher affinity tag system; high resolution achieved for a Hsp90 chaperone particle that previously resisted specimen preparation (Wang et al., 2020) • Glow discharge deposition of ionizable precursor gasses; high resolution achieved for 30S ribosomal particles and for apoferritin (Naydenova et al., 2019)
Monolayers of charged lipids and ligand-functionalized lipids	• Provides excellent control of the type of charged group and the surface-charge density or, alternatively, the type of ligand to present for binding	• Binding varies from weak to intermediate	• Multiple successes were achieved for growth of monolayer protein crystals (Taylor et al., 2007), but not yet productively used for making single-particle specimens; for more on the latter methodology see (Kelly et al., 2010a; Kelly et al., 2010b) and (Benjamin et al., 2016)
Streptavidin monolayer crystals	• Combines exceptionally tight binding and complete passivation of the interface; little risk of preferred orientation when lysine residues are randomly biotinylated	• Strong	• Four high-resolution structures have been obtained for protein complexes that had been refractory to all previous methods tried when making grids for cryo-EM: RNAP-II elongation complex (Lahiri et al., 2019); polycomb repressive complex in complex with co-factors and histones (Kasinath et al., 2021); phycobilisomes (Sauer et al., 2021), and cytoplasmic dynein-1 (Gillies et al., 2021)

produced by blotting will still remain. These include the fact that some sample often finds its way to the back side of grids during blotting (Armstrong et al., 2020); there are large variations in the amount of area over which the sample is effectively opaque to 300 keV electrons; there often are many areas in which the ice may seem to be relatively transparent to the electron beam, but it is still not yet thin enough to get the best result; and there are other areas where the ice is either too thin or where the buffer has even dewetted the support film, causing those areas of the grid to dry before vitrification.

Newer alternatives to blotting with filter paper, which are intended to overcome at least some if not all of these shortcomings, have recently been reviewed in (Weissenberger et al., 2021). These alternatives include different ways in which samples are sprayed onto grids, which can be either self-wicking grids (Wei et al., 2018) or conventional holey-film grids, as well as ways in which samples are spread with either a capillary (Arnold et al., 2017) or a dip pen (Ravelli et al., 2020). However, since those methods are unlikely to be compatible with a washing step, it is hard to imagine ways to remove unbound material when

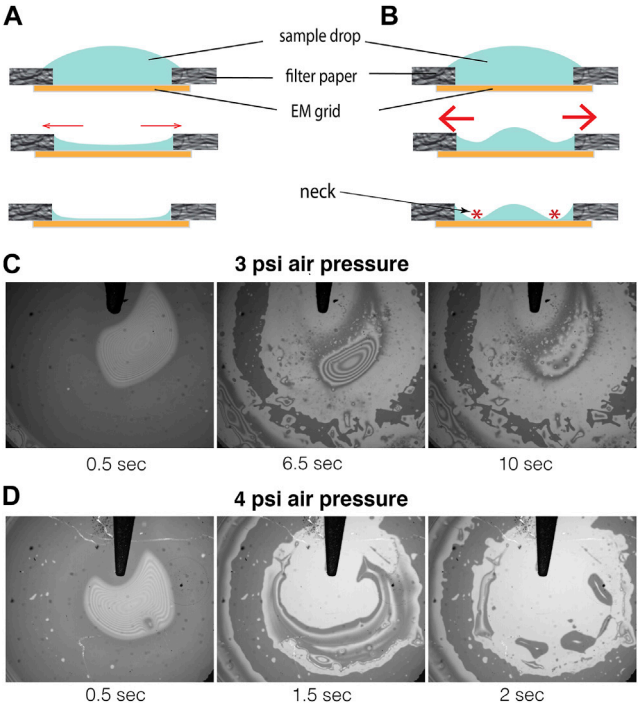

FIGURE 1 | Concept of, and preliminary results obtained by, axisymmetric draining of excess buffer from 3 mm coverslips. **Panel A** shows the desired, ideal outcome if excess buffer is removed adiabatically, indicated by thin red arrows. The sample is expected to become progressively thinner in the center, remaining thick only in the so-called Plateau border, closest to the edge of the filter paper. **Panel B** shows the expected, undesirable result that can occur if buffer is removed too quickly, indicated symbolically by thicker red arrows, thereby producing a thin neck that isolates a too-thick puddle that remains in the middle of the hole. **Panels C** and **D** show two example of preliminary reflection interference contrast microscopy (RICM) results obtained when a gentle stream of humid air was used as an additional driving force to mitigate the problem of necking. A mottled, dark ring remains after most of the buffer has been removed, which corresponds to the still-lubricated regions between the coverslip and the filter paper. Different values of the air pressure were empirically adjusted at the source to values of 3 psi in panel C and to 4 psi in panel D, respectively. The thickness of the buffer, if any, that remains in the extensive, relatively bright areas must be significantly less than 100 nm, as is inferred from the absence of interference fringes.

using affinity grids. As a result, there still is reason to seek alternative ways to produce thinned films on affinity grids.

Among the alternatives that seem to have not yet been investigated, one might think of applying some type of body force, such as the inertial force employed in spin coating (Larson and Rehg, 1997), or using a strong air flow to "blow off" unwanted buffer. Other possibilities might include creation of a gradient of surface tension from one edge of a grid to the other in order to generate Marangoni flow (Velarde and Zeytourian, 2014), or mechanically squeezing excess buffer from the sample with an electron-transparent "coverslip", as was attempted in some of the early work described above.

In addition, conspicuous by its near-absence from the cryo-EM literature, is the idea of simply "wicking" excess buffer by touching filter paper to the edge of a grid, as is often done during negative staining. That approach is unsatisfactory when wicking is done from one edge, of course, because it leaves behind a spherical cap of liquid that is several micrometers thick (Glaeser et al., 2016). Axially symmetric draining (wicking), on the other hand, has the potential to produce a uniformly thin film across much or all of the grid. This latter approach was referred to as "blotting from the perimeter" (Armstrong et al., 2020), or in the oxymoronic description used here, "blotting with a hole".

The Proposal to "Blot With a Hole" has Many Precedents

For clarity, the concept of draining excess buffer from the perimeter of an affinity grid is illustrated here by the cartoon shown in **Figure 1A.** The idea to "wick" (drain) sample in an axisymmetric manner is similar to the one used to form a free-standing, thin-liquid film in a Sheludko cell. For reference, cartoons describing Shelduko cells can be found in Figure 3 of (Sheludko, 1967), or perhaps even better in Figure 8 of (Mysels, 1964). The Sheludko cell, or one of its many descendants, has long been used to study the thickness-dependent interfacial forces that become relevant when the thickness values of liquid films become less than about 100 nm.

Blotting with a hole in the filter paper can also be described as an attempt to scale up the diameter of the blotted area relative to that achieved when using self-wicking EM grids (Wei et al., 2018). In the latter approach, droplets of sample material are sprayed onto the centers of many grid squares. Next, the droplets spontaneously spread until the sample touches the grid bars, upon which excess liquid is wicked away. Thus, in effect, each grid square of a self-wicking grid can be regarded as being a microscale realization of a Sheludko cell. In practice, of course, the droplets are expected to land at random positions, including some that fall directly on top of grid bars. Fortunately, even then the liquid seems to spread over the open areas of the immediately adjacent grid squares.

Understanding what may be required to produce extended, uniformly thin films by axisymmetric wicking from the perimeter of EM grids involves a number of topics that may not be familiar to most in the cryo-EM community, however. As a result, some relevant background is developed in the following section.

PRINCIPLES THAT GOVERN THE FORMATION AND STABILITY OF THIN, LIQUID FILMS

The principles involved in making samples that are suitable for cryo-EM are the same as those involved 1) in making stable foams (juxtaposed air bubbles), emulsions, and colloidal suspensions, as well as 2) in some technological applications that employ modern microfluidics. As a result, an extensive literature exists that addresses the formation and stability of thin liquid films. Recent reviews (Andrieux et al., 2021; Chatzigiannakis et al., 2021), for example, contain much that can inform our approach to making cryo-EM samples on affinity grids, and an older, more extensive review (Stubenrauch and Klitzing, 2003) is also worth pointing to.

Thin Liquid Films can Become Unstable Below a Critical Thickness

When a uniform sheet of liquid becomes thin enough, van der Waals interactions begin to exert a pressure that causes the sheet to become even thinner. It may be a surprise to learn that the pressure is inversely proportional to the 3rd power of the film thickness, see equation 7 in (Chatzigiannakis et al., 2021), even though the van der Waals interaction energy between any two atoms is inversely proportional to the 6th power of the distance. The surprisingly long-range nature of the pressure is a result of the fact that the total van der Waals energy is the sum (integral) of all such pair-wise contributions, and there are many more such interactions if a film is thick than if it is thin (Ruckenstein and Jain, 1974). As a result, it becomes energetically favorable for water molecules to move to places where the liquid is thicker. This forces the film to become thinner, i.e., it drives all thin films of liquid in the direction of rupturing. As a result, it is common experience that free-standing bubbles burst, and foams collapse as adjacent bubbles fuse with one another. Similarly, film-rupture and dewetting occurs if a liquid film, supported on a solid, is spread too thinly.

Liquid films can be made to resist rupture, however, if their apposed interfaces exert a repulsive force between one another. If, for example, the air-water interfaces of a free-standing film of buffer are coated by a charged surfactant, electrostatic repulsion increases exponentially as the interfaces approach one another. Even the polar groups of neutral surfactants exert a strong "hydration force" (Parsegian and Zemb, 2011), or osmotic pressure, that resists further thinning. When the repulsive pressure equals the van der Waals pressure to become thinner, a local minimum occurs in the disjoining pressure—see Figure 1B in (Andrieux et al., 2021), which results in a stable film. Repulsive contributions to the disjoining pressure are normally very short-ranged, however, and liquid films may not begin to resist further thinning until their thicknesses fall below a few nanometers—for an example see (Bergeron and Radke, 1992; Yaros et al., 2003).

Soap films are normally stabilized at significantly greater thickness values, however, corresponding to ones that produce interference colors in bubbles. In this range of thicknesses it may be that Marangoni forces, i.e., forces that occur when surface waves generate gradients in surface tension, stabilize films whose thickness values are hundreds of nanometers (Bhamla et al., 2017). Such films are generally too thick to be used for single-particle cryo-EM.

PRELIMINARY EXPERIMENTS HAVE BEEN DONE TO TEST THE FEASIBILITY OF BLOTTING WITH A HOLE

Equipment used previously to observe the removal of excess buffer from 3 mm diameter coverslips (Armstrong et al., 2020) has since been modified, as is described in **Supplementary Figure S1**, to obtain high-speed movies that show what happens when the same coverslips are blotted with an ~2 mm hole in filter paper. Blotting pads used for the new experiments were fabricated with a laser-beam etching tool, and these are also described in the **Supplementary Figure S1**.

Unwanted Necking can Easily Impede Complete, Axisymmetric Draining

Uniform, axisymmetric removal of buffer, illustrated by the cartoon shown in **Figure 1A**, is not as easy to achieve as might first be imagined. While the uniformly thin, sought-after profile might be achieved when liquid is removed slowly and reversibly, too rapid a removal is likely to cause the liquid to "neck down" somewhere close to the perimeter, as is illustrated schematically in **Figure 1B**. Once such a neck becomes very thin, it impedes further removal of liquid from the center. Although many different materials and designs were tried in a first round of experiments, unfavorable results, like those shown in **Supplementary Figures S2–S4** proved to be challenging to overcome,.

Axisymmetric Draining can Be Assisted by Addition of a Humid Air Stream

A second generation of experiments was then undertaken, in which blotting with an ~2 mm diameter hole was assisted by applying a driving force to the buffer. This was done by directing a stream of humid air through the hole in the filter paper, i.e., onto the sample, as is shown schematically in **Supplementary Figure S1B**. In addition, a shallow trench, shown in **Supplementary Figure S1A**, was milled just outside the empty hole to prevent contact between the filter paper and the edge of the coverslip.

After making these changes, the results of blotting with a hole became quite promising. As is shown in **Figure 1C**, buffer can be removed from nearly all of the area that corresponds to an ~2 mm diameter hole in the filter paper. A thin film of buffer still remains, which is clearly less than 100 nm in thickness, the value at which a first (dark) interference fringe would appear.

DISCUSSION

Both the relative humidity and the flow rate are important parameters to control in an air stream that is used to assist axisymmetric draining. Too little flow will still leave a too-large "cap" of liquid at the center; too large a flow might cause the liquid film to rupture and to dewet the substrate; too low humidity will cause excessive evaporation to occur; and too high humidity may produce condensation to form.

Demonstration of the potential usefulness of blotting with a hole thus requires that similar results first be achieved when using EM grids rather than a surrogate, 3 mm coverslip. In addition, such grids would have to be vitrified and examined in an electron microscope, preferably one equipped with an energy filter, so that their thickness values can be measured, for example, by the

method described in (Rice et al., 2018). The final proof of usefulness will then depend upon whether the resolution achieved in single-particle cryo-EM maps proves to be as good as, or even better than, that achieved with other grid-preparation methods, assuming that all else remains constant.

While axisymmetric draining seems to be an appropriate approach to use with affinity grids, it may be that it will also be an effective alternative to consider when using standard, holey grids any type of affinity grid could be used, of course, to avoid diffusion to the AWI. Of the options already listed in **Table 1**, streptavidin affinity grids have the advantage that the resolution retained in the specimen can be easily and unequivocally determined from the highest spatial frequency at which Bragg peaks remain visible in the Fourier transforms of images (Han et al., 2017).

DATA AVAILABILITY STATEMENT

The datasets presented in this article are not readily available because they refer to work that previously was published to authors of work that is reviewed here. Restrictions do not apply to the datasets. Requests to access the datasets should be directed to RG, rmglaeser@lbl.gov.

AUTHOR CONTRIBUTIONS

Conception and design of preliminary work: MA, DF, RG, and B-GH. Conception and drafting the paper: RG and B-GH. Data acquisition and interpretation of preliminary results: B-GH. Design, assembly, and installation of modifications to the Vitrobot that were made in-house, and which were used to obtain the preliminary results: MA. Design and coding of software to control data acquisition and analysis: MA. Editing and approval of the submitted manuscript: MA, DF, RG, and B-GH.

FUNDING

This work was supported in part by funding awarded as NIH grant R21 GM135666, administered at LBNL under Contract No. DE-AC02-05CH11231.

ACKNOWLEDGMENTS

We thank FEI Inc., now Thermo Fisher Scientific, for donating a modified Vitrobot to the Lawrence Berkeley National Laboratory for work that subsequently led to the preliminary results that have been reported as part of this Perspective.

SUPPLEMENTARY MATERIAL

The Supplementary Material for this article can be found online at: https://www.frontiersin.org/articles/10.3389/fmolb.2022.864829/full#supplementary-material

REFERENCES

Andrieux, S., Muller, P., Kaushal, M., Macias Vera, N. S., Bollache, R., Honorez, C., et al. (2021). Microfluidic Thin Film Pressure Balance for the Study of Complex Thin Films. *Lab. Chip.* 21, 412–420. doi:10.1039/d0lc00974a

Armstrong, M., Han, B.-G., Gomez, S., Turner, J., Fletcher, D. A., and Glaeser, R. M. (2020). Microscale Fluid Behavior During Cryo-EM Sample Blotting. *Biophysical J.* 118, 708–719. doi:10.1016/j.bpj.2019.12.017

Arnold, S. A., Albiez, S., Bieri, A., Syntychaki, A., Adaixo, R., McLeod, R. A., et al. (2017). Blotting-free and Lossless Cryo-Electron Microscopy Grid Preparation from Nanoliter-Sized Protein Samples and Single-Cell Extracts. *J. Struct. Biol.* 197, 220–226. doi:10.1016/j.jsb.2016.11.002

Benjamin, C. J., Wright, K. J., Hyun, S.-H., Krynski, K., Yu, G., Bajaj, R., et al. (2016). Nonfouling NTA-PEG-Based TEM Grid Coatings for Selective Capture of Histidine-Tagged Protein Targets from Cell Lysates. *Langmuir.* 32, 551–559. doi:10.1021/acs.langmuir.5b03445

Bergeron, V., and Radke, C. J. (1992). Equilibrium Measurements of Oscillatory Disjoining Pressures in Aqueous Foam Films. *Langmuir.* 8, 3020–3026. doi:10.1021/la00048a028

Bhamla, M. S., Chai, C., Àlvarez-Valenzuela, M. A., Tajuelo, J., and Fuller, G. G. (2017). Interfacial Mechanisms for Stability of Surfactant-Laden Films. *PloS one.* 12, e0175753. doi:10.1371/journal.pone.0175753

Carragher, B., Cheng, Y., Frost, A., Glaeser, R. M., Lander, G. C., Nogales, E., et al. (2019). Current Outcomes when Optimizing 'standard' Sample Preparation for Single-particle cryo-EM. *J. Microsc.* 276, 39–45. doi:10.1111/jmi.12834

Chang, C. F., Ohno, T., and Glaeser, R. M. (1985a). The Fatty Acid Monolayer Technique for Preparing Frozen-Hydrated Specimens. *J. Elec. Microsc. Tech.* 2, 59–65. doi:10.1002/jemt.1060020108

Chang, C. F., Mizushima, S., and Glaeser, R. M. (1985b). Projected Structure of the Pore-Forming OmpC Protein from *Escherichia coli* Outer Membrane. *Biophysical J.* 47, 629–639. doi:10.1016/s0006-3495(85)83959-x

Chatzigiannakis, E., Jaensson, N., and Vermant, J. (2021). Thin Liquid Films: Where Hydrodynamics, Capillarity, Surface Stresses and Intermolecular Forces Meet. *Curr. Opin. Colloid Interf. Sci.* 53, 101441. doi:10.1016/j.cocis.2021.101441

D'Imprima, E., Floris, D., Joppe, M., Sánchez, R., Grininger, M., and Kühlbrandt, W. (2019). Protein Denaturation at the Air-Water Interface and How to Prevent it. *Elife.* 8, e42747. doi:10.7554/eLife.42747

Drulyte, I., Johnson, R. M., Hesketh, E. L., Hurdiss, D. L., Scarff, C. A., Porav, S. A., et al. (2018). Approaches to Altering Particle Distributions in Cryo-Electron Microscopy Sample Preparation. *Acta Cryst. Sect D Struct. Biol.* 74, 560–571. doi:10.1107/s2059798318006496

Dubochet, J., Adrian, M., Chang, J.-J., Homo, J.-C., Lepault, J., McDowall, A. W., et al. (1988). Cryo-Electron Microscopy of Vitrified Specimens. *Quart. Rev. Biophys.* 21, 129–228. doi:10.1017/s0033583500004297

Fan, X., Wang, J., Zhang, X., Yang, Z., Zhang, J.-C., Zhao, L., et al. (2019). Single Particle Cryo-EM Reconstruction of 52 kDa Streptavidin at 3.2 Angstrom Resolution. *Nat. Commun.* 10, 2386. doi:10.1038/s41467-019-10368-w

Frederik, P. M., Stuart, M. C. A., Bomans, P. H. H., and Busing, W. M. (1989). Phospholipid, Nature's Own Slide and Cover Slip for Cryo-Electron Microscopy. *J. Microscopy-Oxford.* 153, 81–92. doi:10.1111/j.1365-2818.1989.tb01469.x

Gillies, J. P., Reimer, J. M., Karasmanis, E. P., Lahiri, I., Htet, Z. M., Leschziner, A. E., et al. (2021). Structural Basis for Cytoplasmic Dynein-1 Regulation by Lis1. *Elife*, 11, doi:10.1101/2021.06.11.448119

Glaeser, R. M., Han, B.-G., Csencsits, R., Killilea, A., Pulk, A., and Cate, J. H. D. (2016). Factors that Influence the Formation and Stability of Thin, Cryo-EM Specimens. *Biophysical J.* 110, 749–755. doi:10.1016/j.bpj.2015.07.050

Glaeser, R. M., Nogales, E., and Chiu, W. (2021). "Single-Particle Cryo-EM of Biological Macromolecules,". Editor R. M. Glaeser (IOP Publishing).

Glaeser, R. M. (2021). Preparing Better Samples for Cryo-Electron Microscopy: Biochemical Challenges Do Not End with Isolation and Purification. *Annu. Rev. Biochem.* 90, 451–474. doi:10.1146/annurev-biochem-072020-020231

Han, B.-G., and Glaeser, R. M. (2021). Simple Assay for Adsorption of Proteins to the Air-Water Interface. *J. Struct. Biol.* 213, 107798. doi:10.1016/j.jsb.2021.107798

Han, B.-G., Watson, Z., Cate, J. H. D., and Glaeser, R. M. (2017). Monolayer-crystal Streptavidin Support Films Provide an Internal Standard of Cryo-EM Image Quality. *J. Struct. Biol.* 200, 307–313. doi:10.1016/j.jsb.2017.02.009

Hayward, S. B., Grano, D. A., Glaeser, R. M., and Fisher, K. A. (1978). Molecular Orientation of Bacteriorhodopsin Within the Purple Membrane of Halobacterium Halobium. *Proc. Natl. Acad. Sci. U.S.A.* 75, 4320–4324. doi:10.1073/pnas.75.9.4320

Huber, S. T., Sarajlic, E., Huijink, R., Weis, F., Evers, W. H., and Jakobi, A. J. (2022). Nanofluidic Chips for Cryo-EM Structure Determination from Picoliter Sample Volumes. *eLife.* 11, e72629. doi:10.7554/eLife.72629

Joppe, M., D'Imprima, E., Salustros, N., Paithankar, K. S., Vonck, J., Grininger, M., et al. (2020). The Resolution Revolution in cryoEM Requires High-Quality Sample Preparation: a Rapid Pipeline to a High-Resolution Map of Yeast Fatty Acid Synthase. *Int. Union Crystallogr. J.* 7, 220–227. doi:10.1107/s2052252519017366

Kasinath, V., Beck, C., Sauer, P., Poepsel, S., Kosmatka, J., Faini, M., et al. (2021). JARID2 and AEBP2 Regulate PRC2 in the Presence of H2AK119ub1 and Other Histone Modifications. *Science.* 371, eabc3393. doi:10.1126/science.abc3393

Kelly, D. F., Dukovski, D., and Walz, T. (2010a). A Practical Guide to the Use of Monolayer Purification and Affinity Grids. *Methods in Enzymology,Cryo-EM A Sample Preparation and Data Collection.* 481, 83–107. doi:10.1016/s0076-6879(10)81004-3

Kelly, D. F., Dukovski, D., and Walz, T. (2010b). Strategy for the Use of Affinity Grids to Prepare Non-his-Tagged Macromolecular Complexes for Single-Particle Electron Microscopy. *J. Mol. Biol.* 400, 675–681. doi:10.1016/j.jmb.2010.05.045

Klebl, D. P., Gravett, M. S. C., Kontziampasis, D., Wright, D. J., Bon, R. S., Monteiro, D. C. F., et al. (2020). Need for Speed: Examining Protein Behavior during CryoEM Grid Preparation at Different Timescales. *Structure.* 28, 1238–1248. doi:10.1016/j.str.2020.07.018

Lahiri, I., Xu, J., Han, B. G., Oh, J., Wang, D., DiMaio, F., et al. (2019). 3.1 Å Structure of Yeast RNA Polymerase II Elongation Complex Stalled at a Cyclobutane Pyrimidine Dimer Lesion Solved Using Streptavidin Affinity Grids. *J. Struct. Biol.* 207, 270–278. doi:10.1016/j.jsb.2019.06.004

Larson, R. G., and Rehg, T. J. (1997). "Spin Coating," in *Liquid Film Coating: Scientific Principles and Their Technological Implications*. Editors S. F. Kistler and P. M. Schweizer (Dordrecht: Springer Netherlands), 709709–734734. doi:10.1007/978-94-011-5342-3_20

Liu, N., Zhang, J., Chen, Y., Liu, C., Zhang, X., Xu, K., et al. (2019). Bioactive Functionalized Monolayer Graphene for High-Resolution Cryo-Electron Microscopy. *J. Am. Chem. Soc.* 141, 4016–4025. doi:10.1021/jacs.8b13038

Llaguno, M. C., Xu, H., Shi, L., Huang, N., Zhang, H., Liu, Q., et al. (2014). Chemically Functionalized Carbon Films for Single Molecule Imaging. *J. Struct. Biol.* 185, 405–417. doi:10.1016/j.jsb.2014.01.006

Mysels, K. J. (1964). Soap Films and Some Problems in Surface and Colloid Chemistry1. *J. Phys. Chem.* 68, 3441–3448. doi:10.1021/j100794a001

Naydenova, K., Peet, M. J., and Russo, C. J. (2019). Multifunctional Graphene Supports for Electron Cryomicroscopy. *Proc. Natl. Acad. Sci. U.S.A.* 116, 11718–11724. doi:10.1073/pnas.1904766116

Naydenova, K., and Russo, C. J. (2017). Measuring the Effects of Particle Orientation to Improve the Efficiency of Electron Cryomicroscopy. *Nat. Commun.* 8, 629. doi:10.1038/s41467-017-00782-3

Noble, A. J., Dandey, V. P., Wei, H., Brasch, J., Chase, J., Acharya, P., et al. (2018). Routine Single Particle cryoEM Sample and Grid Characterization by Tomography. *Elife.* 7, e34257. doi:10.7554/eLife.34257

Parsegian, V. A., and Zemb, T. (2011). Hydration Forces: Observations, Explanations, Expectations, Questions. *Curr. Opin. Colloid Interf. Sci.* 16, 618–624. doi:10.1016/j.cocis.2011.06.010

Ravelli, R. B. G., Nijpels, F. J. T., Henderikx, R. J. M., Weissenberger, G., Thewessem, S., Gijsbers, A., et al. (2020). Cryo-EM Structures from Sub-nl Volumes Using Pin-Printing and Jet Vitrification. *Nat. Commun.* 11, 2563. doi:10.1038/s41467-020-16392-5

Rice, W. J., Cheng, A., Noble, A. J., Eng, E. T., Kim, L. Y., Carragher, B., et al. (2018). Routine Determination of Ice Thickness for Cryo-EM Grids. *J. Struct. Biol.* 204, 38–44. doi:10.1016/j.jsb.2018.06.007

Ruckenstein, E., and Jain, R. K. (1974). Spontaneous Rupture of Thin Liquid Films. *J. Chem. Soc. Faraday Trans.* 70, 132–147. doi:10.1039/f29747000132

Sauer, P. V., Dominguez-Martin, M. A., Kirst, H., Sutter, M., Bina, D., Greber, B. J., et al. (2021). Structures of the Cyanobacterial Phycobilisome. *bioRxiv.* doi:10.1101/2021.11.15.468712

Sheludko, A. (1967). Thin Liquid Films. *Adv. Colloid Interf. Sci.* 1, 391–464. doi:10.1016/0001-8686(67)85001-2

Stubenrauch, C., and Klitzing, R. v. (2003). Disjoining Pressure in Thin Liquid Foam and Emulsion Films-New Concepts and Perspectives. *J. Phys. Condens. Matter.* 15, R1197–R1232. doi:10.1088/0953-8984/15/27/201

Taylor, D. W., Kelly, D. F., Cheng, A., and Taylor, K. A. (2007). On the Freezing and Identification of Lipid Monolayer 2-D Arrays for Cryoelectron Microscopy. *J. Struct. Biol.* 160, 305–312. doi:10.1016/j.jsb.2007.04.011

Taylor, K. A., and Glaeser, R. M. (1973). Hydrophilic Support Films of Controlled Thickness and Composition. *Rev. Scientific Instr.* 44, 1546–1547. doi:10.1063/1.1685999

Taylor, K. A., and Glaeser, R. M. (1976). Electron Microscopy of Frozen Hydrated Biological Specimens. *J. Ultrastruct. Res.* 55, 448–456. doi:10.1016/s0022-5320(76)80099-8

Taylor, K. A., and Glaeser, R. M. (2008). Retrospective on the Early Development of Cryoelectron Microscopy of Macromolecules and a Prospective on Opportunities for the Future. *J. Struct. Biol.* 163, 214–223. doi:10.1016/j.jsb.2008.06.004

Trurnit, H. J. (1960). A Theory and Method for the Spreading of Protein Monolayers. *J. Colloid Sci.* 15, 1–13. doi:10.1016/0095-8522(60)90002-7

Velarde, M. G., and Zeytourian, R. K. (2014). *Interfacial Phenomena and the Marangoni Effect*. Vienna: Springer.

Vinothkumar, K. R., and Henderson, R. (2016). Single Particle Electron Cryomicroscopy: Trends, Issues and Future Perspective. *Q. Rev. Biophys.* 49, e13–25. doi:10.1017/S0033583516000068

Wang, F., Liu, Y., Yu, Z., Li, S., Feng, S., Cheng, Y., et al. (2020). General and Robust Covalently Linked Graphene Oxide Affinity Grids for High-Resolution Cryo-EM. *Proc. Natl. Acad. Sci. U.S.A.* 117, 24269–24273. doi:10.1073/pnas.2009707117

Wei, H., Dandey, V. P., Zhang, Z., Raczkowski, A., Rice, W. J., Carragher, B., et al. (2018). Optimizing "Self-Wicking" Nanowire Grids. *J. Struct. Biol.* 202, 170–174. doi:10.1016/j.jsb.2018.01.001

Weissenberger, G., Henderikx, R. J. M., and Peters, P. J. (2021). Understanding the Invisible Hands of Sample Preparation for Cryo-EM. *Nat. Methods.* 18, 463–471. doi:10.1038/s41592-021-01130-6

Yaros, H. D., Newman, J., and Radke, C. J. (2003). Evaluation of DLVO Theory with Disjoining-Pressure and Film-Conductance Measurements of Common-Black Films Stabilized with Sodium Dodecyl Sulfate. *J. Colloid Interf. Sci.* 262, 442–455. doi:10.1016/s0021-9797(03)00199-1

Yu, G., Li, K., and Jiang, W. (2016). Antibody-Based Affinity Cryo-EM Grid. *Methods.* 100, 16–24. doi:10.1016/j.ymeth.2016.01.010

Conflict of Interest: The authors declare that the research was conducted in the absence of any commercial or financial relationships that could be construed as a potential conflict of interest.

Publisher's Note: All claims expressed in this article are solely those of the authors and do not necessarily represent those of their affiliated organizations, or those of the publisher, the editors and the reviewers. Any product that may be evaluated in this article, or claim that may be made by its manufacturer, is not guaranteed or endorsed by the publisher.

frontiers | Frontiers in Molecular Biosciences

METHODS
published: 27 May 2022
doi: 10.3389/fmolb.2022.912363

Light 'Em up: Efficient Screening of Gold Foil Grids in Cryo-EM

Wim J. H. Hagen *

European Molecular Biology Laboratory, Structural and Computational Biology Unit, Heidelberg, Germany

Transmission electron cryo-microscopy (cryo-EM) allows for obtaining 3D structural information by imaging macromolecules embedded in thin layers of amorphous ice. To obtain high-resolution structural information, samples need to be thin to minimize inelastic scattering which blurs images. During data collection sessions, time spent on finding areas on the cryo-EM grid with optimal ice thickness should be minimized as imaging time on high-end Transmission Electron Microscope TEM systems is costly. Recently, grids covered with thin gold films have become popular due to their stability and reduced beam-induced motion of the sample. Gold foil grids have substantially different densities between the gold foil and ice, effectively resulting in the loss of dynamic range between thin and thick regions of ice, making it challenging to find areas with suitable ice thickness efficiently during grid screening and thus increase expensive imaging time. Here, an energy filter-based plasmon imaging is presented as a fast and easy method for grid screening of the gold foil grids.

Keywords: cryo electron microscopy (cryo-EM), structural biology, screening, sample preparation, method

OPEN ACCESS

Edited by:
Arjen J. Jakobi,
Delft University of Technology, Netherlands

Reviewed by:
Clint Potter,
New York Structural Biology Center, United States
Rebecca F. Thompson,
University of Leeds, United Kingdom

***Correspondence:**
Wim J. H. Hagen
wim.hagen@embl.de

Specialty section:
This article was submitted to Structural Biology, a section of the journal Frontiers in Molecular Biosciences

Received: *05 April 2022*
Accepted: *11 May 2022*
Published: *27 May 2022*

Citation:
Hagen WJ (2022) Light 'Em up: Efficient Screening of Gold Foil Grids in Cryo-EM. Front. Mol. Biosci. 9:912363. doi: 10.3389/fmolb.2022.912363

INTRODUCTION

Structure determination by cryo-EM (Frank 2006) ideally requires vitrified specimens with a thin frozen-hydrated layer only slightly thicker than the structure of interest, since final image resolution has a direct correlation with ice thickness (Rice et al., 2018; Rheinberger et al., 2021). The sample carrier typically used for vitrification of cryo-EM grids is a metal grid covered with a thin electron-transparent carbon film containing a pattern of holes "holey-carbon grid" (Ermantraut et al., 1998; Quispe et al., 2007) that are to be filled with thin ice during the vitrification process. For this, a thin layer of sample is applied to the grid and then flash-frozen into a cryogen (Adrian et al., 1984). Although the vitrification process has seen several improvements in recent years (Jain et al., 2012; Dandey et al., 2018; Kontziampasis et al., 2019; Rubinstein et al., 2019), controlling ice thickness remains challenging and screening of grids in the TEM is still required to assess particle distribution over a range of ice thickness since ice can be too thin (no or few particles) or too thick (overlapping particles). Screening involves acquiring image montages at low magnification to visualize the entire grid area, optionally followed by images at a medium magnification at selected positions expected to have optimal ice thickness (Carragher et al., 2000; Suloway et al., 2005); particle concentration is subsequently inspected in those selected areas. Several software packages for automated data acquisition, both open source and commercial, exist to aid this screening process (Tan et al., 2016) and the usage strategies of these software packages are similar. Screening typically starts with acquiring a full overview of the EM grid at very low magnification, followed by images or montages of single grid squares at medium magnification, such that holes in the film with sizes of several micrometers can be distinguished. On any TEM system, this requires using 1) the lowest possible magnification in LM mode (the objective lens is switched off) for mapping the entire grid, and 2)

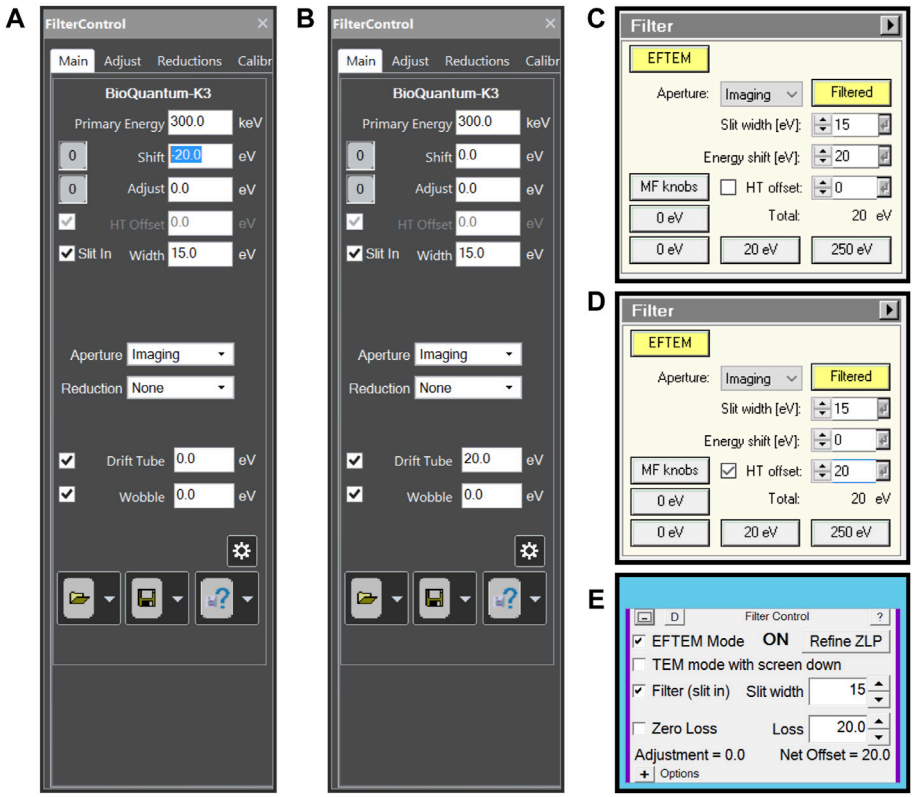

FIGURE 1 | Energy filter settings for plasmon imaging when **(A)** using a Gatan energy filter controlled by Digital Micrograph software and using energy shift, **(B)** using a Gatan energy filter controlled by Digital Micrograph software and using Drift tube offset, **(C)** using a Thermo Scientific Selectris(X) energy filter using energy shift, **(D)** using a Thermo Scientific Selectris(X) energy filter using high tension offset and **(E)** using any energy filter through SerialEM.

using a medium magnification LM mode for imaging or montaging a single grid square or using a low magnification Selected Area SA mode (objective lens switched on) to visualise grid squares. A microscope user will then visually inspect the images to find areas with thin ice based on how dark or light the holes look. Similarly, software packages for automatic data acquisition use grey values of the holes in an image to allow a user to set a filter to select holes within a certain ice-thickness range. This procedure has been very successful for samples prepared on standard holey carbon grids and greatly speeds up the acquisition session setup.

One of many limitations of cryo-EM structure determination has been beam-induced particle movement, in which particles in thin ice move around during exposure to an electron beam. This limitation has been minimized by the development of UltrAuFoil® grids (Naydenova et al., 2020; Russo and Passmore 2016, Russo and Passmore 2014). UltrAuFoil® grids, commercially available from Quantifoil Micro Tools GmbH, use a gold carrier mesh grid covered with a thin gold film with patterned holes, similar grids are also commercially available from Protochips. Compared to the historically used holey carbon films, thin gold films are considerably less electron transparent, while thin ice in the holes of the film is similarly electron transparent. This leads to a larger contrast range in images which include the gold foil grids. The larger contrast difference in the TEM requires some image processing filter or processing to judge relative ice thickness in the holes. The design of such a filtering scheme should be based on how electrons differently interact with the sample.

When electrons used for imaging pass through the sample, several interactions take place with the sample: no scattering, elastic scattering, and inelastic scattering. Electrons that are inelastically scattered lose energy and will be focussed differently by the downstream optics of the microscope leading to image blurring. Inelastic scattering depends on sample thickness: the thicker the sample, the larger the chance that electrons will be scattered once, or multiple times while passing through the sample. The resulting blurring effect can be reduced by using an energy filter, which is a dispersive prism that separates electrons by the energy they possess, followed by an energy selecting slit to only let through elastically scattered electrons that have not lost energy passing through the sample. This is called Zero Loss Imaging. The energy selecting slit can also be offset to only let certain energy loss ranges pass, e.g. the plasmon regime. Plasmons are inelastic scattering events with low energy loss (<50 eV). In the plasmon regime, vitreous, cubic, and hexagonal ice show a broad plasmon peak around 23 eV (Leapman and Sun 1995), while gold shows narrow plasmon peaks at very low energy losses, buried inside the tail of the zero-loss peak as seen

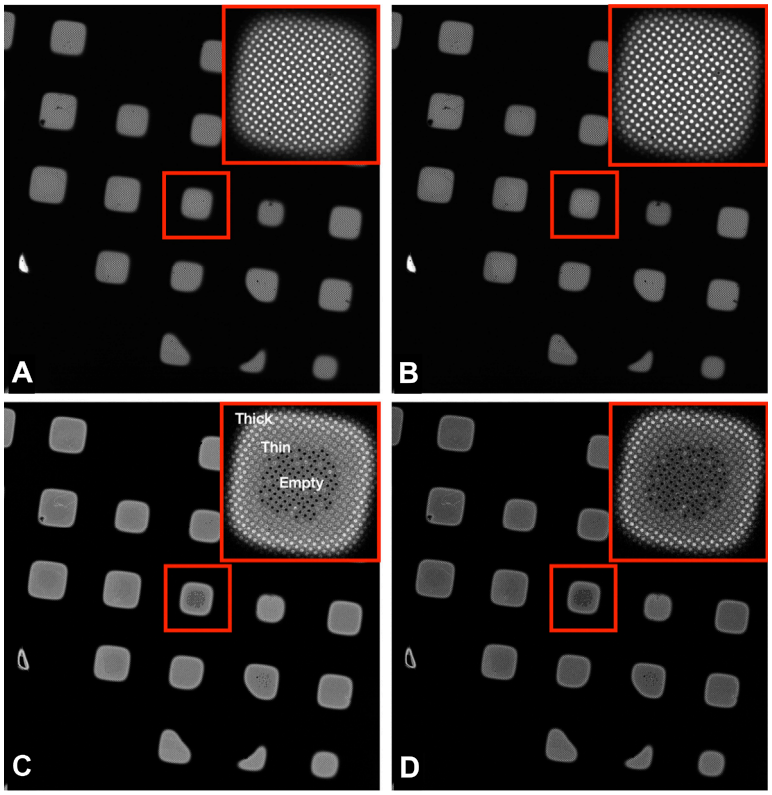

FIGURE 2 | Images of a Quantifoil UltrAuFoil 1.2/1.3 grid, acquired on a Thermo Scientific Titan Krios G1with Gatan Bioquantum K2 detector using EFTEM LM mode ×135 magnification (field of view ×418 433 µm), 1-s exposure, total dose 0.001 e/Å^2. The upper right corners show a magnified inset of the marked central square. Image contrast/brightness has not been changed manually. **(A)** Unfiltered image, **(B)** Zero loss filtered linear mode image, **(C)** plasmon counting mode image, and **(D)** plasmon counting mode image with 40 µm SA aperture inserted.

on non-monochromated TEM systems (Schaffer et al., 2010). Positioning an energy slit around 20 eV energy loss, with an energy slit width of 15 eV to block the zero-loss electrons, produces images with a smaller image contrast range, which simplifies the visual interpretation of ice thickness in the holes. Additionally, using an objective aperture limits the energy filter's collection angle, further decreasing the contrast range of the plasmon images. Under low electron exposure conditions, the intensity of plasmon images is low enough to use counting mode when using direct detectors, which minimizes background noise in the acquired images, while increased specimen thickness will lead to more plasmon events. A properly aligned microscope and a properly tuned energy filter allow identification of relative ice thickness at even the lowest microscope magnifications with very low exposure dose. The nature of the plasmon mechanism does not allow for distinguishing between vitreous, cubic, or hexagonal ice, it only indicates relative thickness, albeit with great detail. Several methods have been published to assist microscope operators with ice thickness determination, mainly based on other variations of energy-filter usage (Rice et al., 2018; Rheinberger et al., 2021). Plasmon imaging provides an additional method especially suitable for screening gold foil grids on TEM systems equipped with an energy filter.

METHODS

Assuming a properly aligned microscope and properly tuned energy filter, the only setting needed is a 15 eV energy slit width and 20 eV energy loss offset. On Thermo Scientific Selectris(X) energy filters, the energy loss offset can be achieved either using the magnetic prism (energy shift) or by the energy filter control panel changing the high tension (HT offset). For certain types of Gatan energy filters, HT offset is not available and the two options then are energy shift or using the drift tube. All options can be done in most currently available software packages as shown in **Figure 1**.

In typical cryo-TEM systems, optimal alignment of the microscope, especially for the lower magnification ranges is a condition rarely met. Several alignments and energy filter settings need to be tweaked, which might not always be possible for the user as it might require service credentials from the microscope vendor. One can, however, work around these issues through the many available data acquisition software packages. All steps required are described next. The minimum starting point is that EFTEM LM and EFTEM SA mode are properly aligned by the microscope vendor, meaning that the energy filter can image at all low magnifications without the differential pumping aperture between the column and the projection chamber

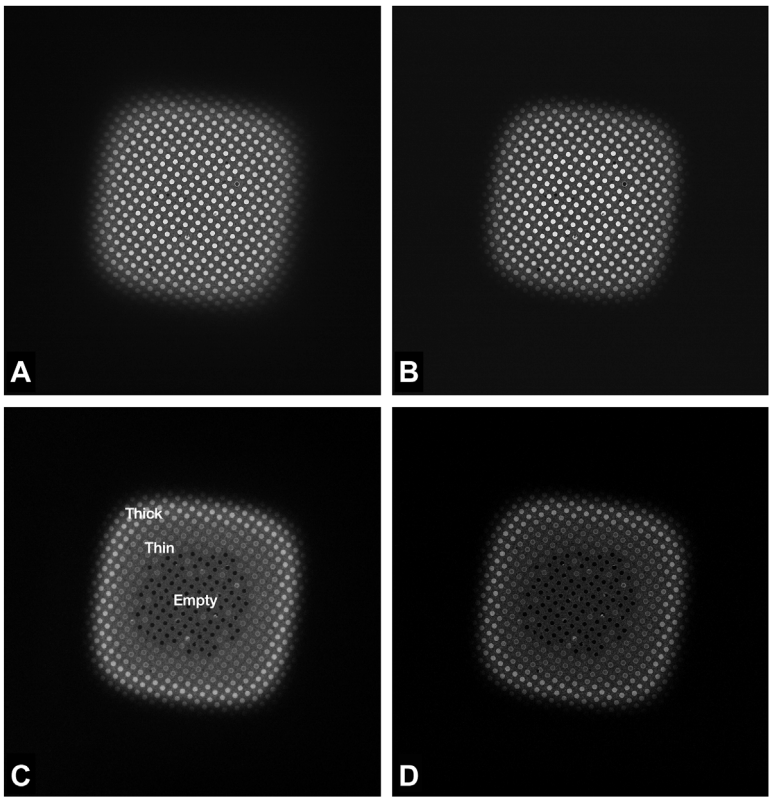

FIGURE 3 | Images of a Quantifoil UltrAuFoil 1.2/1.3 grid square, acquired on a Thermo Scientific Titan Krios G1with Gatan Bioquantum K2 detector using EFTEM LM mode ×740 magnification (field of view ×67 69 µm), 1-s exposure, total dose 0.003 e/Å^2. Image contrast/brightness has not been changed manually. **(A)** Unfiltered image, **(B)** Zero loss filtered linear mode image, **(C)** plasmon counting mode image, and **(D)** plasmon counting mode image with 40 µm SA aperture inserted.

blocking the field of view. Using the plasmon regime requires an energy filter to be properly tuned at several different magnifications. The currently most popular energy filters are made by Gatan, whose Digital Micrograph software has a GIF Settings Manager to store energy filter tuning per microscope magnification. This feature needs to be activated and set up by the Gatan service engineer upon installation of the energy filter. Thermo Scientific Selectris(X) energy filters store tuning values per magnification by default. The energy filter needs to be tuned for each magnification intended to be used for plasmon imaging. Any energy loss imaging has to be done with the sample in focus as defocus leads to image blur. This is more important for SA mode (objective lens on), where tens of micro-meter focus offset lead to extreme blurring, than for LM mode (objective lens off), where hundreds of micro-meter focus offset lead to extreme blurring. Setting correct focus and fixing image astigmatism in LM mode is often overlooked during alignment of the microscope, but it is easy to fix using available data acquisition software:

- Load a vitrified gold grid into the microscope.
- Set the stage to eucentric height (minimum image movement when wobbling specimen tilt using the goniometer).
- Set the energy filter to 15 eV energy slit width and 20 eV energy loss.
- Using live imaging in any capable camera software, adjust defocus and image astigmatism until the image appears sharp. On Thermo Scientific TEM systems, in LM mode the diffraction stigmator acts as the image stigmator. When using a direct detector, this can be done in linear or counting mode depending on the camera dose rate.

On Thermo Scientific TEM systems, the stigmator settings are automatically saved as user settings, and the defocus setting needs to be written down to be used as an offset to be applied in the data acquisition software used. When using LM mode magnification, one can additionally use an SA aperture (in LM mode, the SA aperture acts as the objective aperture). When using a low SA mode magnification, one can use a standard objective aperture. An aperture increases the visible contrast difference of varying ice thickness.

SerialEM software has functionality to set different energy shift values for different low dose modes through its energy Filter Control panel (**Figure 1E**), making plasmon imaging easy to setup. Thermo Scientific EPU does not have such functionality, meaning any energy shift has to be set outside the EPU software package (**Figures 1A–D**). When using direct detectors, the

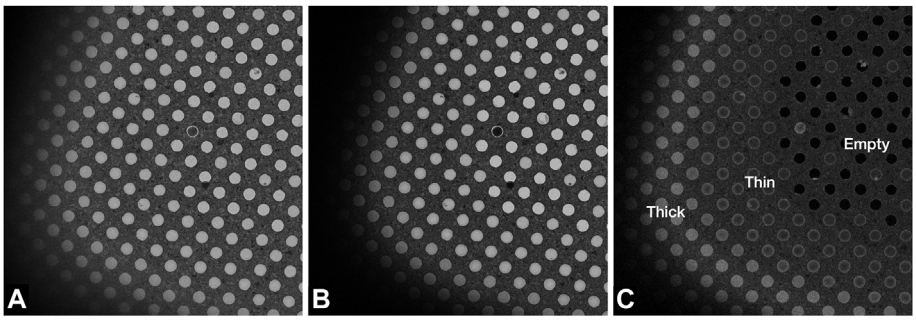

FIGURE 4 | Images of a Quantifoil UltrAuFoil 1.2/1.3 grid, acquired on a Thermo Scientific Titan Krios G1with Gatan Bioquantum K2 detector using EFTEM SA mode 2250x magnification (field of view ×23 24 µm) with a 70 µm objective aperture inserted, 1-s exposure, total dose 0.003 e/Å^2. Image contrast/brightness has not been changed manually. **(A)** Unfiltered image with -100 µm defocus, **(B)** Zero loss filtered linear mode image with −100 µm defocus, and **(C)** plasmon counting mode image without any defocus.

camera dose rate will be very low allowing the use of counting mode.

RESULTS

Plasmon imaging shows empty holes as black since no sample is present and interaction of electrons with the sample is completely absent. Holes covered with thin ice show as signal, with signal level increasing with sample thickness, even in images acquired at the very lowest magnification that can be used on the microscope. Since the plasmon signal is very low, counting mode can be used, which minimizes the background noise of the images. One can additionally use an aperture to improve imaging contrast, which further increases the visibility of ice thickness differences. The differences between the three strategies (LM grid mapping, LM square-mapping, SA square-mapping) typically used when inspecting grids are shown for grid LM mapping (**Figure 2**), visualizing a grid square using a single image (**Figure 3**), and using image montages using a low SA magnification (**Figure 4**). The two most popular SPA data acquisition software packages SerialEM and Thermo Scientific EPU both have functionality to detect light holes against darker background, and dark holes against lighter background, making hole finding algorithms compatible with the plasmon method.

DISCUSSION

A method has been described to assist microscope users in quickly judging relative ice thickness for cryo-EM data acquisition. It requires an energy filter but no additional images and processing steps that are typically required to produce thickness maps (Rheinberger et al., 2021). Although results shown have been obtained using a post-column energy filter, there is no practical limitation for applying the same principle using an in-column energy filter. However, the described method only provides relative thickness information whereas thickness maps provide absolute thickness, albeit with less detail about any ice gradients within single holes in the gold film. The method is less suitable for carbon film grids since plasmon imaging has to be done in-focus, making holes not visible when ice is thick. Zero-loss imaging with high defocus is more suitable for carbon film grids. I hope this simple and readily available plasmon method helps cryo-EM users in choosing optimal areas for imaging on vitrified gold foil grids. Additionally, this method could open new possibilities by skipping the grid square step altogether by targeting holes directly from the lowest magnification montages.

DATA AVAILABILITY STATEMENT

The original contributions presented in the study are included in the article/supplementary material, further inquiries can be directed to the corresponding author.

AUTHOR CONTRIBUTIONS

WH wrote the manuscript.

FUNDING

This work was supported by the European Molecular Biology Laboratory.

ACKNOWLEDGMENTS

I thank Sonja Welsch, Svetlana Dodonova and William Wan for their comments.

REFERENCES

Adrian, M., Dubochet, J., Lepault, J., and McDowall, A. W. (1984). Cryo-electron Microscopy of Viruses. *Nature* 308, 32–36. doi:10.1038/308032a0

Carragher, B., Kisseberth, N., Kriegman, D., Milligan, R. A., Potter, C. S., Pulokas, J., et al. (2000). Leginon: an Automated System for Acquisition of Images from Vitreous Ice Specimens. *J. Struct. Biol.* 132, 33–45. doi:10.1006/jsbi.2000.4314

Dandey, V. P., Wei, H., Zhang, Z., Tan, Y. Z., Acharya, P., Eng, E. T., et al. (2018). Spotiton: New Features and Applications. *J. Struct. Biol.* 202, 161–169. doi:10.1016/j.jsb.2018.01.002

Ermantraut, E., Wohlfart, K., and Tichelaar, W. (1998). Perforated Support Foils with Pre-defined Hole Size, Shape and Arrangement. *Ultramicroscopy* 74, 75–81. doi:10.1016/S0304-3991(98)00025-4

Frank, J. (2006). *Three-Dimensional Electron Microscopy of Macromolecular Assemblies: Visualization of Biological Molecules in Their Native State*. New York: Oxford University Press. doi:10.1093/acprof:oso/9780195182187.001.0001

Jain, T., Sheehan, P., Crum, J., Carragher, B., and Potter, C. S. (2012). Spotiton: A Prototype for an Integrated Inkjet Dispense and Vitrification System for Cryo-TEM. *J. Struct. Biol.* 179, 68–75. doi:10.1016/j.jsb.2012.04.020

Kontziampasis, D., Klebl, D. P., Iadanza, M. G., Scarff, C. A., Kopf, F., Sobott, F., et al. (2019). A Cryo-EM Grid Preparation Device for Time-Resolved Structural Studies. *Int. Union Crystallogr. J.* 6, 1024–1031. doi:10.1107/S2052252519011345

Leapman, R. D., and Sun, S. (1995). Cryo-electron Energy Loss Spectroscopy: Observations on Vitrified Hydrated Specimens and Radiation Damage. *Ultramicroscopy* 59 (1-4), 71–79. doi:10.1016/0304-3991(95)00019-W

Naydenova, K., Jia, P., and Russo, C. J. (2020). Cryo-EM with Sub-1 Å Specimen Movement. *Science* 370, 223–226. doi:10.1126/SCIENCE.ABB7927

Quispe, J., Damiano, J., Mick, S. E., Nackashi, D. P., Fellmann, D., Ajero, T. G., et al. (2007). An Improved Holey Carbon Film for Cryo-Electron Microscopy. *Microsc. Microanal.* 13, 365–371. doi:10.1017/S1431927607070791

Rheinberger, J., Oostergetel, G., Resch, G. P., and Paulino, C. (2021). Optimized Cryo-EM Data-Acquisition Workflow by Sample-Thickness Determination. *Acta Cryst. Sect. D. Struct. Biol.* 77, 565–571. doi:10.1107/S205979832100334X

Rice, W. J., Cheng, A., Noble, A. J., Eng, E. T., Kim, L. Y., Carragher, B., et al. (2018). Routine Determination of Ice Thickness for Cryo-EM Grids. *J. Struct. Biol.* 204, 38–44. doi:10.1016/j.jsb.2018.06.007

Rubinstein, J. L., Guo, H., Ripstein, Z. A., Haydaroglu, A., Au, A., Yip, C. M., et al. (2019). Shake-it-off: a Simple Ultrasonic Cryo-EM Specimen-Preparation Device. *Acta Cryst. Sect. D. Struct. Biol.* 75, 1063–1070. doi:10.1107/S2059798319014372

Russo, C. J., and Passmore, L. A. (2014). Ultrastable Gold Substrates for Electron Cryomicroscopy. *Science* 346, 1377–1380. doi:10.1126/SCIENCE.1259530

Russo, C. J., and Passmore, L. A. (2016). Ultrastable Gold Substrates: Properties of a Support for High-Resolution Electron Cryomicroscopy of Biological Specimens. *J. Struct. Biol.* 193, 33–44. doi:10.1016/J.JSB.2015.11.006

Schaffer, B., Grogger, W., Kothleitner, G., and Hofer, F. (2010). Comparison of EFTEM and STEM EELS Plasmon Imaging of Gold Nanoparticles in a Monochromated TEM. *Ultramicroscopy* 110, 1087–1093. doi:10.1016/j.ultramic.2009.12.012

Suloway, C., Pulokas, J., Fellmann, D., Cheng, A., Guerra, F., Quispe, J., et al. (2005). Automated Molecular Microscopy: the New Leginon System. *J. Struct. Biol.* 151, 41–60. doi:10.1016/j.jsb.2005.03.010

Tan, Y. Z., Cheng, A., Potter, C. S., and Carragher, B. (2016). Automated Data Collection in Single Particle Electron Microscopy. *Microsc. (Tokyo)* 65, 43–56. doi:10.1093/jmicro/dfv369

Conflict of Interest: The author declares that the research was conducted in the absence of any commercial or financial relationships that could be construed as a potential conflict of interest.

frontiers | Frontiers in Molecular Biosciences

METHODS
published: 17 June 2022
doi: 10.3389/fmolb.2022.890390

Thicker Ice Improves the Integrity and Angular Distribution of CDC48A Hexamers on Cryo-EM Grids

Brandon Huntington[1,2], Lingyun Zhao[3], Patrick Bron[4], Umar F. Shahul Hameed[1,2], Stefan T. Arold[1,2,4]* and Bilal M. Qureshi[1,2,5,6]**

[1]Bioscience Program, Biological and Environmental Science and Engineering Division, King Abdullah University of Science and Technology (KAUST), Thuwal, Saudi Arabia, [2]Computational Biology Research Center, King Abdullah University of Science and Technology, Thuwal, Saudi Arabia, [3]Imaging and Characterization Core Lab, King Abdullah University of Science and Technology, Thuwal, Saudi Arabia, [4]Centre de Biologie Structurale (CBS), INSERM, CNRS, Université de Montpellier, Montpellier, France, [5]Division of Structural Biology (Strubi), University of Oxford, Oxford, United Kingdom, [6]Scientific Center of Optical and Electron Microscopy (ScopeM), ETH Zurich, Zurich, Switzerland

OPEN ACCESS

Edited by:
Rebecca F. Thompson,
University of Leeds, United Kingdom

Reviewed by:
Zhao Wang,
Baylor College of Medicine,
United States
Sagar Chittori,
St. Jude Children's Research Hospital,
United States

***Correspondence:**
Umar F. Shahul Hameed
umar.shahulhameed@kaust.edu.sa
Stefan T. Arold
stefan.arold@kaust.edu.sa
Bilal M. Qureshi
bilal.qureshi@scopem.ethz.ch

Specialty section:
This article was submitted to Structural Biology, a section of the journal Frontiers in Molecular Biosciences

Received: 05 March 2022
Accepted: 26 May 2022
Published: 17 June 2022

Citation:
Huntington B, Zhao L, Bron P, Shahul Hameed UF, Arold ST and Qureshi BM (2022) Thicker Ice Improves the Integrity and Angular Distribution of CDC48A Hexamers on Cryo-EM Grids. Front. Mol. Biosci. 9:890390. doi: 10.3389/fmolb.2022.890390

Many cryogenic electron microscopy (cryo-EM) single particle analyses are constrained by the sample preparation step upon which aggregation, dissociation, and/or preferential orientation of particles can be introduced. Here, we report how we solved these problems in the case of CDC48A, a hexameric AAA ATPase from *Arabidopsis thaliana*. CDC48A hexamers are well preserved under negative staining conditions but disassemble during grid freezing using the classical blotting method. Vitrification of grids using the blot-free Chameleon method preserved the integrity of particles but resulted in their strong preferential orientation. We then used a strategy where we improved in parallel the purification of CDC48A and the conditions for cryo-EM data acquisition. Indeed, we noted that images taken from thicker ice presented an even distribution of intact particles with random orientations, but resulted in a lower image resolution. Consequently, in our case, distribution, orientation, image resolution, and the integrity of particles were tightly correlated with ice thickness. By combining the more homogeneous and stable CDC48A hexamers resulting from our improved purification protocol with an iterative search across different ice thicknesses, we identified an intermediate thickness that retained sufficiently high-resolution structural information while maintaining a complete distribution of particle orientations. Our approach may provide a simple, fast, and generally applicable strategy to record data of sufficient quality under standard laboratory and microscope settings. This method may be of particular value when time and resources are limited.

Keywords: cryo-electron microscopy, ice thickness, optimization, preferential orientation, grid preparation, particle integrity, oligomer disassembly, single particle analysis

1 INTRODUCTION

Owing to the "resolution revolution," cryogenic electron microscopy (cryo-EM) has become one of the major structural biology methods (Kühlbrandt, 2014). The number of structures solved by cryo-EM has risen steadily in recent years, and structures of diverse types of biological macromolecules have been successfully determined, ranging from soluble to membrane proteins, from single polypeptides to multi-domain, multi-protein, and protein-nucleic acid complexes (Nogales and Scheres, 2015; Lancey et al., 2021; Kühlbrandt, 2022). The method requires the preparation of high-

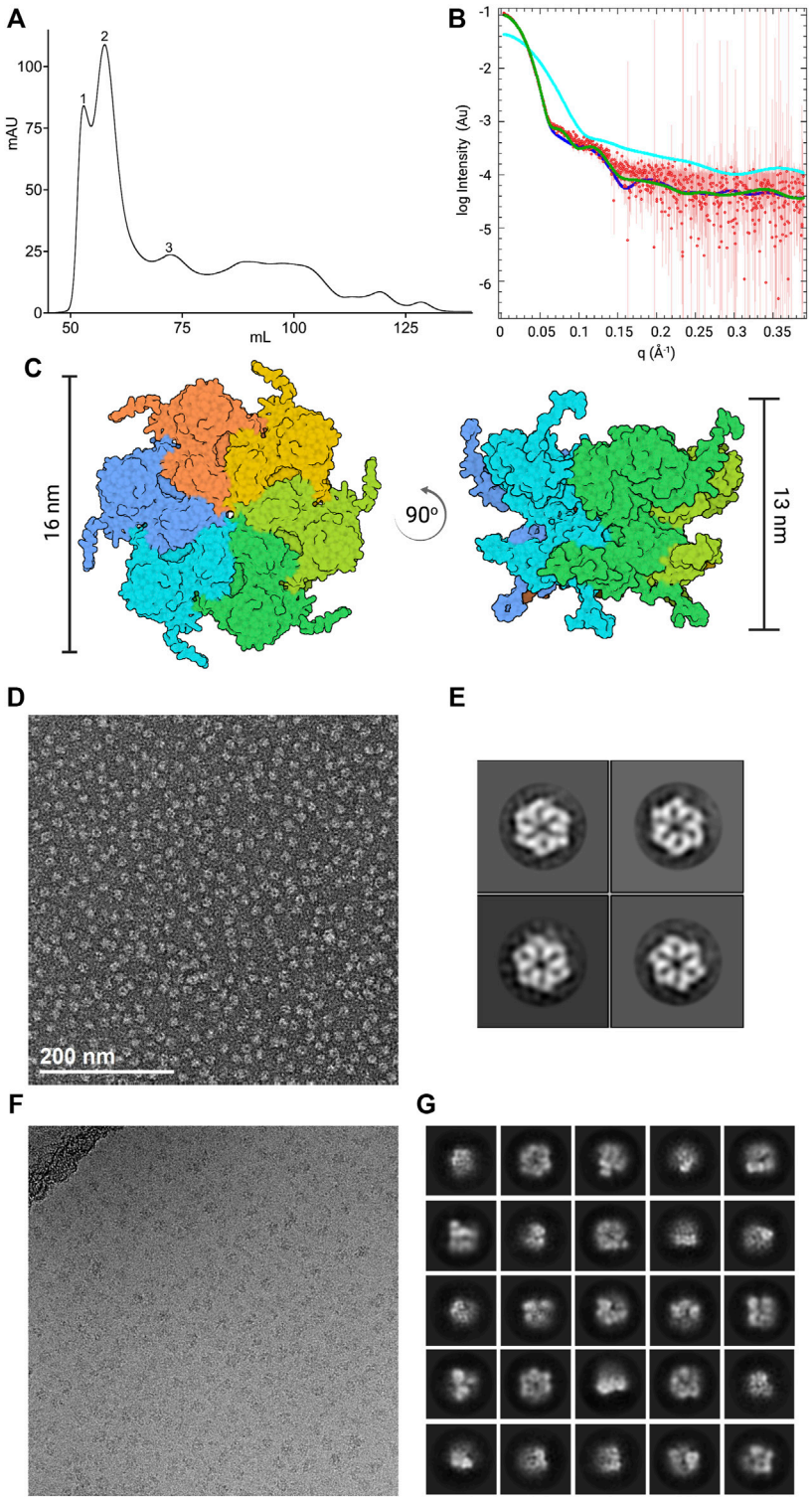

FIGURE 1 | Characterization of the initial CDC48A sample. **(A)** Size-exclusion chromatography profile of CDC48A from the standard method of purification. Samples were analyzed using a HiLoad 16/600 Superdex 200 pg SEC column The trace represents absorbance at 280 nm. Based on the elution volume, the first peak corresponds to aggregates, the second and highest peak corresponds to hexameric CDC48A, and the third peak to monomeric CDC48A. **(B)** SEC-SAXS curve of CDC48A saturated with ATP (red) overlaid with SAXS patterns calculated from homology models based on the ADP-ATP state of p97 (dark blue, PDB entry 5FTN, $\chi^2 = 2.28$), the ATP-ATP state of p97 (green, PDB entry 5FTM, $\chi^2 = 4.27$), and an AlphaFold-derived CDC48A monomer (cyan, $\chi^2 = 2585$). **(C)** Top view (left) and side view (right) of the best fitting model from **(B)**, colored by chain. Vertical bars represent the diameter and height, respectively. **(D)** Representative image from the NS-EM screening. **(E)** Representative 2D class averages from the NS-EM screening. **(F)** Representative cryo-EM image from the initial dataset. **(G)** Representative 2D class averages from the initial cryo-EM dataset.

quality cryo-EM grids where the sample becomes included within a thin film of vitreous ice. It is important that the ice layer contains an even and dense distribution of particles in random orientations. This sample preparation stage remains the major limiting factor for high-resolution cryo-EM analysis.

Especially multi-domain, and multi-protein complexes often require additional steps to prepare them for structural characterization. In particular, two challenges frequently occur when working with such complexes: 1) the complex is structurally heterogeneous, and/or dissociates during cryo-EM grid preparations, and 2) samples in optimally thin ice show a strong preferred orientation, and tend to dissociate or unfold at the air-water interface during grid preparation.

Herein, we describe a simple dual strategy that resolved these challenges in our work on a flexible, multimeric nano-machine, namely the *A. thaliana* cell division cycle 48 A (CDC48A) protein complex. Being targeted to specific substrates by adaptor proteins, CDC48A extracts proteins from their cellular location, unfolds them, and routes them for degradation by the proteasome. By rapidly modifying the protein composition in specific subcellular loci, CDC48A regulates a large variety of fast-response mechanisms in plants (Liu and Li, 2014; Copeland et al., 2016; Ling et al., 2019; Huang et al., 2020). Thus, CDC48A assures a healthy proteome, and allows plants to adapt to changing conditions. CDC48A, and its homologues from fungi, and animals (where CDC48 is often called p97 or VCP) are multi-domain AAA-type ATPases that are catalytically active as a hexamer (Stach and Freemont, 2017). Each of the ~90 kDa subunits comprises three domains, an N-terminal ligand binding domain (termed CDC48-N) followed by two ATP hydrolyzing domains (D1 and D2), and it terminates in a short flexible C-terminal tail (**Figure 1C**; DeLaBarre and Brunger, 2003). The molecular weight (~550 kDa), and flexibility of the CDC48A hexamer make cryo-EM the most suitable method for its structural characterization. Cryo-EM structures of yeast, and mammalian homologues have already been reported (Banerjee et al., 2016; Cooney et al., 2019; Twomey et al., 2019; Caffrey et al., 2021; Pan et al., 2021). However, owing to a billion years of evolutionary separation, and the resulting adaptation to a very different organism, CDC48A is expected to display unique structural, and functional features. Understanding those features would provide insight into plant proteostasis, and adaptation, and may open potential biotechnological applications.

However, our efforts to structurally characterize CDC48A have been hampered by the dissociation of CDC48A hexamers during cryogenic sample preparation. Moreover, we observed large preferential orientation in optimally thin ice for high-resolution image acquisition. We herein describe how we successfully tackled these issues through a parallel approach, including optimizing sample purification, and data acquisition.

2 MATERIALS AND METHODS

2.1 Protein Expression

The cDNA for CDC48A (AT3g09840) were purchased from Integrated DNA Technologies (IDT), and then subcloned to the pGEX6P-1 vector between BamHI, and NotI restriction sites. Proteins were expressed in *Escherichia coli* BL21 (DE3) cells containing an N-terminal GST tag with a PreScission protease cleavage site. The *E. coli* cells were cultured at 37°C in 2% LB Broth containing 100 μg/ml ampicillin, shaking at 200 rpm until the optical density at 600 nm reached 0.6–0.8. Subsequently, expression of CDC48A was induced using 150 μM of IPTG, and allowed to continue overnight, shaking at 200 rpm at 16°C. Cells were then pelleted by centrifugation at 7,500 rpm (12,200 × g) for 15 min at 4°C, and stored at −80°C.

2.2 Protein Purification

CDC48A was purified using two methodologies. The standard method is as follows: frozen cell pellets were thawed on ice, and resuspended in lysis buffer containing [50 mM Tris (pH 7.5), 200 mM NaCl, 3 mM DTT, one tablet of SigmaFast EDTA-free protease inhibitor (Sigma-Aldrich) per 50 ml preparation, and 0.5% Triton]. Cells were lysed by sonication (Branson 450 Digital Sonifier) on ice for 8 min at 35% amplitude with a pulse rate of 1 s on, and 1 s off. The lysate was pelleted by centrifugation at 27,000 rpm (87,207 × g) for 30 min at 4°C. The supernatant was added to a GST-affinity column containing glutathione sepharose beads (Cytiva) for 2 h, shaking at 4°C. The flowthrough was discarded, and the column washed with 3 column volumes (CV) of wash buffer containing [50 mM Tris (pH 7.5), 200 mM NaCl, and 3 mM DTT] followed by 1 CV of an elution buffer containing [20 mM HEPES (pH 7.5), 150 mM NaCl, and 1 mM TCEP] or [50 mM Tris (pH 7.5), 100 mM NaCl, 3 mM DTT] [for samples analyzed at Astbury Centre for Structural Molecular Biology (ACSMB), and Electron Bio-Imaging centre (eBIC), only]. CDC48A was cleaved overnight, shaking at 4°C in 15 ml of elution buffer with 3C protease. For samples analyzed at ACSMB, and eBIC, the cleavage solution additionally contained 15 units of apyrase (NEB). The eluate was then concentrated to a volume of 5 ml using an Ultra-15, 50 kDa MWCO, Amicon filtration device (Millipore), and purified using HiLoad 16/600 Superdex 200 pg (GE Healthcare) size-exclusion chromatography (SEC). Protein purity was analyzed using SDS-PAGE gels, and the relevant fractions were pooled, and stored at −80°C or used fresh, as described.

The optimized purification was carried out as above, with the following changes: one tablet of complete EDTA-containing protease inhibitor was used (Roche) per 50 ml preparation, and the cell lysate was treated with 2.5 μl of benzonase nuclease (Millipore), and incubated for 20 min at room temperature. During GST-affinity chromatography, the supernatant was added to the column for 15 min at 4°C. The flowthrough was retained, and the column washed with 4 CV of high-salt wash buffer containing [50 mM Tris (pH 7.5), 1 M NaCl, and 3 mM DTT]. The retained flowthrough was then added to the column for an additional 15 min, followed by an identical washing step. The flowthrough was discarded, and the column washed with 1 CV of elution buffer. CDC48A was similarly cleaved overnight, further purified using SEC, then stored at −80°C, or used fresh, as described.

2.3 Small-Angle X-Ray Scattering

SAXS data were recorded at the SWING beamline (SOLEIL, Saint-Aubin, France) using a wavelength of 1.03 Å. Scattering

data were collected from a 5 mg/ml sample of CDC48A (from the standard purification after freeze-thawing once) saturated with 2 mM of ATP (Sigma-Aldrich), with the sample passed through Bio SEC-3 HPLC (Agilent) SEC prior to analysis. The distance of the sample to the detector was 1.8 m, resulting in the momentum transfer of a range of 0.1 1/Å < q < 0.5 1/Å. Buffer data were calculated from the buffer [20 mM BisTris (pH 6.5), 150 mM NaCl, 1 mM TCEP] eluted before proteins, and subtracted from the protein data using SWING's on-site software. Data were analyzed using PRIMUS, as part of the ATSAS software package (Manalastas-Cantos et al., 2021), and models were fit to the scattering curve using FOXS (Schneidman-Duhovny et al., 2010). The monomeric CDC48A model was generated by AlphaFold (Jumper et al., 2021), and the hexameric models were generated using SWISS-MODEL (Waterhouse et al., 2018) with p97 as a template (Banerjee et al., 2016; PDB ID 5FTM, and 5FTN). Missing flexible N-terminal, and C-terminal residues were modeled using MultiProt (https://github.com/strubelab/multiprot) in several configurations, and the best fitting models were overlaid on the SAXS profile.

2.4 Analytical Size-Exclusion Chromatography

For comparison of the two methods of purification, an equimolar concentration of cleaved eluate after each method of purification was analyzed using Superdex 200 Increase 10/300 GL (Cytiva) SEC with the elution buffer. The absorbance at 280 and 260 nm were recorded. The protein purity of the optimized method was assessed using SDS-PAGE gels.

2.5 Luminescent Detection of Nucleotide

To detect the presence of nucleotides, the peak hexameric fraction (A11) from both analytical SEC experiments was analyzed using only the ADP detection step of the ADP-Glo assay (Zegzouti et al., 2009). Luminescence was detected using an Infinite M1000 Pro plate reader (Tecan) with an integration time of 1 s by preparing replicates of 10 µl CDC48A (1 mg/ml) with 20 µl of reaction buffer in 384 well plates (Corning Low Volume 384-well Black/Clear Flat Bottom).

2.6 EM Sample Preparation

For the initial EM experiments, CDC48A samples were prepared fresh after SEC from a fraction eluting after the hexamer peak (peak 2) to limit contamination with aggregates eluting in the neighboring peak 1 (**Figure 1A**). When following the optimized method, fresh sample from the center of the hexamer peak was used, unless otherwise described. Cryo-EM samples analyzed at King Abdullah University of Science, and Technology (KAUST) were prepared at 2 mg/ml (2.2 mM) with the addition of 2 mM AMP-PNP (Sigma-Aldrich). Samples analyzed at ACSMB, and eBIC had been frozen then thawed, and prepared at the desired concentration, with no additional nucleotide added.

For negative stain grid preparation, 7 µl of CDC48A (0.1 mg/ml) was placed onto glow discharged grids (Cu, 300 mesh, carbon film, EMS) for 1 min, then blotted with Whatman blotting paper. Next, ~5 µl of 2% uranyl acetate was added to the grid, and immediately blotted. Then, ~5 µl of 2% uranyl acetate was added again, and left to stain for 1 min. Grids were then blotted, and air-dried.

For cryogenic grid preparation at KAUST, samples were prepared using the Vitrobot Mark IV (Thermo Fisher Scientific) at 22°C with 100% humidity. CDC48A samples were prepared as previously described, applying 2 µl of sample, and blotting for 3 s. Samples from the initial CDC48A dataset, and optimized datasets 1 and 2 were prepared on glow discharged Cu grids (C-flat Cu 300 mesh R1.2/1.3, Protoships Inc.), and samples from optimized datasets 3 and 4 were prepared on glow discharged Au grids (C-flat Au 300 mesh R1.2/1.3, Protoships Inc.). For cryogenic grid preparation at ACSMB, samples were prepared using the Vitrobot Mark IV (Thermo Fisher Scientific) at 4°C in 95% humidity, with a blot time of 3 s. Grids were prepared using 2 mg/ml of CDC48A by applying 3 µl of sample to glow discharged Quantifoil Cu R1.2/1.3 grids (EMS). Cryogenic blot-free grids were prepared using the Chameleon instrument (SPT Labtech) at Rosalind Franklin Institute (RFI), United Kingdom (Razinkov et al., 2016; Dandey et al., 2018; Wei et al., 2018). Self-wicking nanowire Cu R1.2/0.8 holey carbon grids with a rectangular bar cross-section were glow discharged in a Pelco Easiglow at 12 mA, 0.39 mbar air pressure. Approximately 6 nl of the samples at 5 mg/ml were applied to each grid at a relative humidity between 75% and 85% at ambient temperature. Details, and comparison of the sample preparation for each cryo-EM dataset can be found in **Supplementary Table S1**.

2.7 EM Data Collection

Negative stain samples were screened on a Titan 80-300 (Thermo Fisher Scientific) operated at an acceleration voltage of 300 kV. Images were taken at different magnifications with a US4000 CCD camera (Gatan). For the 2D analysis of the negative stain sample, 75 images were recorded on Titan ST (Thermo Fisher Scientific) with a OneView camera (Gatan) at a magnification of 69k, and a pixel size of 1.7 Å.

Cryo-EM data were recorded in multiple facilities. At KAUST, cryo-EM data were recorded on a Titan Krios G1 (ThermoFisher Scientific) operated at 300 kV, equipped with a K2 Summit direct detector, and GIF Quantum968 Imaging Filter (Gatan company). Movies were collected at 130k magnification in super-resolution mode yielding a pixel size of 0.52 Å/pixel at specimen level. The initial dataset had 1,242 movies, optimized dataset 1 had 1,073, dataset 2 had 797, dataset 3 had 2,118, and dataset 4 had 2,284. The total exposure time was 5.6 s, dose-fractionated into 32 frames (0.175 s per frame) with a total dose of 50 e/Å^2. At ACSMB, cryo-EM data were recorded on a Titan Krios G2 (Thermo Fisher Scientific) operated at 300 kV equipped with K2 summit direct detector, and GIF BioQuantum967 Imaging Filter (Gatan company). A total of 1,311 movies were collected at 130k magnification in electron counting mode at a pixel size of 1.07 Å/pixel. The total exposure time was 10 s, dose-fractionated into 60 frames (0.167 s per frame) with a total dose of 75 e/Å^2. At eBIC, Diamond Light Source, cryo-EM data were recorded on a Glacios operated at 200 kV equipped Falcon IV direct detector (Thermo Fisher Scientific). A total of 1,472 movies were collected

at 120k magnification in electron counting mode at a pixel size of 1.192 Å/pixel. The total exposure time was 10 s, dose-fractionated into 50 frames (0.200 s per frame), with a total dose of 48.1 e/Å^2. A comparison of the data collection conditions across all cryo-EM datasets can be found in **Supplementary Table S1**.

2.8 EM Data Processing

Negative stain data were processed to compute 2D class averages. Briefly, the contrast transfer function (CTF) parameters were estimated by Gctf (Zhang, 2016), and particles picked automatically by Gautomatch v0.56 (https://www.mrc-lmb.cam.ac.uk/kzhang/Gautomatch/). A total of 74k particles were picked from 75 images, and extracted with a box size of 180 pixels in Relion-4.0-beta-1-commit-11e38ba (Kimanius et al., 2021), and 2D classification was performed using the VDAM algorithm.

Data collected at KAUST were motion-corrected using Warp (Tegunov and Cramer, 2019) with a binning factor of 2 and subsequently imported into cryoSPARC v3.2.0 (Punjani et al., 2017) for further processing. CTF parameters for each image were estimated by patch CTF estimation (multi). Particles were picked automatically using the Topaz wrapper in cryoSPARC (Bepler et al., 2019). Briefly, a Topaz model was trained on a curated subset of CDC48A particles selected using template picking, and subsequently used to pick the particles. Particles were extracted with a box size of 256 pixels in the initial dataset and 380 pixels in the optimized datasets. From the initial dataset, 177k particles were extracted, and subjected to further 2D classification, with no further selection of particles. From the optimized datasets, around 91k particles were extracted from dataset 1 (71k in good classes), 111k from dataset 2 (78k in good classes), 400k from dataset 3 (270k in good classes), and 550k from dataset 4 (430k in good classes). Data collected at eBIC was processed at ETH Zurich using a similar procedure as above using cryoSPARC v3.3.1. The imported movies were motion-corrected using patch motion correction (multi), and CTF parameters were estimated using patch CTF estimation (multi). Particles were picked automatically using the blob picker, and 2D class averages were computed. In a second iteration, these 2D classes were used as templates to automatically pick particles that were subsequently extracted with a box size of 350 pixels. Following 2D classification, 250k particles were retained in the good classes. Data collected at ACSMB were processed at KAUST using Relion-3.1 (Zivanov et al., 2020). Briefly, movies were subjected to motion correction using Relion's own implementation, with no binning, and CTF parameters estimated by CTFFind-4.1 (Rohou and Grigorieff, 2015). Particles were picked automatically using Gautomatch v0.56, and 100k particles were extracted with a box size of 282, and a binning of 3. After 2D classification, 48k particles were selected and re-extracted without binning. To generate consistent figures, these particles were imported into cryoSPARC v3.3.1, and subjected to 2D classification. For each dataset, an *ab initio* reconstruction was computed using the filtered particles through the *ab Initio* Reconstruction job in cryoSPARC v3.3.1. Default reconstruction settings were used, aside from 500 extra final iterations in all, and C6 symmetry was imposed where noted. Details including the number of movies, and particles picked can be found summarized in **Supplementary Table S1**.

2.9 Ice Thickness Measurements

As an indirect measure of ice thickness, all images corresponding to each of the cryo-EM datasets were plotted according to their relative ice thickness, determined using the relative ice thickness parameter in the Manually Curate Exposure option, following patch CTF estimation (multi), in cryoSPARC v3.3.1.

As a direct measure of ice thickness, frozen aliquots of cleaved CDC48A (following the optimized methodology) were further purified using SEC. Fresh sample corresponding to the peak hexameric fraction was used to prepare cryogenic grids under the conditions used for optimized datasets 3 and 4. Ice thickness was measured using the aperture limited scattering method of Rice et al. (2018), by measuring the beam intensity of the specimen vs. the beam intensity of the vacuum (λ = 322 nm) on a Titan Krios operated at 300 kV using 100 micron Objective Aperture, and equipped with Gatan's GIF/K2 detector. Ice thickness was measured from one thin ice region, one thick ice region, and two regions of intermediate ice thicknesses. For each ice thickness, five measurements were averaged.

3 RESULTS

3.1 Quaternary Structure Disassembly During Cryogenic Sample Preparation

We recombinantly expressed *A. thaliana* CDC48A in *E. coli* and purified the protein according to our standard protocol (see *Methods*, **Section 2.2**). We confirmed the identity, and purity of the recombinant purified proteins through SDS-PAGE of SEC fractions (**Figure 1A**; **Supplementary Figure S1**). The SEC fractions of CDC48A that contained aggregates or monomeric protein were discarded, and only fractions from the peak containing hexamers (judged according to molecular weight standards) were retained. Additionally, SEC coupled with small-angle *x*-ray scattering (SEC-SAXS) showed that CDC48A persists as hexamers during gel filtration, and that hexamers are the prevailing species in solution, as homo-hexameric models best fitted the scattering curve (**Figures 1B,C**). These experiments suggested that the sample quality, and integrity was sufficient to proceed with the structural investigation.

We first performed a negative stain (NS) screening to probe the suitability of CDCD48A hexamers for cryo-EM studies. We iteratively optimized the protein concentration, and staining protocol to obtain NS-EM images of densely packed but well-separated particles (see Methods). NS-EM revealed our sample to be sufficiently monodispersed, and mostly hexameric (**Figure 1D**). Indeed, computing 2D class averages from the NS-EM images revealed intact hexamers of CDC48A (**Figure 1E**). Collectively, these analyses suggested that our sample was suitable for cryo-EM.

Next, we prepared cryogenic specimens of CDC48A at a protein concentration of 2 mg/ml (20 fold higher than used in NS) using a Vitrobot (see *Methods*), and collected the initial cryo-EM images at the Imaging, and Characterization Core Lab (IAC) in KAUST. We observed a sufficiently dense distribution of particles throughout grid regions. However, the particles did

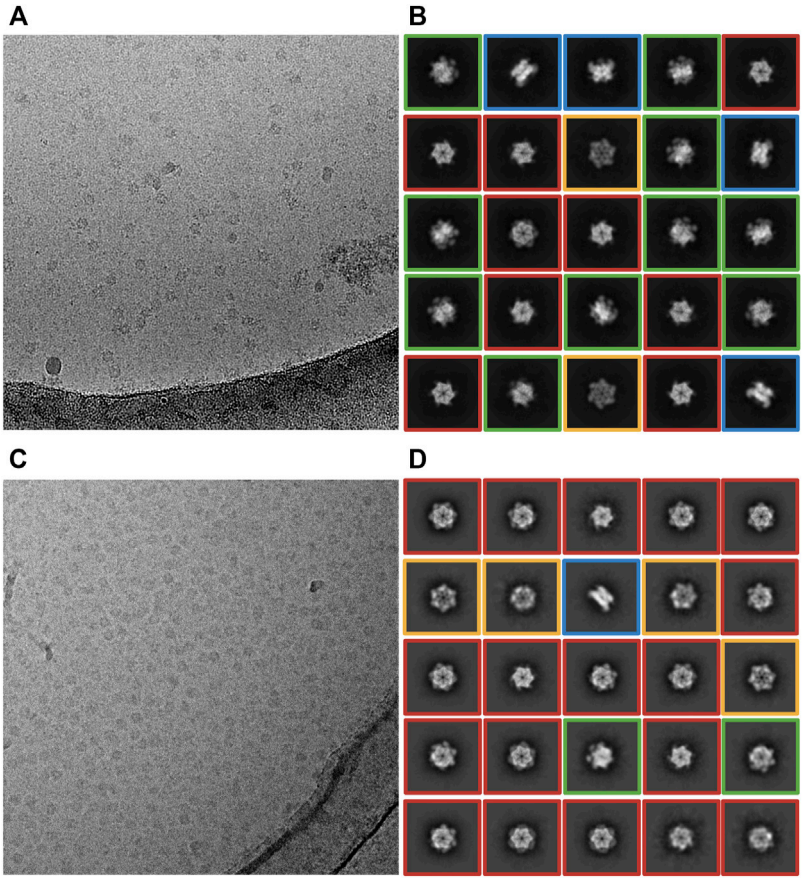

FIGURE 2 | Effect of ice thickness on the distribution of particle orientations. **(A,B)** Cryo-EM data collected at ACSMB from thick ice; grids were prepared using a Vitrobot. **(A)** Representative cryo-EM micrograph. **(B)** Representative 2D class averages. Various particle orientations are noted by red boxes (top view), orange boxes (bottom view), green boxes (intermediate view) or blue boxes (bottom view). **(C,D)** Cryo-EM data collected at eBIC from optimally thin ice; Blot-free grids were prepared using the Chameleon instrument. **(C)** Representative cryo-EM images. **(D)** Representative 2D class averages. Various particle orientations are noted by red boxes (top view), orange boxes (bottom view), green boxes (intermediate view) or blue boxes (bottom view).

not appear homogeneous in size, and shape and differed markedly from the NS-EM images (**Figure 1F**). We collected a dataset of 1,242 movies on these grids and performed image processing to compute 2D class averages (**Figure 1G**). The 2D classes corroborated the presence of significant structural heterogeneity, apparently as a result of CDC48A hexamer dissociation. The strong dissociation of the CDC48A hexamer in cryo-EM was unexpected because intact hexamers prevailed in SEC, SAXS, and NS. The cryo-EM-specific hexamer dissociation warranted further optimization of our workflow, and protocols for the preparation of the protein sample, and cryo-EM grids.

3.2 Parallel Optimization Strategy

We optimized biochemical sample preparation, and cryo-EM data collection in parallel. Below, we first describe our strategy for improving the data collection (which was carried out with the protein from the initial unoptimized standard purification protocol). In the section thereafter, we report our concurrent improvements to the protein production strategy. The benefits of the improvements of grids, and samples were additive, as demonstrated in the final section that reports on the data obtained from the optimized samples with the improved data collection strategy.

3.2.1 Ice Thickness Influences Complex Integrity and Particle Orientation

First, we wanted to investigate whether particle dissociation was caused primarily by our handling of the sample. To this end, we cryogenically prepared grids using a slightly altered Vitrobot protocol (see *Methods*), and used them for a subsequent round of cryo-EM screening at the Astbury Centre for Structural Molecular Biology (ACSMB), University of Leeds, United Kingdom. Inspection of the images confirmed that hexamers largely dissociated in optimally thin ice regions, evidenced by an increase in background noise, and a reduction in visible hexamers. However, when screening regions of the grids that had thicker ice we noted the substantially increased prevalence of intact hexamers (**Figure 2A**). Collecting a dataset of 1,311 movies from thick ice and processing the data to the stage of 2D classification revealed only ~50,000 particles.

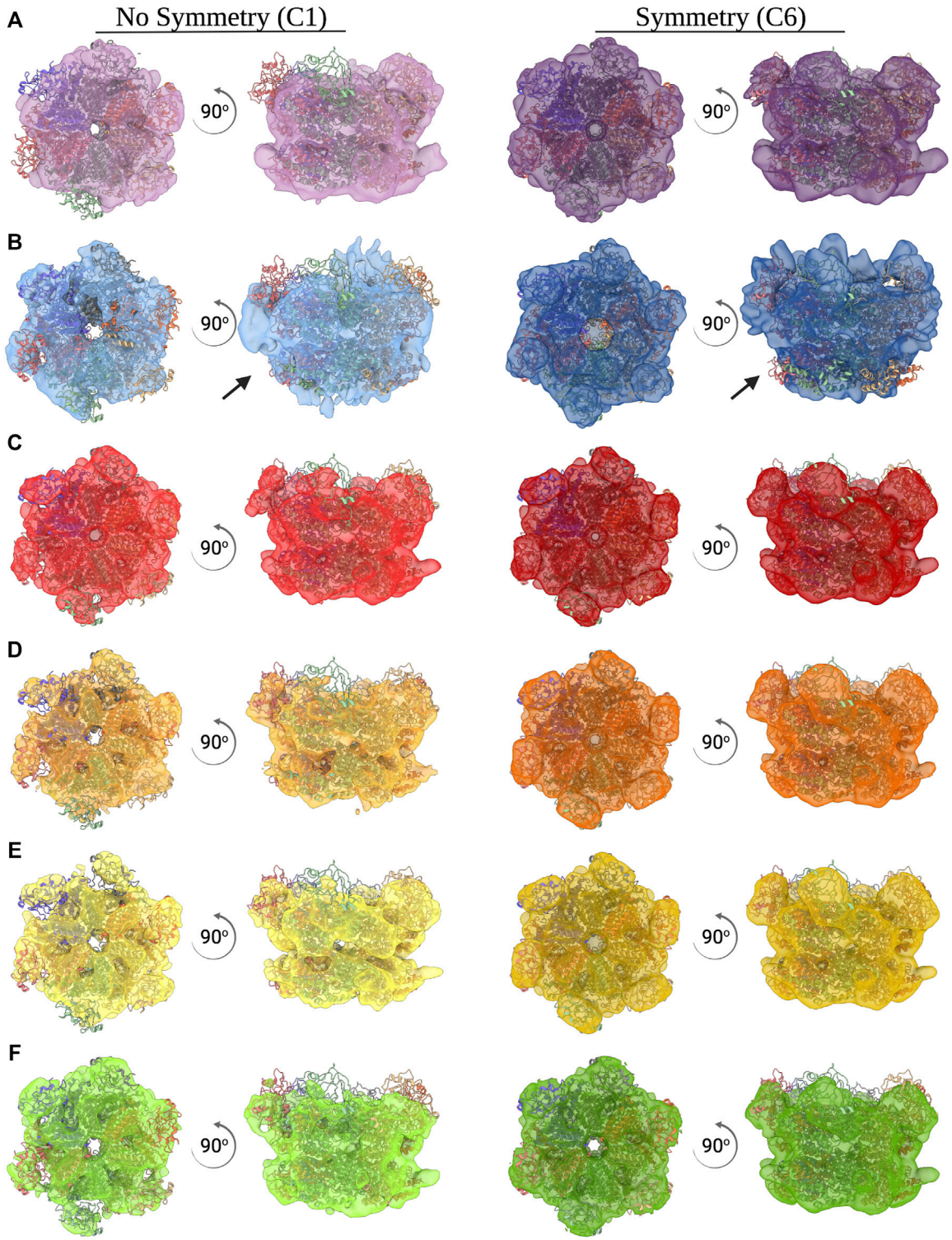

FIGURE 3 | *Ab initio* reconstructions of CDC48A. **(A–F)** Top and side view of an *ab initio* reconstruction of CDC48A with (right, dark color) and without (left, light color) C6 symmetry imposed. All reconstructions from the ACSMB dataset **(A)**, the eBIC dataset **(B)**, optimized dataset 1 **(C)**, optimized dataset 2 **(D)**, optimized dataset 3 **(E)**, and optimized dataset 4 **(F)** are superimposed with the structural homologue p97 (PDB entry 5FTN). Arrows indicate poorly reconstructed regions as a result of preferential orientation.

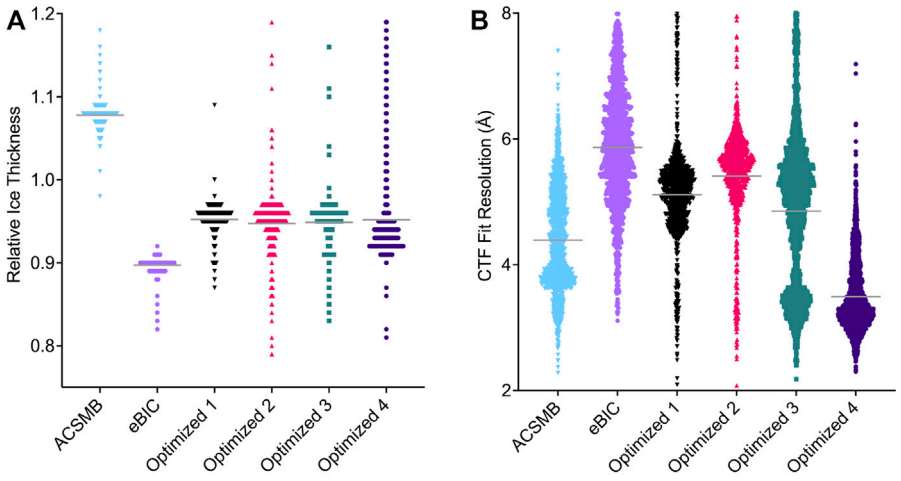

FIGURE 4 | Comparison of CTF parameters estimated for each Cryo-EM dataset. Each point represents an individual image and the width of points is proportional to the number of images estimated at that value. **(A)** Estimated relative ice thickness for each image. Solid gray horizontal lines represent the mean value (ACSMB = 1.10, eBIC = 0.90, optimized dataset 1 = 0.95, 2 = 0.97, 3 = 0.97, 4 = 0.96). Images with an estimated value above 1.2 were excluded. **(B)** Estimated CTF fit resolution for each image. Solid gray horizontal lines represent the mean value (ACSMB = 4.39 Å, eBIC = 5.86 Å, optimized dataset 1 = 5.11 Å, 2 = 5.41 Å, 3 = 4.85 Å, 4 = 3.49 Å). Images with an estimated value above 8 Å were excluded.

The computed 2D class averages reveal a proper distribution of particle orientations, with top and bottom views of CDC48A indicated by red and orange boxes, respectively, a few side views of CDC48A with a crab-like organization in blue and intermediate particle orientations in green (**Figure 2B**). The particle integrity and isotropic orientation of this dataset was also reflected in the template-free *ab initio* reconstructions with and without imposed C6 symmetry (**Figure 3A**). The maximum resolution of images proposed through CTF estimation in cryoSPARC ranges from 4 to 6 Å (**Figure 4**), indicating that these images are not suitable for computing a high resolution 3D reconstruction of CDC48A. Therefore, we concluded that capturing particles in thicker ice maintained the integrity of the hexamers, and provided a more homogeneous distribution of particle orientations.

We reasoned that the hexamer dissociation was lesser in thick ice because of a reduced surface to volume ratio, and hence a lesser exposure of proteins to the destabilizing air-water interface. To test this effect, we used the spray-on method integrated into the Chameleon grid preparation instrument (operated at eBIC, Diamond Light Source), instead of Vitrobot blotting. The faster spray-on method is expected to limit the number of interactions of the protein with the air-water interface prior to vitrification, and thus preserve the integrity of proteins (Klebl et al., 2020). Additionally, self-wicking grids are used in the Chameleon, eliminating the blotting step that may disrupt sample integrity (Wei et al., 2018). The collected dataset comprised 1,472 movies from optimal thin ice regions (**Figure 2C**). We extracted about 250,000 particles. The resulting 2D class averages of CDC48A revealed mainly top and bottom views of a hexameric CDC48A (**Figure 2D**). Thus, although the integrity of the quaternary state was maintained through the use of the Chameleon, unfortunately, only ~2% of the extracted particles displayed the side-view orientation, resulting in a poor quality of the *ab initio* reconstruction (**Table 1**; **Figure 3B**). Therefore, thin-ice collection on Chameleon-prepared grids provided a remedy to particle dissociation but presented the problem of preferred orientation. The ice thickness of this dataset was estimated to be the thinnest of all datasets recorded. Surprisingly, the resolution of images ranged from 3 to 8 Å (**Figure 4**). Using the method developed by Rice et al. (2018), the holes of cryo-EM grids presenting the thinnest ice have a thickness of 21.42 ± 3.17 nm. As the diameter of CDC48A is expected to be around 16 nm, we can speculate that the shape and surface charge distribution of CDC48A, and the thickness of ice are certainly the main parameters explaining the preferential orientation of particles in this dataset. Because our access to the Chameleon was limited, we were not able to test thick-ice conditions on this instrument.

In conclusion, using the standard Vitrobot protocol, we could either observe a dissociated complex in optimally thin ice or an intact complex in thicker ice at the cost of resolution. Conversely, blot-free vitrification by the Chameleon preserved the sample integrity but introduced a strong preferential orientation due to the asymmetrical shape of our complex that compromises its 3D reconstruction. To be able to have a rapid workflow using our in-house Vitrobot, we decided to explore optimizing the ice thickness jointly with improving the intrinsic stability of the protein sample.

3.2.2 Fresh, Unconcentrated Proteins With Minimal Purification Steps Behave Best on EM Grids

To improve the stability of hexameric CDC48A complexes during grid preparation, we refined, and streamlined the purification protocol. Our standard protocol consisted of cell lysis by sonication, followed by a glutathione-S-transferase (GST) affinity column, and then a SEC. With this protocol we observed that the resulting samples displayed an absorption

TABLE 1 | Quantifying the preferential orientation bias. As a proxy for determining the degree of preferred orientation bias in the datasets, the number of particles that belonged to classes representing a complete side view of CDC48A was divided by the number of particles in all good classes, for each dataset. Values of 9.0 ± 1.0% correspond to an even orientational distribution.

Dataset	ACSMB	eBIC	Optimized 1	Optimized 2	Optimized 3	Optimized 4
% 90° Side view	8.40	2.00	9.60	9.70	6.40	5.20

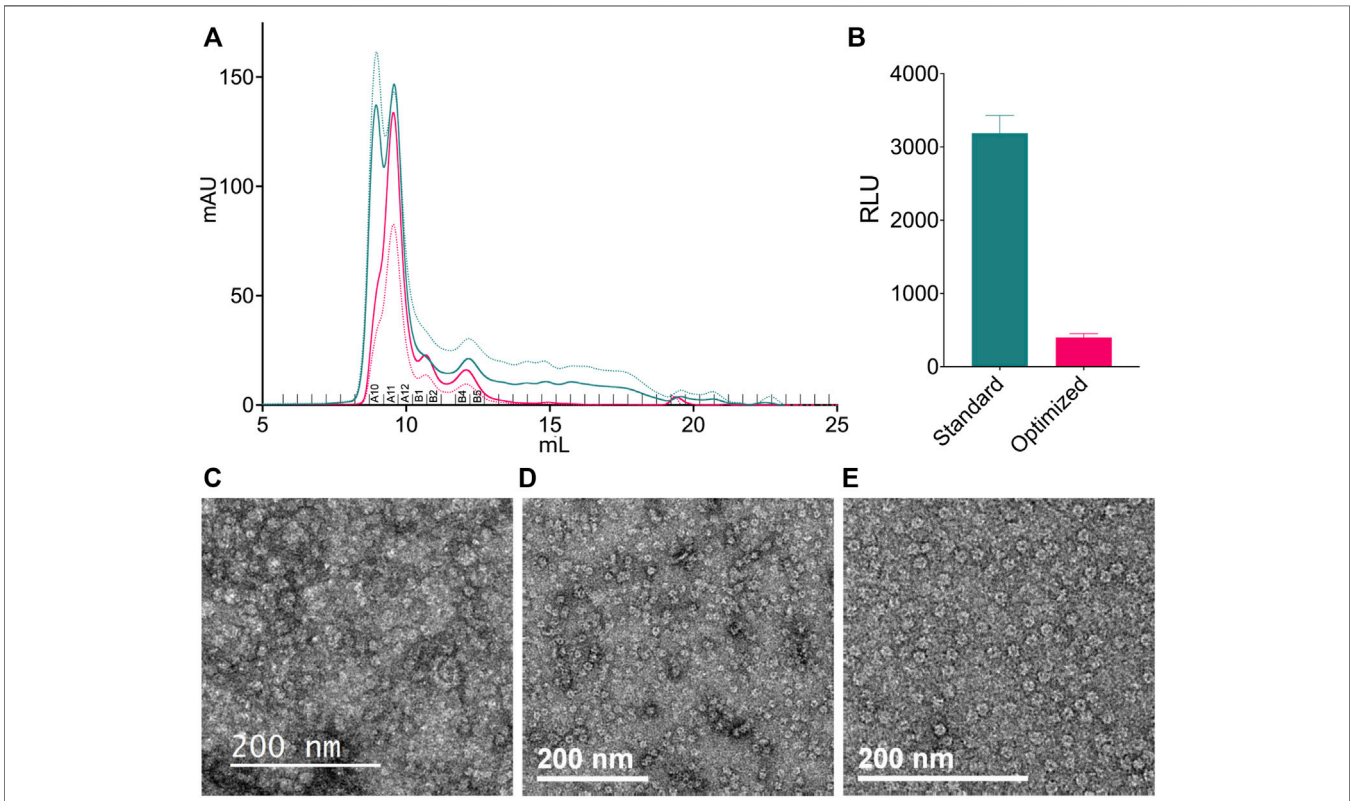

FIGURE 5 | Sample preparation optimization. **(A)** Analytical SEC profiles of the standard (teal) and optimized (pink) methods of purification. Samples were analyzed using a Superdex 200 Increase 10/300 GL SEC column. Solid lines show the absorbance at 280 nm. Dotted lines show the absorbance at 260 nm. Fractions corresponding to **Table 1**; **Supplementary Figure S1** are labeled above the *x*-axis. **(B)** Relative luminescence units (RLU) of nucleotides from fraction A11 of both purification protocols. Samples were prepared using only the detection step of the ADP-Glo assay. Error bars represent 95% confidence interval ($n = 3$). **(C,E)** NS screening of different CDC48A samples. **(C)** CDC48A samples that were thawed after pooling and concentrating for storage. **(D)** CDC48A sample taken fresh from off-center fractions of the hexameric peak (primary peak). **(E)** CDC48A sample taken fresh from the center of the hexameric peak.

ratio of 260–280 nm (A260/280) of above 1 indicating strong contamination of the sample by nucleic acids and/or bound nucleotides (**Table 1**). Therefore, we included benzonase nuclease into the cell lysis buffer. Next, we shortened the GST-affinity column step; rather than incubating the cell lysate to bind the glutathione beads for 2 h as in the initial protocol, we incubated the lysate with the beads twice for 15 min, where each incubation step was followed by subsequent washing with 4 column volumes of a 1 M NaCl high-salt buffer (see *Methods*). This protocol quickly separated the GST-fused protein from contaminants such as proteases and reduced the overall time for the purification (**Supplementary Figure S1**). The high-salt washes jointly with the benzonase treatment removed interactions between our ATPase and DNA, or with other DNA-associating factors from the cell lysate. Indeed, compared with the initial purification protocol, the optimized protocol had a A260/280 ratio of ~0.6 throughout all SEC fractions, indicative of protein alone (**Figures 5A,B**; **Table 2**). SEC also showed a substantially lower peak height for the elution volume corresponding to aggregates, suggesting a reduction of protein aggregates, possible through eliminating DNA-mediated associations (**Figure 5A**). Moreover, the combination of benzonase and high-salt washes also allowed us to produce CDC48A without significant amounts of bound ATP or ADP (**Figure 5B**). ATP is a cofactor for CDC48A, and each monomer binds two adenosine phosphate nucleotides, one each in D1 and D2 domains. The presence of ATP or ADP introduces large structural changes in p97 (Banerjee et al., 2016).

TABLE 2 | Assessing the purity of the standard and optimized purification methods. Concentration (mg/ml) and the ratio of absorbance measured at 260–280 nm (A260/280) of fractions following analytical SEC. Fractions correspond to those labeled in **Figure 5**.

Fraction	Standard		Optimized	
	mg/ml	A260/280	mg/ml	A260/280
A10	1.23	1.13	0.70	0.61
A11	1.41	1.03	1.13	0.63
A12	0.69	1.14	0.65	0.66
B1	0.38	1.33	0.38	0.64
B2	0.20	1.65	0.20	0.65
B4	0.21	1.47	0.18	0.67
B5	0.17	1.60	0.10	0.57

Hence, the production of CDC48A molecules without this cofactor allows the preparation of homogeneous apo, ATP or ADP-loaded samples for structural and functional analysis. In conclusion, the amended purification protocol produced a purer, fresher, and more homogenous sample.

Next, we wanted to assess the impact the new protocol had on the quality of the EM grids using NS-EM. We found that grids prepared from the peak hexameric CDC48A fractions that were pooled, concentrated, and frozen contained large amounts of aggregate clusters and indiscernible individual particles (**Figure 5C**). Conversely, NS-EM grids directly prepared from SEC elution fractions, without additional concentration or freezing steps, were of higher quality with more evenly distributed individual and feature-rich particles (**Figures 5D,E**). We also noted that grids prepared directly from the center of the peak (**Figure 5E**) contained particles that were more homogeneous and contained fewer aggregates compared to grids prepared from off-center peak fractions (**Figure 5D**). Therefore, we subsequently used only the peak fraction for the preparation of cryo-EM grids.

3.3 Combining an Improved Sample With Thicker Ice Yields Sufficient Data Quality

Because our initial cryo-EM work had shown disassembly and preferential orientation in thin ice for our hexameric CDC48A sample, we first investigated the behavior of our biochemically optimized protein sample in thin ice. In line with the improvements we saw in NS-EM, the optimized sample preparation increased the integrity of the sample in cryo-EM, as homogeneous and well-dispersed hexameric particles were observed under thin ice conditions following Vitrobot blotting. However, our screening of thin ice grid regions revealed a high degree of preferential orientation with particles oriented primarily in a top or bottom view. The first movies recorded from grid regions with thick ice showed a homogeneous distribution of orientations, but at the cost of high-resolution information. Therefore, we decided to start from thick ice that displays a wide distribution of particle orientations, and record datasets at different ice thicknesses to identify the optimal compromise between particle resolution, and orientation. In line with our previous observations, we did not record movies in holes presenting the thinnest ice.

Using the image grayscale as a proxy for ice thickness, we collected four separate datasets from grid regions of decreasing ice thickness and processed each dataset individually. Utilizing CTF parameter estimation in cryoSPARC, the relative ice thickness and CTF fit resolution was compared for each dataset (**Figure 4**). The estimated relative ice thickness obtained did not allow us to discriminate between the ice thickness of optimized datasets 1, 2 or 3, but shows clearly that dataset 4 has a thinner mean ice thickness (**Figure 4A**). In a second round of sample preparation using the same type of cryo-EM grids and preparation conditions, we directly measured the ice thickness according to the method of Rice et al. (2018). This indicated three different ice thicknesses for the holes used to collect the optimized datasets: 100.48 ± 6.24, 66.99 ± 8.27, and 30.60 ± 8.57 nm. The estimated CTF fit resolution revealed that datasets 1, 2, and 3 contain a majority of images with resolution ranging from 5 to 6 Å, with dataset 3 additionally containing a minority of images with resolution around 3.5 Å (**Figure 4B**). The estimated CTF fit resolution of the majority of images in dataset 4 range from 3 to 4 Å, indicating that this dataset is suitable to reach a final 3D reconstruction of CDC48A between 3 and 4 Å. According to our measurements, we presume that dataset 4 should have an ice thickness around 30–40 nm, while datasets 1 and 2 certainly correspond to holes having an ice thickness near 100 nm. Dataset 3 should certainly represent a mixture of images recorded in holes having ice thicknesses ranging from 30 to 100 nm, explaining why we have two populations of images within the distribution of estimated CTF fit resolution.

Additionally, 2D class averages and *ab intio* reconstructions were computed for each dataset (**Figure 6**; **Figures 3D-F**). As expected from thick ice, all particle orientations were present as revealed by the top, bottom, side, and intermediate views of CDC48A seen in the 2D class average and further confirmed by the template-free *ab initio* reconstructions. The hexameric organization of CDC48A is perfectly observed in reconstructions without symmetry imposed, in which the double ring structure is evident from the side view. The reconstructions with the applied symmetry reveal a homogeneous organization of CDC48A presenting all expected structural features of CDC48A.

In conclusion, through this iterative selection process, we were able to identify dataset 4 which has an optimal ice thickness that contained both intact complexes with a sufficiently even distribution of particle orientations and sufficiently high-resolution information to allow a confident 3D structural reconstruction.

4 DISCUSSION

Herein we describe our successful strategy for solving two common challenges in cryo-EM single particle analysis, namely sample integrity (in particular oligomer dissociation), and preferential particle orientation. We demonstrate that in our case, the hexameric ATPase CDC48A, these problems could be

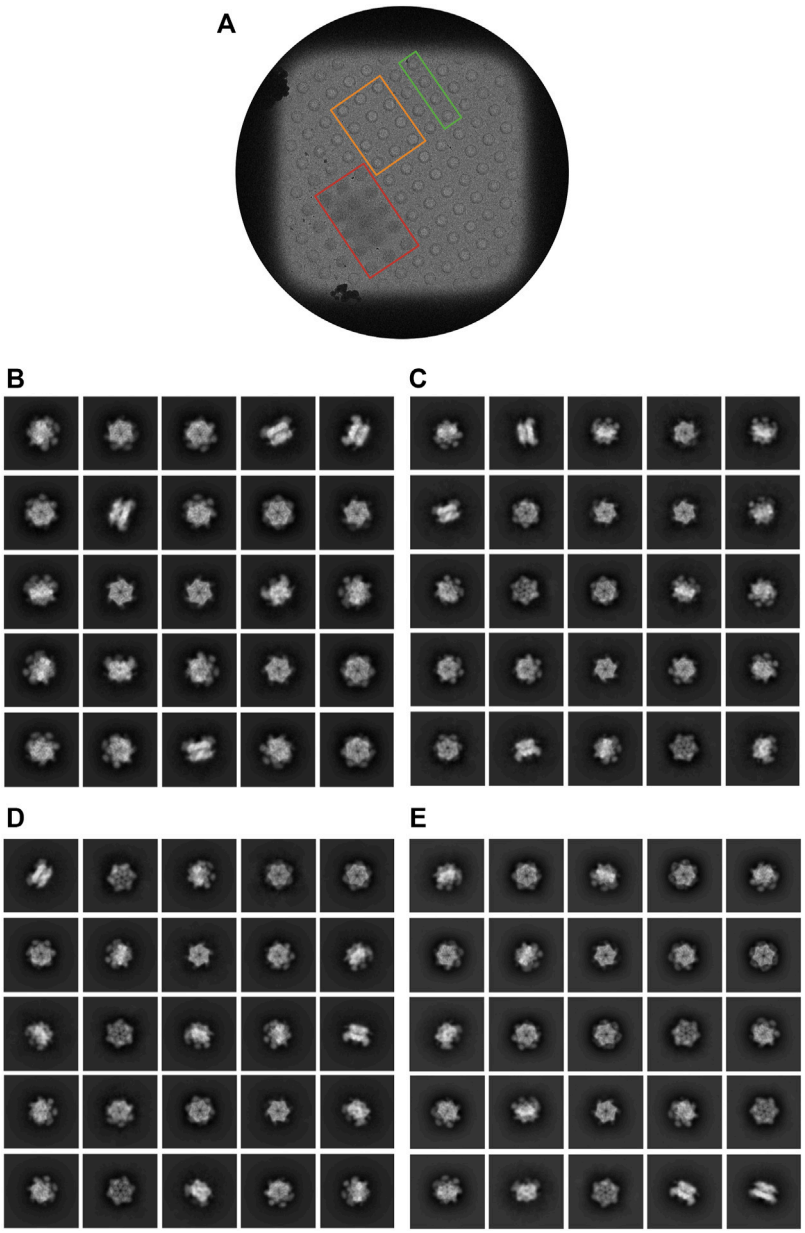

FIGURE 6 | Characterization of cryo-EM data iteratively collected from regions displaying various ice thicknesses. **(A)** Representative grid square from optimized dataset 4. Examples of holes in which the ice was too thick (red), too thin (orange), or was approximately the desired thickness (green) for this dataset are outlined. **(B–E)** Representative 2D class averages from the optimized datasets 1, 2, 3, and 4, respectively.

solved through the combination of efficient but non-conventional methods that led to higher oligomer stability, and orientational homogeneity.

Indeed, we initially observed that purified CDC48A displayed a hexameric organization when observed in negative stain but appeared dissociated in cryo-EM images, likely indicating that the freezing step dramatically impaired the integrity of CDC48A. It is well-described that the interaction of proteins with the air-water interface during the vitrification step can have a strong effect on the integrity of protein complexes. We showed that the Chameleon's blot-free and spray-on method (Razinkov et al., 2016; Dandey et al., 2018; Wei et al., 2018) preserved the hexameric organization of CDC48A, confirming that dissociation of CDC48A subunits was induced during the vitification step of EM grids. In holes containing thin ice, such as those produced using this method, the thickness of the ice layer is only a few tens of nanometers. Based on the specific shape of protein complexes, and the surface charge distribution, this thickness should have an impact on the orientation of particles. In the case of CDC48A, as the hexamer is disk-like with a diameter around 16 nm, this causes particles to have a preferential orientation.

We then decided to develop a strategy where we improved in parallel the purification of CDC48A, and the conditions for cryo-EM data acquisition. One part of our strategy was to improve the workflow from cell lysis to grid preparation. Simple improvements of the handling speed, buffers, and protocols sufficiently enhanced the protein stability to enable data collection without particle dissociation, and that from ice thickness suitable for high resolution acquisition. In our case study we achieved both a higher purity and conformational homogeneity of CDC48A by removing DNA, and nucleotides from our sample. Other means for removing DNA contamination exist but may need to be assessed for unwanted side effects. For example, polyethyleneimine (PEI) treatment may lead to a significant "collateral" precipitation of the protein of interest.

A second part of our strategy was the selection of the most suitable ice thickness. It is not unexpected that thicker ice may improve the integrity of particles and their angular distribution on cryo grids. However, these effects of ice thickness are normally not systematically assessed. Moreover, in most standard settings, obtaining high-resolution data is the main focus, leading to an automated recording of movies in grid regions presenting the thinnest ice layers. In our case, we show that ice thickness correlates positively with the particle orientational coverage (**Table 1**), and with suitable resolution for computing atomic resolution structures of protein complexes (**Figure 4**). Through a simple iterative screening coupled with the analysis of 2D class averages, it was possible to identify an intermediate ice thickness that yielded both a sufficiently homogeneous particle orientation distribution and sufficiently high-resolution images (assessed by having a substantial number of images with a CTF fit resolution in the range of 3–4 Å). In our case, the method of hole selection was manual and involved visual inspection of the ice thickness or its "grayness" in images. However, it should be possible to automate screening holes according to a specific range of this parameter, as implemented via scripting in Gatan's DM software (Rheinberger et al., 2021). Given that the movie recording speed is steadily increasing, a second option would be a "shoot first, ask questions later" approach, where data is recorded on holes of varying ice thickness, and the most appropriate ice thickness is automatically selected using analysis software such as IceBreaker (Olek et al., 2022). Ice thickness-based filtering/selection of micrographs is also implemented in cryoSPARC through the "Curate Exposures" job (Punjani et al., 2017). Although the increased ice thickness reduced the maximal resolution, the achievable resolution was, in our case, suitable for an in-depth structural, and molecular analysis (to be published later). Owing to the substantial advances of AI-based structure prediction algorithms in 2021 (Baek et al., 2021; Jumper et al., 2021), we argue that the resolution limit for addressing a functional, and biological question with cryo-EM can be lower without loss of information when confidently predicted domain structures can replace density-based *ab initio* structure modeling.

There are, of course, also other, more sophisticated ways of achieving a more homogeneous particle orientation (Drulyte et al., 2018). In our case, we could have combined the Chameleon spray-on method (Razinkov et al., 2016; Dandey et al., 2018; Wei et al., 2018), which preserved the hexameric state in thin ice, with recording a single-particle dataset on a tilted stage (Tan et al., 2017). However, access to the Chameleon is still limited for most groups. Moreover, tilting holes with thin ice will also increase the apparent ice thickness for the electrons, leading to a similar drop in maximum resolution (Drulyte et al., 2018). Additionally, setting up measurements with a tilted stage requires additional recording sessions with adjusted parameters (such as total dose), an adapted data processing workflow, and a specific instrument handling expertise that may not be available to all users (Naydenova and Russo, 2017; Tan et al., 2017).

Several other biochemical solutions have been reported to increase the particle orientation coverage in optimally thin ice, such as the use of detergents, biotinylation, antibodies, or DNA origami, in varying the pH and/or the ionic strength (Carragher et al., 2019; Han et al., 2020; Wang et al., 2020; Aissaoui et al., 2021; Patel et al., 2021). But the screening of all these parameters are extremely time consuming. In some cases, non-standard grids with a carbon or graphene support film have reduced the bias in particle orientation (Drulyte et al., 2018). However, if the anisotropy results from the particle's shape and surface charge, it is likely that a particle that shows preferential orientation in NS-EM also does so on grids with hydrophobic support films.

In summary, although more sophisticated alternative methods exist to increase particle stability, integrity, and orientation, our parallel approach has the advantage of not requiring specific chemicals, expertise, or instruments, being based on off-the-shelf ingredients and standard procedures (chemicals, Vitroblot, untilted stage). Hence, our approach provides a robust and fast method applicable to all standard laboratory settings and cryo-EM facilities. Although our dual strategy was only tested on one project, the method is general enough to apply to other non-covalently linked oligomeric samples, samples with DNA contamination, and/or samples that show a preferential orientation in thin ice. In particular, our approach can help "salvage" grids for achieving sufficient data quality without further delays. Indeed, speed may have become a more important parameter than maximum resolution in the highly competitive cryo-EM field.

DATA AVAILABILITY STATEMENT

The raw data supporting the conclusion of this article will be made available by the authors, without undue reservation.

AUTHOR CONTRIBUTIONS

Conceptualization, BH, UH, and SA; methodology, BH, LZ, and SA; formal analysis, BH, PB, and BQ; investigation, BH and LZ; resources, BH, LZ, and UH; writing—original draft, BH, SA, and BQ; writing—review and editing BH, LZ, PB, SA, and BQ; visualization, BH; supervision, UH, SA, and BQ; project administration, SA and BQ; funding acquisition, SA.

FUNDING

We acknowledge the contributions by the King Abdullah University of Science and Technology (KAUST) through the

baseline fund and the award number URF/1/4039-01-01 and URF/1/4080-01-01 from the Office of Sponsored Research (OSR). We acknowledge Diamond Light Source for access and support of the cryo-EM facilities at the United Kingdom's national Electron Bio-imaging Centre (eBIC), proposal EM NT21004-430, funded by the Wellcome Trust, MRC, and BBSRC. Additionally, We acknowledge The Rosalind Franklin Institute Structural Biology theme at Harwell Campus, United Kingdom, including EPSRC grant P2019-0006, for access to the Chameleon Instrument.

ACKNOWLEDGMENTS

We would like to thank the Imaging and Characterization core lab and the Supercomputing Laboratories at KAUST for the use of their resources and support. We thank Miriam Weckener and Yuriy Chaban for data collection at eBIC, Diamond Light Source. We acknowledge the Research Complex at Harwell for access to their cryo-EM facilities and we are especially thankful to Miriam Weckener for preparing grids using the Chameleon. We would like to express our gratitude for access and support in the cryo-EM work carried out at the Astbury Centre for Structural Molecular Biology, University of Leeds, United Kingdom; especially to Rebecca F. Thompson, Emma Hesketh, and Daniel Maskell for their great support for sample preparation and data collection. We are grateful to ETH Zurich for access to the computational resources at ScopeM and Euler cluster. We acknowledge SOLEIL for the provision of synchrotron radiation facilities and we would like to thank A. Thureau for assistance in using the beamline. We would also like to acknowledge that a portion of this work was also included in the M.Sc thesis of BH.

SUPPLEMENTARY MATERIAL

The Supplementary Material for this article can be found online at: https://www.frontiersin.org/articles/10.3389/fmolb.2022.890390/full#supplementary-material

REFERENCES

Aissaoui, N., Lai-Kee-Him, J., Mills, A., Declerck, N., Morichaud, Z., Brodolin, K., et al. (2021). Modular Imaging Scaffold for Single-Particle Electron Microscopy. *ACS Nano* 15, 4186–4196. doi:10.1021/acsnano.0c05113

Baek, M., DiMaio, F., Anishchenko, I., Dauparas, J., Ovchinnikov, S., Lee, G. R., et al. (2021). Accurate Prediction of Protein Structures and Interactions Using a Three-Track Neural Network. *Science* 373, 871–876. doi:10.1126/SCIENCE.ABJ8754/

Banerjee, S., Bartesaghi, A., Merk, A., Rao, P., Bulfer, S. L., Yan, Y., et al. (2016). 2.3 A Resolution Cryo-EM Structure of Human P97 and Mechanism of Allosteric Inhibition. *Science* 351, 871–875. doi:10.1126/science.aad7974

Bepler, T., Morin, A., Rapp, M., Brasch, J., Shapiro, L., Noble, A. J., et al. (2019). Positive-unlabeled Convolutional Neural Networks for Particle Picking in Cryo-Electron Micrographs. *Nat. Methods* 16, 1153–1160. doi:10.1038/s41592-019-0575-8

Caffrey, B., Zhu, X., Berezuk, A., Tuttle, K., Chittori, S., and Subramaniam, S. (2021). AAA+ ATPase P97/VCP Mutants and Inhibitor Binding Disrupt Inter-domain Coupling and Subsequent Allosteric Activation. *J. Biol. Chem.* 297, 101187. doi:10.1016/J.JBC.2021.101187

Carragher, B., Cheng, Y., Frost, A., Glaeser, R. M., Lander, G. C., Nogales, E., et al. (2019). Current Outcomes when Optimizing 'standard' Sample Preparation for Single-Particle Cryo-EM. *J. Microsc.* 276, 39–45. doi:10.1111/JMI.12834

Cooney, I., Han, H., Stewart, M. G., Carson, R. H., Hansen, D. T., Iwasa, J. H., et al. (2019). Structure of the Cdc48 Segregase in the Act of Unfolding an Authentic Substrate. *Science* 365, 502–505. doi:10.1126/science.aax0486

Copeland, C., Woloshen, V., Huang, Y., and Li, X. (2016). AtCDC48A Is Involved in the Turnover of an NLR Immune Receptor. *Plant J.* 88, 294–305. doi:10.1111/tpj.13251

Dandey, V. P., Wei, H., Zhang, Z., Tan, Y. Z., Acharya, P., Eng, E. T., et al. (2018). Spotiton: New Features and Applications. *J. Struct. Biol.* 202, 161–169. doi:10.1016/J.JSB.2018.01.002

DeLaBarre, B., and Brunger, A. T. (2003). Complete Structure of P97/valosin-Containing Protein Reveals Communication between Nucleotide Domains. *Nat. Struct. Mol. Biol.* 10, 856–863. doi:10.1038/nsb972

Drulyte, I., Johnson, R. M., Hesketh, E. L., Hurdiss, D. L., Scarff, C. A., Porav, S. A., et al. (2018). Approaches to Altering Particle Distributions in Cryo-Electron Microscopy Sample Preparation. *Acta Cryst. Sect. D. Struct. Biol.* 74, 560–571. doi:10.1107/S2059798318006496

Han, Y., Fan, X., Wang, H., Zhao, F., Tully, C. G., Kong, J., et al. (2020). High-yield Monolayer Graphene Grids for Near-Atomic Resolution Cryoelectron Microscopy. *Proc. Natl. Acad. Sci. U.S.A.* 117, 1009–1014. doi:10.1073/PNAS.1919114117/

Huang, A., Tang, Y., Shi, X., Jia, M., Zhu, J., Yan, X., et al. (2020). Proximity Labeling Proteomics Reveals Critical Regulators for Inner Nuclear Membrane Protein Degradation in Plants. *Nat. Commun.* 11, 1–10. doi:10.1038/s41467-020-16744-1

Jumper, J., Evans, R., Pritzel, A., Green, T., Figurnov, M., Ronneberger, O., et al. (20212021). Highly Accurate Protein Structure Prediction with AlphaFold. *Nature* 596, 583–589. doi:10.1038/s41586-021-03819-2

Kimanius, D., Dong, L., Sharov, G., Nakane, T., and Scheres, S. H. W. (2021). New Tools for Automated Cryo-EM Single-Particle Analysis in RELION-4.0. *Biochem. J.* 478, 4169–4185. doi:10.1042/BCJ20210708

Klebl, D., Gravett, M., Kontziampasis, D., Wright, D., Bon, R., Monteiro, D., et al. (2020). Need for Speed: Examining Protein Behaviour during CryoEM Grid Preparation at Different Timescales. *Structure* 28 (11), 1238. doi:10.2139/ssrn.3608388

Kühlbrandt, W. (2022). Forty Years in cryoEM of Membrane Proteins. *Microscopy* 71, i30–i50. doi:10.1093/JMICRO/DFAB041

Kühlbrandt, W. (2014). The Resolution Revolution. *Science* 343, 1443–1444. doi:10.1126/SCIENCE.1251652/

Lancey, C., Tehseen, M., Bakshi, S., Percival, M., Takahashi, M., Sobhy, M. A., et al. (20212021). Cryo-EM Structure of Human Pol κ Bound to DNA and Mono-Ubiquitylated PCNA. *Nat. Commun.* 12, 6095. doi:10.1038/s41467-021-26251-6

Ling, Q., Broad, W., Trösch, R., Töpel, M., Demiral Sert, T., Lymperopoulos, P., et al. (2019). Ubiquitin-dependent Chloroplast-Associated Protein Degradation in Plants. *Science* 363, eaav4467. doi:10.1126/science.aav4467

Liu, Y., and Li, J. (2014). Endoplasmic Reticulum-Mediated Protein Quality Control in Arabidopsis. *Front. Plant Sci.* 5, 162. doi:10.3389/fpls.2014.00162

Manalastas-Cantos, K., Konarev, P. v., Hajizadeh, N. R., Kikhney, A. G., Petoukhov, M. v., Molodenskiy, D. S., et al. (2021). ATSAS 3.0: Expanded Functionality and New Tools for Small-Angle Scattering Data Analysis. *J. Appl. Cryst.* 54, 343–355. doi:10.1107/S1600576720013412

Naydenova, K., and Russo, C. J. (2017). Measuring the Effects of Particle Orientation to Improve the Efficiency of Electron Cryomicroscopy. *Nat. Commun.* 8, 629. doi:10.1038/s41467-017-00782-3

Nogales, E., and Scheres, S. H. W. (2015). Cryo-EM: A Unique Tool for the Visualization of Macromolecular Complexity. *Mol. Cell* 58, 677–689. doi:10.1016/J.MOLCEL.2015.02.019

Olek, M., Cowtan, K., Webb, D., Chaban, Y., and Zhang, P. (2022). IceBreaker: Software for High-Resolution Single-Particle Cryo-EM with Non-uniform Ice. *Structure* 30, 522–531. doi:10.1016/j.str.2022.01.005

Pan, M., Zheng, Q., Yu, Y., Ai, H., Xie, Y., Zeng, X., et al. (2021). Seesaw Conformations of Npl4 in the Human P97 Complex and the Inhibitory Mechanism of a Disulfiram Derivative. *Nat. Commun.* 12, 121. doi:10.1038/s41467-020-20359-x

Patel, A., Toso, D., Litvak, A., and Nogales, E. (2021). Efficient Graphene Oxide Coating Improves Cryo-EM Sample Preparation and Data Collection from Tilted Grids. *bioRxiv*. 2021.03.08.434344. doi:10.1101/2021.03.08.434344

Punjani, A., Rubinstein, J. L., Fleet, D. J., and Brubaker, M. A. (2017). cryoSPARC: Algorithms for Rapid Unsupervised Cryo-EM Structure Determination. *Nat. Methods* 14, 290–296. doi:10.1038/NMETH.4169

Razinkov, I., Dandey, V. P., Wei, H., Zhang, Z., Melnekoff, D., Rice, W. J., et al. (2016). A New Method for Vitrifying Samples for cryoEM. *J. Struct. Biol.* 195, 190–198. doi:10.1016/J.JSB.2016.06.001

Rheinberger, J., Oostergetel, G., Resch, G. P., and Paulino, C. (2021). Optimized Cryo-EM Data-Acquisition Workflow by Sample-Thickness Determination. *Acta Cryst. Sect. D. Struct. Biol.* 77, 565–571. doi:10.1107/S205979832100334X/

Rice, W. J., Cheng, A., Noble, A. J., Eng, E. T., Kim, L. Y., Carragher, B., et al. (2018). Routine Determination of Ice Thickness for Cryo-EM Grids. *J. Struct. Biol.* 204 (1), 38–44. doi:10.1016/J.JSB.2018.06.007

Rohou, A., and Grigorieff, N. (2015). CTFFIND4: Fast and Accurate Defocus Estimation from Electron Micrographs. *J. Struct. Biol.* 192, 216–221. doi:10.1016/J.JSB.2015.08.008

Schneidman-Duhovny, D., Hammel, M., and Sali, A. (2010). FoXS: a Web Server for Rapid Computation and Fitting of SAXS Profiles. *Nucleic Acids Res.* 38, W540–W544. doi:10.1093/NAR/GKQ461

Stach, L., and Freemont, P. S. (2017). The AAA+ ATPase P97, a Cellular Multitool. *Biochem. J.* 474, 2953–2976. doi:10.1042/BCJ20160783

Tan, Y. Z., Baldwin, P. R., Davis, J. H., Williamson, J. R., Potter, C. S., Carragher, B., et al. (2017). Addressing Preferred Specimen Orientation in Single-Particle Cryo-EM through Tilting. *Nat. Methods* 14, 793–796. doi:10.1038/NMETH.4347

Tegunov, D., and Cramer, P. (2019). Real-time Cryo-Electron Microscopy Data Preprocessing with Warp. *Nat. Methods* 16, 1146–1152. doi:10.1038/s41592-019-0580-y

Twomey, E. C., Ji, Z., Wales, T. E., Bodnar, N. O., Ficarro, S. B., Marto, J. A., et al. (2019). Substrate Processing by the Cdc48 ATPase Complex Is Initiated by Ubiquitin Unfolding. *Science* 365, eaax1033. doi:10.1126/science.aax1033

Wang, F., Liu, Y., Yu, Z., Li, S., Feng, S., Cheng, Y., et al. (2020). General and Robust Covalently Linked Graphene Oxide Affinity Grids for High-Resolution Cryo-EM. *Proc. Natl. Acad. Sci. U.S.A.* 117, 24269–24273. doi:10.1073/PNAS.2009707117

Waterhouse, A., Bertoni, M., Bienert, S., Studer, G., Tauriello, G., Gumienny, R., et al. (2018). SWISS-MODEL: Homology Modelling of Protein Structures and Complexes. *Nucleic Acids Res.* 46, W296–W303. doi:10.1093/NAR/GKY427

Wei, H., Dandey, V. P., Zhang, Z., Raczkowski, A., Rice, W. J., Carragher, B., et al. (2018). Optimizing "Self-Wicking" Nanowire Grids. *J. Struct. Biol.* 202, 170–174. doi:10.1016/J.JSB.2018.01.001

Zegzouti, H., Zdanovskaia, M., Hsiao, K., and Goueli, S. A. (2009). ADP-glo: A Bioluminescent and Homogeneous Adp Monitoring Assay for Kinases. *Assay Drug Dev. Technol.* 7, 560–572. doi:10.1089/ADT.2009.0222

Zhang, K. (2016). Gctf: Real-Time CTF Determination and Correction. *J. Struct. Biol.* 193, 1–12. doi:10.1016/J.JSB.2015.11.003

Zivanov, J., Nakane, T., and Scheres, S. H. W. (2020). Estimation of High-Order Aberrations and Anisotropic Magnification from Cryo-EM Data Sets in RELION-3.1. *Int. Union Crystallogr. J.* 7, 253–267. doi:10.1107/S2052252520000081

Conflict of Interest: The authors declare that the research was conducted in the absence of any commercial or financial relationships that could be construed as a potential conflict of interest.

Publisher's Note: All claims expressed in this article are solely those of the authors and do not necessarily represent those of their affiliated organizations, or those of the publisher, the editors and the reviewers. Any product that may be evaluated in this article, or claim that may be made by its manufacturer, is not guaranteed or endorsed by the publisher.

frontiers | Frontiers in Molecular Biosciences

ORIGINAL RESEARCH
published: 23 June 2022
doi: 10.3389/fmolb.2022.903148

Approaches to Using the Chameleon: Robust, Automated, Fast-Plunge cryoEM Specimen Preparation

*Talya S. Levitz[1†], Miriam Weckener[2,3†], Ivan Fong[4], James H. Naismith[2,3], Catherine L. Drennan[1,5,6], Edward J. Brignole[1,7], Daniel K. Clare[8] and Michele C. Darrow[4,9]**

[1]Department of Biology, Massachusetts Institute of Technology, Cambridge, MA, United States, [2]Structural Biology, The Rosalind Franklin Institute, Harwell Science Campus, Didcot, United Kingdom, [3]Division of Structural Biology, The Wellcome Centre for Human Genetics, University of Oxford, Oxford, United Kingdom, [4]SPT Labtech, Melbourn, United Kingdom, [5]Department of Chemistry, Massachusetts Institute of Technology, Cambridge, MA, United States, [6]Howard Hughes Medical Institute, Massachusetts Institute of Technology, Cambridge, MA, United States, [7]MIT.nano, Massachusetts Institute of Technology, Cambridge, MA, United States, [8]Diamond Light Source Ltd., Harwell Science Campus, Didcot, United Kingdom, [9]Artificial Intelligence and Informatics, The Rosalind Franklin Institute, Harwell Science Campus, Didcot, United Kingdom

The specimen preparation process is a key determinant in the success of any cryo electron microscopy (cryoEM) structural study and until recently had remained largely unchanged from the initial designs of Jacques Dubochet and others in the 1980s. The process has transformed structural biology, but it is largely manual and can require extensive optimisation for each protein sample. The chameleon instrument with its self-wicking grids and fast-plunge freezing represents a shift towards a robust, automated, and highly controllable future for specimen preparation. However, these new technologies require new workflows and an understanding of their limitations and strengths. As early adopters of the chameleon technology, we report on our experiences and lessons learned through case studies. We use these to make recommendations for the benefit of future users of the chameleon system and the field of cryoEM specimen preparation generally.

Keywords: cryoEM specimen preparation, vitrification, automation, self-wicking grids, air-water interface issues, preferred orientation, denaturation/dissociation

OPEN ACCESS

Edited by:
Felix Weis,
European Molecular Biology Laboratory Heidelberg, Germany

Reviewed by:
Christopher Arthur,
Genentech, Inc., United States
Marta Carroni,
Science for Life Laboratory (SciLifeLab), Sweden

****Correspondence:***
Michele C. Darrow
michele.darrow@sptlabtech.com

[†]These authors have contributed equally to this work

Specialty section:
This article was submitted to Structural Biology, a section of the journal Frontiers in Molecular Biosciences

Received: *23 March 2022*
Accepted: *31 May 2022*
Published: *23 June 2022*

Citation:
Levitz TS, Weckener M, Fong I, Naismith JH, Drennan CL, Brignole EJ, Clare DK and Darrow MC (2022) Approaches to Using the Chameleon: Robust, Automated, Fast-Plunge cryoEM Specimen Preparation. Front. Mol. Biosci. 9:903148. doi: 10.3389/fmolb.2022.903148

INTRODUCTION

Electron microscopy of biological molecules requires that they are frozen or chemically fixed prior to their placement under high vacuum and exposure to damaging electrons (Taylor and Glaeser, 1976; Henderson, 1990). Crystalline ice strongly diffracts electrons, obscuring the image of the sample, and must be avoided. Thus, the vitrification of biological samples is a key step in electron microscopy. The chameleon is a blot-free, pico-litre dispensing instrument designed to automate the specimen preparation process for cryo electron microscopy (cryoEM) (Darrow et al., 2019) and is based on the original Spotiton design (Wei et al., 2019). It is a free-standing instrument, approximately 1.7 m tall (**Figure 1**) with an upper cabinet that houses the robotic equipment needed to handle the sample and grids and an on-board glow discharger. The cryogens are contained in a motorised drawer, and supporting systems (humidifier, cleaning, waste, etc.) and storage space are available in the built-in cupboard below. A computer monitor, keyboard and mouse sit to one side of the chameleon system.

The typical workflow is composed of three main parts: setup, freezing grids, and clean up (**Figure 2**). During the setup stage, the required reagents (high purity water, a proprietary cleaning solution - chamclean, ethanol, methanol) and consumables (vials, dispenser cleaning pads) are

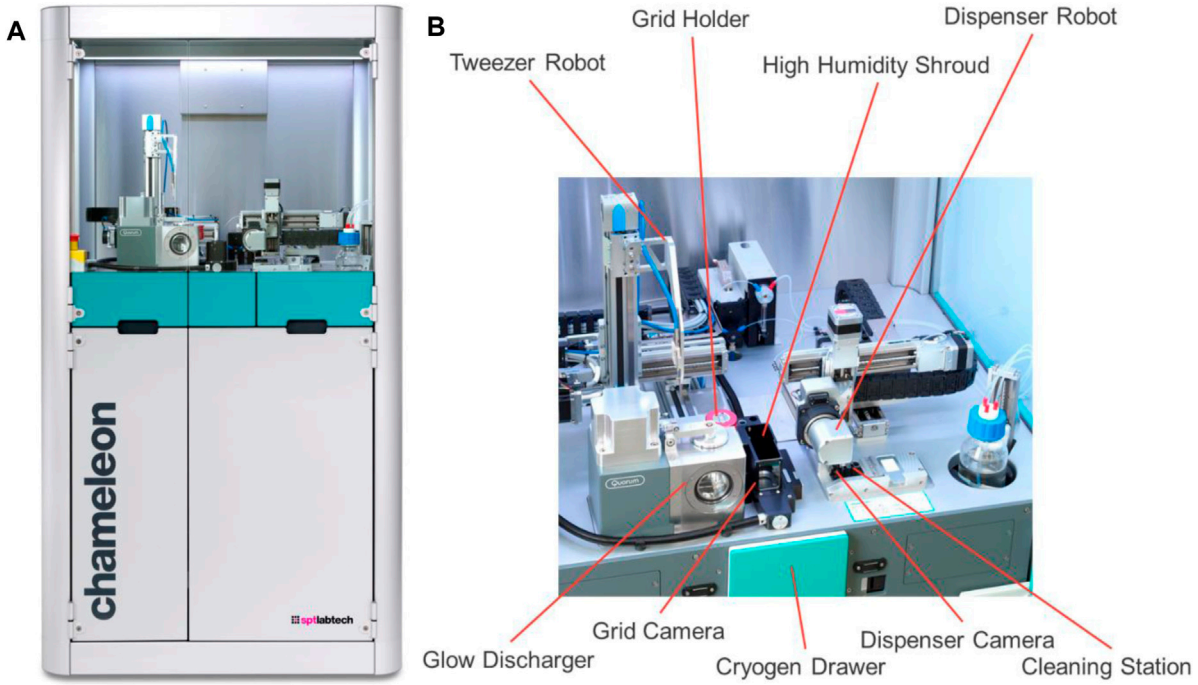

FIGURE 1 | Overview of the chameleon system. **(A)** The entire system with the robotic equipment at the top and the built-in cupboard underneath. **(B)** A close-up of the top deck with the robotic equipment needed for specimen preparation highlighted.

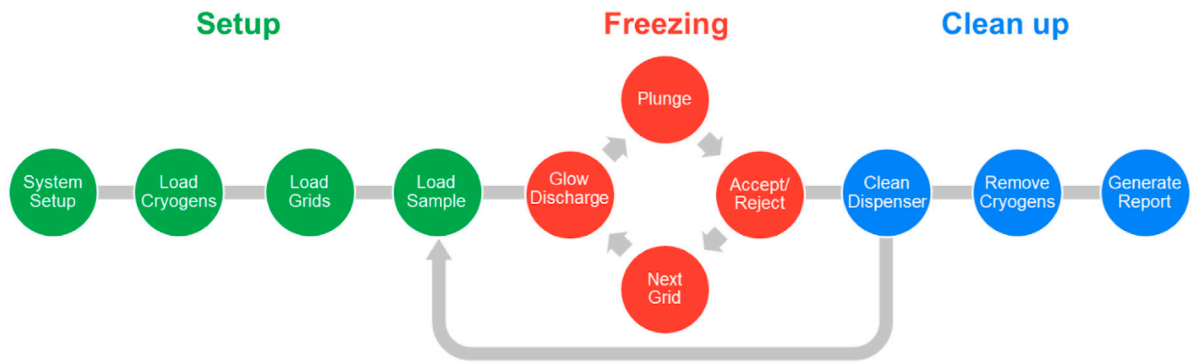

FIGURE 2 | Schematic representation of the chameleon workflow. Steps taken to set up the system are indicated in green. The iterative freezing loop (red) cycles between glow discharging, plunging, accepting/rejecting a grid and then moving on to the next. Each freezing session finishes with clean up steps (blue); however, if a second sample is to be frozen, it can be loaded into the system within the same session, just after the dispenser has been cleaned.

loaded, and the dispenser fluidics system primed in an automated process. The user interface directs the steps necessary to load the cryogens, self-wicking grids, and the sample into the instrument. Up to eight grids can be loaded into the system, of which four can be glow discharged simultaneously. Session and sample information including grid type, sample identity, molecular weight and concentration, and buffer components are recorded to generate a freezing session report. Having set up the system, the specified number of grids are glow discharged, the sample is applied to the grid using the piezoelectric dispenser, and the grid plunge frozen. After freezing, each grid is held in liquid nitrogen and a video of the wicking process can be assessed to decide whether to accept or discard the grid. The system allows full control over glow discharge strength (time and current) and the dispense-to-plunge time which allows optimisation of the specimen preparation process. After grid freezing has been completed the system is cleaned in a semi-automatic manner. The system is then ready for a new sample, or the freezing session can be ended, the accepted grids removed, and a report generated. Generally, a freezing session to produce 6-8 grids of a single

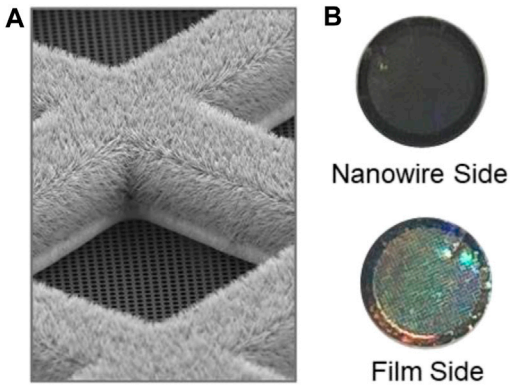

FIGURE 3 | Self-wicking nanowire grids. **(A)**. SEM image showing a grid bar junction with the nanowire side of the grid facing up, with the 1.2 µm diameter holes, 0.8 µm edge-to-edge spacing holey carbon film facing down. **(B)**. The nanowire side of the grid should face towards the dispenser in the chameleon system (to the right). The nanowire side of the grid is characterised by a darker, copper colour, whereas the film side of the grid is characterised by a silver-coloured rim and a more obvious rainbow appearance of the film.

sample takes approximately 45 min in its entirety. Switching to a second sample takes approximately 10 min due to the dispenser cleaning protocol, and because many aspects of setting up the system do not need to be repeated, the second sample will require less time to freeze the equivalent number of grids.

Self-wicking grids and low-volume sample dispensing are key enabling technologies for the chameleon (Jain et al., 2012; Razinkov et al., 2016; Wei et al., 2018). The nanowires provide a controllable wicking mechanism to create a thin film and the low-volume dispenser delivers consistent volumes that do not overwhelm the wicking capacity of the grid. The amount of liquid transported through the nanowires by wicking is a function of the liquid itself and of time, for this reason the time from sample application to frozen grid (dispense-to-plunge time) is a crucial parameter. Self-wicking grids have copper hydroxide nanowires on one side and a holey carbon film on the other (**Figure 3A**). The holey carbon pattern currently in use is 1.2 µm in diameter with 0.8 µm between each hole (edge-to-edge), producing a more densely packed pattern of holes than is typical. When using these grids, the nanowire side faces towards the dispenser (to the right in the chameleon system). The nanowire side of the grid is generally a darker, copper colour, whereas the film side of the grid is characterised by a silver-coloured rim and a more obvious rainbow appearance of the film (**Figure 3B**).

RESULTS AND DISCUSSION

Manufacturing and Quality Control of Self-Wicking Grids

The manufacturing process for self-wicking grids requires additional steps when compared to non-self-wicking grids. The challenge is to control the growth of the nanowires and ensure consistency (**Figure 4A**). Consistency can be assessed through multiple quality control tests integrated into the manufacturing process. The first of these quality checks consists of testing a small subset of starting (base) grids of each batch to identify batches exhibiting the most common manufacturing imperfections (bent or distorted base grids) (**Figure 4B**). Base grid batches meeting quality criteria enter the full manufacturing process, starting with a series of pre-treatment steps followed by nanowire growth (adapted from Wei et al., 2018). The growth of the nanowires is assessed by a visual inspection using light microscopy of each grid, looking for grid bar defects and nanowire growth consistency. A regular holey plastic film is floated onto the grids, which is then coated in a layer of carbon and the plastic film is dissolved, leaving a thin layer of holey carbon film (adapted from Marr et al., 2014). The carbon film is assessed optically for defects such as tears and pseudoholes in the film of each grid and any such damaged grids are removed.

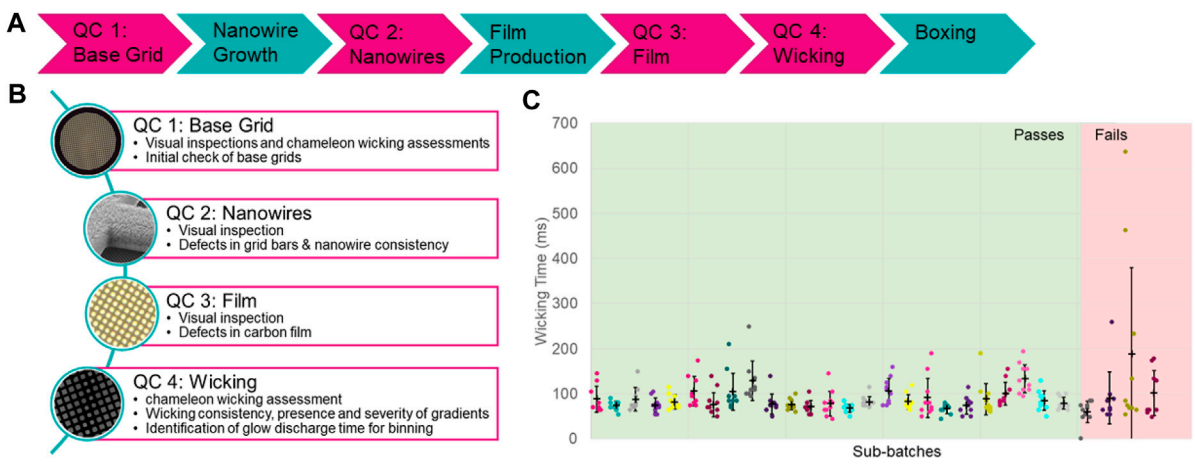

FIGURE 4 | The self-wicking grid manufacturing and quality assessment process. **(A)** A schematic overview of the steps taken to both manufacture (teal) and assess the quality (magenta) of self-wicking grids. **(B)** Descriptions of the quality control checks that are in place. **(C)** Example wicking QC data, indicating sub-batches that have passed or failed. Sub-batches are tested using a standard sample and range of glow discharge times.

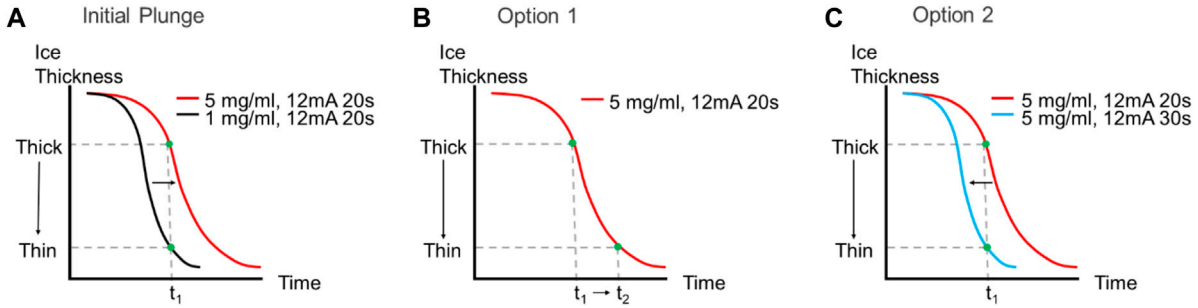

FIGURE 5 | Effect of increased sample concentration on ice thickness and dispense-to-plunge time. **(A)** The same sample at higher concentrations will lead to thicker ice observed on the grid if the dispense-to-plunge time and glow discharge strength are both held constant. There are two options to obtain thinner ice with a more concentrated sample: either increase the dispense-to-plunge time [**(B)**, Option 1] or increase the glow discharge time (or current) and keep the dispense-to-plunge time constant [**(C)**, Option 2].

In the next step of the manufacturing process, ~10% of final grids from each batch are quality control tested on a chameleon using 5 mg/ml apoferritin in phosphate buffered saline (PBS) to assess glow discharge and wicking behaviour. Following on-board glow discharge that varies between 30–90 s at 12 mA, a single stripe of sample is placed on each grid. The glow discharge settings that result in a wicking time in the range of 60–160 ms are identified. A minimum of 10 grids are then tested at this glow discharge time to assess for consistency and severity of gradients if present (**Figure 4C**). Subsets of final grids can wick too quickly or too slowly, and these are removed. Only grids in subsets that show a wicking time between 60 and 160 ms when glow discharged for between 30 and 90 s at 12 mA are prepared for use on the instrument.

Employing these grids, the chameleon can provide even a novice user, in less than 2 days, a reliable and straightforward workflow to prepare frozen specimens. We found that a deeper understanding of the interplay between sample characteristics and wicking, and how best to approach a freezing session is beneficial to optimise the process. Here, we describe our current understanding of how these factors interplay and some practical insights into the process.

Specimen Preparation Using the Chameleon System

When a cryoEM project begins with a new sample, different parameters including sample concentration, buffer components, detergent (identity and concentration), and the sample storage/handling temperature need to be optimised. In addition, a range of different blot times or forces, grid types and sample concentrations often need to be evaluated. Multiple iterative rounds of specimen preparation and screening grids are often required to optimise specimen preparation conditions, which is exacerbated by the variability inherent in the standard blot-freezing method (for more information on standard cryoEM methods, see Thompson et al., 2016; Drulyte et al., 2018). The chameleon system does not remove the iterative nature of grid optimisation but makes it faster because the specimen preparation is reproducible with precise control of glow discharge and dispense-to-plunge time (together these influence the ice thickness). We observed that the thickness of ice is inversely proportional to strength of glow discharge (higher current or longer time gives thinner ice) and to the dispense-to-plunge time (longer times give thinner ice) (**Figures 5B,C**). Thus, in contrast to standard blot-based plungers, the time that grids are glow discharged for and the dispense-to-plunge time are variables that must be empirically determined depending on desired ice thickness and other grid characteristics. Other factors, such as sample viscosity and concentration, influence the precise relationship between glow discharge and dispense-to-plunge time. A more highly concentrated sample will lead to thicker ice for the same glow discharge strength and dispense-to-plunge time (**Figure 5A**). Empirically exploring these parameters using the chameleon and a screening cryoEM microscope can be required to determine optimal conditions. CryoEM microscope evaluation is essential where particle characteristics such as preferred orientation and/or denaturation at the air-water interface (AWI) (Dandey et al., 2018; Noble et al., 2018b; Klebl et al., 2020; Levitz et al., 2022) are being investigated.

The perfect specimen presentation is one that has well separated uniformly sized particles in their native state, embedded in thin ice (<200 nm thick) (**Figure 6**). Achieving this ideal presentation is dependent on the interplay between the input sample characteristics, the grid preparation device used and the desired output characteristics of the frozen grid (**Figure 6**). Operational experience of the chameleon system has identified some general trends; the first is that as dispense-to-plunge time decreases, the protein concentration has to be increased for the same number of particles to be seen on the grid (Klebl et al., 2020; Levitz et al., 2022). Additionally, smaller molecular weight samples appear to require less concentration than larger molecular weight samples to achieve the same density of particles on grids (**Figure 6B**) (Passmore and Russo, 2016).

The chameleon operates over a wide range of buffer conditions, tolerating glycerol and detergents. Especially high sample viscosity may require changes to dispensing parameters such as the amplitude or back pressure used in the piezoelectric dispenser. During the workflow, different sample concentrations or buffer conditions are treated as separate samples with a full

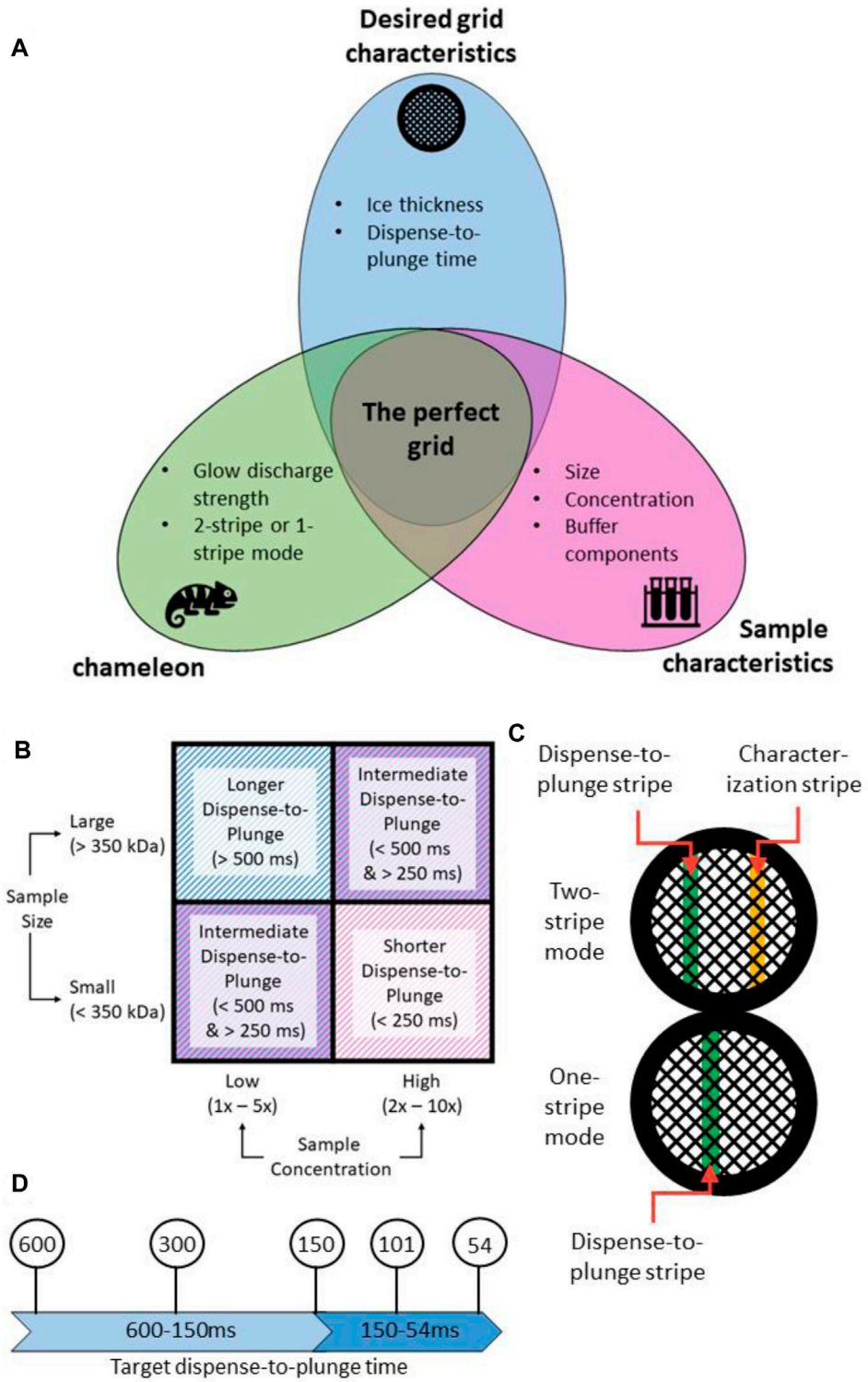

FIGURE 6 | A strategy for approaching chameleon specimen preparation. **(A)** Creation of the "perfect grid" relies on the relationship between the input sample characteristics, the settings used on the chameleon system, and the desired output grid characteristics. **(B)** Sample characteristics such as concentration and size can affect the range of dispense-to-plunge times that are achievable. Shorter dispense-to-plunge times generally require a higher concentration of sample, though this effect is also modulated by the sample size. **(C)** The chameleon system has two modes for grid preparation: one-stripe and two-stripe. In two-stripe mode, a characterization stripe is first applied to determine the ideal wicking time. The second, plunge stripe, is then deposited on a different part of the grid. In one-stripe mode, only one stripe is applied before plunge freezing. **(D)** Any target dispense-to-plunge time can be achieved by adjusting various parameters on the chameleon system. Because of the relationship between dispense-to-plunge time and specimen concentration observed on the grid (see **Supplementary Case Study S1**), a range of dispense-to-plunge times should be assessed.

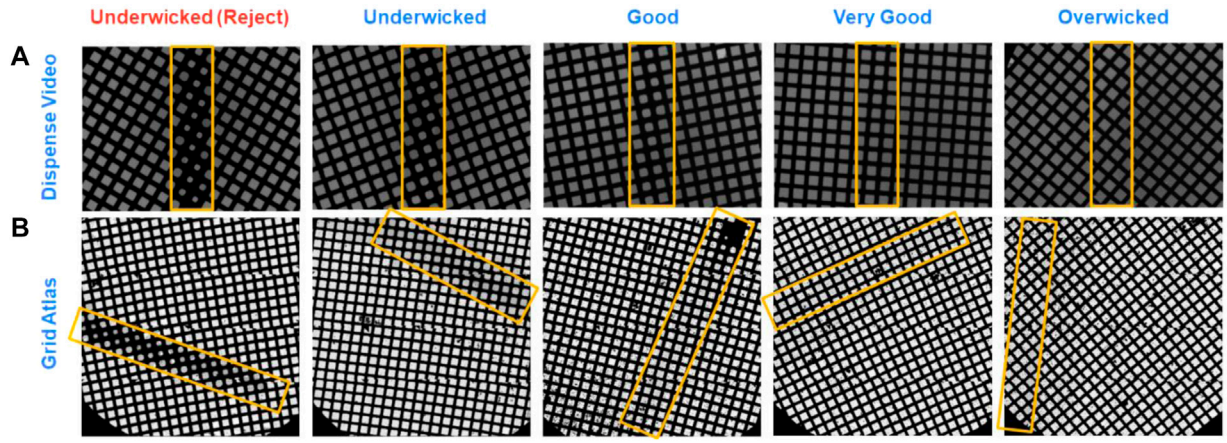

FIGURE 7 | Comparison of grids just prior to freezing on a chameleon and after imaging on a cryo electron microscope. In both two-stripe and one-stripe modes, a video is recorded between sample application and grid freezing that allows the user to judge if the desired film thickness has been obtained. There are five categories a grid can fall into based on its wicking state **(A)**. The **(B)** shows the corresponding grids as imaged on a cryo electron microscope demonstrating the correlation in ice thickness. Stripes in the chameleon dispense video are centrally located and vertical (marked by yellow boxes), whereas the corresponding stripes during imaging (marked by yellow boxes) are randomly located relative to the microscope cryobox and stage.

cleaning protocol in between to ensure no carryover. Since the sample inside the dispenser equilibrates to ambient temperature, samples that require strict temperature regulation are currently incompatible with this workflow.

The current version of the chameleon software (1.12.0) allows for the system to be used in two different modes: two-stripe and one-stripe (**Figure 6C**). In two-stripe mode, a stripe of sample (the "characterization stripe") is deposited onto one part of a glow discharged grid. The wicking process is then followed over 2.5 s and a video recorded (**Supplementary Video S1**). A proprietary algorithm automatically determines the optimal dispense-to-plunge time for the second stripe, including estimation of an offset since wicking occurs more slowly for the second stripe than the first stripe; however, the user can choose a different dispense-to-plunge time. Next, the sample is sprayed onto a different area of the same grid for the second stripe and plunge frozen. The instrument displays another video of the second stripe prior to the grid entering the ethane, allowing the user to assess if the desired film thickness was obtained and to reject grids that do not match the user's desired film thickness (**Figure 7**).

In one-stripe mode, only a single stripe of sample is dispensed near the middle of the grid (**Figure 6C**). The instrument then displays a video of the grid prior to entering the ethane that informs the decision to accept or reject the grid, in the same way as for two-stripe mode (**Figure 7**). The one-stripe mode provides a 54 ms dispense-to-plunge time option for users attempting to address AWI issues. When using the 54 ms option, the grid does not stop in front of the camera for a video to be collected; instead, a single frame is captured as the grid moves past the camera.

Since the two-stripe mode offers the possibility to view and then vary the dispense-to-plunge time on an individual grid basis, it is often preferred by newer users, but the offset estimate required in this mode can introduce grid-to-grid variability not seen with the one-stripe mode. Because no offset is required in one-stripe mode, shorter dispense-to-plunge times are available (including the 54 ms option); however, prior knowledge about the appropriate glow discharge strength is necessary when using one-stripe mode. These two modes are complementary, and experience suggests a workflow where two-stripe is used initially followed by one-stripe, once the glow discharge strength and dispense-to-plunge time are optimised (see **Supplementary Case Study S3**).

Considerations for Specimen Preparation Session

Freezing Strategy With no Prior Knowledge

For proteins of molecular weight below 350 kDa, concentrations starting at 1.0 mg/ml and varied down to 0.2 mg/ml empirically encompass most samples tried. For targets above 350 kDa the concentration range of 2.0 mg/ml down to 0.5 mg/ml works well. However, these concentrations can vary for individual samples. Testing with dispense-to-plunge times such as 600, 300, 150, and 101 ms usually provides sufficient insight to optimise the dispense-to-plunge time and concentration necessary (**Figure 6D**), particularly if the sample displays time-dependent behaviour (migration to the AWI, preferred orientation) on the grids. **Supplementary Form S1** is useful for capturing sample information for assessment prior to the freezing session to guide parameter choice.

The optimal glow discharge conditions vary by sample and can shift between grid batches. The default glow discharge conditions of 20 s and 12 mA represent a useful starting point that has been chosen to allow greater control over the wicking process. Both the current and time can be modified as needed to address sample-specific characteristics. For the first grid of a new grid batch or a new sample, it is helpful to use two-stripe mode as the characterization stripe provides additional information on the wicking speed. If the characterization stripe of the first grid wicks more slowly than desired, the glow discharge time can be

extended for the second and any subsequent grids. The characterization stripe of two-stripe mode offers the opportunity to view the entire wicking process and evaluate the glow discharge conditions (**Supplementary Video S1**). Once an appropriate glow discharge strength has been identified, one-stripe mode can be used.

Setting permissive acceptance criteria during the initial investigation allows a wide range of conditions including ice thickness, sample concentrations and dispense-to-plunge times to be evaluated. The specimens can also be screened to determine if a shorter dispense-to-plunge time is imperative to overcome poor sample behaviour such as denaturation/dissociation or preferred orientation; if this is the case and sufficient protein concentrations can be provided, future plunging sessions can focus on achieving grids with shorter dispense-to-plunge times (see *Strategy for a targeted freezing session* below).

Freezing Strategy With Prior Knowledge

Where a sample has been screened on a blot-based plunging instrument, this knowledge informs the starting conditions for chameleon sessions. For targets below 350 kDa the concentration of protein needed for the chameleon appears to be approximately equal to the concentration of protein needed for blot-based plunging instruments for longer dispense-to-plunge times (>250 ms). For short dispense-to-plunge times, the concentration should be increased between two and five-fold. Proteins above 350 kDa typically require a two-fold increase in concentration even for dispense-to-plunge times >250 ms compared to blotting. For short dispense-to-plunge times, an increase of up to ten-fold in concentration can be required. For membrane proteins where detergents are present, in some cases a need to double or triple the sample concentration has been observed. However, in individual cases the required concentrations can deviate from these suggestions and further research is required to fully understand these trends.

Where preferred orientation or signs of denaturation at the AWI are known to be a problem, dispense-to-plunge times in the 54–300 ms range are most likely to be successful in overcoming or mitigating these outcomes (see **Supplementary Case Studies S1, S2**). Improvements in AWI issues have been seen as a gradual shift based on dispense-to-plunge times, with some samples showing improvements only with 54 ms dispense-to-plunge time and others at 150–300 ms dispense-to-plunge times (Klebl et al., 2020; Levitz et al., 2022). Because of the decrease in particles observed on the grid, and the fewer frames available in the dispense-to-plunge video at shorter dispense-to-plunge times, it is recommended to only go as fast as is necessary and to still prepare specimens with a range of dispense-to-plunge times biased to accommodate the available protein concentration. Permissive acceptance criteria are still advisable to provide a range of conditions for the initial screening session.

Strategy for a Targeted Freezing Session

Once glow discharge strength, protein concentration, and ice thicknesses have been investigated, the next step is a focused freezing session with stringent grid acceptance criteria and a specific dispense-to-plunge time range (see **Supplementary Case Study S3**). In general, one-stripe mode is more productive in a targeted freezing session and any grids that do not meet the desired grid characteristics (film thickness, dispense-to-plunge time, enough squares for productive data collection) should be rejected. Where 54 ms dispense-to-plunge time is required, it can be difficult to assess film thickness due to the reduced level of information available in the dispense-to-plunge video. To mitigate this issue, preparing and screening additional grids can help ensure a desired outcome is achieved.

Best Practices for Imaging Chameleon Grids

In either mode of operation, chameleon systems produce a grid with one stripe of vitrified sample that extends the full distance across the grid and is approximately two grid squares wide (**Figures 7**, **8**) (Darrow et al., 2019; Wei et al., 2019). Although there is variability in the measurement due to microscope stage and cryobox configurations, in our hands, this pattern equates to 22 ± 5 grid squares (n = 28 grids) in two-stripe mode and 24 ± 5 grid squares (n = 54 grids) in one-stripe mode. The remainder of the grid is 'dry' which introduces an attraction for contaminating ice crystals. Normally such crystals denote a problematic grid but for chameleon grids, crystals outside the stripe have no practical impact. Usually locating the sample stripe is straightforward at low magnification (135–1×55), however if the grid has been overwicked, higher magnifications (540–940x) may be required (**Figure 8**). In general, the sample stripe completely covers the grid squares, but partial coverage is also observed, especially with 54 ms dispense-to-plunge time grids. An optimal stripe has consistent ice thickness over the length of the stripe, but thickness gradients (between squares) are also observed. Gradients can be useful during screening as they provide an assessment of the particle distribution relative to ice thickness. Importantly, gradient location and severity can be seen during the screening step on the chameleon, meaning they can be excluded if undesired.

At the grid square level, the ice is thickest in the centre of the grid square and thinnest near the grid bars (**Figure 8**). Electron imaging of at least two squares per grid (selected from different regions of the stripe) and three holes per square (central area, half-way to the edge, and edge) allows a good assessment of the quality of the grid for structural analysis.

Once a square or squares have been identified to use for data collection, imaging schemes are similar to those used on grids prepared using traditional plunging techniques and collection can be completed as normal (**Supplementary Table S1**). Occasionally, due to the lack of liquid on the carbon, there is a reverse pattern of intensity such that the holes appear darker than the surrounding carbon necessitating the use of alternative image processing options to reliably find holes. The close spacing of the holes on a chameleon grid allows for more holes to be imaged per stage shift, accelerating data collection (**Supplementary Table S1**, **Supplementary Figure S1**). For screening purposes, one grid square will yield 400–700 images. For high-resolution data collection, a chameleon grid imaged at

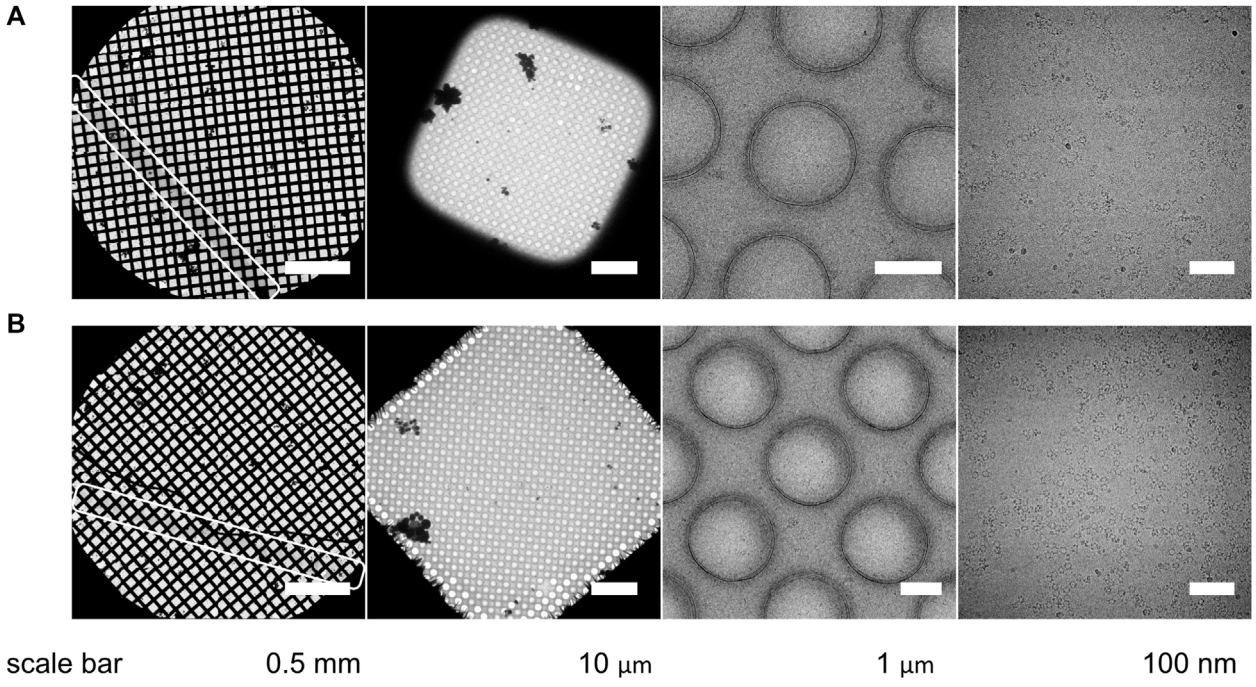

FIGURE 8 | Atlas, grid square, foil hole, and micrograph level images of two different chameleon-plunged grids with the same sample. **(A)** A grid with thicker ice (note the square shown here is not representative of most of the squares within this stripe). **(B)** A grid with thinner ice. The stripes in the atlas-level view are indicated by white rectangles; scale bars are indicated at the bottom.

two shots per hole can regularly yield more than 10,000–15,000 images (**Figures 7**, **8**).

The chameleon system is often presented as a next step for users that have encountered difficulties with preferred orientation or AWI denaturation/dissociation using blot-based sample application techniques or as a first step for users anticipating these issues. Although some improvements to complex denaturation or preferred orientation may be noticeable at the micrograph level, the 2D classification step is generally the earliest step that the presence of rare orientations or improvements to complex denaturation can be assessed. Therefore, only by collecting a series of small data sets (~400–1000 images) at various dispense-to-plunge times can these sample trends be rigorously assessed.

Tomography is still the gold-standard approach for identifying AWI effects as it provides a clear visualisation of the distribution of particles within the ice alongside an empirically determined ice thickness. These pieces of information are crucial in designing future experimental protocols (Noble et al., 2018a; Noble et al., 2018b; Levitz et al., 2022) thus integration of tomographic data collection as a standard part of the single particle data collection process would be ideal.

Even well-behaved samples may still benefit from the chameleon for specimen preparation since it can improve specimen quality in a systematic manner. Quality can be assessed quantitatively by calculating the percentage of particles that contribute to a certain view or final reconstruction, or that are intact versus denatured (Levitz et al., 2022). Higher resolution structures have been determined using many fewer but higher quality specimen particles (Malik et al., 2020).

CONCLUSION AND THE FUTURE OF SPECIMEN PREPARATION

The chameleon system is the first specimen preparation system that provides information about the quality of a grid during the grid preparation process, as opposed to during or after an electron microscopy session. Importantly the chameleon offers the ability to control key experimental variables in a reproducible manner meaning that specimen preparation can begin to move to a more systematic activity where knowledge becomes additive. The systematic nature of the study of specimen preparation will be expanded in the future through additional grid hole sizes and spacings, foil, and support options. As we learn more about the influence of spraying samples, sample and buffer characteristics, dispense-to-plunge times, and AWI interactions on sample quality, the methods for specimen preparation will develop and improve.

The information currently captured during the chameleon specimen preparation process offers future opportunities to increase the throughput of the workflow. We have already shown that sample characteristics (molecular weight, concentration, buffer constituents) help to guide, empirically, the glow discharge parameters and dispense-to-plunge times. Production of robust rules of thumb for operation will require

a large increase in the number of samples evaluated. This increase in samples will happen in time as EM continues to dominate experimental structural biology and will afford the opportunity for systematic evaluation of the meta data and chameleon parameters. The increase in samples and data is likely to yield more defined correlations that can be used to make the chameleon system "smarter" and more automated in the future. In addition, the videos and images captured on the chameleon just prior to grid vitrification could inform cryoEM data acquisition, allowing for more automated targeting of appropriate grid squares. This relationship will provide advances in both directions as understanding grid characteristics related to ice thickness, sample concentration and constituents, as well as linked downstream outcomes around particle orientation and denaturation can be fed back into the on-board chameleon image analysis and recommendation algorithms to further reduce the number of screening loops necessary. A key enabling measurement within this relationship is that of ice thickness; due to confounding factors arising from the variability between sample constituents, and the non-routine nature of the analysis, it is not yet a commonly available or reliable measure.

The purpose of robust automation with highly controllable parameters is to shift the effort away from adjusting the biochemical nature of the sample to match a standard freezing protocol and toward using the sample to drive an effective freezing strategy. The systematic exploration of specimen preparation parameters is only possible with the reproducibility of automated systems. Experienced and novice scientists alike will benefit from improved decision-making due to reproduceable outcomes, leading to high-resolution structures more quickly.

DATA AVAILABILITY STATEMENT

The original contributions presented in the study are included in the article/**Supplementary Material**, further inquiries can be directed to the corresponding author.

AUTHOR CONTRIBUTIONS

TL and MW provided case studies and hands-on examples. TL, MW and MD wrote the manuscript. IF contributed figures. MD, TL, MW, DC and EB conceived of the manuscript. All authors reviewed the manuscript before submission.

FUNDING

This work was supported by NIH grant GM126982 to CD and NSF GRFP 2017246757 to TL as well as NIH T32 Training Grant 5T32GM007287 awarded to the MIT Biology Department. CD is a Howard Hughes Medical Institute Investigator and Senior Fellow for the Canadian Institute for Advanced Research Bio-Inspired Solar Energy program. The chameleon was purchased using funds from the HHMI Transformative Technology 2019 Award. Work at the Rosalind Franklin Institute was supported by core funding by EPSRC.

ACKNOWLEDGMENTS

This article is subject to HHMI's Open Access to Publications policy. HHMI lab heads have previously granted a nonexclusive CC BY 4.0 licence to the public and a sublicensable licence to HHMI in their research articles. Pursuant to those licences, the author-accepted manuscript of this article can be made freely available under a CC BY 4.0 licence immediately upon publication. We acknowledge the Research Complex at Harwell, Didcot, United Kingdom for providing laboratory facilities.

SUPPLEMENTARY MATERIAL

The Supplementary Material for this article can be found online at: https://www.frontiersin.org/articles/10.3389/fmolb.2022.903148/full#supplementary-material

REFERENCES

Dandey, V. P., Wei, H., Zhang, Z., Tan, Y. Z., Acharya, P., Eng, E. T., et al. (2018). Spotiton: New Features and Applications. *J. Struct. Biol.* 202, 161–169. doi:10.1016/j.jsb.2018.01.002

Darrow, M. C., Moore, J. P., Walker, R. J., Doering, K., and King, R. S. (2019). Chameleon: Next Generation Sample Preparation for CryoEM Based on Spotiton. *Microsc. Microanal.* 25, 994–995. doi:10.1017/S1431927619005701

Drulyte, I., Johnson, R. M., Hesketh, E. L., Hurdiss, D. L., Scarff, C. A., Porav, S. A., et al. (2018). Approaches to Altering Particle Distributions in Cryo-Electron Microscopy Sample Preparation. *Acta Cryst. Sect. D. Struct. Biol.* 74 (6), 560–571. doi:10.1107/S2059798318006496

Henderson, R. (1990). Cryo-protection of Protein Crystals against Radiation Damage in Electron and X-Ray Diffraction. *Proc. R. Soc. Lond. B* 241, 6–8. doi:10.1098/rspb.1990.0057

Jain, T., Sheehan, P., Crum, J., Carragher, B., and Potter, C. S. (2012). Spotiton: A Prototype for an Integrated Inkjet Dispense and Vitrification System for Cryo-TEM. *J. Struct. Biol.* 179, 68–75. doi:10.1016/j.jsb.2012.04.020

Klebl, D. P., Gravett, M. S. C., Kontziampasis, D., Wright, D. J., Bon, R. S., Monteiro, D. C. F., et al. (2020). Need for Speed: Examining Protein Behavior during CryoEM Grid Preparation at Different Timescales. *Structure* 28, 1238–1248.e4. doi:10.1016/j.str.2020.07.018

Levitz, T. S., Brignole, E. J., Fong, I., Darrow, M. C., and Drennan, C. L. (2022). Effects of Chameleon Dispense-To-Plunge Speed on Particle Concentration, Complex Formation, and Final Resolution: A Case Study Using the Neisseria Gonorrhoeae Ribonucleotide Reductase Inactive Complex. *J. Struct. Biol.* 214, 107825. doi:10.1016/j.jsb.2021.107825

Malik, R., Kopylov, M., Gomez-Llorente, Y., Jain, R., Johnson, R. E., Prakash, L., et al. (2020). Structure and Mechanism of B-Family DNA Polymerase ζ Specialized for Translesion DNA Synthesis. *Nat. Struct. Mol. Biol.* 27, 913–924. doi:10.1038/s41594-020-0476-7

Marr, C. R., Benlekbir, S., and Rubinstein, J. L. (2014). Fabrication of Carbon Films with ~500nm Holes for Cryo-EM with a Direct Detector Device. *J. Struct. Biol.* 185, 42–47. doi:10.1016/j.jsb.2013.11.002

Noble, A. J., Dandey, V. P., Wei, H., Brasch, J., Chase, J., Acharya, P., et al. (2018a). Routine Single Particle CryoEM Sample and Grid Characterization by Tomography. *eLife* 7, e34257. doi:10.7554/eLife.34257

Noble, A. J., Wei, H., Dandey, V. P., Zhang, Z., Tan, Y. Z., Potter, C. S., et al. (2018b). Reducing Effects of Particle Adsorption to the Air-Water Interface in Cryo-EM. *Nat. Methods* 15, 793–795. doi:10.1038/s41592-018-0139-3

Passmore, L. A., and Russo, C. J. (2016). Specimen Preparation for High-Resolution Cryo-EM. *Methods Enzymol.* 579, 51–86. doi:10.1016/bs.mie.2016.04.011

Razinkov, I., Dandey, V. P., Wei, H., Zhang, Z., Melnekoff, D., Rice, W. J., et al. (2016). A New Method for Vitrifying Samples for cryoEM. *J. Struct. Biol.* 195, 190–198. doi:10.1016/j.jsb.2016.06.001

Taylor, K. A., and Glaeser, R. M. (1976). Electron Microscopy of Frozen Hydrated Biological Specimens. *J. Ultrastruct. Res.* 55, 448–456. doi:10.1016/s0022-5320(76)80099-8

Thompson, R. F., Walker, M., Siebert, C. A., Muench, S. P., and Ranson, N. A. (2016). An Introduction to Sample Preparation and Imaging by Cryo-Electron Microscopy for Structural Biology. *Methods* 100, 3–15. doi:10.1016/j.ymeth.2016.02.017

Wei, H., Dandey, V. P., Kopylov, M., Eng, E. T., Kahn, P., Potter, C. S., et al. (2019). Spotiton and Chameleon Vitrification Robots. *Microsc. Microanal.* 25, 1010–1011. doi:10.1017/S1431927619005786

Wei, H., Dandey, V. P., Zhang, W. J., Raczkowski, C. S., Rice, W. J., Carragher, B., et al. (2018). Optimizing "Self-Wicking" Nanowire Gridss. *J. Struct. Biol.* 202, 170–174. doi:10.1016/j.jsb.2018.01.001

Conflict of Interest: Authors MD and IF were employed by the company SPT Labtech.

The remaining authors declare that the research was conducted in the absence of any commercial or financial relationships that could be construed as a potential conflict of interest.

frontiers | Frontiers in Molecular Biosciences

METHODS
published: 23 June 2022
doi: 10.3389/fmolb.2022.882288

OPEN ACCESS

Edited by:
Arjen J. Jakobi,
Delft University of Technology,
Netherlands

Reviewed by:
Albert Guskov,
University of Groningen, Netherlands
Beatriz Herguedas,
University of Zaragoza, Spain
Francesca Vallese,
Columbia University, United States

***Correspondence:**
María García-Alai
garcia@embl-hamburg.de

‡ORCID:
Stephan Niebling
orcid.org/0000-0001-6582-5984
Katharina Veith
orcid.org/0000-0001-7454-5490
Benjamin Vollmer
orcid.org/0000-0002-7526-0582
Javier Lizarrondo
orcid.org/0000-0001-5199-4170
Angelica Struve García
orcid.org/0000-0002-1134-7152
Osvaldo Burastero
orcid.org/0000-0003-4089-0434
Carolin Seuring
orcid.org/0000-0003-1000-0859
Susanne Witt
orcid.org/0000-0001-9102-1517
María García-Alai
orcid.org/0000-0002-5200-7816

†These authors have contributed equally to this work and share first authorship

Specialty section:
This article was submitted to Structural Biology, a section of the journal Frontiers in Molecular Biosciences

Received: 23 February 2022
Accepted: 04 May 2022
Published: 23 June 2022

Citation:
Niebling S, Veith K, Vollmer B, Lizarrondo J, Burastero O, Schiller J, Struve García A, Lewe P, Seuring C, Witt S and García-Alai M (2022) Biophysical Screening Pipeline for Cryo-EM Grid Preparation of Membrane Proteins. Front. Mol. Biosci. 9:882288. doi: 10.3389/fmolb.2022.882288

Biophysical Screening Pipeline for Cryo-EM Grid Preparation of Membrane Proteins

Stephan Niebling[1,2†‡], Katharina Veith[1†‡], Benjamin Vollmer[3†‡], Javier Lizarrondo[1‡], Osvaldo Burastero[1,2‡], Janina Schiller[1], Angelica Struve García[1,2‡], Philipp Lewe[4], Carolin Seuring[5‡], Susanne Witt[4‡] and María García-Alai[1,2‡]*

[1]European Molecular Biology Laboratory Hamburg, Hamburg, Germany, [2]Centre for Structural Systems Biology (CSSB), Hamburg, Germany, [3]Centre for Structural Systems Biology (CSSB), Leibniz Institute of Virology (LIV), Hamburg, Germany, [4]Centre for Structural Systems Biology (CSSB), University Medical Center Hamburg-Eppendorf, Hamburg, Germany, [5]Centre for Structural Systems Biology (CSSB), Department of Chemistry, University of Hamburg, Hamburg, Germany

Successful sample preparation is the foundation to any structural biology technique. Membrane proteins are of particular interest as these are important targets for drug design, but also notoriously difficult to work with. For electron cryo-microscopy (cryo-EM), the biophysical characterization of sample purity, homogeneity, and integrity as well as biochemical activity is the prerequisite for the preparation of good quality cryo-EM grids as these factors impact the result of the computational reconstruction. Here, we present a quality control pipeline prior to single particle cryo-EM grid preparation using a combination of biophysical techniques to address the integrity, purity, and oligomeric states of membrane proteins and its complexes to enable reproducible conditions for sample vitrification. Differential scanning fluorimetry following the intrinsic protein fluorescence (nDSF) is used for optimizing buffer and detergent conditions, whereas mass photometry and dynamic light scattering are used to assess aggregation behavior, reconstitution efficiency, and oligomerization. The data collected on nDSF and mass photometry instruments can be analyzed with web servers publicly available at spc.embl-hamburg.de. Case studies to optimize conditions prior to cryo-EM sample preparation of membrane proteins present an example quality assessment to corroborate the usefulness of our pipeline.

Keywords: mass photometry, differential scanning fluorimetry (DSF), membrane proteins, dynamic light scattering, sample preparation, electron cryo-microscopy (cryo-EM), biophysical characterization

INTRODUCTION

Since the resolution revolution in cryo-EM, it became evident that high-quality samples are required to arrive at high-resolution structures (Kühlbrandt, 2014; Joppe et al., 2020). Obtaining good quality frozen-hydrated samples suitable for the study by cryo-EM can be challenging, even when starting from highly purified homogeneous protein solutions (Glaeser, 2021). Some common problems encountered when moving from soluble to vitrified samples include unexplained aggregation (D'Imprima et al., 2019), disintegrated particles and loss of subunits from complexes, crowded coated or low number of particles found within holes, and particles adopting a preferential orientation (Tan et al., 2017). These problems are often caused by the tendency of particles to adsorb to the air–water interface, a problem widely discussed in the literature for cryo-EM (Noble

et al., 2018; D'Imprima et al., 2019). The effect of the interaction with the air–water interface can be mitigated by the addition of mild detergents like fluorinated octyl maltoside (Efremov et al., 2015), but will not be further addressed in this article.

To identify optimal vitrification parameters, it is often necessary to try a variety of experimental conditions, following an iterative process, before arriving at optimal thin aqueous ice films on grids. Importantly, the use of protein samples that vary in quality from batch-to-batch purification should be prevented during grid optimization. Addressing the sample quality control (QC) of proteins is not trivial; however, guidelines have been established for the improvement of research data reproducibility (Passmore and Russo, 2016; de Marco et al., 2021). Addressing the quality of membrane protein samples is even more challenging, which usually makes their structural determination difficult. Efforts have been made with respect to the expression of membrane proteins in mammalian systems (Goehring et al., 2014) and initial quality control steps focusing on screening strategies prior to protein purification (Nji et al., 2018; Chatzikyriakidou et al., 2021). Structural methods investigating membrane proteins require the extraction and solubilization from the membrane using detergents, and the use of glycerol gradient centrifugation has proven to be efficient for the mild removal of free detergent prior to cryo-EM studies (Hauer et al., 2015).

Within this protocol, we introduce a simple pipeline for benchmarking the quality of purified membrane protein samples prior to their vitrification. Purified and biophysically characterized proteins would be the starting material to obtain well-dispersed particles on grids for high resolution cryo-EM single particle structural studies (**Figure 1**). Membrane protein sample optimization has indeed several bottlenecks throughout the sample preparation process. A crucial step would be probing protein stability after detergent solubilization (Kotov et al., 2019). Here, we apply differential scanning fluorimetry (nDSF) in combination with static light scattering upon thermal denaturation and dynamic light scattering (DLS) to optimize buffer/detergent selection and to minimize the aggregation of membrane protein samples. The evaluation of the particle size and distribution in the reconstituted sample is further characterized by mass photometry (MP) and negative-stain transmission electron microscopy (negative-stain EM). nDSF allows the study of the unfolding of membrane proteins, following the intrinsic fluorescence of tryptophan residues during a thermal ramp in different buffers and detergents. In addition to the calculation of the melting temperature, the device follows the onset of aggregation by monitoring static light scattering (Kotov et al., 2019). DLS reports on the polydispersity or aggregational state of a membrane protein in solution (Murphy, 1997; Raynal et al., 2014). Particles of different sizes move, creating flickering, and all the motions and measurements are described by auto-correlation functions. The technique provides a batch average of spherical modelled particles in suspension, and only those populations for which hydrodynamic radii differ by a factor of 3 are efficiently resolved. Finally, MP linearly correlates the interference of the scattered light of single particles landing on the measuring surface with

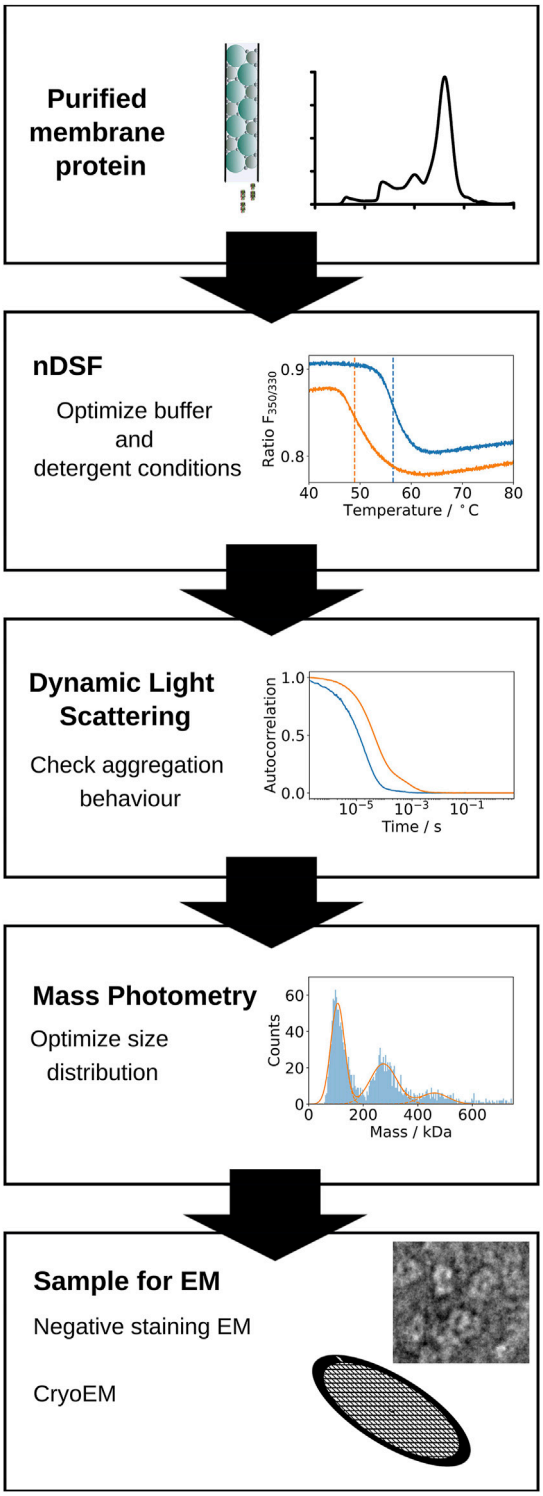

FIGURE 1 | Schematic representation of the screening pipeline proposed. First, optimal buffer and detergent conditions for the stability of a purified membrane protein sample are identified by nDSF. Selected conditions are used for further screening by Dynamic Light Scattering (DLS) to determine the aggregation status of the protein under the specific buffer and detergent conditions. Mass photometry measurements are used to confirm the expected molecular weight of the protein and the distribution of masses present in the sample. Finally, the sample is imaged successively by negative stain and cryo-EM.

their mass, allowing the characterization of mass distributions of macromolecules in solution (Young et al., 2018; Hundt, 2021). Furthermore, the quantification of complex assembly formation (Häußermann et al., 2019; Soltermann et al., 2020; Wu and Piszczek, 2020) and the characterization of membrane proteins using different solubilization approaches has successfully been applied (Olerinyova et al., 2020; Heermann et al., 2021; Steiert et al., 2022). Advantages of this technique are the low sample-consumption and the simple and fast measurement (Wu and Piszczek, 2021). The working concentration is in the 100 nM range (a few microliters needed), which is close to concentrations used for negative-stain EM (Lai et al., 2021) and measurements are performed typically in 60 s. It is therefore a powerful screening tool to characterize protein samples before electron microscopy (Sonn-Segev et al., 2020). In addition, we developed an online tool for analyzing the results of mass photometry experiments. This new module, called PhotoMol, is freely available in the eSPC data analysis platform (spc.embl-hamburg.de).

After confirming the mass distribution of the sample by mass photometry, our quality control pipeline (**Figure 1**) foresees a visual inspection of the sample by negative-stain EM, a technique where the sample is embedded in a film of heavy atoms (Hall 1955; Brenner and Horne, 1959). There are a lot of excellent descriptions on how to prepare negatively stained samples for electron microscopy (Brenner and Horne, 1959; Horne et al., 1975) or in the form of cryo-negative staining (Adrian et al., 1998). Amongst the more recent protocols, Scarff et al. outline the potential pitfalls and available workarounds (Scarff et al., 2018). Generally, negative-stained samples are fairly easy to prepare and can give valuable insights on sample morphology, protein homogeneity, and dispersity of particles on EM grids including aggregation and particle concentration early on. In the past, images of well-stained, evenly dispersed particles have been used to create a first, low resolution (~17 Å) reconstruction (De Rosier and Klug 1968; Ohi et al., 2004; Gallagher et al., 2019), which can be used as initial model in later processing steps of cryo-EM sample images. Also, the conditions (buffer composition, protein concentration) found to be suitable for negative stain sample preparation can inform about the concentrations necessary for cryo-EM samples, which are usually a factor of 10 higher. Our standard protocol for negative stain is described in the "Stepwise Procedures" section and uses 2–20 µM protein concentration and 2% uranyl acetate solution as stain for a first sample quality assessment.

While negative stain is suited to characterize rigid, globular proteins, for membrane proteins, it does not necessarily allow conclusions to be drawn whether the protein is amenable to high-resolution studies by cryo-EM (Hoenger and Aebi, 1996). For the latter, parameters including protein concentration, buffer (Drulyte et al., 2018), and grid type as well as the solubilization method using detergents, amphipols, or nanodiscs have to be optimized and are determined best directly from vitrified cryo-EM specimens. Glow-discharging parameters are also strongly affecting the ice layer and sample dispersion. The preparation of vitrified EM specimens is outlined in the "Stepwise Procedures" section.

Sample preparation of cryo-EM grids for membrane proteins remains, and will remain, mostly an empirical and iterative process for each specific target. However, there is literature available that helps in the trouble-shooting, providing systematic investigations for buffer, blotting, and grid type selection (Kampjut et al., 2021). Here, we are presenting a biophysical pipeline to be used for challenging samples and complexes, prior to cryo-EM experiments, where having a better characterized sample can be advantageous during the grid optimization stage.

MATERIALS AND EQUIPMENT

Protein Production and Purification

IJ1: The IJ1 protein was expressed in *E.coli* LEMO21 cells and ZY-autoinduction media with an addition of 0.3 mM rhamnose. Cultures were grown to an OD_{600nm} of 1 and cooled down to 20°C, induced with 0.1 mM isopropyl-β-d-1-thiogalactopyranoside (IPTG) and left for expression overnight. Cells were collected by centrifuging 25 min at 5,000 × g and pellets were stored at −20°C. To obtain the membrane fraction, cells were resuspended in 2 ml/g pellets with buffer [30 mM tris(hydroxymethyl)aminomethane hydrochloride (Tris-HCl) pH 7.5, 250 mM NaCl, 10% glycerol, 200 µg/ml DNaseI (AppliChem), 2 mM $MgCl_2$ and 200 µg/ml Lysozyme (Sigma)] and lysed with an Avestin Emusiflex by passing the solution three times. Lysate was centrifuged for 30 min at 25,000 × g followed by an ultracentrifugation step of the supernatant for 1.5 h at 150,000 × g. The membrane pellets were resuspended in 2 ml buffer/g membrane pellets (30 mM Tris-HCl pH 7.5, 250 mM NaCl, 10% glycerol), flash frozen in liquid nitrogen, and stored at −20°C. Membranes were solubilized in 10 ml/g pellet buffer [30 mM Tris-HCl pH 7.5, 250 mM NaCl, 10% glycerol, and 1% n-Dodecyl-β-D-Maltoside (DDM, Glycon Biochemicals GmbH)] by stirring for 2 h at 4°C, followed by centrifugation at 50000 × g for 20 min. To the supernatant, 10 mM imidazole was added and applied to 2 × 3 ml ROTI®Garose-His/Ni NTA-Beads (Roth) in a gravity column. The column was washed with 20x column volume (CV) of buffer (30 mM Tris-HCl pH 7.5, 300 mM NaCl, 10% glycerol, 25 mM imidazole, 0.03% DDM) and eluted with 5 CV buffer with 250 mM imidazole. Elution fractions containing the protein were collected, and His-tag was removed by adding 3C-protease and an overnight incubation at 4°C. A "reverse" nickel chromatography was performed; the protein was concentrated with a 50 kDa MWCO Amicon Ultra 4 ml filter, followed by a size exclusion chromatography (SEC) with a Superdex 200 10/300 column; and here, the used buffer was DDM-buffer (30 mM Tris-HCl pH 7.5, 250 mM NaCl, 0.03% DDM) or LMNG-buffer (30 mM Tris-HCl pH 7.5, 250 mM NaCl, 0.001% lauryl maltose neopentyl glycol (LMNG, Anatrace)). For reconstitution of IJ1, amphipol A8-35 (Anatrace) was added in a 1:5 ratio (2 mg/ml protein: 10 mg/ml amphipol) to the protein in a total volume of 1 ml. 50 µL of a

70% slurry of buffer equilibrated and degassed SM-2 Bio-Beads (Bio-Rad Laboratories) was added to the mixture before incubation for 12 h at 4°C. After Bio-Bead removal, the sample was concentrated to 120 µL in 50 kDa MWCO Amicon Ultra-0.5 ml centrifugal filters and loaded onto a SEC column S200 Increase 3.2/300 or Superose 6 Increase 3.2/300 (30 mM Tris-HCl pH 7.5, 250 mM NaCl, 0.02% A8-35). Peak fractions containing IJ1 were pooled, aliquoted, flashfrozen with liquid nitrogen, and kept at −80°C until further use. Chromatograms are shown in the supplementary information (**Supplementary Figure S1**).

TolC: TolC protein was expressed in *E.coli* C43(DE3)ΔAcrAB cells. Cultures were grown in terrific broth (TB) media at 37°C and 200 RPM to an OD_{600nm} of 1.3, and expression was induced with 0.5 mM IPTG. Cultures kept growing overnight (~16 h) at 20°C and 200 RPM. Cells were harvested by centrifugation (5,000 × g, 15 min, 4°C). Pellets were flashfrozen with liquid nitrogen and stored at −80°C until further use. To obtain the membrane fraction, cells were resuspended in 5 ml/g pellets in lysis buffer (20 mM Tris-HCl pH 7.5, 150 mM NaCl, 2 mM $MgCl_2$, Protease Inhibitor (ROCHE), spatula DNaseI) and lysed with a LM10 microfluidizer (Microfluidics) by passing the solution four times at 10000 PSI. Cell debris was pelleted at 12000 RPM for 30 min at 4°C. Subsequently, membranes were pelleted by centrifugation at 35000 RPM for 1 h at 4°C. The pelleted membranes were resuspended in loading buffer (20 mM Tris-HCl pH 7.5, 150 mM NaCl, 10 mM ImidazoleHCl pH 7.5) at a concentration of 10 ml/g pellet. TolC protein was solubilized by adding DDM (Carl Roth, CN26) to a final concentration of 1% by stirring for 1 h at 4°C followed by a centrifugation at 35000 RPM for 1 h at 4°C. Cleared lysate was applied to a 5 ml Hitrap HP column using an automated ÄKTA system. After application, the column was washed with 15 CV loading buffer to which 0.03% DDM was added. To minimize contaminants, the column was washed with 10 CV washing buffer (20 mM Tris-HCl pH 7.5, 150 mM NaCl, 40 mM ImidazoleHCl pH 7.5, 0.03% DDM) and TolC was eluted using 10 CV elution buffer (20 mM Tris-HCl pH 7.5, 150 mM NaCl, 290 mM ImidazoleHCl pH 7.5, 0.03% DDM). Elution fractions containing the target protein were pooled and loaded onto a size exclusion chromatography column S200 16/600 PG equilibrated with SEC buffer (20 mM N-2-hydroxyethylpiperazine-N′-2-ethanesulfonic acid (HEPES)/ NaOH pH 7.5, 150 mM NaCl, 0.03% DDM). Fractions containing trimeric TolC were pooled and concentrated using 50 kDa MWCO Vivaspin until 5 mg/ml concentration. Protein was aliquoted and flash frozen with liquid nitrogen and kept at −80°C until further use. Chromatograms are shown in the supplementary information (**Supplementary Figure S2**).

ANTH and ENTH: The expression and purification of human and yeast proteins are already described elsewhere (Garcia-Alai et al., 2018). Recombinant human ENTH domain from epsin-1 (hENTH) was expressed in *E. coli* BL21 DE3 (Novagen) as GST-fusion protein containing an N-terminal His-tag and a TEV (Hisx6-GST-TEV) cleavage site. 800 ml cultures in LB media were grown at 37°C shaking at 180 RPM until an optical density at 600 nm (OD600) of 0.8 was reached. After induction with 0.5 mM IPTG, the cultures were grown at 20°C for 4 h and harvested by centrifugation (4,000 × g for 30 min at 4°C). The cell pellet was lysed by sonication in the presence of 1 mg/ml DNase in 50 mM Tris-HCl pH 7.5, 250 mM NaCl, and 20 mM imidazole. Lysed cell extract was centrifuged (17,000 × g, 45 min at 4°C), and the supernatant was purified by nickel-nitrilotriacetic acid (Ni-NTA) purification (Qiagen). Protein was eluted in a final elution buffer of 50 mM Tris-HCl pH 8.0, 250 mM NaCl, and 250 mM imidazole. Excess of TEV protease was added to the imidazole-eluted fractions for cleavage of the Hisx6-GST tag. Digestion was performed during dialysis at 4°C overnight against 4 L of 50 mM Tris-HCl pH 8.0, 250 mM NaCl, and 1 mM dithiothreitol (DTT). To remove the tags, the dialyzed fractions were subjected to a second Ni-NTA, and the flow-through was concentrated to 5 mg/ml to be then injected in a size exclusion chromatography (SEC). SEC was performed using an ÄKTA liquid chromatography system (Amersham Biosciences) and a Superdex 75 10/300 GL (Tricorn) column (GE Healthcare) in 20 mM Tris-HCl pH 8.0 and 250 mM NaCl, 1 mM DTT. After SEC, the fractions were pooled and concentrated to 10 mg/ml and flash-frozen in liquid nitrogen and stored at −80°C. Chromatograms are shown in the supplementary information (**Supplementary Figure S3**).

Electron microscopy and data collection: Grids were screened according to the workflow depicted in **Figure 2** on a Thermo Fisher Scientific 200 kV Talos Arctica equipped with a Falcon 3 EC direct detector or a 300 kV Titan Krios G3i equipped with a Gatan Bioquantum energy filter and K3 direct detector. Grid maps and images were recorded using SerialEM (Mastronarde, 2005) with scripts from the SerialEM Script Repository (https://serialemscripts.nexperion.net/). Negative Staining electron micrographs of TolC were acquired on a Jeol 200 kV cryo-TEM using in-house carbon coated grids. Data collection for IJ1 was done on the same Titan Krios system using EPU (Thermo Fisher Scientific). The electron dose rate was 15 electrons/pixel/s with a total dose of 60 electrons/$Å^2$ (~1 electron/Å2/frame). 3,228 movies were collected at 0.681 Å/px.

Cryo-EM Data Processing: Motion correction of movies was done using Relion 3.1.3's own implementation (Zivanov et al., 2018). The contrast transfer function (CTF) was estimated using GCTF (Rohou and Grigorieff, 2015). Automated particle picking was performed in WARP (Tegunov and Cramer, 2019), coordinates for 417375 particles were imported in Relion 3.1.3, and 2D classification was performed after particle extraction (Zivanov et al., 2018).

Mass photometry: All measurements shown here were acquired on a commercial Refeyn OneMP mass photometer using the programs Acquire MP v2.5.0 and Discover MP v2.5.0 (Refeyn Ltd.).

STEPWISE PROCEDURES

Differential Scanning Fluorimetry (nDSF)

Required materials:

- Prometheus NT.48 Series nanoDSF Grade High Sensitivity Capillaries from Nanotemper

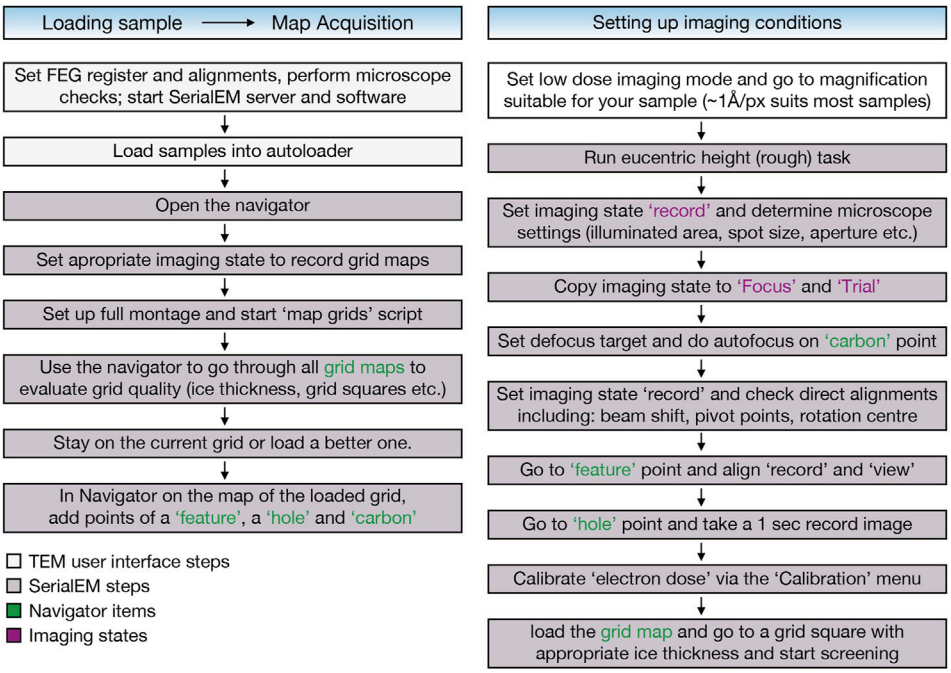

FIGURE 2 | EM sample screening workflow using the SerialEM software (Mastronarde, 2005) includes automatic grid map acquisition of all loaded grids using the "map grids" script (https://serialemscripts.nexperion.net) followed by setting up imaging conditions for visual inspection of the samples.

- Prometheus NT.48 from Nanotemper
- Buffers/detergents of interest
- Sample volume: usually around 50 µL for having several measurements (10 µL are needed for each measurement)

Stepwise procedure:

1. Having an initial idea of the extinction coefficient of the protein of interest can be helpful to determine the final experimental concentration. Check the amount of Trp and Tyr residues (and their position, if known) present on your protein, and usually aim for a final concentration between 5 and 10 µM. This concentration can be significantly lower for large proteins or proteins with a high number of Trp and Tyr residues.
2. Prepare a set of three serial dilutions from your stock of protein and do an initial scan with the Prometheus to observe the signal of the different dilutions. Also add the buffer of interest as control in order to rule out signal interference caused by buffer components.
3. Adjust the excitation power so that all of the samples are in the recommended regime of initial fluorescence (between 2000 and 15000 counts)
4. Perform a dilution of your protein in the buffers of interest using the same dilution performed for the initial scan to ensure a good initial signal for the experiment.
5. Remember to include a capillary with buffer only as a control to discard possible fluorescence effects coming from the buffer. In case of performing a titration with a compound (e.g., ligand), a buffer control with the highest concentration of the added compound must be measured in order to discard fluorescence contribution from the compound.
6. Load the nDSF capillaries, set a measurement from 20°C to 90°C using a heating rate of 1°C/min, and start the experiment.
7. While running or before: Add labels for each capillary in the acquisition software to know which sample corresponds to each curve.
8. Export the processed curves from the instrument and analyze the data using the SPC web server for the MoltenProt module (available at https://spc.embl-hamburg.de/).

Dynamic Light Scattering

The following instructions are valid for a Wyatt DynaPro Nanostar. Other DLS machines can be used as well. However, the described stepwise procedure needs to be adapted individually for each instrument type.

Required materials:

- 4 µL Wyatt cuvettes
- Buffers of interest
- DynaPro Nanostar device (Wyatt Technology Corporation)
- Spin filters to remove large aggregates (e.g., Durapore® Membrane Filter, 0.22 µm from Millipore®)
- Protein stock: 10 ul with a protein concentration of ca. 0.5 mg/ml

Stepwise procedure:

1. Measurements should be performed at a concentration of around 0.5 mg/ml in order to obtain a good signal (starting

at a concentration of around 1–2 mg/ml is usually a good starting point). The volume required per measurement depends on the instrument and cuvettes used. In our case, we have used 4–5 µL of sample.
2. Before measurements, spin the samples at maximum speed for 10 min to avoid aggregates that could hamper measurements. Optionally, 0.22 µm mini-spin filters are recommended to be used to remove large aggregates from the sample.
3. To enhance the quality of the measurements, switch on the instrument and the laser at least 30 min before measuring to warm up the laser. Also, set the temperature (usually 20 or 25°C).
4. Measure the buffer to discard any signal that could come from buffer components such as detergent micelles. If the buffer contains impurities that display a particle-like auto-correlation function, it probably needs to be filtered.
5. Set the collection parameters to 30 curves and average the results. The acquisition time of 5 s with a total of 30 acquisitions averaged. Measurements to be performed at 25°C.
6. If the curves show a "bump" towards higher correlation-times, the sample contains large macromolecular aggregates and it is most likely not in ideal buffer conditions and therefore not suitable for structural studies (see **Supplementary Figure S4A** for an example).

Dynamic Light Scattering Data Analysis

The measured autocorrelation curve of the sample of interest can be analyzed with a variety of algorithms to obtain the hydrodynamic radius of gyration (Hr) (Koppel, 1972; Provencher, 1982; Schuck, 2000). This includes fitting one/two Hrs, a smooth distribution of Hrs, or a distribution of Hrs that follow a certain function (e.g., a Gaussian). The standard way of analyzing the autocorrelation function consists of employing the so-called method of cumulants (Koppel, 1972); however, this analysis can be completely hampered by really small amounts of aggregates. The other algorithms are more robust, but the estimated hydrodynamic radius should be nevertheless considered to be in all cases semi-quantitative. Regarding the DynaPro Nanostar device, results from fitting the data with the cumulants method and a smoothed distribution are provided.

Mass Photometry

Cleaning of Cover Slides for Mass Photometry

The sonication is executed in batches of 10 microscope coverslips following the instruction of Soltermann et al. (2020).

Required materials:

- Microscope coverslips (CG15KH - Precision Cover Glasses from Thorlabs)
- Rack for microscope cover slips (e.g., from Electron Microscopy Sciences, catalogue number 72243)
- 600 ml beaker
- Ultrasound bath
- MilliQ Ultrapure water, e.g., Millipore© system filtered water
- Isopropanol
- Nitrogen outlet for drying coverslips
- Container for storing coverslips (e.g., GlW, Slidebox K25W)

Stepwise procedure:

1. Place the microscope coverslips in a suitable rack (EMS, Adjustable Cover-Slip Rack, #72243).
2. Place the rack with the coverslips in a 600 ml beaker and fill this beaker with ultrapure water so that the slides are fully submerged.
3. Sonicate for 5 min at full power.
4. Remove water from the beaker and repeat steps 2.+3. with isopropanol.
5. Remove isopropanol and repeat steps 2.+3. with ultrapure water (optional: the isopropanol can be stored and reused).
6. Remove water and dry each coverslip under a stream of dry nitrogen.
7. Cleaned coverslips can be stored in a clean container (GlW, Slidebox K25W) with inserted spacers.

Buffer Filtering Prior to the Mass Photometry Experiment

Due to the high background signal of detergent containing buffers, it is often necessary to dilute the protein into detergent-free buffer prior to the mass photometry measurement. A key factor for successful mass photometry measurements is ensuring a low background signal from buffers during the measurement. It can occur that even detergent-free buffers used for other biophysical techniques yield a significant number of counts that can hamper accurate mass determination. In many cases, we could observe a strong signal in the region around 50–80 kDa (**Figure 3A,B**). In our experience, filtering with a 30 k spin filter (e.g., Amicon Ultra 30 k) could in these cases drastically decrease the background signal and enhance the data quality.

Required materials:

- 30 kDa spin filter (e.g., Amicon Ultra 30 k)
- Table-top centrifuge
- Detergent-free buffer

Stepwise procedure:

1. Fill the spin filter with buffer and centrifuge with the speed and time recommended for this spin filter.
2. Discard filtered solution.
3. Repeat step 1. and 2. (equilibration of filter device).
4. Repeat step 1. once more.
5. The filtered buffer is now ready to use.

Calibration of Mass Photometer

The mass photometer detects the signal in terms of contrast, which can be transformed into mass, thanks to a reference calibration using protein standards. The accurate detection of masses requires the diligent performance of this calibration. Usually, a calibration with the standard native marker uses three points to calibrate the mass with a

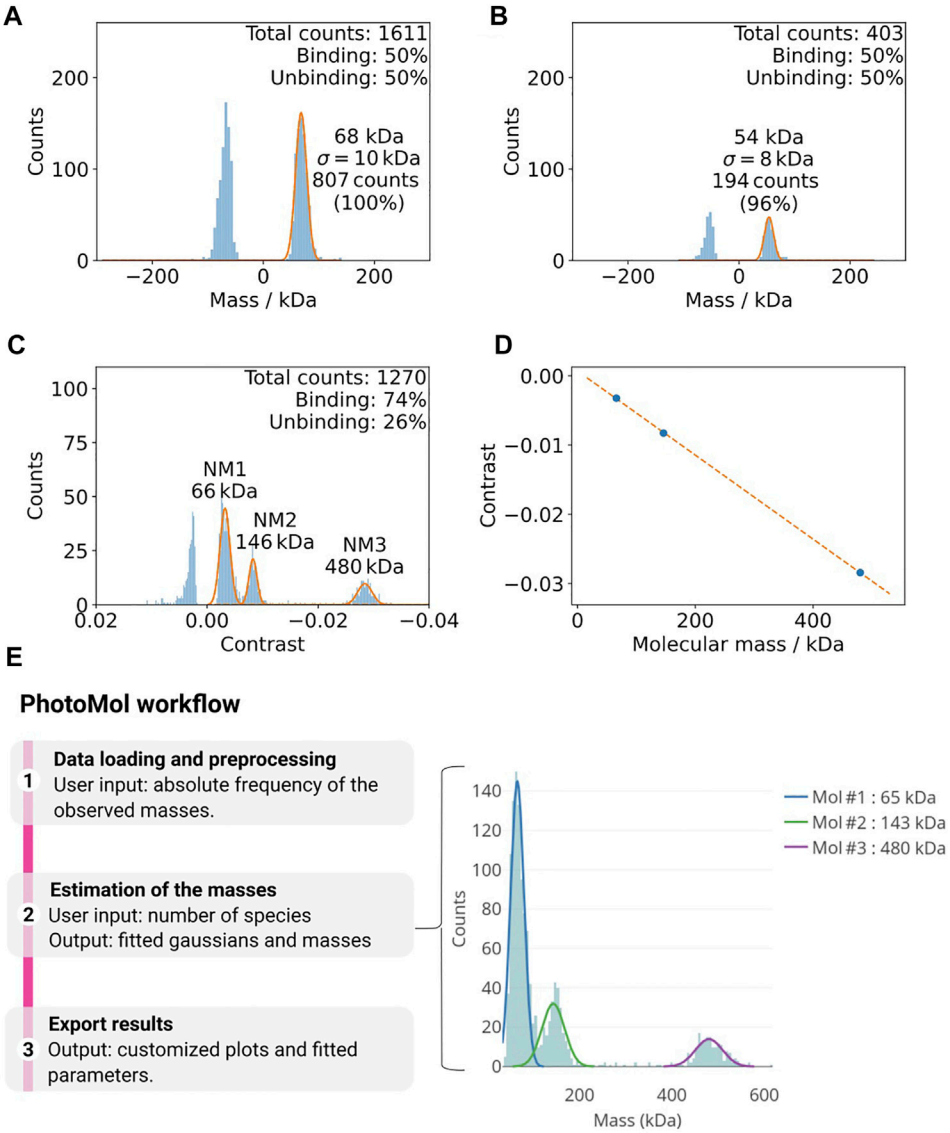

FIGURE 3 | (A,B) Example of how buffer impurities can negatively affect mass photometry measurements (Tris-HCl 100 mM, pH 8.5, 100 mM NaCl, 1 mM DTT). **(A)** The vacuum filtered buffer on the left shows a considerable amount of counts at ca. 68 kDa. **(B)** An additional filter step (right) drastically decreases this background. **(C,D)** Calibration of mass photometer. **(C)** Histogram of the mass distributions used for the calibration of the mass photometer using the native marker in PBS buffer (pH 7.4). The Gaussian fittings for the different populations are shown in orange. **(D)** The contrast values from **(A)** and the known masses of the calibration standards are used for a calibration line (maximum error here 0.3%). **(E)**The PhotoMol pipeline consists of three steps. First, the user loads an input file that contains the frequency of the observed masses (or contrasts). Pre-processing is first performed by selecting a bin width and a window range to build the histogram. Second, the user defines the number of Gaussians (species) present in the distribution and a truncated multi-Gaussian fit is executed. Finally, publication-grade figures can be downloaded together with information about the fitted parameters.

maximum error that should be lower than 5% (**Figure 3C,D**).

Required materials:

- Protein marker (here: NM, Invitrogen, NativeMarker Unstained Protein Standard, #LC0725)
- Buffer that will later be used for the protein of interest
- Mass Photometer (here: Refeyn One)
- Computer with AcquireMP and DiscoverMP software
- Cleaned coverslip
- Reusable silicone gaskets (Sigma GBL103250-10 EA or Grace BioLabs 103250)
- Optional: Vortex for mixing protein standard dilution

Stepwise Procedure:

1. Add 98 µL of buffer to 2 µL of the native marker. Mix thoroughly by pipetting up and down or using a vortexer.

2. Add 18 µL of the buffer in an empty well on the coverslip.
3. Select a suitable field of view (FOV) depending on the mass of the protein of interest. For most systems, the regular FOV is suitable.
4. Focus the laser manually or using the autofocus function.
5. Add 2 µL of pre-diluted native marker (from 1.) and mix by pipetting up and down using a 20 µL pipette. Note: Only the proteins with masses corresponding to 66, 146, 480, and 1,048 kDa are visible with the instrument. The higher mass is however only detectable with the medium and high field of view (FOV). In our pipeline, we use the regular FOV where only 66, 146, and 480 kDa masses are detectable.
6. Start the acquisition as soon as the mixing is finished.
7. Open the mp file with DiscoverMP and analyze data.
8. Check if the number of counts is in the recommended range for the used FOV and the particular instrument type. For a RefeynOne and the regular FOV, the recommended maximum number of counts is 3000. Note: Ideally, the majority of counts should be attributed to binding events. However, for different buffer systems, the ratio between binding and unbinding events can differ.
9. If the number of counts is too high or too low, repeat steps 4.–8. adjusting the dilution of the native marker.
10. Once the number of counts is satisfactory, fit Gaussians to the peaks. For the regular FOV, we usually use the peaks of bovine serum albumin (NM1: 66 kDa), lactate dehydrogenase (NM2: 146 kDa), and apoferritin band 2 (NM3: 480 kDa). For medium and large FOV, we usually use NM2, NM3, and NM4 (1,048 kDa).
11. Calibrate with the calibration function in the software and save the calibration file. This can be used for calibrating the measurement of the sample of interest later.
12. Process the raw data using DiscoverMP and export the events fitted file (h5 format) for later use with the webserver.

Mass Photometry of Protein of Interest

Required materials:

- Filtered buffer
- Mass Photometer (here: Refeyn One)
- Computer with the AcquireMP and DiscoverMP software
- Cleaned coverslip
- Reusable silicon gaskets (Sigma GBL103250-10 EA or Grace BioLabs 103250)
- Protein stock: 2–10 µl at a concentration of at least 500 nM

Stepwise procedure:

1. Create a pre-dilution of the protein stock with a protein concentration of 500–1,000 nM using filtered buffer.

Note: For concentrated detergent samples (those proceeding from concentrating devices), we recommend starting with a pre-dilution with protein concentration around 1.5 µM and then using only 0.5 µL of it (and 19.5 µL of non-detergent buffer on the slide) in step 3. This could highly reduce the detergent background in the cases presented here.

2. Add 18 µL of filtered detergent-free buffer into an empty well on the cover slide.
3. Add 2 µL of pre-diluted protein solution (from 1.) and mix by pipetting up and down using a 20 µL pipette.
4. Start the acquisition as soon as the mixing is finished.
5. Open the mp file with DiscoverMP and analyze data.
6. Check if the number of counts is in the recommended range for the used FOV (this depends also whether a RefeynOne or RefeynTwo is used). For a RefeynOne and the regular FOV, the recommended maximum number of counts is 3000.
7. If the number of counts is too high, repeat steps 2–6 using a smaller volume of the pre-diluted protein solution in a new well.

Important Quality Checks for Mass Photometry

- The cleanliness of the slide can be checked after adding the buffer. Local impurities show up as bright spots in the native view. Move the objective position by changing the x/y position of the stage with the Acquire MP software. If no clean area can be found in a well, change to another well or use another slide.
- Always check the signal of the pure buffer before measuring the protein of interest. If a high number of counts (larger than a few 100) is detected, this could be caused by the detergent. In this case, try to decrease the detergent concentration by diluting it below its CMC. This is a requirement for MP measurements since concentrated detergents lead to high levels of noise background. Given that the measurement is fast, the membrane protein mass remains adequate during the measurement (Olerinyova et al., 2020). For instance, the mass photometry with TolC shown later (cf. **Figure 7**) was acquired with one third of the CMC of DDM. For other detergents, this needs to be empirically confirmed case to case. A good summary of different detergents and their respective signals at different concentrations can be found in this application note by Refeyn: https://www.refeyn.com/mass-photometry-with-detergents.

Mass Photometry Data Analysis

Mass photometry data acquired on a Refeyn instrument can be analyzed using the proprietary software that requires a license by Refeyn DiscoverMP. Here, we are releasing a new user-friendly software module for MP analysis and publicly available at the eSPC data analysis platform: spc.embl-hamburg.de (Burastero et al., 2021). This is particularly important when the proprietary software is not accessible. It allows fast and easy high-quality data analysis with the possibility of exporting publication-grade figures (**Figure 3E**). The eSPC module PhotoMol allows quantifying the masses of different species in a sample after a mass photometry experiment. The required input file is an .h5 file (data file saved in the hierarchical data format) with the fitted events generated by the software Refeyn DiscoverMP. In the DiscoverMP version <2.5, the file events, Fitted.h5 is saved in the folder when saving the results. In version 2.5, the events can be exported individually selecting a custom file name.

Moreover, a comma-separated-values (csv) file can be also loaded. If the file was generated after mass calibration, the masses in kDa are included. In case that only the contrasts are present ("contrasts" dataset in the .h5 file), another file with known masses can be used for calibration and to transform the observed contrasts into masses.

Once the one-dimensional dataset of the observed masses is loaded, a histogram is built based on a chosen bin width and range. The estimation of the masses consists of fitting a truncated multi-Gaussian to correctly fit data with multiple mass distributions. An initial number of Gaussians based on detected peaks are provided but should be only used as a starting point. The user should change, if desired, the number of Gaussians together with initial guesses. We chose to fit left-side truncated Gaussians to take into account the mass range of the instrument, i.e., there are no counts for masses below a certain threshold (i.e., below 30 kDa). Further information regarding the PhotoMol software is available as Supplementary Information (PhotoMol User Documentation).

Sample Preparation for Negative-Stain EM

Required materials:

- Protein Stock Solution: 20 µl at a concentration of 2–20 µM for serial dilutions
- Protein Buffer (low salt, low phosphate). Note: In our experience, salt concentrations higher than 300 mM and phosphate containing buffers should be avoided as this may lead to precipitations on the grid.
- Carbon or Carbon/Formvar support film on copper grids 300 mesh
- 2% uranyl acetate solution
- Harrick Plasma Cleaner PDC-002-CE, GloQube or similar instrument
- High quality tweezers like Dumont Type N5 for EM grids (from Plano)
- Whatman filter paper grade 1
- Designated bench space and waste container to handle uranyl acetate samples

Hazards: Uranyl acetate is radioactive and toxic.

Stepwise procedure:

Note: Negative staining is not necessarily the best method to characterize membrane proteins. It has been reported (Boekema, 1991) that the heavy metal stain, in combination with the lipid/detergent environment can cause aggregation. However, it is quick and easy to do, and may allow a quick first assessment of sample quality.

1. An EM specimen is typically prepared using 3.5 µl protein solution at a concentration of 0.05–5 µM. Set 20 µl of your stock solution aside.
2. Glow-discharge carbon-coated grids with the glow discharger for 60 s using negative polarity at 25 mA intensity. Make sure to use freshly glow discharged grids as the glow discharging effect degrades over time.
3. Prepare a few (between 10–100 fold) dilutions of your protein stock solution in its buffer based on the previous characterization, preferably using low salt and no phosphate.
4. Attach a slice of parafilm with a few drops of water on a surface designated to work with heavy metals.
5. On the parafilm, prepare for each sample a row of droplets starting with two 20 µl droplets of MilliQ water and two 4 µl droplets of a 2% uranyl acetate solution.
6. Using the tweezers, grab a glow-discharged grid only on the copper rim at the edge.
7. Apply 3.5 µl of a sample on top of the glow-discharged grid without touching the grid with the tip of the pipette.
8. Incubate the sample on the grid for 30 s.
9. Carefully remove excess liquid by side-blotting the grid. Proceed before drying the grid completely.
10. Quickly dip the grid into the first water droplet to remove unbound proteins. Then remove the excess water by side blotting. Repeat with the second droplet of water. Proceed with staining before drying the grid.
11. Quickly dip the grid into the uranyl acetate droplet and blot. Then incubate on the second uranyl acetate drop for 1 min. Carefully remove excess stain by side blotting.

Note: Uranyl acetate is a hazardous substance. Alternatives are ammonium molybdate and phosphotungsten acid, NanoVan & NanoW (Tedpella Inc.). However, in our experience, these alternatives do not result in such a good contrast as the one obtained with uranyl acetate.

12. Finally, let the grid air-dry for 2 min. Store in a grid box until the sample can be imaged.

Cryo-EM Sample Preparation for Single Particle Analysis of Membrane Proteins (Preferred)

Vitrification of membrane proteins in different buffers and/or detergents is the best method to assess the sample behavior. In most cases, sample morphology, protein homogeneity, and dispersity of particles on EM grids including aggregation and particle concentration can only be determined from vitrified EM specimens. In our experience, membrane proteins are notoriously difficult to be deposited into the holes of the grid during grid preparation and tend to localize on the carbon support. To increase the density of membrane proteins in grid holes, it is necessary to vary the used concentration, but also the type of grid support can have a substantial impact on protein distribution (cf. **Figure 6**). The following stepwise procedure can be used to prepare grids of any type, but the necessary conditions and especially the protein concentration–grid type relation have to be determined individually. Our standard starting setup uses QuantiFoil MultiA Cu 200 grids and three dilutions of the protein of interest (e.g., 1, 0.3, 0.1 mg/ml).

Required materials:

- EM grids:
  - Copper grids 2 nm Carbon R2/1 Cu 200

- ○ Copper grids QuantiFoil R 1.2/1.3 Cu 200
- ○ Copper grids QuantiFoil MultiA Cu 200
- ○ Gold grids UltrAuFoil® R1.2/R1.3 Au 300

- Blotting device like Thermo Fisher Vitrobot Mark IV
- Harrick Plasma Cleaner PDC-002-CE, GloQube or similar instrument
- Buffers/detergents of interest
- Sample volume: 20 µl of 20–200 µM is usually a good starting concentration.

Stepwise procedure:

1. Prepare a set of three dilutions from your stock of protein as 1:2–1:10 in the appropriate buffer. Usually, around 20 µl per dilution is needed for preparing several grids (3.5 µL is needed for each grid).
2. Fill cryoplunger reservoir with a maximum of 60 ml fresh deionized water using a syringe.
3. Equilibrate Thermo Fisher Vitrobot Mark IV to 4°C and 95% relative humidity in the climate chamber. Under "miscellaneous," select the "switch off during process" option to avoid ice contamination due to the humidifier.
4. Assemble the dedicated styrofoam plunging container, the inner brass cup and the temperature conductor (spider), and the grid box holder. Cool down the plunging container with dry liquid nitrogen.
5. When the inner brass cup reaches liquid nitrogen temperature, slowly fill it with either ethane or a mixture of ethane and propane (63%/37%). The latter is preferably used as it does not freeze over time.
6. Remove the spider. Top-up the plunging container with liquid nitrogen, avoiding liquid nitrogen penetration into the brass cup.
7. Using grid box tweezers, put an empty grid box in the designated position and remove the lid.
8. Move to plasma cleaner, e.g., GloQube or Harrick and glow discharge grids. For Quantifoil MultiA grids, use 60 s at 25 mA (giving ~350 V). For grids coated with a thin (2 nm) carbon film, reduce the glow discharge time to 10–20 s.
9. Move with freshly glow-discharged grids back to Vitrobot. Note: Use grids within the next 30 min, while the surface of the grids is hydrophilic.
10. Select the "place new grid" function on the display.
11. Pick up the first grid using a pair of dedicated Vitrobot tweezers and attach them carefully to the metal rod of the Vitrobot.
12. Select "continue" to transfer the tweezers into the climate chamber followed by "start process".
13. Apply 3.5 µL of your sample to the grid using the side entry port.
14. Select "continue" to start the blotting and plunging procedure.

Note: The blot force is usually calibrated by service using millimeter paper. Changing the blotting force and time can have an influence on the resulting ice thickness and ice gradient on the grid. It makes sense to start with generally used/"known to work" standard settings (wait time: 4 s, blotting force: 4, blotting time: 4 s in our case). After screening the first set of grids, these settings can be adjusted and tested. For the test protein used here, "Case 1—IJ1" blotting force settings between 0 and 4 and blotting times between 3 and 6 s were used.

15. After plunging the grid into the liquid ethane:propane container, move to grid transfer position.
16. Carefully detach the tweezers from the Vitrobot while keeping the grid in the liquid ethane:propane mix. Transfer the grid to the liquid nitrogen storage ring and then into the grid box for storage. During transfer keep the grid in either liquid or gas phase nitrogen to minimize ice contamination.
17. After the grid has been stored in its box, refill the liquid nitrogen storage ring with dry liquid nitrogen.
18. Pick up the next grid with the tweezers and continue as before starting with step 10 to prepare more samples. It is advisable to make duplicates of each sample.
19. After the last grid is prepared, you may either continue (a) imaging grids, (b) clipping grids, and (c) transfer grid boxes for later use into a long-term liquid nitrogen storage Dewar.
20. Shut down and switch off the Vitrobot, and remove and empty the humidifier. Last, place the coolant container under a fume hood to allow evaporation of the remaining liquid nitrogen, ethane, and propane.

EM Sample Screening

The EM sample screening protocol is depicted in **Figure 2**.

Anticipated Results: Membrane Protein Examples

We applied the biophysics pipeline described above to three membrane protein systems.

Case 1: Integral Membrane Protein Ij1

Ij1 is an *E.coli* ABC-transporter involved in ion transport (Kotov et al., 2019). To determine the optimal buffer condition for protein stability, differential scanning fluorimetry was used as described in Kotov et al. Sci. Reports 2019. Five different detergents were selected and are shown in **Figures 4A–D**. The highest melting temperatures were detected for LMNG, which are almost 10°C higher than the initial detergent used for membrane solubilization, DDM. The effects on the aggregation behavior were afterwards tested using DLS for samples solubilized in DDM and later exchanged to LMNG and amphipol A8-35 (**Figure 4E,F**). DLS data indicate similar distributions for the hydrodynamic radii for DDM and A8-35 with main radii of 11 and 9.7 nm, respectively. LMNG showed two separate distributions with hydrodynamic radii of 5 nm (72% of mass) and 21.5 nm (27% of mass). All three samples have good quality autocorrelation functions displaying only one inflection point and are considered to be monodisperse.

In **Figure 5**, mass photometry experiments of IJ1 with LMNG, DDM, and A8-35 are shown. Mixing 0.5 µL of protein pre-dilution

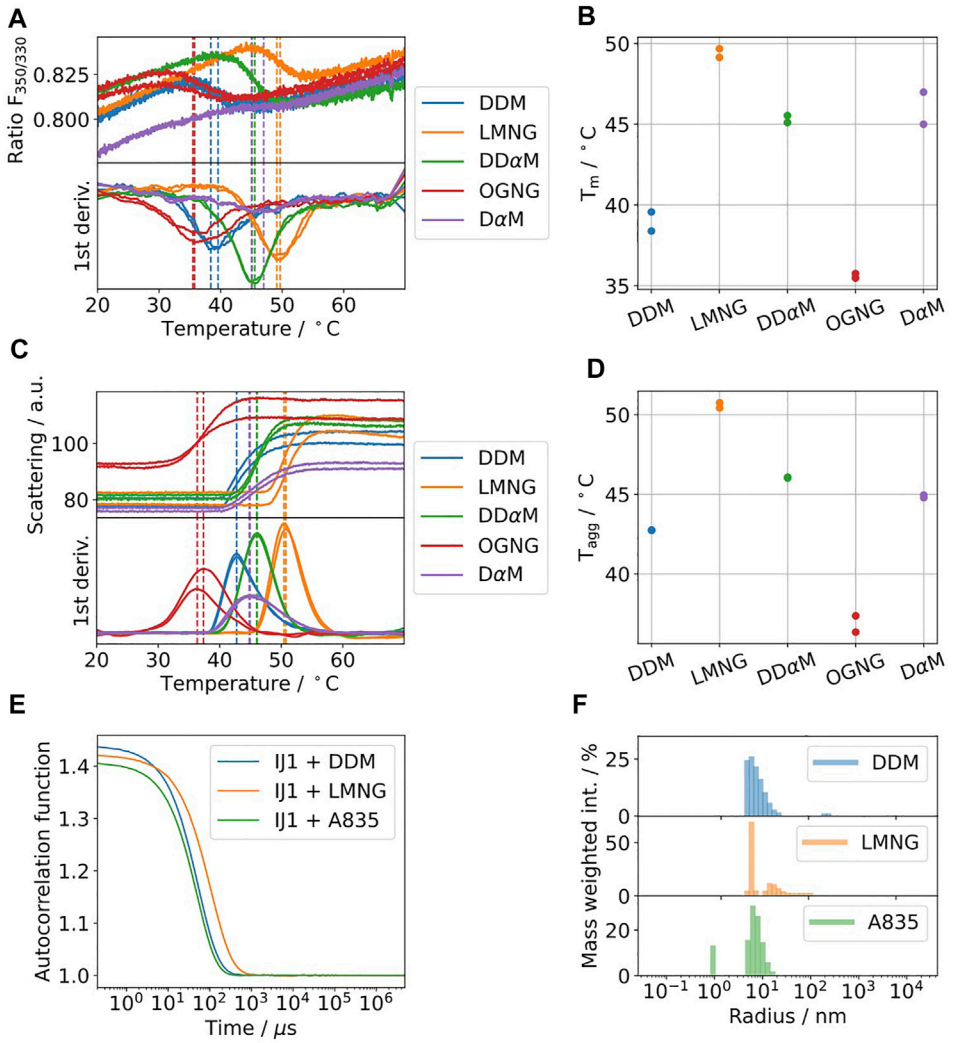

FIGURE 4 | (A–D) Five commonly used detergents were selected for protein solubilization of IJ1. DSF fluorescence ratio of IJ1 for the selected detergents **(A)** and melting temperatures as determined by the minimum of the first derivative **(B)**. The backscattering signal **(C)** indicates aggregation and shows similar transition temperatures **(D)** as the fluorescence ratio. LMNG was identified as the detergent with the highest stabilization amongst a screen of 96 conditions. The detergent concentrations used here were 0.6 mM (0.03%) DDM (used as reference), 1 mM LMNG, 8.5 mM DDαM, 3.1 mM OGNG, and 4.8 mM DαM. **(E)** DLS autocorrelation function of IJ1 in the presence of 0.6 mM (0.03%) DDM and 0.5 mM (0.05%) LMNG and reconstituted in amphipols (A8-35). **(F)** Mass weighted intensity histograms for the autocorrelation functions shown in **(A)** obtained by the application of the Stokes–Einstein equation for determining the average size particle: DDM 11.0 nm (921.0 kDa), LMNG 5 nm (147.6 kDa) and 21.5 nm (4,394.2 kDa), and A8-35 0.9 nm (2.8 kDa) and 9.7 nm (683.1 kDa).

with a DDM concentration of 0.036% with 19.5 μL of detergent-free buffer on the slide resulted in broader mass distributions (**Figure 5A**) and a considerable amount of unbinding events, which did not allow reliable mass quantification. This became more obvious when looking at the oscillating background of the native image during the mass photometry measurement (inlay of **Figure 5A**). However, starting from a pre-diluted sample (0.006% DDM) in non-detergent buffer resulted in a more distinct mass distribution with clear peaks at 147 and 278 kDa (**Figure 5B**) and a very low number of unbinding events. The final DDM concentration for this measurement was around 0.00015%. The control measurements with buffer only for the two DDM concentrations are shown in **Figure 5C,D**. The background effect of the detergent LMNG is less pronounced compared to DDM. Even at the higher concentration of LMNG, the number of detected events is only slightly above 3000 counts (**Figure 5E,F**). When using amphipol A8-35 reconstituted protein, decreasing the protein concentration resulted in better separated peaks at 108 and 200 kDa (**Figure 5G,H**). In summary, LMNG and A8-35 solubilized IJ1 showed superior behavior compared to DDM.

Three different detergent conditions were used for cryo-EM sample preparation of IJ1and combined with different grid types. This illustrates the effect of detergents and amphipol on the protein distribution and the influence of different grid supports on the protein distribution and density. On copper QuantiFoil and gold UltrAuFoil grids, IJ1 in LMNG localizes

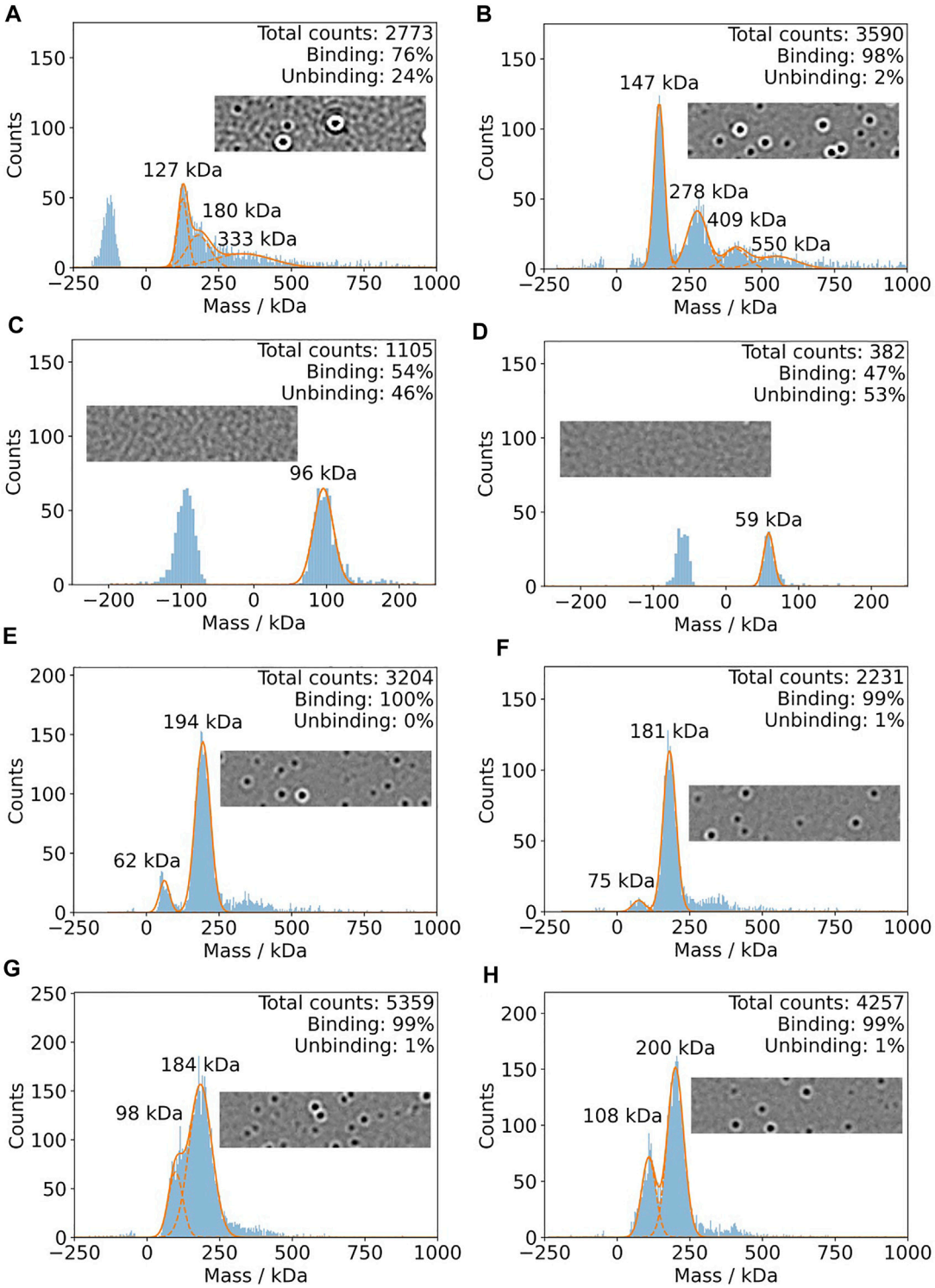

FIGURE 5 | Mass photometry of IJ1. For each experiment, 0.5 ul of pre-dilution was added to 19.5 detergent-free buffer on the mass photometry slide. **(A)** Measurement using a protein pre-dilution with 0.036% DDM. The final DDM concentration is 0.0009% and 40 nM protein. **(B)** Pre-dilution of protein solution into detergent-free buffer results in a DDM concentration of 0.006%. The final DDM concentration is 0.00015% and 80 nM protein. **(C,D)** Control experiments using similar DDM concentrations and no protein. **(C)** 0.03% DDM. **(D)** 0.003% DDM. **(E)** and **(F)** show the mass histograms for IJ1 in the presence of different concentrations of LMNG as detergent at a final protein concentration of 40 nM. Since the protein was concentrated, we can only give estimations for the final LMNG concentrations: 0.00004% for panel E and 0.000015% for panels **(F)**, **(G)**, and **(H)**. Amphipol solubilized IJ1 at two different pre-dilution concentrations: **(G)** 3.2 uM IJ1 and 0.0042% A8-35. **(H)** 1.6 uM IJ1 and 0.0021% A8-35. The final protein concentrations were 80 nM **(G)** and 40 nM **(H)**.

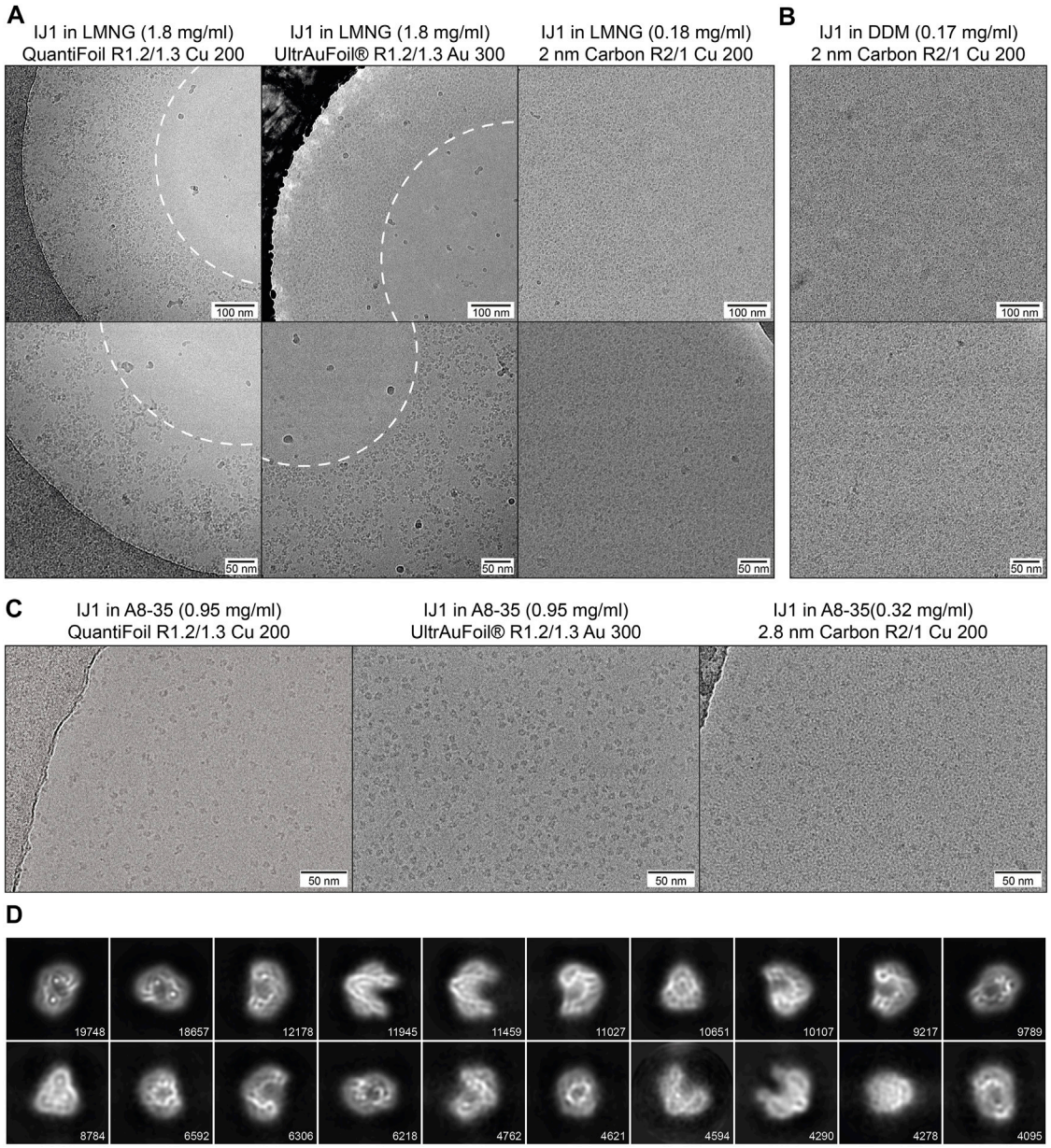

FIGURE 6 | (A) Influence of different grid types on the particle distribution of IJ1 in LMNG. The protein localizes to regions of thick ice on copper QuantiFoil and UltrAuFoil grids and is omitted from regions of thin ice in the middle of the holes (marked by the white dashed line). A 2 nm layer of carbon leads to an even distribution of particles throughout the grid holes. **(B)** A similar distribution is seen for IJ1 in DDM on 2 nm carbon-coated grids. Shown are example images in two magnifications (1.58 Å/px upper row, 1.23 Å/px lower row). **(C)** IJ1 in A8-35 on QuantiFoil, UltrAuFoil, and 2.8 nm carbon-coated grids (0.68 Å/px). IJ1 reconstituted in A8-35 is more evenly distributed compared to LMNG solubilized particles. **(D)** 2D class averages for A8-35 reconstituted Ij1 on the QuantiFoil R1.2/1.3 grid. Shown are the 20 most populated classes of 80. The number of particles is shown for each class.

to regions of thicker ice and is omitted from regions of thin ice in the middle of the holes. Using grids with a 2 nm layer of carbon leads to an even distribution of particles throughout the grid holes (**Figure 6A**). The same effect is seen for the protein solubilized in DDM (**Figure 6B**). It should be noted that the 2 nm carbon layer leads to a slightly reduced contrast in the images and that protein concentrations 10 times lower than on holey grids should be used. Exchanging the detergent for amphipol A8-35 allows the protein to be more evenly distributed on holey grids without an additional carbon layer (**Figure 6C**). Particles in LMNG are more crammed together and often overlap each other, while A8-35 reconstituted particles are better separated. The improved display of amphipol reconstituted Ij1 on grids matches the biophysical results (**Figure 5G,H**, **Figure 6C**), resulting in well-aligned 2D class averages (**Figure 6D**).

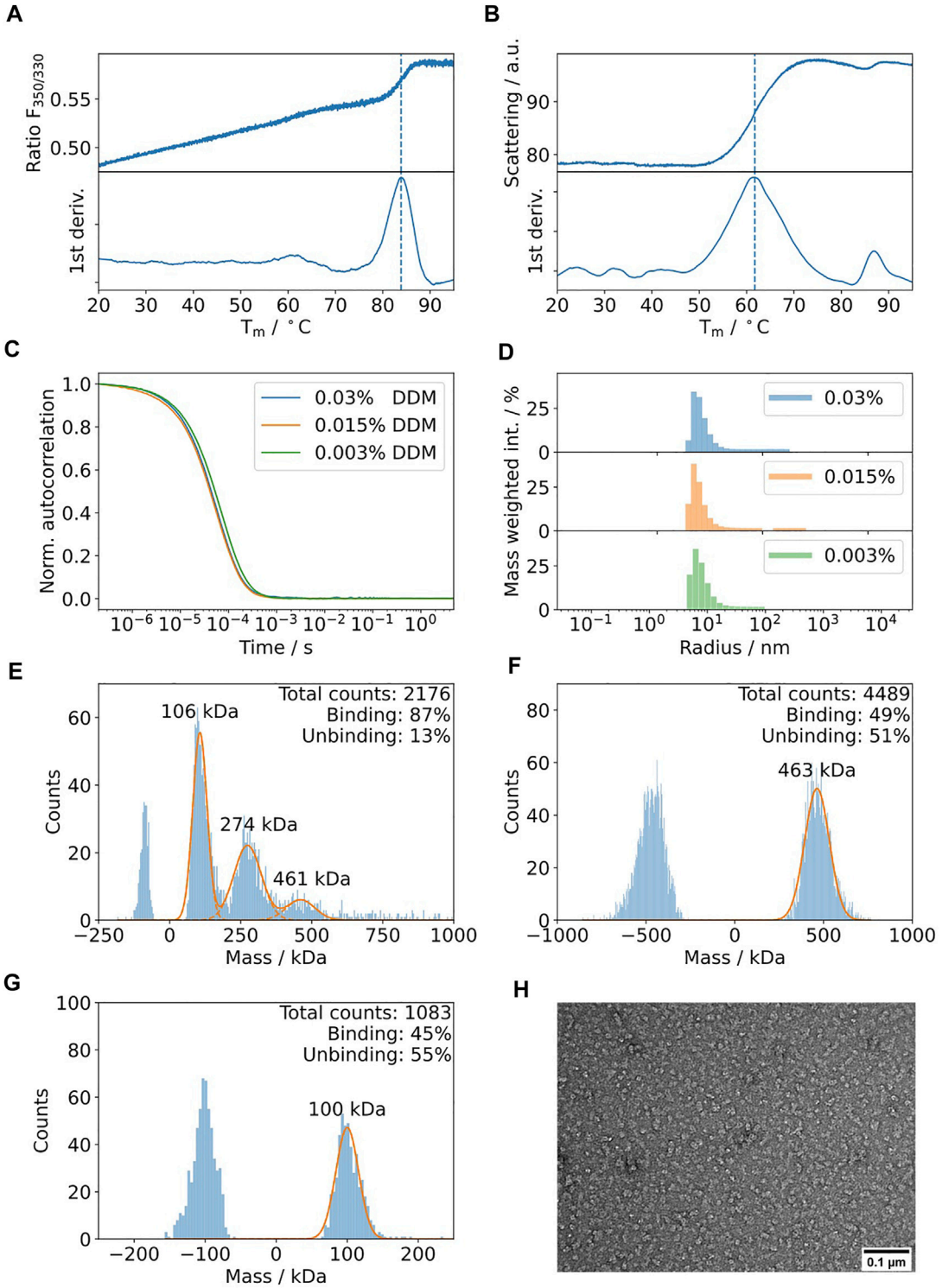

FIGURE 7 | Biophysical characterization of TolC in detergent DDM. **(A)** nDSF of 5 µM TolC in 0.03% DDM buffer with a heating rate of 1°C/min indicates a high thermal stability with a weak transition around 84°C. **(B)** The scattering curve acquired during the nDSF indicates aggregation at a lower temperature of 62°C. **(C)** The DLS autocorrelation curves suggest similar polydispersity and hydrodynamic radii for DDM concentrations in the range of 0.003 and 0.03%. **(D)** Mass weighted histograms for the curves displayed in **Figure 7C (E)**. Mass photometry of 150 nM TolC in the presence of 0.003% DDM. Three bands are detectable at 106, 274, and 461 kDa. Control measurements at 0.03% **(F)** and 0.003% DDM **(G)** suggest that the bands at 106 and 461 kDa can be assigned to DDM. The band at 274 kDa can be assigned to the TolC-DDM complex (the theoretical mass of TolC is 162 kDa). **(H)** Negative staining electron micrographs of TolC at 0.015 mg/ml using 40000 x magnification on a Jeol 200 kV cryo-TEM using in-house carbon-coated grids.

Case 2: Integral Membrane Protein TolC

TolC is an integral membrane protein from *Escherichia coli* (Husain et al., 2004) with a molecular weight of 161.7 kDa for its trimeric state. Collectively, the trimer forms a β-barrel that is embedded into the outer membrane and its α-helical part spanning into the periplasm. Upon assembly with AcrAB, its main function is the efflux of diverse molecules, such as toxins and antibacterial drugs (Koronakis et al., 2004). The results of the biophysics pipeline are shown in **Figure 7**. According to nDSF, the protein is highly stable in DDM with a dominant transition at 84°C (**Figure 7A**). Therefore, no further detergent screening was performed. It is important to note that this is based on the signal of one single tryptophan in the protein, probably buried in a more stable region of the protein (T_m of 84°C vs. T_{agg} of 62°C). Hence, for the identification of stabilizing conditions during sample preparation, it is relevant to consider the onset of scattering that relates to the change in the slope of the curve, equivalent to the temperature where 1% of protein aggregates (**Figure 7B**). Additionally, DLS was used to determine the lowest DDM detergent concentration that can be used to prevent the aggregation of the protein sample (**Figure 7C,D**). The results show that decreasing the DDM protein from 0.03 to 0.003% does not modify the autocorrelation curve. Therefore, mass photometry was performed at a concentration of 0.003% DDM, resulting in the detection of three peaks at 106, 274 and 461 kDa (**Figure 7E**). Based on control experiments at two different DDM concentrations (**Figure 7F,G**), the peaks at 106 and 461 kDa can be assigned to DDM empty micelles and the peak at 274 kDa can be assigned to DDM micelles with integrated TolC.

Case 3: Membrane Remodelling Complexes: hENTH and AENTH

Epsin is an adaptor protein involved in clathrin-mediated endocytosis (Ford et al., 2002; Yoon et al., 2010; Lai et al., 2012; Skruzny et al., 2015; Joseph et al., 2020). It contains an amphitropic membrane binding domain, hENTH (Epsin-N-terminal Homology), which induces membrane tubulation upon binding to the phospholipid $PI(4,5)P_2$ (Ford et al., 2002). To structurally characterize these oligomers, we performed the proposed biophysical characterization of the sample using Dynamic Light Scattering (DLS), nDSF, and mass photometry (MP) of hENTH in the absence and presence of $PI(4,5)P_2$ (**Figure 8**). hENTH shows a shift melting temperature (T_m) in nDSF in the presence of $PI(4,5)P_2$, indicating that the protein unfolds earlier when in the presence of the lipids (**Figure 8A**). The sample is also more prone to aggregation, as evidenced by the earlier T_{agg} from the static scattering measured as well using the nDSF device (**Figure 8B**). DLS experiments showed a shift in the auto-correlation curve when in the presence of 200 μM $PI(4,5)P_2$ (**Figure 8C**). Plotting the radius of the particles in solution when in the presence of $PI(4,5)P_2$ reveals a shift towards larger radius, indicating the formation of a soluble oligomer of hENTH domains (**Figure 8D**). Mass photometry revealed that a buffer containing 200 μM $PI(4,5)P_2$ gives a distribution around 50 kDa, corresponding to the $PI(4,5)P_2$ micelles present in the buffer (**Figure 8F**). While the mass of the monomeric hENTH (18 kDa) is not detectable by mass photometry, a clear mass distribution corresponding to 108 kDa and in agreement with what was previously described as an hENTH hexamer by SAXS and native MS (**Figure 8G**) is detected in the presence of 200 μM $PI(4,5)P_2$ (**Figure 8E**). This characterization pipeline confirms that the particles observed in negative staining and cryo-EM micrographs of hENTH in the presence of $PI(4,5)P_2$ correspond indeed to hENTH hexamers (**Figure 8H**).

Both DLS and MP can provide useful information regarding sample quality prior to cryo-EM sample preparation. To showcase the complementarity of both methods over a challenging sample, we have used membrane binding domains from endocytic adaptors Sla2 and Ent1 from yeast. During clathrin-mediated endocytosis, these proteins form a phosphatidylinositol 4,5-bisphosphate (PIP_2)-dependent complex, essential for membrane remodelling and invagination. It has been shown that their membrane binding domains, ANTH and ENTH, oligomerize *in-vitro* into different assemblies through lipid interfaces forming the AENTH complex (Garcia-Alai et al., 2018; Lizarrondo et al., 2021). Here, DLS has been a powerful tool to assess the aggregation of the individual ANTH and ENTH domains upon mixing with PIP_2 (**Supplementary Figure S4A**) and during the AENTH complex formation. However, even when DLS could help in the optimization of a non-aggregated sample, it would only provide an average radius of gyration of particles in solution (**Supplementary Figure S4B,C**). In addition, MP allowed us to accurately determine several of the AENTH assemblies providing a good platform for screening conditions that allowed us to determine the structure of the complexes by native mass spectrometry and single particle cryo-EM (**Supplementary Figure S4D**). Importantly, the macromolecular complex species identified as 12mers and 16mers by MP cannot be resolved by DLS (see the orange and red lines between 6 and 10 nm on the right panel of **Supplementary Figure S4C**). These assemblies were later on visualized on cryo-EM micrographs from where the structure for 12mers and 16-mers could be resolved (**Supplementary Figure S4E**, and Lizarrondo et al., 2021).

DISCUSSION

The presented biophysical pipeline allows us to efficiently optimize conditions for sample preparation for structural biology studies prior to electron microscopy, helping to reduce the costly and time-consuming cryo-EM screening of grids. DSF is used to optimize buffer conditions and to select the optimal detergent. Additionally, DLS gives information regarding the presence of large aggregates in the sample and can be used to identify the lowest possible detergent concentration preventing aggregation. It is crucial to monitor the onset of denaturation by DSF to minimize the presence of aggregates that can be detrimental for cryo-EM. Here, the limitation is that it does not account for those

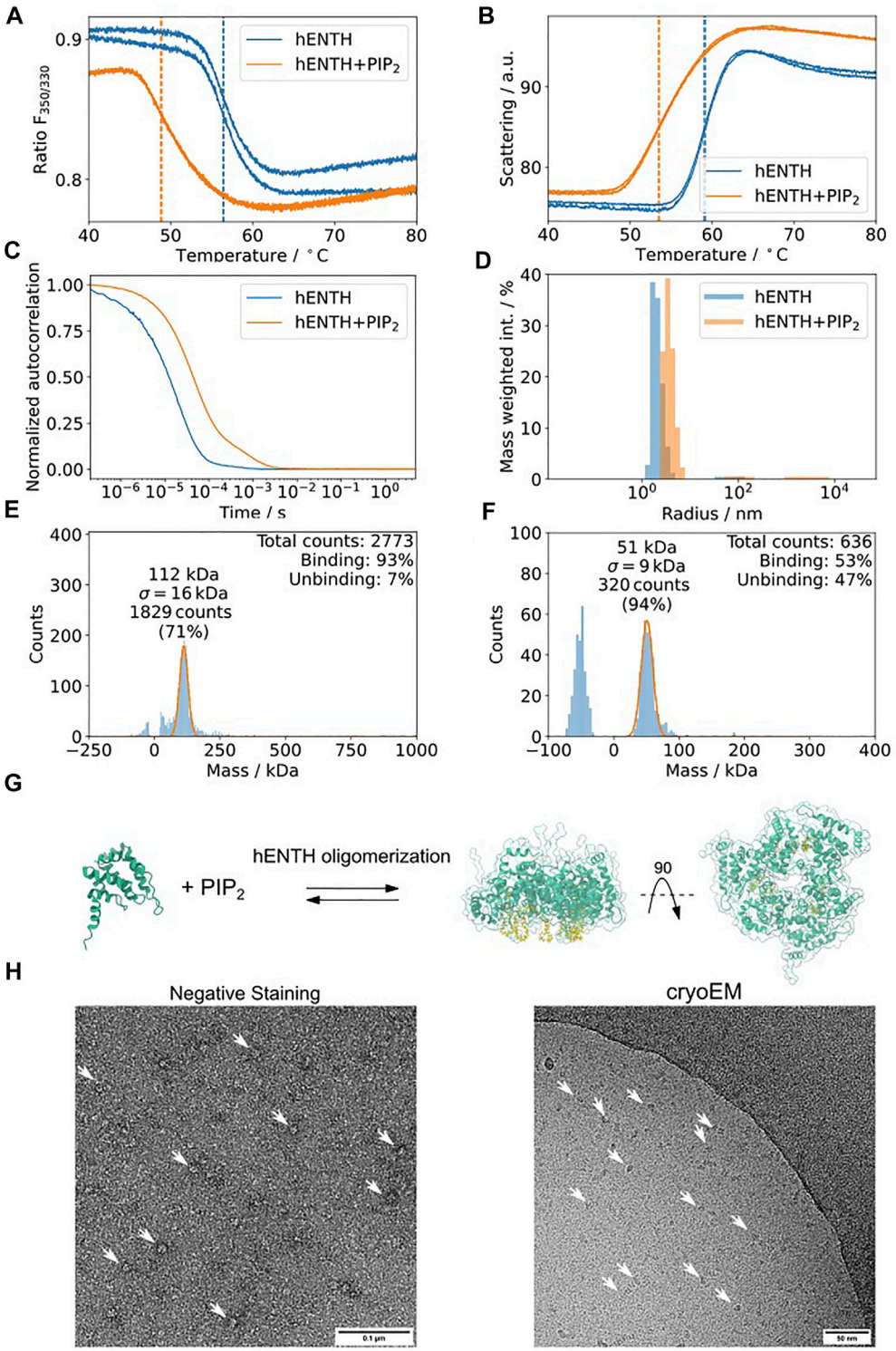

FIGURE 8 | hENTH forms complexes in micellar concentrations of $PI(4,5)P_2$. **(A)** nDSF transitions for hENTH at 30 μM in the absence and presence of 200 μM $PI(4,5)P_2$. The shift in the sample with $PI(4,5)P_2$ indicates that the oligomer unfolds before the monomers. **(B)** Scattering curves of hENTH in the absence and presence of 200 μM $PI(4,5)P_2$. The hENTH aggregates at lower temperature in the presence of $PI(4,5)P_2$. **(C)** DLS auto-correlation curves of hENTH at 30 μM in the absence and presence of 200 μM $PI(4,5)P_2$. The shift in the autocorrelation curve indicates that the hENTH domain oligomerizes in the presence of $PI(4,5)P_2$. **(D)** Histogram of the masses present on the DLS samples in the absence and presence of $PI(4,5)P_2$. hENTH shifts towards higher masses in the presence of $PI(4,5)P_2$, consistent with oligomer formation. **(E)** hENTH at 100 nM (monomer MW = 18.5 kDa) shows a peak at 108 kDa, corresponding to a hexamer of hENTH in the presence of 200 μM $PI(4,5)P_2$ at 112 kDa. **(F)** Control: mass photometry histogram of buffer with 200 μM $PI(4,5)P_2$. A peak at ca. 51 kDa corresponds to $PI(4,5)P_2$ micelles. **(G)** Schematic of the hENTH domain (green) (PDB ID: 5ONF) and the oligomer model with $PI(4,5)P_2$ molecules (yellow) from Garcia-Alai et al., 2018. **(H)** Representative negative staining and cryo-electron micrograph of hENTH + $PI(4,5)P_2$ where hENTH hexamers can be observed. Particles of interest are indicated with white arrows.

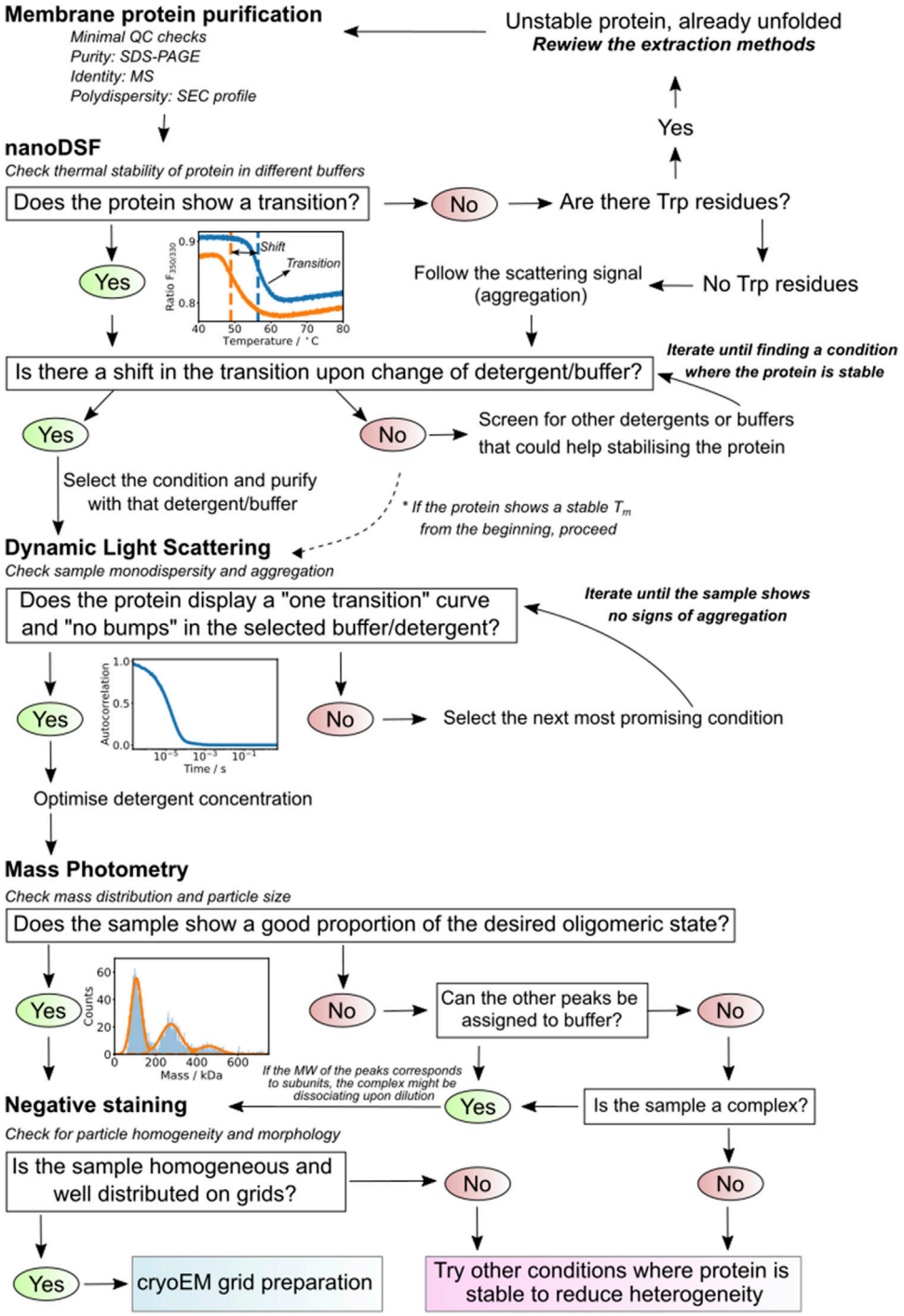

FIGURE 9 | Summary diagram. The scheme presents a defined decision-making strategy based on the results of each of the used techniques. It guides the researcher on how to proceed depending on the results of the steps previously applied.

aggregates that arise upon vitrification, interaction with the grid, and at the air–water interface (Noble et al., 2018). Finally, mass photometry is used to check the size distribution, oligomeric states and integrity of complexes, providing information of molecular masses at the single particle level and their abundance in the sample (see **Figure 9** for "decision making" after each step of the pipeline). Importantly, the eSPC platform offers tools to analyze and understand DSF and mass photometry experiments in a user-friendly webserver (spc.embl-hamburg.de). A detailed EM sample screening

workflow is provided with instructions for performing negative stain and cryo-EM sample preparation for single particle analysis. Each biological system will require adjustments at different steps, and sample preparation still remains to be an iterative empirical procedure. The provided pipeline could be used as a guide and would help in the decision making when working with challenging samples. We are aware that most laboratories might not have all the equipment described in our pipeline. However, there are different opportunities offering trans-national access to cutting-edge biophysical infrastructures that only require a simple application and description of the project. Information regarding access to our facility and others can be provided upon request (contact us at spc@embl-hamburg.de).

DATA AVAILABILITY STATEMENT

The original contributions presented in the study are included in the article/**Supplementary Material**; further inquiries can be directed to the corresponding author.

AUTHOR CONTRIBUTIONS

Conceptualization: SN, KV, OB, AS, JL, and MG-A; methodology: SN, KV, OB, AS, JL, JS, BV, CS, PL, SW, and MG-A; investigation: KV, SN, JL, OB, AS, BV, CS, PL, and MG-A; writing—original draft: SN, KV, OB, AS, JL, and MG-A; editing: all authors; resources and funding acquisition: KG; SW and MG-A; supervision: MG-A.

FUNDING

This work is supported in part by CSSB Seed grant KIF 2019/002 (MG-A). Part of this work was performed at the Cryo-EM Facility at CSSB, supported by the UHH and DFG grant numbers (INST 152/772-1|152/774-1|152/775-1|152/776-1|152/777-1 FUGG). This project has received funding from the European Union's Horizon 2020 research and innovation programme under the Marie Sklodowska-Curie grant agreement No. 945405. OB was supported by the ARISE fellowship from EMBL. JL is funded by the EMBL International Ph.D. programme.

ACKNOWLEDGMENTS

We thank Henning Tidow and Inokentijs Josts for providing us with the plasmid for the IJ1 protein. We acknowledge the use of the XBI biological sample preparation laboratory (Han et al., 2021), enabled by the XBI User Consortium (and thank Ekaterina Round for excellent user support). We acknowledge technical support by the SPC facility at EMBL Hamburg and the PP facility, University Medical Center Hamburg-Eppendorf, Hamburg, Germany, at CSSB Hamburg.

SUPPLEMENTARY MATERIAL

The supplementary material for this article can be found online at: https://www.frontiersin.org/articles/10.3389/fmolb.2022.882288/full#supplementary-material

REFERENCES

Adrian, M., Dubochet, J., Fuller, S. D., and Harris, J. R. (1998). Cryo-negative Staining. *Micron* 29 (2-3), 145–160. doi:10.1016/s0968-4328(97)00068-1

Boekema, E. J. (1991). Negative Staining of Integral Membrane Proteins. *Micron Microsc. Acta* 22 (4), 361–369. doi:10.1016/0739-6260(91)90054-4

Brenner, S., and Horne, R. W. (1959). A Negative Staining Method for High Resolution Electron Microscopy of Viruses. *Biochimica Biophysica Acta* 34, 103–110. doi:10.1016/0006-3002(59)90237-9

Burastero, O., Niebling, S., Defelipe, L. A., Günther, C., Struve, A., and Garcia Alai, M. M. (2021). eSPC: an Online Data-Analysis Platform for Molecular Biophysics. *Acta Cryst. Sect. D. Struct. Biol.* 77 (10), 1241–1250. doi:10.1107/s2059798321008998

Chatzikyriakidou, Y., Ahn, D.-H., Nji, E., and Drew, D. (2021). The GFP Thermal Shift Assay for Screening Ligand and Lipid Interactions to Solute Carrier Transporters. *Nat. Protoc.* 16 (12), 5357–5376. doi:10.1038/s41596-021-00619-w

D'Imprima, E., Floris, D., Joppe, M., Sánchez, R., Grininger, M., and Kühlbrandt, W. (2019). Protein Denaturation at the Air-Water Interface and How to Prevent it. *eLife* 8, e42747. doi:10.7554/eLife.42747

de Marco, A., Berrow, N., Lebendiker, M., Garcia-Alai, M., Knauer, S. H., Lopez-Mendez, B., et al. (2021). Quality Control of Protein Reagents for the Improvement of Research Data Reproducibility. *Nat. Commun.* 12 (1), 2795. doi:10.1038/s41467-021-23167-z

De Rosier, D. J., and Klug, A. (1968). Reconstruction of Three Dimensional Structures from Electron Micrographs. *Nature* 217 (5124), 130–134. doi:10.1038/217130a0

Drulyte, I., Johnson, R. M., Hesketh, E. L., Hurdiss, D. L., Scarff, C. A., Porav, S. A., et al. (2018). Approaches to Altering Particle Distributions in Cryo-Electron Microscopy Sample Preparation. *Acta Crystallogr. D. Struct. Biol.* 74 (6), 560–571. doi:10.1107/S2059798318006496

Efremov, R. G., Leitner, A., Aebersold, R., and Raunser, S. (2015). Architecture and Conformational Switch Mechanism of the Ryanodine Receptor. *Nature* 517 (7532), 39–43. doi:10.1038/nature13916

Ford, M. G. J., Mills, I. G., Peter, B. J., Vallis, Y., Praefcke, G. J. K., Evans, P. R., et al. (2002). Curvature of Clathrin-Coated Pits Driven by Epsin. *Nature* 419 (6905), 361–366. doi:10.1038/nature01020

Gallagher, J. R., Kim, A. J., Gulati, N. M., and Harris, A. K. (2019). Negative-stain Transmission Electron Microscopy of Molecular Complexes for Image Analysis by 2d Class Averaging. *Curr. Protoc. Microbiol.* 54 (1), e90. doi:10.1002/cpmc.90

Garcia-Alai, M. M., Heidemann, J., Skruzny, M., Gieras, A., Mertens, H. D. T., Svergun, D. I., et al. (2018). Epsin and Sla2 Form Assemblies through Phospholipid Interfaces. *Nat. Commun.* 9 (1), 328. doi:10.1038/s41467-017-02443-x

Glaeser, R. M. (2021). Preparing Better Samples for Cryo-Electron Microscopy: Biochemical Challenges Do Not End with Isolation and Purification. *Annu. Rev. Biochem.* 90 (1), 451–474. doi:10.1146/annurev-biochem-072020-020231

Goehring, A., Lee, C.-H., Wang, K. H., Michel, J. C., Claxton, D. P., Baconguis, I., et al. (2014). Screening and Large-Scale Expression of Membrane Proteins in Mammalian Cells for Structural Studies. *Nat. Protoc.* 9 (11), 2574–2585. doi:10.1038/nprot.2014.173

Hall, C. E. (1955). Electron Densitometry of Stained Virus Particles. *J. Biophys. Biochem. Cyt.* 1 (1), 1–12. doi:10.1083/jcb.1.1.1

Han, H., Round, E., Schubert, R., Gül, Y., Makroczyová, J., Meza, D., et al. (2021). The XBI BioLab for Life Science Experiments at the European XFEL. *J. Appl. Cryst.* 54 (1), 7–21. doi:10.1107/s1600576720013989

Hauer, F., Gerle, C., Fischer, N., Oshima, A., Shinzawa-Itoh, K., Shimada, S., et al. (2015). GraDeR: Membrane Protein Complex Preparation for Single-Particle Cryo-EM. *Structure* 23 (9), 1769–1775. doi:10.1016/j.str.2015.06.029

Häußermann, K., Young, G., Kukura, P., and Dietz, H. (2019). Dissecting FOXP2 Oligomerization and DNA Binding. *Angew. Chem. Int. Ed.* 58 (23), 7662–7667. doi:10.1002/anie.201901734

Heermann, T., Steiert, F., Ramm, B., Hundt, N., and Schwille, P. (2021). Mass-sensitive Particle Tracking (Mspt) to Elucidate the Membrane-Associated Minde Reaction Cycle. *Nat. Meth.* (18), 1239–1246.doi:10.1038/s41592-021-01260-x

Hoenger, A., and Aebi, U. (1996). 3-d Reconstructions from Ice-Embedded and Negatively Stained Biomacromolecular Assemblies: A Critical Comparison. *J. Struct. Biol.* 117 (2), 99–116. doi:10.1006/jsbi.1996.0075

Horne, R. W., Hobart, J. M., and Pasquali-Ronchetti, I. (1975). A Negative Staining-Carbon Film Technique for Studying Viruses in the Electron Microscope. *J. Ultrastruct. Res.* 53 (3), 319–330. doi:10.1016/s0022-5320(75)80033-5

Hundt, N. (2021). Label-free, Mass-Sensitive Single-Molecule Imaging Using Interferometric Scattering Microscopy. *Essays Biochem.* 65 (1), 81–91. doi:10.1042/ebc20200023

Husain, F., Humbard, M., and Misra, R. (2004). Interaction between the TolC and AcrA Proteins of a Multidrug Efflux System of escherichia Coli. *J. Bacteriol.* 186 (24), 8533–8536. doi:10.1128/jb.186.24.8533-8536.2004

Joppe, M., D'Imprima, E., Salustros, N., Paithankar, K. S., Vonck, J., Grininger, M., et al. (2020). The Resolution Revolution in cryoEM Requires High-Quality Sample Preparation: a Rapid Pipeline to a High-Resolution Map of Yeast Fatty Acid Synthase. *Int. Union Crystallogr. J.* 7 (2), 220–227. doi:10.1107/s2052252519017366

Joseph, J. G., Osorio, C., Yee, V., Agrawal, A., and Liu, A. P. (2020). Complimentary Action of Structured and Unstructured Domains of Epsin Supports Clathrin-Mediated Endocytosis at High Tension. *Commun. Biol.* 3 (1), 743. doi:10.1038/s42003-020-01471-6

Kampjut, D., Steiner, J., and Sazanov, L. A. (2021). Cryo-EM Grid Optimization for Membrane Proteins. *iScience* 24 (3), 102139. doi:10.1016/j.isci.2021.102139

Koppel, D. E. (1972). Analysis of Macromolecular Polydispersity in Intensity Correlation Spectroscopy: The Method of Cumulants. *J. Chem. Phys.* 57 (11), 4814–4820. doi:10.1063/1.1678153

Koronakis, V., Eswaran, J., and Hughes, C. (2004). Structure and Function of TolC: The Bacterial Exit Duct for Proteins and Drugs. *Annu. Rev. Biochem.* 73 (1), 467–489. doi:10.1146/annurev.biochem.73.011303.074104

Kotov, V., Bartels, K., Veith, K., Josts, I., Subhramanyam, U. K. T., Günther, C., et al. (2019). High-throughput Stability Screening for Detergent-Solubilized Membrane Proteins. *Sci. Rep.* 9, 10379. doi:10.1038/s41598-019-46686-8

Kühlbrandt, W. (2014). The Resolution Revolution. *Science* 343 (6178), 1443–1444. doi:10.1126/science.1251652

Lai, C.-L., Jao, C. C., Lyman, E., Gallop, J. L., Peter, B. J., McMahon, H. T., et al. (2012). Membrane Binding and Self-Association of the Epsin N-Terminal Homology Domain. *J. Mol. Biol.* 423 (5), 800–817. doi:10.1016/j.jmb.2012.08.010

Lai, S.-H., Tamara, S., and Heck, A. J. R. (2021). Single-particle Mass Analysis of Intact Ribosomes by Mass Photometry and Orbitrap-Based Charge Detection Mass Spectrometry. *iScience* 24, 103211. doi:10.1016/j.isci.2021.103211

Lizarrondo, J., Klebl, D. P., Niebling, S., Abella, M., Schroer, M. A., Mertens, H. D. T., et al. (2021). Structure of the Endocytic Adaptor Complex Reveals the Basis for Efficient Membrane Anchoring during Clathrin-Mediated Endocytosis. *Nat. Comm.* 12 (1), 2889. doi:10.1038/s41467-021-23151-7

Mastronarde, D. N. (2005). Automated Electron Microscope Tomography Using Robust Prediction of Specimen Movements. *J. Struct. Biol.* 152 (1), 36–51. doi:10.1016/j.jsb.2005.07.007

Murphy, R. M. (1997). Static and Dynamic Light Scattering of Biological Macromolecules: what Can We Learn? *Curr. Opin. Biotechnol.* 8 (1), 25–30. doi:10.1016/s0958-1669(97)80153-x

Nji, E., Chatzikyriakidou, Y., Landreh, M., and Drew, D. (2018). An Engineered Thermal-Shift Screen Reveals Specific Lipid Preferences of Eukaryotic and Prokaryotic Membrane Proteins. *Nat. Commun.* 9 (1), 4253. doi:10.1038/s41467-018-06702-3

Noble, A. J., Dandey, V. P., Wei, H., Brasch, J., Chase, J., Acharya, P., et al. (2018). Routine Single Particle CryoEM Sample and Grid Characterization by Tomography. *eLife* 7, e34257. doi:10.7554/eLife.34257

Ohi, M., Li, Y., Cheng, Y., and Walz, T. (2004). Negative Staining and Image Classification - Powerful Tools in Modern Electron Microscopy. *Biol. Proced. Online* 6 (1), 23–34. doi:10.1251/bpo70

Olerinyova, A., Sonn-Segev, A., Gault, J., Eichmann, C., Schimpf, J., Kopf, A. H., et al. (2020). Mass Photometry of Membrane Proteins. *Chem* 7 (1), 224–236. doi:10.1016/j.chempr.2020.11.011

Passmore, L. A., and Russo, C. J. (2016). "Specimen Preparation for High-Resolution Cryo-EM," in *Methods in Enzymology* (Cambridge, USA: Academic Press), 51–86. doi:10.1016/bs.mie.2016.04.011

Provencher, S. W. (1982). CONTIN: A General Purpose Constrained Regularization Program for Inverting Noisy Linear Algebraic and Integral Equations. *Comput. Phys. Commun.* 27 (3), 229–242. doi:10.1016/0010-4655(82)90174-6

Raynal, B., Lenormand, P., Baron, B., Hoos, S., and England, P. (2014). Quality Assessment and Optimization of Purified Protein Samples: Why and How? *Microb. Cell Fact.* 13 (1), 180. doi:10.1186/s12934-014-0180-6

Rohou, A., and Grigorieff, N. (2015). CTFFIND4: Fast and Accurate Defocus Estimation from Electron Micrographs. *J. Struct. Biol.* 192 (2), 216–221. doi:10.1016/j.jsb.2015.08.008

Scarff, C. A., Fuller, M. J. G., Thompson, R. F., and Iadanza, M. G. (2018). Variations on Negative Stain Electron Microscopy Methods: Tools for Tackling Challenging Systems. *J. Vis. Exp.* 132, 57199. doi:10.3791/57199

Schuck, P. (2000). Size-distribution Analysis of Macromolecules by Sedimentation Velocity Ultracentrifugation and Lamm Equation Modeling. *Biophysical J.* 78 (3), 1606–1619. doi:10.1016/s0006-3495(00)76713-0

Skruzny, M., Desfosses, A., Prinz, S., Dodonova, S. O., Gieras, A., Uetrecht, C., et al. (2015). An Organized Co-assembly of Clathrin Adaptors Is Essential for Endocytosis. *Dev. Cell* 33 (2), 150–162. doi:10.1016/j.devcel.2015.02.023

Soltermann, F., Foley, E. D. B., Pagnoni, V., Galpin, M., Benesch, J. L. P., Kukura, P., et al. (2020). Quantifying Protein-Protein Interactions by Molecular Counting with Mass Photometry. *Angew. Chem. Int. Ed.* 59 (27), 10774–10779. doi:10.1002/anie.202001578

Sonn-Segev, A., Belacic, K., Bodrug, T., Young, G., VanderLinden, R. T., Schulman, B. A., et al. (2020). Quantifying the Heterogeneity of Macromolecular Machines by Mass Photometry. *Nat. Commun.* 11 (1), 1772. doi:10.1038/s41467-020-15642-w

Steiert, F., Heermann, T., Hundt, N., and Schwille, P. (2022). Mass-sensitive Particle Tracking to Characterize Membrane-Associated Macromolecule Dynamics. *J. Vis. Exp.* (180), e63583. doi:10.3791/63583

Tan, Y. Z., Baldwin, P. R., Davis, J. H., Williamson, J. R., Potter, C. S., Carragher, B., et al. (2017). Addressing Preferred Specimen Orientation in Single-Particle Cryo-EM through Tilting. *Nat. Methods* 14 (8), 793–796. doi:10.1038/nmeth.4347

Tegunov, D., and Cramer, P. (2019). Real-time Cryo-Electron Microscopy Data Preprocessing with Warp. *Nat. Methods* 16 (11), 1146–1152. doi:10.1038/s41592-019-0580-y

Wu, D., and Piszczek, G. (2020). Measuring the Affinity of Protein-Protein Interactions on a Single-Molecule Level by Mass Photometry. *Anal. Biochem.* 592, 113575. doi:10.1016/j.ab.2020.113575

Wu, D., and Piszczek, G. (2021). Standard Protocol for Mass Photometry Experiments. *Eur. Biophysics J.* 50 (3-4), 403–409. doi:10.1007/s00249-021-01513-9

Yoon, Y., Tong, J., Lee, P. J., Albanese, A., Bhardwaj, N., Källberg, M., et al. (2010). Molecular Basis of the Potent Membrane-Remodeling Activity of the Epsin 1 N-Terminal Homology Domain. *J. Biol. Chem.* 285 (1), 531–540. doi:10.1074/jbc.m109.068015

Young, G., Hundt, N., Cole, D., Fineberg, A., Andrecka, J., Tyler, A., et al. (2018). Quantitative Mass Imaging of Single Biological Macromolecules. *Science* 360 (6387), 423–427. doi:10.1126/science.aar5839

Zivanov, J., Nakane, T., Forsberg, B. O., Kimanius, D., Hagen, W. J., Lindahl, E., et al. (2018). New Tools for Automated High-Resolution Cryo-EM Structure Determination in RELION-3. *eLife* 7, e42166. doi:10.7554/eLife.42166

Conflict of Interest: The authors declare that the research was conducted in the absence of any commercial or financial relationships that could be construed as a potential conflict of interest.

Publisher's Note: All claims expressed in this article are solely those of the authors and do not necessarily represent those of their affiliated organizations, or those of the publisher, the editors, and the reviewers. Any product that may be evaluated in this article, or claim that may be made by its manufacturer, is not guaranteed or endorsed by the publisher.

frontiers | Frontiers in Molecular Biosciences

REVIEW
published: 24 June 2022
doi: 10.3389/fmolb.2022.892459

Recent Technical Advances in Sample Preparation for Single-Particle Cryo-EM

Yixin Xu[1] *and Shangyu Dang*[1,2,3]*

[1]Division of Life Science, The Hong Kong University of Science and Technology, Kowloon, Hong Kong SAR, China, [2]Southern Marine Science and Engineering Guangdong Laboratory (Guangzhou), Guangzhou, China, [3]Center of Systems Biology and Human Health, The Hong Kong University of Science and Technology, Kowloon, Hong Kong SAR, China

Cryo-sample preparation is a vital step in the process of obtaining high-resolution structures of macromolecules by using the single-particle cryo–electron microscopy (cryo-EM) method; however, cryo-sample preparation is commonly hampered by high uncertainty and low reproducibility. Specifically, the existence of air-water interfaces during the sample vitrification process could cause protein denaturation and aggregation, complex disassembly, adoption of preferred orientations, and other serious problems affecting the protein particles, thereby making it challenging to pursue high-resolution 3D reconstruction. Therefore, sample preparation has emerged as a critical research topic, and several new methods for application at various preparation stages have been proposed to overcome the aforementioned hurdles. Here, we summarize the methods developed for enhancing the quality of cryo-samples at distinct stages of sample preparation, and we offer insights for developing future strategies based on diverse viewpoints. We anticipate that cryo-sample preparation will no longer be a limiting step in the single-particle cryo-EM field as increasing numbers of methods are developed in the near future, which will ultimately benefit the entire research community.

Keywords: single-particle cryo-electron microscopy, sample preparation, air-water interface, grid modification, particle distribution

OPEN ACCESS

Edited by:
Felix Weis,
European Molecular Biology Laboratory Heidelberg, Germany

Reviewed by:
Ki Hyun Nam,
Pohang University of Science and Technology, South Korea
Esko Oksanen,
European Spallation Source, Sweden
Christos Savva,
University of Leicester, United Kingdom

***Correspondence:**
Shangyu Dang
sdang@ust.hk

Specialty section:
This article was submitted to Structural Biology, a section of the journal Frontiers in Molecular Biosciences

Received: *09 March 2022*
Accepted: *12 May 2022*
Published: *24 June 2022*

Citation:
Xu Y and Dang S (2022) Recent Technical Advances in Sample Preparation for Single-Particle Cryo-EM. Front. Mol. Biosci. 9:892459. doi: 10.3389/fmolb.2022.892459

INTRODUCTION

Single-particle cryo-electron microscopy (cryo-EM) is emerging as one of the most effective techniques in the field of structural biology (Lyumkis, 2019; Bai, 2021). Purified biological macromolecules and/or complexes, isolated from endogenous or recombinant overexpression sources, are first applied to cryo-EM grids and rapidly frozen to generate an extremely thin layer of vitreous ice (**Figure 1A**). Next, the cryo-specimen is transferred to an electron microscope, and the images are acquired at liquid nitrogen temperature. Lastly, single particles are boxed out for iterative classification to sort out suitable particles for the final three-dimensional (3D) reconstruction (Cheng et al., 2015; Lyumkis, 2019). The obtained structural details of biological macromolecules at atomic resolution provide valuable information for not only unravelling the fundamental mechanisms of myriad biological processes but also driving the development of drugs for treating diseases caused by the dysfunctional biological macromolecules (Zhu et al., 2018; Han et al., 2022; Liang et al., 2022). Recent technical breakthroughs in single-particle cryo-EM have created a "resolution revolution" in structural biology by circumventing the major challenges faced when using the traditional X-ray crystallography methods (Cheng, 2015; Cheng, 2018).

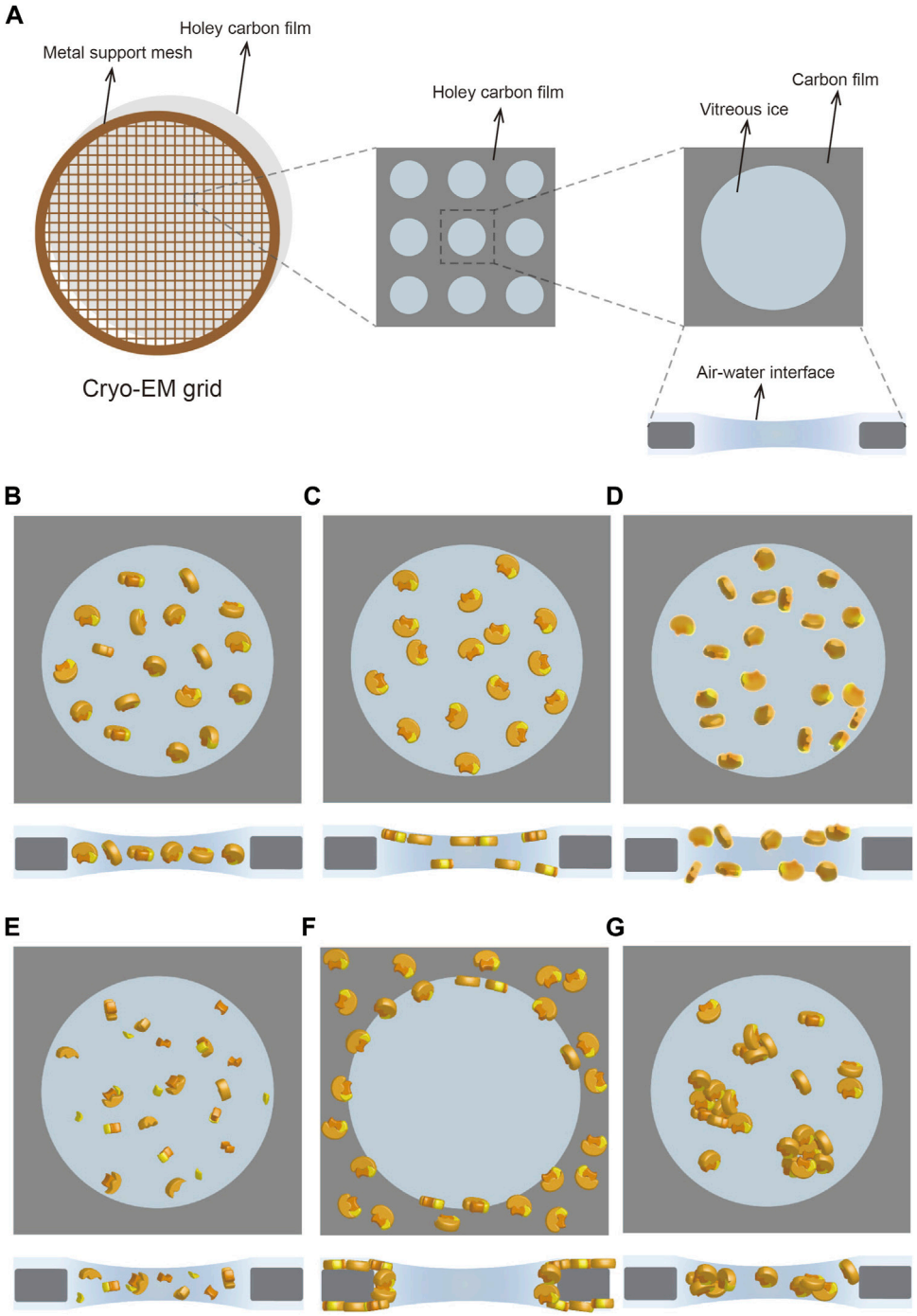

FIGURE 1 | Cryo-specimen in single-particle cryo-EM. **(A)** Cryo-EM grid usually has a metal support mesh and a holey carbon film to carry the sample solution. The particles are frozen in vitreous ice in the holes for image acquisition **(B–G)** Different states of particles in vitreous ice, including ideal situation **(B)**, preferred orientation **(C)**, denaturation **(D)**, disassembly **(E)**, adsorption on carbon film **(F)**, and aggregation **(G)**. Subunits in the protein complex are shown in yellow, orange, and lemon, respectively.

The technical breakthroughs in cryo-EM, such as advances in hardware and updating of software, are attracting increasing attention in the field of structural biology (Egelman, 2016). The key driver of this "resolution revolution" is the replacement of the traditional charge-coupled device (CCD) cameras with new direct detection device (DDD) cameras (McMullan et al., 2016; Hurtley, 2018). The DDD camera can detect electrons directly at higher frame rates than the CCD camera, which results in relatively higher detective quantum efficiency and enables movie recording during exposure to

correct the beam-induced image blurring (Li et al., 2013; Bai et al., 2015; McMullan et al., 2016). Moreover, introduction of new data processing algorithms, such as RELION (Scheres, 2012), Frealign (Grigorieff, 2016), cisTEM (Grant et al., 2018), cryoSPARC (Punjani et al., 2017), and automation of the work pipeline (Wang et al., 2016; Li et al., 2020; Stabrin et al., 2020) have also led cryo-EM technology into a new era. In 2020, cryo-EM hardware improvements pushed resolution to the atomic level (Nakane et al., 2020; Yip et al., 2020; Zhang et al., 2020), refreshing a limitation of cryo-EM structures. By contrast, the development of sample preparation methods in cryo-EM has been slowed by several obstacles (Passmore and Russo, 2016), and this has widely hindered the structure determination studies in the field.

Sample preparation in cryo-EM generally consists of two key procedures: purification and vitrification (Weissenberger et al., 2021). The first step in the macromolecular structure analysis is the preparation of purified macromolecules in an optimal biochemical environment (Passmore and Russo, 2016). However, obtaining a high-quality specimen after purification does not guarantee a suitable cryo-specimen after vitrification. This is because cryo-grid preparation is a trial and error process that is affected by diverse factors such as grid material, glow discharge, incubation, and blotting (Weissenberger et al., 2021). Variations of these external factors and the characteristics of the samples themselves could lead to an undesirable state of the particles, making it challenging to reconstruct a high-resolution structure. In real-world cases, the adoption of all preferred orientations by particles and the denaturation, disassembly, adsorption on carbon film, and aggregation of particles (**Figures 1B–G**) are problems commonly encountered in sample preparation (Drulyte et al., 2018). Besides sample quality at the biochemical level, the main reason for these recurring problems is the adsorption of particles on the air–water interface (AWI) during vitrification (Glaeser and Han, 2017; Glaeser, 2018).

The AWI can severely affect particles because the extremely thin layer of liquid remaining on the cryo-grid after blotting can generate a large surface-to-volume ratio (Glaeser and Han, 2017). Typically, free-floating particles collide with the AWI thousands of times before vitrification (Klebl et al., 2020) even though plunge freezing takes only a few seconds. When the particles reach the AWI, certain hydrophobic side chains or small hydrophobic patches on the surface can facilitate particle adsorption on the AWI. Whereas slight adsorption might generate preferred orientations, substantial adsorption could result in partial or complete denaturation due to hydrophobic residues being exposed to air but hydrophilic residues being retained in water (Glaeser and Han, 2017; Glaeser, 2018). Although this protein-unfolding interaction at the AWI occurs within a very short time, the interaction can lethally affect subsequent structural analysis (Klebl et al., 2020). Thus, diverse methods have been proposed to reduce the effect of the AWI (Tan et al., 2017; Noble et al., 2018; Chen et al., 2019; Wang and Yu, 2020), but the AWI influence remains a challenging problem to solve comprehensively.

Here, we summarize and classify distinct strategies aimed at improving the quality of cryo-specimens. We illustrate the technical methods and list the benefits and drawbacks of these strategies to compare the differences between the strategies and develop an evaluation system. We also offer certain new perspectives for optimizing the particle behavior in vitreous ice in order to facilitate high-resolution structure determination by using single-particle cryo-EM.

SAMPLE BIOCHEMISTRY

Purification of an adequate amount of high-quality protein samples is the key for high-resolution cryo-EM studies. Besides the technique used to isolate the target protein at a high level of purity, the buffer condition is another critical factor because it not only helps ensure a well-behaved protein in solution but also affects protein behavior in vitreous ice when preparing the cryo-specimen (Cheung et al., 2013; Glaeser et al., 2016; Passmore and Russo, 2016). Accordingly, the same proteins purified under distinct conditions display divergent behaviors in vitreous ice (Dang et al., 2017; Paulino et al., 2017; Feng et al., 2019). Therefore, screening of the purification conditions, including but not limited to pH, salt, ligands, small molecules, and detergents (for membrane proteins), relies heavily on the properties of the target protein itself, and this represents one approach for improving the cryo-sample quality. The efficiency of the screening purification conditions, which can be a time-consuming process, could be increased by introducing several screening and optimization methods to overcome the compositional heterogeneity problems of the protein sample (**Table 1**). The thermofluor screening assay (Ericsson et al., 2006), which is typically used to identify the appropriate buffer conditions for protein stabilization and crystallization, reports the melting temperature of a protein based on fluorescence and thereby reveals the distinct states of the sample, such as protein denaturation and disassembly. ProteoPlex (Chari et al., 2015), CPM (Alexandrov et al., 2008; Ashok and Jaakola, 2016), DSF-GFP (Moreau et al., 2012), and MoltenProt (Kotov et al., 2021) can serve the same purpose as thermofluor screening to enhance the sample quality by monitoring the unfolding behavior of a protein. Furthermore, methods have also been developed to facilitate sample optimization, as exemplified by mass photometry (MP) (Sonn-Segev et al., 2020; Olerinyova et al., 2021), size-exclusion chromatography coupled to multi-angle light scattering (SEC-MALS) (Some et al., 2019), and other similar methods.

Macromolecular complex disassembly is another recurrent problem in cryo-sample preparation, particularly in the case of a complex in which the inter-subunit interactions are weak and/or transient. Chemical crosslinking has been used to stabilize protein complex for structural studies (Zhao et al., 2019; Partin et al., 2020), despite that the heterogeneity (subcomplex, aggregation, and unspecific artifacts) could be introduced by direct crosslinking in many cases. GraFix, a combination of gradient centrifugation and crosslinking, can be used to stabilize the protein complexes in a highly homogeneous state suitable for cryo-EM studies by removing the aggregation and undesired subcomplexes

TABLE 1 | Summary of biochemical methods to improve the quality of cryo-specimen.

	Method	Mechanism	Representative research
Condition Screening	Thermal unfolding screening	Improvement of buffer optimization by screening thermal unfolding behavior of proteins	**ThermoFluor**: Assess thermal stability of protein under varying conditions by comparing its melting points in a thermofluor-based high-throughput approach (Ericsson et al., 2006). **DSF-GFP**: Assess GFP-tagged protein stability by using differential scanning fluorimetry (DSF) in a high-throughput way (Moreau et al., 2012). **ProteoPlex**: Optimize stability, homogeneity, and solubility of protein complexes by screening thermal unfolding behavior under variant buffer conditions (Chari et al., 2015); cryo-EM structure of HTT-HAP40 complex at 4 Å (Guo et al., 2018). **CPM**: Assess membrane protein stability by using thiol-specific fluorochrome N-[4-(7-diethylamino-4-methyl-3-coumarinyl)phenyl]maleimide (CPM) (Alexandrov et al., 2008; Ashok and Jaakola, 2016)
	Mass photometry	The light scattering of single molecules is quantified to determine the molecular mass	Evaluate sample homogeneity and complex stability by measuring the molecular mass of the sample (Sonn-Segev et al., 2020; Olerinyova et al., 2021); structural studies of mutant ACE2 and RBD complex (Higuchi et al., 2021)
	SEC-MALS	MALS combined with SEC to characterize sample behavior by measuring molecular mass with a higher accuracy	Facilitate cryo-EM structure determination of NLRP3 at 3.9 Å (Hochheiser et al., 2022)
Stabilization of complex	Chemical crosslinking	Inter cross-links make protein stable	Crosslinking to stabilize complex for structure studies of rhodopsin dimers at 4.7 Å (Zhao et al., 2019) and Drosha-DGCR8–pri-miRNA complex at 3.7 Å (Partin et al., 2020) by using single-particle cryo-EM
	GraFix	Combination of glycerol gradient centrifugation and crosslinking to prevent denaturation and aggregation	GraFix to stabilize complex for cryo-EM studies of MCM double hexamer bound with Dbf4-Cdc7 kinase (Cheng et al., 2022), human spliceosome at 3.7 Å (Zhang et al., 2017), preinitiation complex (Chen et al., 2021), and ALB1 nucleosome at 4.0 Å (Takizawa et al., 2018)
	Crosslinking coupled SEC	SEC combined with crosslinking to increase homogeneity of the sample	Stabilize complex for structural study of β_2V_2R-β-arrestin-1-Fab30 (28.8 Å) (Shukla et al., 2014), RNA polymerase I-Rrn3 (4.8 Å) (Engel et al., 2016), *E. coli* RNAP TEC (4.1 Å), and Nun/TEC (3.07 Å) complexes (Kang et al., 2017)
	AgarFix	Prevent aggregate formation during chemical crosslinking by incorporating the agarose matrix	Stabilize complex of Spt-Ada-Gcn5 acetyltransferase (SAGA) and prevent denaturation and aggregation (Adamus et al., 2019)
	GraDeR	Glycerol gradient centrifugation can remove free detergent monomers and micelles	GraDeR method used to remove extra detergent in sample for structural studies of monomeric PSI at 3.2 Å (Çoruh et al., 2021) and innexin-6 gap junction channel at 3.6 Å (Oshima et al., 2016)
Additives	Detergents	Detergent molecules occupy and change feature of AWI	Adding CHAPSO to remove orientation bias for RNA polymerase at 3.5–4 Å (Chen et al., 2019). Adding CATB to change particles' orientation distribution for HA trimer at 3.3 Å (Li et al., 2021)
Protein modification	Protein PEGylation	Change surface charge of proteins by modifying primary amines with PEG chain	Cryo-EM studies of PEGylation-modified β-amylase at 2.3 Å, ADH at 3.3 Å, and NOD2 at 3.7 Å (Zhang et al., 2021)

(Kastner et al., 2008). Similarly, combinations of chemical crosslinking with other approaches, as with size-exclusion chromatography (Shukla et al., 2014) and AgarFix (an agarose matrix–based method) (Adamus et al., 2019), provide an alternative strategy for improving the cryo-sample quality in the case of large complexes. For membrane proteins and protein complexes, GraDeR, a strategy based on glycerol gradient centrifugation, has been shown to enhance sample homogeneity by efficiently and gently removing excess detergents and micelles (Hauer et al., 2015).

Two other common strategies employed at the sample biochemistry state to improve cryo-sample behavior are the alteration of the solution environment by including additives (Chen et al., 2019; Li et al., 2021) and modification of the target protein itself (Zhang et al., 2021).

In certain cases, adding specific detergents at a low concentration can reduce the particle adsorption on the AWI. As amphipathic molecules, detergents are commonly used during the purification of membrane proteins to protect and stabilize the exposed hydrophobic regions of the proteins by mimicking the environment of the lipid bilayer (Autzen et al., 2019). Moreover, a few detergents, such as CHAPSO, can enhance the quality of cryo-specimens, when included as extra additives. CHAPSO, a zwitterionic detergent, was shown to mitigate the preferred orientation problem in the case of bacterial RNA polymerase (Chen et al., 2019). Moreover, different types of detergents distinctly affect the interactions between proteins and the AWI: whereas cationic and anionic detergents exert little effect, certain nonionic and zwitterionic detergents can keep the protein particles away from the AWI (Li et al., 2021). The potential underlying mechanism here is that nonionic and

zwitterionic detergents (compared to other detergents) occupy the AWI without protein adsorption due to their neutral charge properties, and thus yield more evenly distributed particles in vitreous ice. Intriguingly, adding a very low concentration (0.002–0.005%) of cetyltrimethylammonium bromide (CTAB), a cationic detergent, enabled the high-resolution structure determination of a hemagglutinin (HA) trimer by introducing particles those exhibit side-view features, although the protein particles remained attached to the AWI (Li et al., 2021).

Modification of protein properties, particularly surface properties, might alter protein behavior in vitreous ice. A PEGylation method has been reported to reduce the AWI influence by modifying the exposed primary amines in proteins (Zhang et al., 2021). The PEG chains attached in the PEGylated proteins could form a shielding layer on the surface to keep the protein particles away from the AWI and improve particle behavior in vitreous ice as compared to the behavior of unmodified proteins. Notably, the structures of PEGylated proteins are almost identical to those of their unmodified counterparts. This suggests that PEGylation is a mild modification that barely introduces any artificial features in the structure determination process, as demonstrated in the case of several proteins, such as apoferritin and β-galactosidase (Zhang et al., 2021).

Introducing additives, such as detergents, in the preparation of cryo-specimens is a simple process, much like the conventional protocols. However, our practical experience in cryo-EM sample preparation indicates that distinct proteins respond differently to the inclusion of additives. Thus, identification of potential additives through screening might consume a considerable amount of effort and time, particularly if data collection is required to evaluate the effect of the additives. Furthermore, in the case of several samples, identifying suitable additives and optimal conditions might be extremely challenging, if not impossible. Modification of protein properties, as exemplified by PEGylation, is also a protein-dependent approach, and although a modified protein shares identical structures with the unmodified protein, the possibility that these chemical modifications could generate artificial structures cannot be excluded. Nevertheless, these optimization methods at the protein sample level have provided approaches to enhance the quality of cryo-specimens and are thus suitable for application during sample preparation, particularly considering that the methods involve simple processes.

GRID FABRICATION

Sample solutions must be loaded onto the cryo-grids for vitrification before being transferred to an electron microscope for image acquisition. Cryo-EM grids typically include a metal (copper, gold, nickel, and others) support bearing different amounts of mesh mounted with a holey carbon film featuring distinct patterns of holes to satisfy the requirements of distinct samples (**Figure 1A**). Replacement of the holey carbon film by a highly conductive holey metal film, such as a film of gold (Russo and Passmore, 2014) or amorphous nickel–titanium alloy (ANTA) (Huang et al., 2020), can improve the image quality by reducing beam-induced motion. Moreover, hydrophilic treatment of the cryo-grids through glow discharging or plasma cleaning is critical for carrying the sample solution because the carbon film is a hydrophobic substance (Passmore and Russo, 2016). In the case of samples that are prone to being adsorbed on the carbon film, this can make high-resolution reconstruction challenging due to the collection of an insufficient number of particles. The reasons for protein particles failing to enter holes can be complex, and optimizing the sample itself, such as by increasing the protein concentration, might help in certain cases. Another promising strategy is the modification of cryo-grids by introducing carbon film-like properties in the holes (**Table 2**). Coating the holey carbon grids with a thin layer (2–4 nm) of continuous carbon to eliminate the influence of this adverse adsorption has long been used as a strategy in cryo-EM studies of the ribosome (Grassucci et al., 2007; Bai et al., 2013) and in other cases (Nguyen et al., 2018; Liu et al., 2020; Perederina et al., 2020). Although application of a continuous carbon layer in cryo-grids has enabled the determination of high-resolution structures of several proteins, the thin layer of carbon reduces the signal-to-noise ratio (SNR) of micrographs, leading to a further loss of high-resolution information, particularly for small proteins.

Introduction of graphene and graphene derivatives to modify cryo-grids can address the problem of SNR reduction and is becoming a mainstream strategy in cryo-grid modification (**Table 2**) (Palovcak et al., 2018; Han et al., 2020; Wang and Liu, 2020; Wang and Yu, 2020). Attachment of a continuous monolayer of graphene, invisible in the high-resolution range of cryo-EM due to its conductive property (Naydenova et al., 2019), to a holey carbon foil markedly increased the amount of particles in holes. Furthermore, structure determination of a 52-kDa streptavidin at 2.6 Å also confirmed the suitability of graphene grids for high-resolution cryo-EM analysis of small proteins (Han et al., 2020). As compared with graphene, graphene oxide (GO) is more widely used because of its hydrophilic property and capability of introducing other functional groups, such as covalently linked affinity tags. Such GO-based affinity grids can improve particle distribution and orientation in vitreous ice by keeping the particles away from the AWI through interactions with chemical groups covalently linked to the GO layer (Wang and Liu, 2020; Wang and Yu, 2020). Monolayer graphene grids can also be covalently functionalized by using a plasma surface-modification system with different chemicals, as in the case of the amylamine-functionalized graphene grid (Naydenova et al., 2019).

Other cryo-EM grids modified to serve as the affinity substrate include grids coated with lipid monolayers containing Ni-NTA–functionalized lipids (Kelly et al., 2008; Kelly et al., 2010) and 2D streptavidin crystal films (Wang et al., 2008; Han et al., 2016) (**Table 2**). Recently, a new cryo-grid featuring a support film formed by the 2D crystals of hydrophobin HFBI based on the ANTA foil was developed to facilitate high-quality cryo-sample preparation (**Table 2**) (Fan et al., 2021). The amphipathic HFBIs adhere to the AWI and form a crystalline monolayer film through self-assembly, and this

TABLE 2 | Summary of methods in grid fabrication, device development, and data collection to improve the quality of cryo-specimen.

	Method	Mechanism	Representative Research
Grids fabrication	Carbon film grids	Continuous carbon film attracts proteins	Apply on 80S ribosome at 4.5 Å (Bai et al., 2013), lipid transporter YebT at 3.0 Å (Liu et al., 2020), and RNase MRP holoenzyme at 3.0 Å (Perederina et al., 2020)
	Graphene and graphene oxide grids	Graphene and graphene oxide attract proteins into holes	Graphene grids: streptavidin at 2.6 Å (Han et al., 2020), AcrB embedded in liposomes at 3.9 Å (Yao et al., 2020), and 20S proteasomes at 2.36 Å (Zheng et al., 2020); Graphene Oxide grids: 20S proteasome at 2.5 Å (Palovcak et al., 2018) and separase–securing at 3.8 Å (Boland et al., 2017)
	Affinity tag grids	Chemical groups linked with grid surface can capture proteins	Graphene oxide based grids: TRPA1 at 3.5 Å (Wang and Yu, 2020) and 3.3 Å (Wang and Liu, 2020); Lipid monolayer based grids of 50S ribosomal subunit at 21 Å, 30S ribosomal subunit at 24 Å, 70S ribosome at 28 Å, (Kelly et al., 2008) and RNA polymerase II at 25 Å (Kelly et al., 2010); Streptavidin crystal film based grids of 70S ribosomes at 4.0 Å (Han et al., 2016)
	HFBI film grid	Hydrophilic side of the HFBI film can adsorb proteins	HFBI grids of haemoglobin at 3.60 Å, aldolase at 3.28 Å, HA trimer at 2.56 Å, catalase at 2.29 Å, GDH at 2.26 Å, and apoferritin at 1.96 Å (Fan et al., 2021)
Sample preparation device	Fast vitrification	Reduce dwell time to avoid particles adsorbed to AWI by spraying or printing sample to grids using different ways	Apply Spotiton on HA trimer at 3.77 Å and insulin receptor at 4.93 Å (Noble et al., 2018) and 70S ribosome at 4.75 Å (Dandey et al., 2020); Apply microfluidic device on apoferritin at 2.77 Å (Mäeots et al., 2020) and 3.0 Å (Feng et al., 2017); apply VitroJet on apoferritin at 2.49 Å, GroEL at 2.94 Å, worm hemoglobin at 3.11 Å, and beta-galactosidase at 3.11 Å (Ravelli et al., 2020); apply ultrasonic spray device on 70S ribosome at 3.4 Å (Ashtiani et al., 2018) and apoferritin at 2.6 Å (Rubinstein et al., 2019); apply cryoWriter on urease at 5.03 Å (Arnold et al., 2017)
	Nanofluidic chip	Electron-transparent nanochannels encapsulate sample solution	Apply nanofluidic chip on apoferritin at 2.99 Å, TMV at 3.65 Å, and T20S at 5.42 Å (Huber et al., 2022)
Data collection	Tilting	Obtain more views of particles by collecting data at tilted angles	Addressing the preferred orientation of HA trimer at 4.2 Å (Tan et al., 2017)

effectively sequesters the particles away from the AWI (**Figure 2A**) and thereby eliminates the preferred orientation problem and enables high-resolution structural analysis of small proteins (Fan et al., 2021).

Grids coated with graphene or graphene oxide are applicable to a wide range of macromolecules (Boland et al., 2017; Narayanan et al., 2018; Rapisarda et al., 2019; Yao et al., 2020) with which problems might be encountered in vitrification. The procedure of cryo-sample preparation employing graphene and GO grids as the carrier is as simple as the procedure involving the use of conventional holey grids. Although the fabrication process required for the new method is becoming progressively easier and more widely available than before, additional materials and specific operations are required for the preparation of GO grids (Palovcak et al., 2018; Han et al., 2020). Moreover, variations in the quality of commercially available graphene and GO grids lower the efficiency of grid preparation, and surface contamination of these grids also affects protein behavior after vitrification (Palovcak et al., 2018; Lin et al., 2019). The emergence of HFBI girds points to a new direction in grid modification, although practical application here requires further investigation. Functionalized graphene membrane (FGM) grids have also been reported, wherein the bioactive ligands are linked on the monolayer graphene, and these exhibit affinity for His-tagged proteins and show improved particle distribution (Liu et al., 2019). However, the application of affinity grids currently remains limited due to the requirement of specific binding with a target protein. Although future improvements are necessary, the incorporation of protein purification into cryo-sample preparation by using the affinity grids warrants attention because this can considerably lower the complexity of sample preparation and reduce the time cost. Specifically, affinity grids developed based on graphene and GO films are expected to attract an increased interest in the future (Liu et al., 2019; Wang and Liu, 2020). Realization of grid fabrication and high specificity represent two factors for future improvement in the preparation of affinity grids, and the shelf-life of the affinity grids must also be considered in the optimization process.

SAMPLE PREPARATION DEVICE

The most widely used cryo-EM sample preparation devices for plunge freezing include Vitrobot (Thermo Fisher Scientific), Cryoplunge 3 (Gatan), and EM GP (Leica) (**Table 3**). The cryo-specimen are prepared by pipetting a few microliters of the sample solution on a cryo-grid and incubating for several seconds (or not incubating for an unsupported foil grid) to facilitate particle deposition. Subsequently, the grid is blotted with a filter paper to remove excess solution and then plunge-frozen in liquid ethane cooled by liquid nitrogen. With the use of these conventional devices, the dwell time of the specimen on the

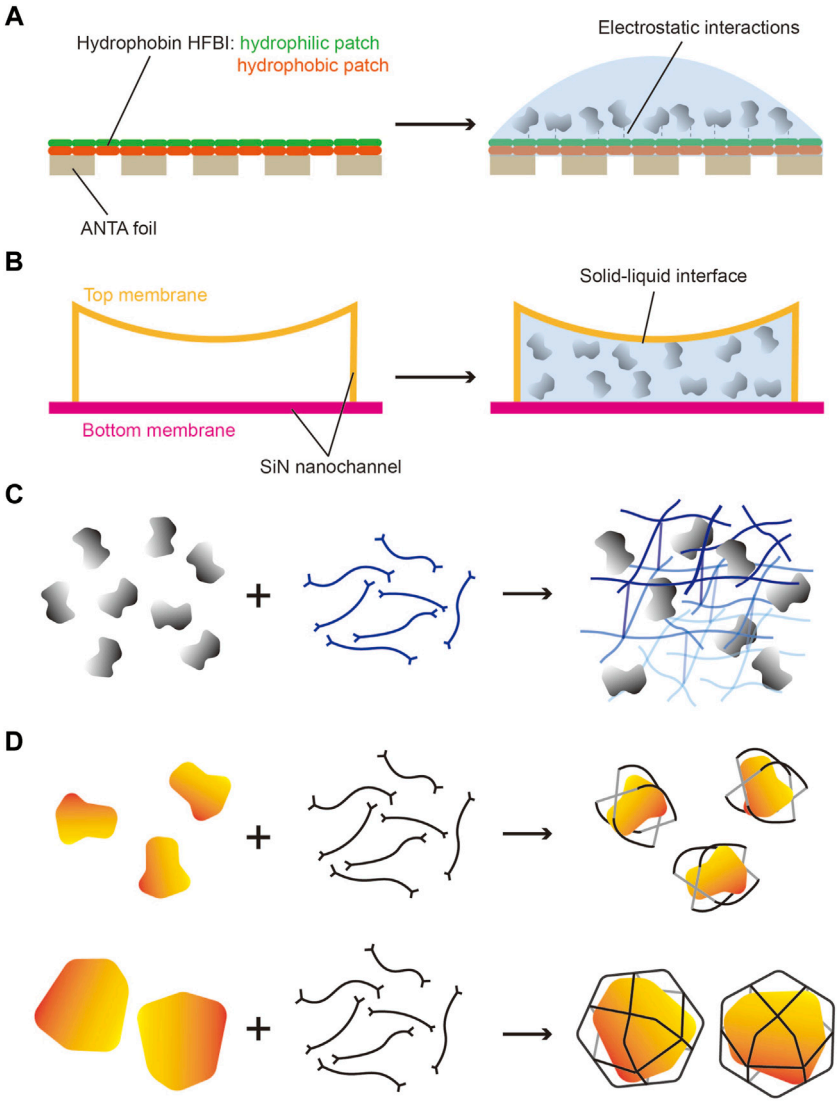

FIGURE 2 | Potential strategies for addressing problems in cryo-sample preparation. **(A)** HFBI grid has a continuous hydrophobin HFBI 2D crystals film on the ANTA foil. The hydrophilic patches of HFBI load sample and adsorb particles by electrostatic interactions to keep particles away from the AWI. **(B)** Nanofluidic cryo-chip has many electron-transparent nanochannels made of SiN_X membrane. The sample solution is applied in closed nanochannels by capillary action without the AWI in vitrification. **(C)** 3D chemical network can be designed to fix particles in different orientations and uniform distribution. **(D)** Some chemical cages can be used to carry protein particles of different sizes to protect particles away from the AWI and provide random orientations.

grids before freezing is at the level of seconds, but this dwell time is adequately long for specimen particles to be adsorbed on the AWI. In order to avoid the AWI interference, various devices have been designed to reduce the time of vitrification to the millisecond level through rapid freezing without blotting, including devices employing inkjet printing (Spotiton) (Jain et al., 2012; Noble et al., 2018; Dandey et al., 2020), gas pressure spray (microfluidic devices) (Feng et al., 2017; Kaledhonkar et al., 2018; Mäeots et al., 2020), ultrasonic spray (Ashtiani et al., 2018; Rubinstein et al., 2019), and electrostatic spray (White et al., 2003). Here, we mainly focus on Spotiton and the microfluidic devices (**Table 2**).

In the Spotiton system, picoliter-sized droplets of the sample solution are sprayed on the grid by using the inkjet mechanism. The total volume (number of droplets) can be accurately dispensed through the piezoelectric inkjet head by applying voltage pulses to control the thickness of ice (Jain et al., 2012). Noble et al. showed that reducing the dwell time (spot-to-plunge time) on the grids to hundreds of milliseconds or even less when using the Spotiton system could substantially decrease the particles' opportunities to be adsorbed on the AWI (Noble et al., 2018). An increase in the non-adsorbed particles in vitreous ice enhanced the particle distribution and alleviated the preferred orientation problem. Dandey *et al.* further

TABLE 3 | Comparison of widely used devices for plunge freezing.

Features	Vitrobot (Thermo Fisher Scientific)	Cryoplunge 3 (Gatan)	EM GP (Leica)
Automaticity	Automatic	Semiautomatic	Automatic
Humidity	Ambient—100%	Ambient—100%	Ambient—99%
Working temperature	4–60°C	4—Ambient	4–60°C
Blot manner	Two side	One or two side	One side +/– the other side
Ice shape (blot angle)	Angular	Straight	Straight
Cryogen temperature monitor	No	Yes	Yes
Multiple loading	No	Yes	Yes
Multiple blotting	Yes	Yes	Yes
Foot pedal	Yes	No	Yes
Blotting force	Yes	Yes (manual)	Yes
Pre-blotting time	Yes	Manual	Yes
Drain time	Yes	No	Yes
Moving apparatus	Ethane container	Safety shield	Chamber
Stereomicroscope	No	No	Yes
LN2 overflow control	No	Yes	Yes
Filter paper	Automatic rotate	Manual rotate	Automatic rotate

pushed the limit of the dwell time to 50 ms for the Spotiton system and enabled time-resolved cryo-EM studies through the capture of intermediate states (Jain et al., 2012; Noble et al., 2018; Dandey et al., 2020). Based on this high-resolution and fast-freezing system, Spotiton has been commercialized in the form of a next-generation device, Chameleon (Darrow et al., 2019). Moreover, the "self-wicking" nanowire grids applied in combination with Spotiton can wick away excess liquid and generate an ice layer of suitable thickness for high-quality image acquisition (Wei et al., 2018).

A microfluidic device designed for time-resolved cryo-EM contains a microfluidic chip for the incubation of reactants, and a nozzle under gas pressure to spray the sample on the grid. The microfluidic time-resolved cryo-EM was used for demonstrating the dynamics of the ribosome complex in bacterial translation initiation, with the resolution at 3.9 Å for the 70S elongation-competent complex (Kaledhonkar et al., 2019). The time of incubation can be tuned from 10 to 1,000 ms to capture the distinct intermediate states by adjusting the length of the channel integrated on the chip (Feng et al., 2017). By using a microfluidic device, the dwell time (spray-to-plunge time) of the sample on the grids can be reduced to as little as 2.5 ms to further restrain particle adsorption on the AWI. A subsequent study further showed that a modular microfluidic system, featuring a dwell time as low as 16 ms and a minimal solution volume of ~20 μl, improved the particle distribution of apoferritin and eliminated the aggregation of the CSN^{5H138A}-SCF-$N8^{Skp2/Cks1}$ complex in the grid hole (Mäeots et al., 2020). Recently, a nanofluidic chip has been reported in preparing the cryo-EM samples with increased reproducibility (Huber et al., 2022). The cryo-chip contains several nanofluidic channels formed by thin silicon-rich nitride (SiN_x) membranes to provide a predefined space to control ice thickness while maintaining electron transparency for cryo-EM imaging (**Figure 2B**). Because the sample solution here is encapsulated in nanochannels by using a microelectromechanical system, the AWI is replaced by a solid–liquid interface, thus providing a new strategy to avoid the influence of the AWI.

Another advantage of the aforementioned printing and spraying sample preparation devices is that the devices can be used in time-resolved cryo-EM studies (Chen and Frank, 2016; Kontziampasis et al., 2019; Dandey et al., 2020; Mäeots et al., 2020). The reaction time can be limited to milliseconds to allow the capture of intermediate states and thus depict the transient biological reaction in high resolution. However, these methods require larger amounts of sample solution at higher concentration than in the case of the blotting method (Klebl et al., 2020), which is not suitable for proteins that cannot be readily purified in a large quantity. Moreover, the extremely short time used for sample incubation on the grid might result in the sample droplet not spreading sufficiently and the particles not being deposited completely on the grid surface. Consequently, generating high-quality ice for data collection is time consuming (Klebl et al., 2020). Furthermore, although the nanofluidic cryo-chip featuring the SiN_x membrane eliminates the AWI problem, the solid–liquid interfaces can also affect the distribution of particles (Huber et al., 2022).

Notably, the design of the nanofluidic system also represents an attempt to automate the cryo-EM workflow and facilitate the sample preparation process (Huber et al., 2022). Whereas automation of the cryo-EM data processing has been widely studied (Li et al., 2020; Maruthi et al., 2020; Stabrin et al., 2020), research on automation of the sample preparation process remains limited. If the distinct procedures involved can be integrated, the efficiency of sample preparation will be improved markedly. The VitroJet device was reported as an integrated system, which is composed of a glow-discharge module, a process chamber, a pin printing system, and a vitrification module. The total time is ~3 min with this automation, which thus serves as a template for the other automation designs (Ravelli et al., 2020).

DATA COLLECTION

In the case of samples that adopt preferred orientations and the problem cannot be alleviated by using the aforementioned strategies focused on the sample preparation stage, an alternative approach could be applied in data collection. To compensate for the information missing due to the adoption of the preferred orientations, the specimen is tilted during data collection. In

practice, the smallest titling angle is selected because large tilting angles cause instability and difficulty in data collection and data processing, respectively. The data collected from the different tilting angles can provide additional views that are missed due to the preferred orientations and thus improve map quality for 3D reconstruction. Tan et al. demonstrated the feasibility of this strategy by determining the structure of HA trimer at near-atomic resolution with less stretching and superior features in the reconstructed map from the dataset of 40°-tilted images (Tan et al., 2017). The generality and practicability of this method were also confirmed in subsequent studies (Davis et al., 2016; Balchin et al., 2018; Scapin et al., 2018).

The tilting method does not alter the sample characteristics and thus represents a sample-independent approach. However, micrographs collected at the titling angle introduce difficulties at the data processing stage. It is crucial to appropriately estimate the focus gradient at distinct tilting angles and apply additional accurate defocusing for individual particles, because tilting can cause variations in defocusing in the same micrograph. The constant tilting of the grid stage could also lead to increased beam-induced motion and loss of high-resolution information (Lyumkis, 2019). Furthermore, ice thickness is also inevitably increased, which lowers image contrast. Although data collection by using the tilting strategy can only solve a specific preferred orientation problem caused by the AWI, if superior algorithms improving the data processing of the tilted data emerge in the future, this method might be more widely applied (than currently) because of its sample-independent property.

DISCUSSION

Cryo-EM has become a mainstream method in structural biology for supporting numerous fundamental studies of various macromolecules. Moreover, in the majority of cases, cryo-EM now provides satisfactory results due to continuous improvements in hardware, such as the upgrading of direct electron detectors, and the application of Volta phase plate (Danev et al., 2014), chromatic aberration corrector (Cc) and other microscope accessories, and the cold field emission gun (CFEG) (Hamaguchi et al., 2019; Kato et al., 2019; Konings and Bischoff, 2020; Nakane et al., 2020), as well as software, such as for automated particle picking (Wang et al., 2016) and preprocessing (Maruthi et al., 2020). Conversely, the sample preparation process is the bottleneck that hinders high-resolution structure determination in several cases. To enhance the quality of cryo-specimens, different stages of cryo-sample preparation can be optimized.

Besides the classical techniques, new methods featuring creative strategies are emerging, such as those employing the HFBI grid (Fan et al., 2021) and the nanofluidic chip (Huber et al., 2022). In these new methods, special materials or unique designs are used to seek breakthroughs against the bottleneck of sample preparation, which is greatly encouraging for the cryo-EM community.

Recent work has also shown that the application of branched polymers in cryo-specimen preparation improves sample behavior in vitreous ice by keeping particles away from the AWI and thus protecting the particles (Xu et al., 2022). Theoretically, introducing a biocompatible network, formed by chemical molecules or proteins, might help avoid recurring problems by trapping proteins in the center layer of vitreous ice and thereby providing more evenly distributed particles (**Figure 2C**). Moreover, surface properties, such as the distribution of charge and hydrophobicity, play key roles in sample behavior in vitrification. Another potential strategy is burying the protein surface by putting the proteins in chemical cages. Chemical cages of different diameters are designed to fit proteins of distinct sizes (**Figure 2D**), and the proteins are enclosed in the cages by adding them during the self-assembly of the chemical cages under mild reaction conditions. The symmetry of these chemical cages offers at least two advantages: one, the carried proteins are randomly distributed in vitreous ice, which eliminates the occurrence of the preferred orientation problem, and two, effects on data processing are limited because the background noise introduced by the chemical cages could be averaged out due to the random distribution related to the density of the carrying protein.

Several chemical gels have already been applied in biological research, such as certain PEG hydrogels used for protein delivery and release (Kim and Cha, 2018; Sharma et al., 2019). Moreover, chemical cages are well studied in the fields of chemistry and synthetic biology (Zhukhovitskiy et al., 2016a; Zhukhovitskiy et al., 2016b; Wang et al., 2017). However, chemical cages are currently assembled under conditions (such as high temperature) that are not friendly to most biological macromolecules. If these hurdles can be overcome in future studies, the application of these networks and chemical cages to cryo-sample preparation will attract increased interest and have the potential to serve as a universal approach.

Lastly, an evaluation system that considers various factors, such as cost, applicability, flexibility, operation complexity, and sample solution requirements, could be established to assess the advantages and disadvantages of distinct modification methods through direct comparison and thus help the users make appropriate choices. We believe that this will benefit several researchers and strongly promote improvements in cryo-EM sample preparation. Given the increasing effort being devoted to the development of new technologies to mitigate recurring problems in the cryo-specimen preparation step, we expect an increase in the number of available methods, providing either alternative approaches or a universal approach, to address common obstacles encountered in cryo-sample preparation for high-resolution structure determination.

AUTHOR CONTRIBUTIONS

All authors listed have made a substantial, direct, and intellectual contribution to the work and approved it for publication.

FUNDING

The research in Dang laboratory is supported by grants from Hong Kong Research Grants Council (ECS26101919, GRF16103321, C7009-20GF, C6001-21 EF), Southern Marine

Science and Engineering Guangdong Laboratory (Guangzhou) (SMSEGL20SC01), Guangdong Natural Science Foundation (GDST21SC04), Shenzhen Science and Technology Innovation Committee (SZ-SZSTI2108), and HKUST start-up and initiation grants.

ACKNOWLEDGMENTS

The authors apologize to colleagues whose important works are not cited here due to space limitations. The authors also thank members of the Dang laboratory for discussion.

REFERENCES

Adamus, K., Le, S. N., Elmlund, H., Boudes, M., and Elmlund, D. (2019). AgarFix: Simple and Accessible Stabilization of Challenging Single-Particle Cryo-EM Specimens through Crosslinking in a Matrix of Agar. *J. Struct. Biol.* 207 (3), 327–331. doi:10.1016/j.jsb.2019.07.004

Alexandrov, A. I., Mileni, M., Chien, E. Y. T., Hanson, M. A., and Stevens, R. C. (2008). Microscale Fluorescent Thermal Stability Assay for Membrane Proteins. *Structure* 16 (3), 351–359. doi:10.1016/j.str.2008.02.004

Arnold, S. A., Albiez, S., Bieri, A., Syntychaki, A., Adaixo, R., McLeod, R. A., et al. (2017). Blotting-free and Lossless Cryo-Electron Microscopy Grid Preparation from Nanoliter-Sized Protein Samples and Single-Cell Extracts. *J. Struct. Biol.* 197 (3), 220–226. doi:10.1016/j.jsb.2016.11.002

Ashok, Y., and Jaakola, V.-P. (2016). Nanodisc-Tm: Rapid Functional Assessment of Nanodisc Reconstituted Membrane Proteins by CPM Assay. *MethodsX* 3, 212–218. doi:10.1016/j.mex.2016.03.009

Ashtiani, D., Venugopal, H., Belousoff, M., Spicer, B., Mak, J., Neild, A., et al. (2018). Delivery of Femtolitre Droplets Using Surface Acoustic Wave Based Atomisation for Cryo-EM Grid Preparation. *J. Struct. Biol.* 203 (2), 94–101. doi:10.1016/j.jsb.2018.03.012

Autzen, H. E., Julius, D., and Cheng, Y. (2019). Membrane Mimetic Systems in CryoEM: Keeping Membrane Proteins in Their Native Environment. *Curr. Opin. Struct. Biol.* 58, 259–268. doi:10.1016/j.sbi.2019.05.022

Bai, X.-c., Fernandez, I. S., McMullan, G., and Scheres, S. H. (2013). Ribosome Structures to Near-Atomic Resolution from Thirty Thousand Cryo-EM Particles. *eLife* 2 (2). doi:10.7554/eLife.00461

Bai, X.-c., McMullan, G., and Scheres, S. H. W. (2015). How Cryo-EM Is Revolutionizing Structural Biology. *Trends Biochem. Sci.* 40, 49–57. doi:10.1016/j.tibs.2014.10.005

Bai, X.-c. (2021). Seeing Atoms by Single-Particle Cryo-EM. *Trends Biochem. Sci.* 46, 253–254. doi:10.1016/j.tibs.2021.01.001

Balchin, D., Miličić, G., Strauss, M., Hayer-Hartl, M., and Hartl, F. U. (2018). Pathway of Actin Folding Directed by the Eukaryotic Chaperonin TRiC. *Cell* 174 (6), 1507–1521. e16. doi:10.1016/j.cell.2018.07.006

Boland, A., Martin, T. G., Zhang, Z., Yang, J., Bai, X.-c., Chang, L., et al. (2017). Cryo-EM Structure of a Metazoan Separase-Securin Complex at Near-Atomic Resolution. *Nat. Struct. Mol. Biol.* 24 (4), 414–418. doi:10.1038/nsmb.3386

Chari, A., Haselbach, D., Kirves, J.-M., Ohmer, J., Paknia, E., Fischer, N., et al. (2015). ProteoPlex: Stability Optimization of Macromolecular Complexes by Sparse-Matrix Screening of Chemical Space. *Nat. Methods* 12 (9), 859–865. doi:10.1038/nmeth.3493

Chen, B., and Frank, J. (2016). Two Promising Future Developments of Cryo-EM: Capturing Short-Lived States and Mapping a Continuum of States of a Macromolecule. *Microsc. Oxf. Engl.* 65, 69–79. doi:10.1093/jmicro/dfv344

Chen, J., Noble, A. J., Kang, J. Y., and Darst, S. A. (2019). Eliminating Effects of Particle Adsorption to the Air/water Interface in Single-Particle Cryo-Electron Microscopy: Bacterial RNA Polymerase and CHAPSO. *J. Struct. Biol. X* 1, 100005. doi:10.1016/j.yjsbx.2019.100005

Chen, X., Qi, Y., Wu, Z., Wang, X., Li, J., Zhao, D., et al. (2021). Structural Insights into Preinitiation Complex Assembly on Core Promoters. *Science* 372 (6541), eaba8490. doi:10.1126/science.aba8490

Cheng, J., Li, N., Huo, Y., Dang, S., Tye, B.-K., Gao, N., et al. (2022). Structural Insight into the MCM Double Hexamer Activation by Dbf4-Cdc7 Kinase. *Nat. Commun.* 13 (1), 1–13. doi:10.1038/s41467-022-29070-5

Cheng, Y., Grigorieff, N., Penczek, P. A., and Walz, T. (2015). A Primer to Single-Particle Cryo-Electron Microscopy. *Cell* 161, 438–449. doi:10.1016/j.cell.2015.03.050

Cheng, Y. (2018). Membrane Protein Structural Biology in the Era of Single Particle Cryo-EM. *Curr. Opin. Struct. Biol.* 52, 58–63. doi:10.1016/J.SBI.2018.08.008

Cheng, Y. (2015). Single-Particle Cryo-EM at Crystallographic Resolution. *Cell* 161 (3), 450–457. doi:10.1016/j.cell.2015.03.049

Cheung, M., Kajimura, N., Makino, F., Ashihara, M., Miyata, T., Kato, T., et al. (2013). A Method to Achieve Homogeneous Dispersion of Large Transmembrane Complexes within the Holes of Carbon Films for Electron Cryomicroscopy. *J. Struct. Biol.* 182 (1), 51–56. doi:10.1016/j.jsb.2013.01.004

Çoruh, O., Frank, A., Tanaka, H., Kawamoto, A., El-Mohsnawy, E., Kato, T., et al. (2021). Cryo-EM Structure of a Functional Monomeric Photosystem I from Thermosynechococcus Elongatus Reveals Red Chlorophyll Cluster. *Commun. Biol.* 4 (1), 1–16. doi:10.1038/s42003-021-01808-9

Dandey, V. P., Budell, W. C., Wei, H., Bobe, D., Maruthi, K., Kopylov, M., et al. (2020). Time-resolved Cryo-EM Using Spotiton. *Nat. Methods* 17 (9), 897–900. doi:10.1038/s41592-020-0925-6

Danev, R., Buijsse, B., Khoshouei, M., Plitzko, J. M., and Baumeister, W. (2014). Volta Potential Phase Plate for In-Focus Phase Contrast Transmission Electron Microscopy. *Proc. Natl. Acad. Sci. U.S.A.* 111 (44), 15635–15640. doi:10.1073/pnas.1418377111

Dang, S., Feng, S., Tien, J., Peters, C. J., Bulkley, D., Lolicato, M., et al. (2017). Cryo-EM Structures of the TMEM16A Calcium-Activated Chloride Channel. *Nature* 552 (7685), 426–429. doi:10.1038/nature25024

Darrow, M. C., Moore, J. P., Walker, R. J., Doering, K., and King, R. S. (2019). Chameleon: Next Generation Sample Preparation for CryoEM Based on Spotiton. *Microsc. Microanal.* 25 (S2), 994–995. doi:10.1017/s1431927619005701

Davis, J. H., Tan, Y. Z., Carragher, B., Potter, C. S., Lyumkis, D., and Williamson, J. R. (2016). Modular Assembly of the Bacterial Large Ribosomal Subunit. *Cell* 167 (6), 1610–1622. e15. doi:10.1016/j.cell.2016.11.020

Drulyte, I., Johnson, R. M., Hesketh, E. L., Hurdiss, D. L., Scarff, C. A., Porav, S. A., et al. (2018). Approaches to Altering Particle Distributions in Cryo-Electron Microscopy Sample Preparation. *Acta Cryst. Sect. D. Struct. Biol.* 74 (6), 560–571. doi:10.1107/S2059798318006496

Egelman, E. H. (2016). The Current Revolution in Cryo-EM. *Biophysical J.* 110 (5), 1008–1012. doi:10.1016/j.bpj.2016.02.001

Engel, C., Plitzko, J., and Cramer, P. (2016). RNA Polymerase I-Rrn3 Complex at 4.8 Å Resolution. *Nat. Commun.* 7 (1), 1–5. doi:10.1038/ncomms12129

Ericsson, U. B., Hallberg, B. M., DeTitta, G. T., Dekker, N., and Nordlund, P. (2006). Thermofluor-based High-Throughput Stability Optimization of Proteins for Structural Studies. *Anal. Biochem.* 357 (2), 289–298. doi:10.1016/j.ab.2006.07.027

Fan, H., Wang, B., Zhang, Y., Zhu, Y., Song, B., Xu, H., et al. (2021). A Cryo-Electron Microscopy Support Film Formed by 2D Crystals of Hydrophobin HFBI. *Nat. Commun.* 12 (1), 1–13. doi:10.1038/s41467-021-27596-8

Feng, S., Dang, S., Han, T. W., Ye, W., Jin, P., Cheng, T., et al. (2019). Cryo-EM Studies of TMEM16F Calcium-Activated Ion Channel Suggest Features Important for Lipid Scrambling. *Cell Rep.* 28 (2), 567–579. e4. doi:10.1016/j.celrep.2019.06.023

Feng, X., Fu, Z., Kaledhonkar, S., Jia, Y., Shah, B., Jin, A., et al. (2017). A Fast and Effective Microfluidic Spraying-Plunging Method for High-Resolution Single-Particle Cryo-EM. *Structure* 25 (4), 663–670. e3. doi:10.1016/j.str.2017.02.005

Glaeser, R. M., Han, B.-G., Csencsits, R., Killilea, A., Pulk, A., and Cate, J. H. D. (2016). Factors that Influence the Formation and Stability of Thin, Cryo-EM Specimens. *Biophysical J.* 110, 749–755. doi:10.1016/j.bpj.2015.07.050

Glaeser, R. M., and Han, B.-G. (2017). Opinion: Hazards Faced by Macromolecules when Confined to Thin Aqueous Films. *Biophys. Rep.* 3 (1–3), 1–7. doi:10.1007/s41048-016-0026-3

Glaeser, R. M. (2018). Proteins, Interfaces, and Cryo-EM Grids. *Curr. Opin. Colloid & Interface Sci.* 34, 1–8. doi:10.1016/j.cocis.2017.12.009

Grant, T., Rohou, A., and Grigorieff, N. (2018). CisTEM, User-Friendly Software for Single-Particle Image Processing. *eLife* 7, e35383. doi:10.7554/eLife.35383

Grassucci, R. A., Taylor, D. J., and Frank, J. (2007). Preparation of Macromolecular Complexes for Cryo-Electron Microscopy. *Nat. Protoc.* 2 (12), 3239–3246. doi:10.1038/nprot.2007.452

Grigorieff, N. (2016). Frealign: An Exploratory Tool for Single-Particle Cryo-EM. *Methods Enzym.* 579, 191–226. doi:10.1016/bs.mie.2016.04.013

Guo, Q., Bin Huang, fnm., Cheng, J., Seefelder, M., Engler, T., Pfeifer, G., et al. (2018). The Cryo-Electron Microscopy Structure of Huntingtin. *Nature* 555 (7694), 117–120. doi:10.1038/nature25502

Hamaguchi, T., Maki-Yonekura, S., Naitow, H., Matsuura, Y., Ishikawa, T., and Yonekura, K. (2019). A New Cryo-EM System for Single Particle Analysis. *J. Struct. Biol.* 207 (1), 40–48. doi:10.1016/j.jsb.2019.04.011

Han, B.-G., Watson, Z., Kang, H., Pulk, A., Downing, K. H., Cate, J., et al. (2016). Long Shelf-Life Streptavidin Support-Films Suitable for Electron Microscopy of Biological Macromolecules. *J. Struct. Biol.* 195 (2), 238–244. doi:10.1016/j.jsb.2016.06.009

Han, L., Qu, Q., Aydin, D., Panova, O., Robertson, M. J., Xu, Y., et al. (2022). Structure and Mechanism of the SGLT Family of Glucose Transporters. *Nature* 601 (7892), 274–279. doi:10.1038/s41586-021-04211-w

Han, Y., Fan, X., Wang, H., Zhao, F., Tully, C. G., Kong, J., et al. (2020). High-yield Monolayer Graphene Grids for Near-Atomic Resolution Cryoelectron Microscopy. *Proc. Natl. Acad. Sci. U.S.A.* 117 (2), 1009–1014. doi:10.1073/pnas.1919114117

Hauer, F., Gerle, C., Fischer, N., Oshima, A., Shinzawa-Itoh, K., Shimada, S., et al. (2015). GraDeR: Membrane Protein Complex Preparation for Single-Particle Cryo-EM. *Structure* 23 (9), 1769–1775. doi:10.1016/j.str.2015.06.029

Higuchi, Y., Suzuki, T., Arimori, T., Ikemura, N., Mihara, E., Kirita, Y., et al. (2021). Engineered ACE2 Receptor Therapy Overcomes Mutational Escape of SARS-CoV-2. *Nat. Commun.* 12 (1), 1–13. doi:10.1038/s41467-021-24013-y

Hochheiser, I. V., Pilsl, M., Hagelueken, G., Moecking, J., Marleaux, M., Brinkschulte, R., et al. (2022). Structure of the NLRP3 Decamer Bound to the Cytokine Release Inhibitor CRID3. *Nature* 604 (7904), 184–189. doi:10.1038/s41586-022-04467-w

Huang, X., Zhang, L., Wen, Z., Chen, H., Li, S., Ji, G., et al. (2020). Amorphous Nickel Titanium Alloy Film: A New Choice for Cryo Electron Microscopy Sample Preparation. *Prog. Biophysics Mol. Biol.* 156, 3–13. doi:10.1016/j.pbiomolbio.2020.07.009

Huber, S. T., Sarajlic, E., Huijink, R., Weis, F., Evers, W. H., and Jakobi, A. J. (2022). Nanofluidic Chips for Cryo-EM Structure Determination from Picoliter Sample Volumes. *eLife* 11. doi:10.7554/eLife.72629

Hurtley, S. M. (2018). Continuing the Resolution Revolution. *Science* 360, 11–282. doi:10.1126/science.360.6386.280-k

Jain, T., Sheehan, P., Crum, J., Carragher, B., and Potter, C. S. (2012). Spotiton: A Prototype for an Integrated Inkjet Dispense and Vitrification System for Cryo-TEM. *J. Struct. Biol.* 179 (1), 68–75. doi:10.1016/j.jsb.2012.04.020

Kaledhonkar, S., Fu, Z., Caban, K., Li, W., Chen, B., Sun, M., et al. (2019). Late Steps in Bacterial Translation Initiation Visualized Using Time-Resolved Cryo-EM. *Nature* 570 (7761), 400–404. doi:10.1038/s41586-019-1249-5

Kaledhonkar, S., Fu, Z., White, H., and Frank, J. (2018). Time-Resolved Cryo-Electron Microscopy Using a Microfluidic Chip. *Methods Mol. Biol.* 1764, 59–71. doi:10.1007/978-1-4939-7759-8_4

Kang, J. Y., Olinares, P. D. B., Chen, J., Campbell, E. A., Mustaev, A., Chait, B. T., et al. (2017). Structural Basis of Transcription Arrest by Coliphage HK022 Nun in an escherichia Coli Rna Polymerase Elongation Complex. *eLife* 6. doi:10.7554/eLife.25478

Kastner, B., Fischer, N., Golas, M. M., Sander, B., Dube, P., Boehringer, D., et al. (2008). GraFix: Sample Preparation for Single-Particle Electron Cryomicroscopy. *Nat. Methods* 5 (1), 53–55. doi:10.1038/nmeth1139

Kato, T., Makino, F., Nakane, T., Terahara, N., Kaneko, T., Shimizu, Y., et al. (2019). CryoTEM with a Cold Field Emission Gun that Moves Structural Biology into a New Stage. *Microsc. Microanal.* 25 (S2), 998–999. doi:10.1017/s1431927619005725

Kelly, D. F., Abeyrathne, P. D., Dukovski, D., and Walz, T. (2008). The Affinity Grid: A Pre-fabricated EM Grid for Monolayer Purification. *J. Mol. Biol.* 382 (2), 423–433. doi:10.1016/j.jmb.2008.07.023

Kelly, D. F., Dukovski, D., and Walz, T. (2010). Strategy for the Use of Affinity Grids to Prepare Non-his-tagged Macromolecular Complexes for Single-Particle Electron Microscopy. *J. Mol. Biol.* 400 (4), 675–681. doi:10.1016/j.jmb.2010.05.045

Kim, M., and Cha, C. (2018). Modulation of Functional Pendant Chains within Poly(ethylene Glycol) Hydrogels for Refined Control of Protein Release. *Sci. Rep.* 8 (1), 1–12. doi:10.1038/s41598-018-22249-1

Klebl, D. P., Gravett, M. S. C., Kontziampasis, D., Wright, D. J., Bon, R. S., Monteiro, D. C. F., et al. (2020). Need for Speed: Examining Protein Behavior during CryoEM Grid Preparation at Different Timescales. *Structure* 28 (0), 1238–1248. doi:10.1016/j.str.2020.07.018

Konings, S., and Bischoff, M. (2020). A Cold Field Emission Gun Optimized for Cryo-EM Applications. *Microsc. Microanal.* 26, 566–567. doi:10.1017/S143192762001510X

Kontziampasis, D., Klebl, D. P., Iadanza, M. G., Scarff, C. A., Kopf, F., Sobott, F., et al. (2019). A Cryo-EM Grid Preparation Device for Time-Resolved Structural Studies. *Int. Union Crystallogr. J.* 6 (6), 1024–1031. doi:10.1107/S2052252519011345

Kotov, V., Mlynek, G., Vesper, O., Pletzer, M., Wald, J., Teixeira-Duarte, C. M., et al. (2021). Indepth Interrogation of Protein Thermal Unfolding Data withMoltenProt. *Protein Sci.* 30 (1), 201–217. doi:10.1002/pro.3986

Li, B., Zhu, D., Shi, H., and Zhang, X. (2021). Effect of Charge on Protein Preferred Orientation at the Air-Water Interface in Cryo-Electron Microscopy. *J. Struct. Biol.* 213 (4), 107783. doi:10.1016/j.jsb.2021.107783

Li, X., Mooney, P., Zheng, S., Booth, C. R., Braunfeld, M. B., Gubbens, S., et al. (2013). Electron Counting and Beam-Induced Motion Correction Enable Near-Atomic-Resolution Single-Particle Cryo-EM. *Nat. Methods* 10 (6), 584–590. doi:10.1038/nmeth.2472

Li, Y., Cash, J. N., Tesmer, J. J. G., and Cianfrocco, M. A. (2020). High-Throughput Cryo-EM Enabled by User-free Preprocessing Routines. *Structure* 28 (7), 858–869. e3. doi:10.1016/j.str.2020.03.008

Liang, S., Thomas, S. E., Chaplin, A. K., Hardwick, S. W., Chirgadze, D. Y., and Blundell, T. L. (2022). Structural Insights into Inhibitor Regulation of the DNA Repair Protein DNA-PKcs. *Nature* 601 (7894), 643–648. doi:10.1038/s41586-021-04274-9

Lin, L., Zhang, J., Su, H., Li, J., Sun, L., Wang, Z., et al. (2019). Towards Super-clean Graphene. *Nat. Commun.* 10 (1), 1–7. doi:10.1038/s41467-019-09565-4

Liu, C., Ma, J., Wang, J., Wang, H., and Zhang, L. (2020). Cryo-EM Structure of a Bacterial Lipid Transporter YebT. *J. Mol. Biol.* 432 (4), 1008–1019. doi:10.1016/j.jmb.2019.12.008

Liu, N., Zhang, J., Chen, Y., Liu, C., Zhang, X., Xu, K., et al. (2019). Bioactive Functionalized Monolayer Graphene for High-Resolution Cryo-Electron Microscopy. *J. Am. Chem. Soc.* 141 (9), 4016–4025. doi:10.1021/jacs.8b13038

Lyumkis, D. (2019). Challenges and Opportunities in Cryo-EM Single-Particle Analysis. *J. Biol. Chem.* 294 (13), 5181–5197. doi:10.1074/jbc.REV118.005602

Mäeots, M.-E., Lee, B., Nans, A., Jeong, S.-G., Esfahani, M. M. N., Ding, S., et al. (2020). Modular Microfluidics Enables Kinetic Insight from Time-Resolved Cryo-EM. *Nat. Commun.* 11 (1), 1–14. doi:10.1038/s41467-020-17230-4

Maruthi, K., Kopylov, M., and Carragher, B. (2020). Automating Decision Making in the Cryo-EM Pre-processing Pipelines. *Structure* 28 (7), 727–729. doi:10.1016/j.str.2020.06.004

McMullan, G., Faruqi, A. R., and Henderson, R. (2016). Direct Electron Detectors. *Methods Enzym.* 2016, 1–17. doi:10.1016/bs.mie.2016.05.056

Moreau, M. J. J., Morin, I., Askin, S. P., Cooper, A., Moreland, N. J., Vasudevan, S. G., et al. (2012). Rapid Determination of Protein Stability and Ligand Binding by Differential Scanning Fluorimetry of GFP-Tagged Proteins. *RSC Adv.* 2 (31), 11892–11900. doi:10.1039/c2ra22368f

Nakane, T., Kotecha, A., Sente, A., McMullan, G., Masiulis, S., Brown, P. M. G. E., et al. (2020). Single-particle Cryo-EM at Atomic Resolution. *Nature* 587 (7832), 152–156. doi:10.1038/s41586-020-2829-0

Narayanan, A., Vago, F. S., Li, K., Qayyum, M. Z., Yernool, D., Jiang, W., et al. (2018). Cryo-EM Structure of *Escherichia coli* σ70 RNA Polymerase and Promoter DNA Complex Revealed a Role of σ Non-conserved Region during the Open Complex Formation. *J. Biol. Chem.* 293 (19), 7367–7375. doi:10.1074/jbc.RA118.002161

Naydenova, K., Peet, M. J., and Russo, C. J. (2019). Multifunctional Graphene Supports for Electron Cryomicroscopy. *Proc. Natl. Acad. Sci. U.S.A.* 116 (24), 11718–11724. doi:10.1073/pnas.1904766116

Nguyen, T. H. D., Tam, J., Wu, R. A., Greber, B. J., Toso, D., Nogales, E., et al. (2018). Cryo-EM Structure of Substrate-Bound Human Telomerase Holoenzyme. *Nature* 557 (7704), 190–195. doi:10.1038/s41586-018-0062-x

Noble, A. J., Wei, H., Dandey, V. P., Zhang, Z., Tan, Y. Z., Potter, C. S., et al. (2018). Reducing Effects of Particle Adsorption to the Air-Water Interface in Cryo-EM. *Nat. Methods* 15 (10), 793–795. doi:10.1038/s41592-018-0139-3

Olerinyova, A., Sonn-Segev, A., Gault, J., Eichmann, C., Schimpf, J., Kopf, A. H., et al. (2021). Mass Photometry of Membrane Proteins. *Chem* 7 (1), 224–236. doi:10.1016/j.chempr.2020.11.011

Oshima, A., Tani, K., and Fujiyoshi, Y. (2016). Atomic Structure of the Innexin-6 Gap Junction Channel Determined by Cryo-EM. *Nat. Commun.* 7 (1), 1–8. doi:10.1038/ncomms13681

Palovcak, E., Wang, F., Zheng, S. Q., Yu, Z., Li, S., Betegon, M., et al. (2018). A Simple and Robust Procedure for Preparing Graphene-Oxide Cryo-EM Grids. *J. Struct. Biol.* 204 (1), 80–84. doi:10.1016/j.jsb.2018.07.007

Partin, A. C., Zhang, K., Jeong, B.-C., Herrell, E., Li, S., Chiu, W., et al. (2020). Cryo-EM Structures of Human Drosha and DGCR8 in Complex with Primary MicroRNA. *Mol. Cell* 78 (3), 411–422. e4. doi:10.1016/j.molcel.2020.02.016

Passmore, L. A., and Russo, C. J. (2016). Specimen Preparation for High-Resolution Cryo-EM. *Methods Enzym.* 579, 51–86. doi:10.1016/bs.mie.2016.04.011

Paulino, C., Kalienkova, V., Lam, A. K. M., Neldner, Y., and Dutzler, R. (2017). Activation Mechanism of the Calcium-Activated Chloride Channel TMEM16A Revealed by Cryo-EM. *Nature* 552, 421–425. doi:10.1038/nature24652

Perederina, A., Li, D., Lee, H., Bator, C., Berezin, I., Hafenstein, S. L., et al. (2020). Cryo-EM Structure of Catalytic Ribonucleoprotein Complex RNase MRP. *Nat. Commun.* 11 (1), 1–10. doi:10.1038/s41467-020-17308-z

Punjani, A., Rubinstein, J. L., Fleet, D. J., and Brubaker, M. A. (2017). CryoSPARC: Algorithms for Rapid Unsupervised Cryo-EM Structure Determination. *Nat. Methods* 14 (3), 290–296. doi:10.1038/nmeth.4169

Rapisarda, C., Cherrak, Y., Kooger, R., Schmidt, V., Pellarin, R., Logger, L., et al. (2019). *In Situ* and High-Resolution Cryo- EM Structure of a Bacterial Type VI Secretion System Membrane Complex. *EMBO J.* 38 (10), e100886. doi:10.15252/embj.2018100886

Ravelli, R. B. G., Nijpels, F. J. T., Henderikx, R. J. M., Weissenberger, G., Thewessem, S., Gijsbers, A., et al. (2020). Cryo-EM Structures from Sub-nl Volumes Using Pin-Printing and Jet Vitrification. *Nat. Commun.* 11 (1), 1–9. doi:10.1038/s41467-020-16392-5

Rubinstein, J. L., Guo, H., Ripstein, Z. A., Haydaroglu, A., Au, A., Yip, C. M., et al. (2019). Shake-it-off: a Simple Ultrasonic Cryo-EM Specimen-Preparation Device. *Acta Cryst. Sect. D. Struct. Biol.* 75 (12), 1063–1070. doi:10.1107/S2059798319014372/IH5001SUP3.MP4

Russo, C. J., and Passmore, L. A. (2014). Ultrastable Gold Substrates for Electron Cryomicroscopy. *Science* 346 (6215), 1377–1380. doi:10.1126/science.1259530

Scapin, G., Dandey, V. P., Zhang, Z., Prosise, W., Hruza, A., Kelly, T., et al. (2018). Structure of the Insulin Receptor-Insulin Complex by Single-Particle Cryo-EM Analysis. *Nature* 556 (7699), 122–125. doi:10.1038/nature26153

Scheres, S. H. W. (2012). RELION: Implementation of a Bayesian Approach to Cryo-EM Structure Determination. *J. Struct. Biol.* 180 (3), 519–530. doi:10.1016/j.jsb.2012.09.006

Sharma, P. K., Halder, M., Srivastava, U., and Singh, Y. (2019). Antibacterial PEG-Chitosan Hydrogels for Controlled Antibiotic/Protein Delivery. *ACS Appl. Bio Mat.* 2 (12), 5313–5322. doi:10.1021/acsabm.9b00570

Shukla, A. K., Westfield, G. H., Xiao, K., Reis, R. I., Huang, L.-Y., Tripathi-Shukla, P., et al. (2014). Visualization of Arrestin Recruitment by a G-Protein-Coupled Receptor. *Nature* 512 (7513), 218–222. doi:10.1038/nature13430

Some, D., Amartely, H., Tsadok, A., and Lebendiker, M. (2019). Characterization of Proteins by Size-Exclusion Chromatography Coupled to Multi-Angle Light Scattering (SEC-MALS). *JoVE* 2019 (148), e59615. doi:10.3791/59615

Sonn-Segev, A., Belacic, K., Bodrug, T., Young, G., VanderLinden, R. T., Schulman, B. A., et al. (2020). Quantifying the Heterogeneity of Macromolecular Machines by Mass Photometry. *Nat. Commun.* 11 (1), 1–10. doi:10.1038/s41467-020-15642-w

Stabrin, M., Schoenfeld, F., Wagner, T., Pospich, S., Gatsogiannis, C., and Raunser, S. (2020). TranSPHIRE: Automated and Feedback-Optimized On-The-Fly Processing for Cryo-EM. *Nat. Commun.* 11 (1), 1–14. doi:10.1038/s41467-020-19513-2

Takizawa, Y., Tanaka, H., Machida, S., Koyama, M., Maehara, K., Ohkawa, Y., et al. (2018). Cryo-EM Structure of the Nucleosome Containing the ALB1 Enhancer DNA Sequence. *Open Biol.* 8 (3), 170255. doi:10.1098/rsob.170255

Tan, Y. Z., Baldwin, P. R., Davis, J. H., Williamson, J. R., Potter, C. S., Carragher, B., et al. (2017). Addressing Preferred Specimen Orientation in Single-Particle Cryo-EM through Tilting. *Nat. Methods* 14 (8), 793–796. doi:10.1038/nmeth.4347

Wang, F., Gong, H., Liu, G., Li, M., Yan, C., Xia, T., et al. (2016). DeepPicker: A Deep Learning Approach for Fully Automated Particle Picking in Cryo-EM. *J. Struct. Biol.* 195 (3), 325–336. doi:10.1016/j.jsb.2016.07.006

Wang, F., Liu, Y., Yu, Z., Li, S., Feng, S., Cheng, Y., et al. (2020). General and Robust Covalently Linked Graphene Oxide Affinity Grids for High-Resolution Cryo-EM. *Proc. Natl. Acad. Sci. U.S.A.* 117 (39), 24269–24273. doi:10.1073/pnas.2009707117

Wang, F., Yu, Z., Betegon, M., Campbell, M. G., Aksel, T., Zhao, J., et al. (2020). Amino and PEG-Amino Graphene Oxide Grids Enrich and Protect Samples for High-Resolution Single Particle Cryo-Electron Microscopy. *J. Struct. Biol.* 209 (2), 107437. doi:10.1016/j.jsb.2019.107437

Wang, L., Ounjai, P., and Sigworth, F. J. (2008). Streptavidin Crystals as Nanostructured Supports and Image-Calibration References for Cryo-EM Data Collection. *J. Struct. Biol.* 164 (2), 190–198. doi:10.1016/j.jsb.2008.07.008

Wang, Y., Gu, Y., Keeler, E. G., Park, J. V., Griffin, R. G., and Johnson, J. A. (2017). Star PolyMOCs with Diverse Structures, Dynamics, and Functions by Three-Component Assembly. *Angew. Chem. - Int. Ed.* 56 (1), 188–192. doi:10.1002/anie.201609261

Wei, H., Dandey, V. P., Zhang, Z., Raczkowski, A., Rice, W. J., Carragher, B., et al. (2018). Optimizing "Self-Wicking" Nanowire Grids. *J. Struct. Biol.* 202 (2), 170–174. doi:10.1016/j.jsb.2018.01.001

Weissenberger, G., Henderikx, R. J. M., and Peters, P. J. (2021). Understanding the Invisible Hands of Sample Preparation for Cryo-EM. *Nat. Methods* 18, 463–471. doi:10.1038/s41592-021-01130-6

White, H. D., Thirumurugan, K., Walker, M. L., and Trinick, J. (2003). A Second Generation Apparatus for Time-Resolved Electron Cryo-Microscopy Using Stepper Motors and Electrospray. *J. Struct. Biol.* 144 (1–2), 246–252. doi:10.1016/j.jsb.2003.09.027

Xu, Y., Wang, L., Qin, Y., Zhang, Y., Wang, Y., and Dang, S. (2022). Application of Metallo-Supramolecular Branched Polymer Improves Particle Distribution and Orientation in Single-Particle Cryo-EM. *BioRxiv*. doi:10.1101/2022.06.08.495397

Yao, X., Fan, X., and Yan, N. (2020). Cryo-EM Analysis of a Membrane Protein Embedded in the Liposome. *Proc. Natl. Acad. Sci. U.S.A.* 117 (31), 18497–18503. doi:10.1073/pnas.2009385117

Yip, K. M., Fischer, N., Paknia, E., Chari, A., and Stark, H. (2020). Atomic-resolution Protein Structure Determination by Cryo-EM. *Nature* 587 (7832), 157–161. doi:10.1038/s41586-020-2833-4

Zhang, K., Pintilie, G. D., Li, S., Schmid, M. F., and Chiu, W. (2020). Resolving Individual Atoms of Protein Complex by Cryo-Electron Microscopy. *Cell Res.* 30, 1136–1139. doi:10.1038/s41422-020-00432-2

Zhang, X., Yan, C., Hang, J., Finci, L. I., Lei, J., and Shi, Y. (2017). An Atomic Structure of the Human Spliceosome. *Cell* 169 (5), 918–929. e14. doi:10.1016/j.cell.2017.04.033

Zhang, Z., Shigematsu, H., Shimizu, T., and Ohto, U. (2021). Improving Particle Quality in Cryo-EM Analysis Using a PEGylation Method. *Structure* 29 (10), 1192–1199. e4. doi:10.1016/j.str.2021.05.004

Zhao, D. Y., Pöge, M., Morizumi, T., Gulati, S., Van Eps, N., Zhang, J., et al. (2019). Cryo-EM Structure of the Native Rhodopsin Dimer in Nanodiscs. *J. Biol. Chem.* 294 (39), 14215–14230. doi:10.1074/jbc.RA119.010089

Zheng, L., Chen, Y., Li, N., Zhang, J., Liu, N., Liu, J., et al. (2020). Robust Ultraclean Atomically Thin Membranes for Atomic-Resolution Electron Microscopy. *Nat. Commun.* 11 (1), 1–8. doi:10.1038/s41467-020-14359-0

Zhu, S., Noviello, C. M., Teng, J., Walsh, R. M., Kim, J. J., and Hibbs, R. E. (2018). Structure of a Human Synaptic GABAA Receptor. *Nature* 559 (7712), 67–72. doi:10.1038/s41586-018-0255-3

Zhukhovitskiy, A. V., Zhao, J., Zhong, M., Keeler, E. G., Alt, E. A., Teichen, P., et al. (2016a). Polymer Structure Dependent Hierarchy in PolyMOC Gels. *Macromolecules* 49 (18), 6896–6902. doi:10.1021/acs.macromol.6b01607

Zhukhovitskiy, A. V., Zhong, M., Keeler, E. G., Michaelis, V. K., Sun, J. E. P., Hore, M. J. A., et al. (2016b). Highly Branched and Loop-Rich Gels via Formation of Metal-Organic Cages Linked by Polymers. *Nat. Chem.* 8 (1), 33–41. doi:10.1038/nchem.2390

Conflict of Interest: The authors declare that the research was conducted in the absence of any commercial or financial relationships that could be construed as a potential conflict of interest.

Publisher's Note: All claims expressed in this article are solely those of the authors and do not necessarily represent those of their affiliated organizations, or those of the publisher, the editors, and the reviewers. Any product that may be evaluated in this article, or claim that may be made by its manufacturer, is not guaranteed or endorsed by the publisher.

frontiers | Frontiers in Molecular Biosciences

ORIGINAL RESEARCH
published: 11 July 2022
doi: 10.3389/fmolb.2022.917725

Cryo-EM Structure of an Atypical Proton-Coupled Peptide Transporter: Di- and Tripeptide Permease C

Maxime Killer[1,2,3], *Giada Finocchio*[1,2], *Haydyn D. T. Mertens*[2], *Dmitri I. Svergun*[2], *Els Pardon*[4,5], *Jan Steyaert*[4,5] *and Christian Löw*[1,2]*

[1]Centre for Structural Systems Biology (CSSB), Hamburg, Germany, [2]Molecular Biology Laboratory (EMBL), Hamburg Unit C/o Deutsches Elektronen Synchrotron (DESY), Hamburg, Germany, [3]Collaboration for Joint PhD Degree Between EMBL and Heidelberg University, Faculty of Biosciences, Heidelberg, Germany, [4]Structural Biology Brussels, Vrije Universiteit Brussel (VUB), Brussels, Belgium, [5]VIB-VUB Center for Structural Biology, VIB, Brussels, Belgium

Proton-coupled Oligopeptide Transporters (POTs) of the Major Facilitator Superfamily (MFS) mediate the uptake of short di- and tripeptides in all phyla of life. POTs are thought to constitute the most promiscuous class of MFS transporters, with the potential to transport more than 8400 unique substrates. Over the past two decades, transport assays and biophysical studies have shown that various orthologues and paralogues display differences in substrate selectivity. The *E. coli* genome codes for four different POTs, known as Di- and tripeptide permeases A-D (DtpA-D). DtpC was shown previously to favor positively charged peptides as substrates. In this study, we describe, how we determined the structure of the 53 kDa DtpC by cryogenic electron microscopy (cryo-EM), and provide structural insights into the ligand specificity of this atypical POT. We collected and analyzed data on the transporter fused to split superfolder GFP (split sfGFP), in complex with a 52 kDa Pro-macrobody and with a 13 kDa nanobody. The latter sample was more stable, rigid and a significant fraction dimeric, allowing us to reconstruct a 3D volume of DtpC at a resolution of 2.7 Å. This work provides a molecular explanation for the selectivity of DtpC, and highlights the value of small and rigid fiducial markers such as nanobodies for structure determination of low molecular weight integral membrane proteins lacking soluble domains.

Keywords: peptide transporter, SLC15, nanobody, Pro-macrobody, single particle cryo-EM, DtpC, YjdL, proton-dependent oligopeptide transporter

OPEN ACCESS

Edited by:
Arjen J. Jakobi, Delft University of Technology, Netherlands

Reviewed by:
Ekaitz Errasti Murugarren, University of Barcelona. Spain
Giorgos Gouridis, Foundation for Research and Technology Hellas (FORTH), Greece

***Correspondence:**
Christian Löw
christian.loew@embl-hamburg.de

Specialty section:
This article was submitted to Structural Biology, a section of the journal Frontiers in Molecular Biosciences

Received: *11 April 2022*
Accepted: *16 June 2022*
Published: *11 July 2022*

Citation:
Killer M, Finocchio G, Mertens HDT, Svergun DI, Pardon E, Steyaert J and Löw C (2022) Cryo-EM Structure of an Atypical Proton-Coupled Peptide Transporter: Di- and Tripeptide Permease C. Front. Mol. Biosci. 9:917725. doi: 10.3389/fmolb.2022.917725

1 INTRODUCTION

Membranes of cells compartmentalize metabolic processes and present a selective barrier for permeation. To preserve the characteristic intracellular milieu, membrane transporters with specialized functions have evolved to maintain the nutrient homeostasis of cells (Hediger et al., 2013; Zhang et al., 2019). Many of those are energized by an electrochemical proton gradient, providing a powerful driving force for transport and accumulation of nutrients above extracellular concentrations. Proton-dependent oligopeptide transporters (POTs) of the Solute Carrier 15 family (SLC15) are representatives of such secondary active transport systems and occur in all living organisms except in Archaea. They allow an efficient uptake of peptides and amino acids in bulk quantities (Daniel et al., 2006; Thwaites and Anderson, 2007). The best characterized members are the two mammalian PepT1 and PepT2 transporters which are known to play crucial roles in human

health, being responsible for the uptake and distribution of nutrients such as di- and tripeptides (Brandsch et al., 2004; Smith et al., 2013; Spanier and Rohm, 2018; Viennois et al., 2018). They also play key roles in human diseases, and impact the pharmacokinetic profiles of orally administered drug molecules (Daniel, 2004; Brandsch, 2009; Ingersoll et al., 2012; Hillgren et al., 2013; Colas et al., 2017; Heinz et al., 2020). SLC15 transporters belong to the Major Facilitator superfamily (MFS). MFS transporters share a well-characterized fold, consisting of twelve transmembrane helices organized in two six-helix bundles, expected to function according to the alternate access mechanisms (Jardetzky, 1966) where either side of the transporter is alternately exposed to one side of the membrane. Therefore, substantial conformational changes are required to complete an entire transport cycle with at least three postulated states: (i) inward-open, (ii) occluded, and (iii) outward-open (Yan, 2015; Drew and Boudker, 2016; Quistgaard et al., 2016; Bartels et al., 2021; Drew et al., 2021). POTs have been intensively studied on a structural and biochemical level over the last 30 years. More than 50 entries for this transporter class can be found in the protein data bank, representing ten different bacterial homologues and the mammalian PepT1 and PepT2 transporters, bound to a limited set of substrates and drugs (Newstead et al., 2011; Solcan et al., 2012; Doki et al., 2013; Guettou et al., 2013; Guettou et al., 2014; Lyons et al., 2014; Zhao et al., 2014; Quistgaard et al., 2017; Martinez Molledo et al., 2018a; Martinez Molledo et al., 2018b; Minhas et al., 2018; Nagamura et al., 2019; Ural-Blimke et al., 2019; Killer et al., 2021; Parker et al., 2021; Shen et al., 2022; Stauffer et al., 2022). Although bacterial and eukaryotic POTs share an overall conserved binding site, individual amino acids changes in or in close vicinity of the binding site are likely responsible for observed differences in affinities and selectivity for particular peptides and drugs among the studied POT homologues. Here, structural biology studies are particularly crucial to understand substrate promiscuity and drug coordination on a molecular level. While bacterial POT structures, determined by mainly X-ray crystallography, represent exclusively the inward-open or inward-open-partially occluded state, the mammalian PepT1 and PepT2 transporters were recently captured in various conformations by single particle cryo-EM, advancing the mechanistic understanding of the entire transport cycle (Killer et al., 2021; Parker et al., 2021). Despite their small size of typically only 50 kDa for an individual transporter unit, these systems become more and more accessible for single-particle cryo-EM approaches. Indeed, in 2021, more MFS transporter structures were determined by single-particle Cryo-EM (17 pdb entries; resolution range 3.0—4.2 Å) than X-ray crystallography (14 pdb entries; resolution range 1.8—3.6 Å).

Although known POT structures show a high level of similarity, various works have indicated that homologues can differ in their range of transported substrate and drug molecules (Lyons et al., 2014; Prabhala et al., 2014; Boggavarapu et al., 2015; Sharma et al., 2016; Martinez Molledo et al., 2018a). The *E. coli* genome codes for four different POTs named Di- and tripeptide permease A-D (DtpA-D), also known as YdgR (=DtpA), YhiP (=DtpB), YjdL (=DtpC) and YbgH (=DtpD). They cluster in pairs, DtpA and B (sequence identity 51%), and DtpC and D (sequence identity 56%) with around 25% identity between them. DtpA and B exhibit a prototypical substrate preference similar to the human PepT1 transporter (Chen et al., 2000; Harder et al., 2008; Foley et al., 2010; Prabhala et al., 2017; Prabhala et al., 2018), while DtpC and D have been classified as atypical POTs, because DtpC prefers dipeptides in particular those with a lysine residue in the second position. Although DtpC has been well characterized in terms of function over the last years (Ernst et al., 2009; Jensen et al., 2012a; Jensen et al., 2012b; Jensen et al., 2012c; Jensen et al., 2014; Prabhala et al., 2014; Aduri et al., 2015), it has resisted structure determination by X-ray crystallography so far (Gabrielsen et al., 2011).

Here we describe the structure determination of the bacterial POT transporter DtpC by single particle cryo-EM. Considering that the transporter displays no characteristic cytoplasmic or periplasmic features which are helpful to drive the particle alignment, we applied different strategies previously described in the literature to increase the overall size of the transporter to overcome these limitations. We i) fused the transporter to split-sfGFP (Liu et al., 2020; Liu et al., 2022), ii) raised different nanobodies against DtpC (Pardon et al., 2014) and iii) extended the nanobody to a Pro-macrobody (Brunner et al., 2020; Botte et al., 2022). The various samples were subsequently imaged by cryo-EM and analysed. DtpC in complex with the conformation specific nanobody 26 turned out to be more rigid and a significant fraction of the sample dimeric, allowing us to reconstruct DtpC to 2.7 Å resolution. The DtpC structure now provides molecular insights into how selectivity within this transporter family is achieved.

2 RESULTS AND DISCUSSION

2.1 Different Fiducial Marker Strategies for Structure Determination

Since MFS transporters typically lack additional domains outside their transport unit, which is a major impediment for accurate particle alignment in single particle cryo-EM approaches, we assessed three fiducial marker strategies introducing additional density outside of detergent micelles containing DtpC, by analyzing the quality of 2D class averages (**Figure 1**). To obtain conformation specific binders against DtpC, we first immunized llamas with recombinant DtpC and selected nanobodies (Nbs) following standard procedures (Pardon et al., 2014). Three out of five selected binders (Nb17, Nb26, and Nb38) co-eluted with DtpC on gel filtration (**Supplementary Figure S1**) and increased the melting temperature of the respective DtpC-Nb complex by 20°C, 16°C, and 12°C. (**Figures 2A,B**). DtpC in complex with Nb17 and Nb26 yielded crystals in various conditions, but despite extensive optimization efforts, the crystals of the DtpC-Nb26 complex did not diffract X-rays better than 5 Å resolution. In a second step, we decided to increase the size of Nb26, which formed a tight complex with DtpC, by fusing one copy of the maltose binding protein (MBP) to its C-terminus as described previously (Botte et al., 2022). This resulted in a

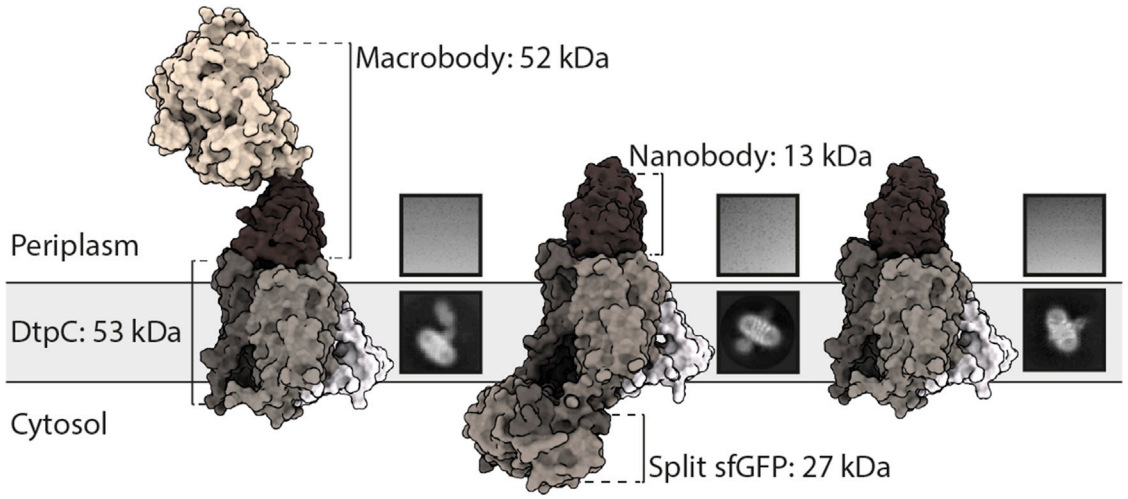

FIGURE 1 | Utilization of different fiducial markers to improve particle alignment and 2D averaging from cryo-EM images. From left to right: DtpC-Mb26, split-sfGFP-DtpC$_{1\text{-}475}$-Nb26, and DtpC-Nb26 were purified, vitrified on grids and imaged. Single particles were identified, clustered and averaged. The best average from each sample is shown under a representative raw micrograph.

52 kDa Pro-macrobody (short Mb26), and we expected it to bind to the periplasmic side of the transporter as seen in other MFS transporter-Nb complexes (**Figure 1**). In a third approach, we fused the two self-assembling parts of split-sfGFP; with β1-6 on the N-terminus of DtpC, and β7-11 on the C-terminus. We named this construct split sfGFP-DtpC$_{FL}$. In order to minimize the mobility between the membrane protein and the split sfGFP fiducial, we also generated two additional constructs where the last five (split sfGFP-DtpC$_{1\text{-}475}$), or ten residues (split sfGFP-DtpC$_{1\text{-}470}$) of the transporter were deleted. We then assessed proper folding and complementation by monitoring the fluorescence of the chromophore on an HPLC system (**Figure 2C**). All constructs eluted at similar retention times and the fluorescence was highest in the non-truncated construct (split sfGFP-DtpC$_{FL}$) and lowest in the most truncated version (split sfGFP-DtpC$_{1\text{-}470}$). In order to extend this observation to other MFS transporters, we repeated this experiment with the human POT homologue PepT1, and noticed a similar trend upon shortening of the termini. Yet, since the decrease of fluorescence was only minor in split sfGFP-DtpC$_{1\text{-}475}$ in comparison to split sfGFP-DtpC$_{FL}$, we proceeded to imaging with the shorter construct in the presence of Nb26.

The particle density and distribution in the vitrified solution was similar in the three imaged samples. However, DtpC-Nb26 produced the best 2D class averages considering the sharpness of secondary structure elements inside the micelle, as judged by visual inspection (**Figure 1**, **Supplementary Figure S2**). The Pro-macrobody Mb26 fiducial was clearly visible in 2D class averages, but it adopted various positions in relation to the transporter, therefore making accurate alignment of the particles more difficult than in its shorter but more rigid and stable nanobody version (**Figure 1**, **Figure 3A, B**, **Supplementary Figure S2**). The split sfGFP-DtpC$_{(1\text{–}475)}$-Nb26 sample allowed clear visualization of the transmembrane helices after clustering a small subset of particles, but the majority of particles clustered in classes with blurry density for the split sfGFP fiducial, or with the two complementary parts β1-6 and β7-11 not assembled (**Supplementary Figure S2**). AlphaFold2 predictions on the imaged construct, as well as on the full length construct later suggested a destabilization of the beta-barrel upon increasing termini restrains, resulting in partial unfolding of β7 and exposure of the chromophore to solvent quenching. Interestingly, this effect could partially be reverted by adding a linker of five glycine residues between the C-bundle and β7 based on *in silico* data. We conclude that termini restraining using the split-sfGFP approach is a promising fiducial strategy for structural studies of MFS transporters, in addition to the previous demonstrated showcases on small membrane proteins (2, 4 and 6TMs) (Liu et al., 2020; Liu et al., 2022). However, the amount of restraining in larger membrane proteins such as MFS transporters where both termini are placed far from each other need to be optimized experimentally or *in silico*, to produce a stable and rigid fiducial; two crucial aspects for high resolution structure determination of MFS transporters by single particle cryo-EM.

As we obtained the best 2D class averages for DtpC with the fiducial marker Nb26, we proceeded to a large data collection (**Table 1**) and could cluster a subset of dimers within this data set (**Figure 3**). The presence of different oligomeric species was already expected based on the peak shape of the gel filtration run (**Figure 4A**). The large mass of the dimer, and the stable and rigid signal of the Nb26 fiducial, allowed us to reconstruct the DtpC-Nb26 dimer to 3.0 Å resolution and model this assembly (**Figures 3**, **4**, **Supplementary Figure S3**). The quaternary structure consists of a non-symmetrical inverted dimer mediated by interactions through a large hydrophobic interface between the HA-HB helices of DtpC (**Supplementary Figure S3**). Although other inverted dimers were reported in

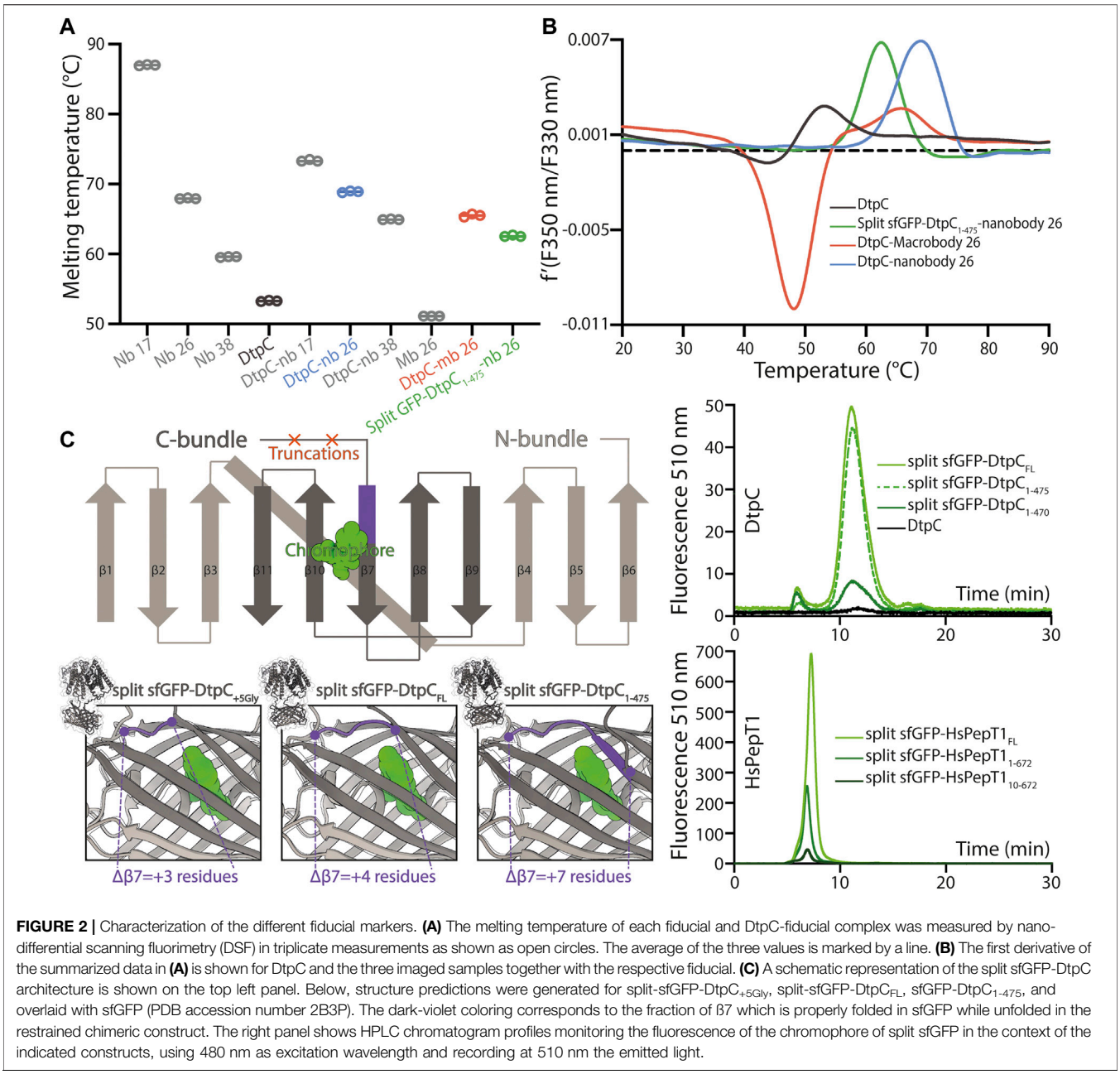

FIGURE 2 | Characterization of the different fiducial markers. **(A)** The melting temperature of each fiducial and DtpC-fiducial complex was measured by nano-differential scanning fluorimetry (DSF) in triplicate measurements as shown as open circles. The average of the three values is marked by a line. **(B)** The first derivative of the summarized data in **(A)** is shown for DtpC and the three imaged samples together with the respective fiducial. **(C)** A schematic representation of the split sfGFP-DtpC architecture is shown on the top left panel. Below, structure predictions were generated for split-sfGFP-DtpC$_{+5Gly}$, split-sfGFP-DtpC$_{FL}$, sfGFP-DtpC$_{1-475}$, and overlaid with sfGFP (PDB accession number 2B3P). The dark-violet coloring corresponds to the fraction of ß7 which is properly folded in sfGFP while unfolded in the restrained chimeric construct. The right panel shows HPLC chromatogram profiles monitoring the fluorescence of the chromophore of split sfGFP in the context of the indicated constructs, using 480 nm as excitation wavelength and recording at 510 nm the emitted light.

homologous POT structures (Quistgaard et al., 2017), the source of such arrangements is likely to be artificial. We also investigated the oligomer heterogeneity in solution with small angle X-ray scattering and obtained a good fit at low angles (corresponding to the overall shape of particles in solution) for the cryo-EM volume of the dimer (**Supplementary Figure S4**). The fit to a monomeric cryo-EM volume was poor, indicating that in detergent solution a significant fraction of DtpC-Nb26 is dimeric. As for the interaction between the membrane protein and the fiducial marker, the CDR3 loop of Nb26 accounts for the strongest interactions with the periplasmic surface of the transporter with two salt bridges, while CDR1 and CDR2 contribute via hydrogen bonding (**Figure 5**). 3D variability analysis (Punjani and Fleet, 2021) revealed a small degree of flexibility between the two DtpC-Nb26 copies. Therefore, we performed a local refinement, focused on one copy of the membrane protein, which extended the resolution of the reconstruction to 2.7 Å and improved the accuracy of the atomic model for subsequent structural analysis (**Figure 4**).

2.3 Structural Basis for Ligand Selectivity in DtpC

The DtpC structure revealed the expected and well-known MFS transporter fold, with twelve transmembrane helices (TMs)

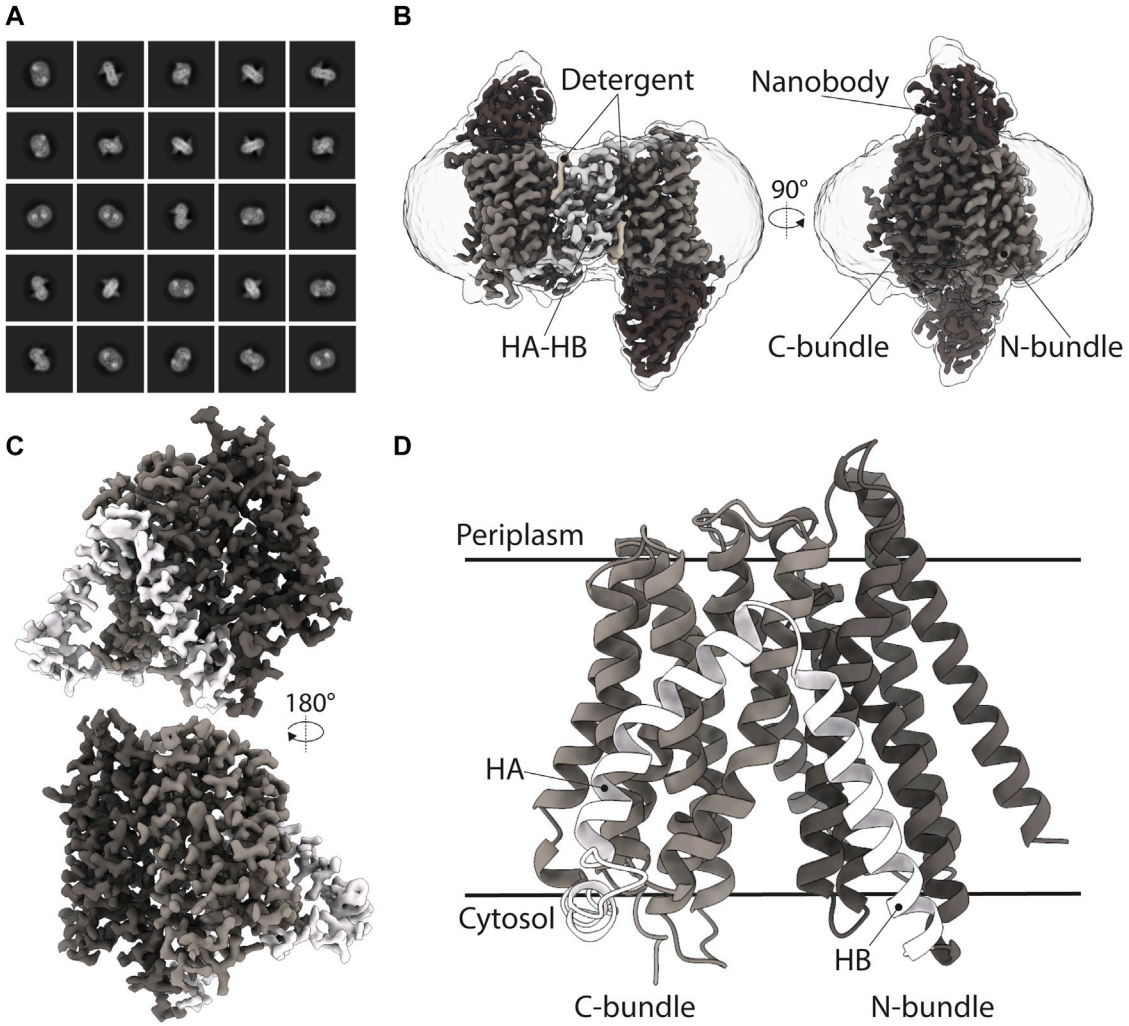

FIGURE 3 | Cryo-EM structure of DtpC-Nb26. **(A)** Representative 2D class averages of the dimeric population. **(B)** 3D reconstruction of the DtpC-Nb26 inverted dimer used for local focused refinement on one copy of the transporter, shown in **(C)**. **(D)** Atomic model of DtpC displayed as ribbon diagram. The different structural elements are labelled.

organized in two helical bundles and additional two TMs specific for the POT family (known as HA and HB domains). It is highly similar compared to the previously determined DtpD structure (Zhao et al., 2014) with an overall RMSD value of 1.06 Å between the two (for 335 out of 436 C_α-atoms). The peptide binding site of DtpC is exposed to the cytoplasmic side (**Figures 3**, **4**). Almost all bacterial POT structures described so far were determined by X-ray methods in a similar inward facing (IF) conformation. The extent to which the central cavity is open to the cytosol is regulated by a mechanism of occlusion mediated by TM4, TM5, TM10, and TM11, as supported by structures in IF occluded, partially occluded, and open states. In the case of the here described DtpC structure, the IF state is open (**Figure 3**).

Molecules from the periplasmic side, on the contrary, cannot enter the central cavity. Tight closure of both bundles above the binding site is mediated by a salt bridge between D43 (TM2, N-bundle) and R294 (TM7, C-bundle) and hydrogen bonds between H37 (TM1, N-bundle) and D293 (TM7) as well as R28 (TM1) and N421 (TM11, C-bundle) (**Figure 6A**). We also analyzed previously determined POT structures with clearly resolved side chain densities, to understand how the IF state is generally maintained in this transporter family. Except for human PepT2 and the POT transporter from *Shewanella oneidensis* ($PepT_{So}$), where the inter-bundle periplasmic salt bridge is formed between TM5 and TM7, the IF state is in all other analyzed structures stabilized by a salt bridge on the tip of TM2 and TM7 (**Figure 6B**). Additional hydrogen bonding networks as described in other studies, can occur, but vary greatly among different homologues. This analysis highlights that the alternate access mechanism in canonical and in so called 'atypical' POTs share similarities such as electrostatic clamping by formation and disruption of salt bridges. The differences in hydrogen bonding patterns however, could account for the various turnover rates seen among POT homologues.

TABLE 1 | Data collection and refinement statistics of the deposited DtpC structure.

Protein Reconstructed	Di- and Tripeptide Permease C (DtpC)
PDB accession code	7ZC2
EMDB accession code	EMD-14618
Data acquisition	
Microscope/Detector	Titan Krios/Gatan K3
Imaging software	EPU
Magnification	105,000
Voltage (kV)	300
Electron exposure (e-/Å^2)	75
Dose rate (e-/pix/s)	19.5
Frame exposure (e-/Å^2)	1.5
Defocus range (μm)	-0.9 to -1.8
Physical pixel size (Å)	0.85
Micrographs	24,333
Reconstruction	
Picked coordinates (cryolo)	6,464,070
Particles in 3D classification (RELION)	6,365,235
Particles in final refinement (CryoSPARC)	878,428
Symmetry imposed	C1
Map sharpening method	Phenix Resolve_cryo_em
Map resolution, $FSC_{half\ maps;\ 0.143}$ masked/unmasked (Å)	2.72/3.43
Refinement	
Initial model used for refinement	AlphaFold2 model, relaxed with Amber
Model resolution (Å)	
FSC 0.143, masked/unmasked	2.64/5.43
Model composition	
Non-hydrogen atoms	7334
Protein residues	471
ADP B factor (Å^2) mean	12.73
R.m.s deviations	
Bond lengths (Å) (#>4σ)	0.003 (0)
Bond angles (°) (#>4σ)	0.616 (0)
Validation	
MolProbity score	1.44
Clashscore	8.04
Rotamer outliers (%)	0.00
Ramachandran plot	
Favored (%)	98.29
Allowed (%)	1.71
Outliers (%)	0.00

Canonical POTs are characterized by i) the presence of the E_1XXE_2R motif on TM1 involved in proton coupling and ligand binding, and ii) the ability to accommodate dipeptides, tripeptides, and peptidomimetics, which relies on a set of conserved residues located in the central binding cavity. In DtpC, the E_1XXE_2R motif, has evolved to Q_1XXE_2Y (where Q_1 = N17, E_2 = E20, Y=Y21). In all high resolution X-ray structures of canonical POTs, R is in salt-bridge distance to E_2 and the C-terminus of substrate peptides. Mutation of either E_1 or E_2 in the conventional E_1XXE_2R motif to glutamine residues abolishes uptake (Aduri et al., 2015). A reverse mutation in DtpC, from Q_1XXE_2Y to E_1XXE_2Y or to E_1XXQ_2Y preserves high transport rates, while a Q_1XXQ_2Y motif significantly decreases it (Aduri et al., 2015). In addition, based on previous molecular dynamics experiments, a salt bridge switching mechanism from R-E_2 to R-E_1, upon protonation of E_2 in the E_1XXE_2R motif, was proposed (Aduri et al., 2015). This biochemical and *in silico* data strongly support a dual role of the E_1XXE_2R motif for both proton and peptide transport, where R can form a salt bridge interaction with the C-terminus of peptides or with E_1 when E_2 is protonated, and where the deprotonation event of the latter is required to disrupt the R-peptide interaction.

In DtpC, we now observe that the side chain pocket has a different architecture and characteristic in comparison with the one of canonical POTs. It displays an overall more acidic groove caused by the presence of the aspartate residue 392, conserved among atypical POTs. This residue has been predicted to be involved in substrate coordination and mutation of this residues in DtpC and homologues DtpD (corresponding residue is D395) abolished transport activity (Jensen et al., 2012b; Zhao et al., 2014). Canonical POTs have a conserved serine residue instead, yielding a slightly changed hydrophobicity pattern in the binding site (**Figures 7A–D**). A structural overlay of DtpC with a canonical POT structure bound to the dipeptide Ala-Phe allows us to position the peptide in the binding site. By replacing the phenyl group with a lysine side chain (generating the known DtpC dipeptide substrate Ala-Lys instead of Ala-Phe), we postulate a putative salt bridge between the carboxyl group of D392 and the ε-amino group of the lysine side chain. This observation, together with previous biochemical work (Jensen et al., 2012b; Aduri et al., 2015) allows us to hypothesize that the selectivity of DtpC for dipeptides with C-terminal lysine or arginine residues is caused by swapping a salt bridge between the recurrent carboxyl group of the peptide terminus and the transporter (R21Y mutation), to a side chain specific salt bridge with D392. Since the R-peptide interaction is lost in DtpC, there is no requirement for E1 to destabilize R-peptide for release, which would explain the presence of a Q_1XXE_2Y motif instead of E_1XXE_2R.

In summary, our work provides new insights into promiscuous versus selective substrate recognition in POTs and constitutes a step forward towards completing the family of *E. coli* POTs structures. Lastly, it displays some of the challenges related to high resolution cryo-EM structure determination of MFS transporters devoid of soluble domains, and manifests once again, the benefit of fiducial markers in overcoming those.

3 MATERIAL AND METHODS

3.1 Expression and purification of membrane protein constructs: DtpC; split sfGFP-DtpC (full length split sfGFP-DtpC$_{FL}$, and truncated constructs split sfGFP-DtpC$_{1-475}$ and split sfGFP-DtpC$_{1-470}$); split sfGFP-*Hs*PepT1 (full length split sfGFP-*Hs*PepT1$_{FL}$, and truncated constructs split sfGFP-*Hs*PepT1$_{1-672}$ and split sfGFP-*Hs*PepT1$_{10-672}$)

The full-length cDNA of DtpC wild type (WT) was amplified from the *Escherichia coli* genome, and cloned into a pNIC-CTHF vector by ligation-independent cloning (LIC). This vector contains a

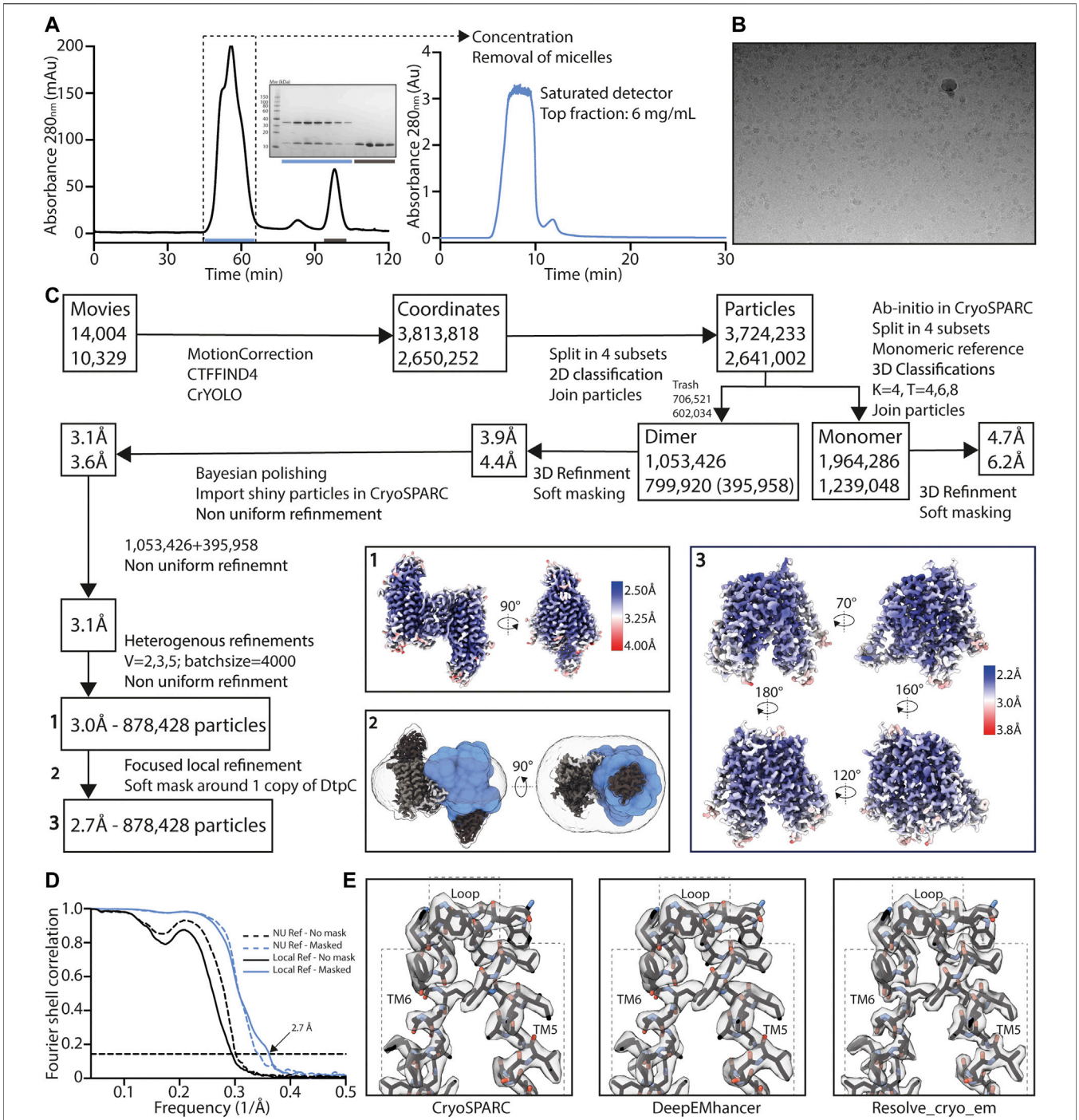

FIGURE 4 | High resolution structure determination of DtpC-Nb26. **(A)** Gel filtration was performed on a preparative column (left) before concentrating the sample to 60 mg/ml and rerunning it on an analytic column on an HPLC system (right), in order to obtain a highly concentrated sample, free of empty detergent micelles. Peak shape already indicates a mixture of different oligomeric species. **(B)** Representative raw micrograph of the acquired dataset. The applied defocus is -1.5 µm. **(C)** Summary of the image analysis. The angular assignments from the dimeric reconstruction were used as prior to perform a local focused refinement with reduced angular and translational searches on the masked region illustrated in blue. **(D)** The Fourier transforms over different shells on frequency space, of two independent volumes (half maps) were compared (FSC) and plotted as a function of spatial frequency, to estimate the overall resolution using the 0.143 cutoff threshold. **(E)** The two half maps were used as inputs to assess various post-processing strategies.

C-terminal His-Tag and a Tobacco Etch virus (TEV) cleavage site and a kanamycin resistance gene as selectable marker. The first 6 N-terminal beta strands of sfGFP were fused to the N-terminus of DtpC, and the beta strands 7 to 11 fused to the C-terminus. We named this construct split sfGFP-DtpC$_{FL}$. Two additional constructs were cloned with truncations of 5 (split sfGFP-

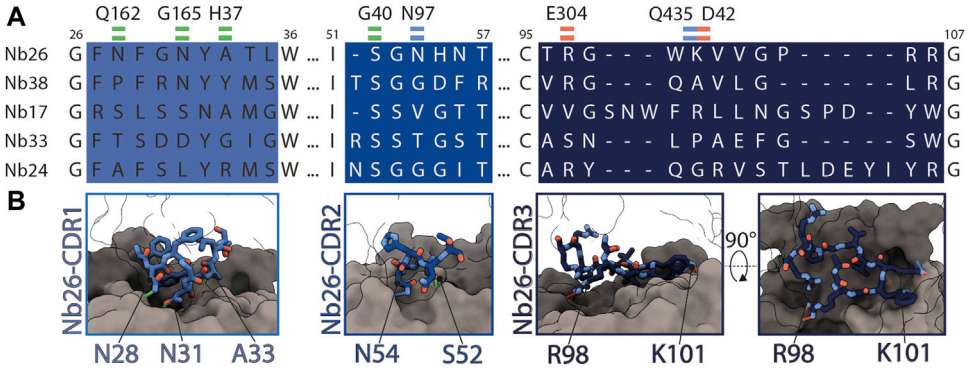

FIGURE 5 | Interactions between Nb26 and DtpC. **(A)** The sequences of the five nanobodies representing five different families, obtained after selection, with their complementary determining regions (CDR) are shown. Interactions of Nb26 with DtpC are highlighted as green (hydrogen bonds involving the protein backbone), blue (hydrogen bonds involving side chains) and red dashes (salt bridges). **(B)** These interactions are further displayed in 3D. CDR regions are depicted as sticks on the surface of DtpC where the N-terminal bundle is colored in grey, and the C-terminal bundle in dark grey.

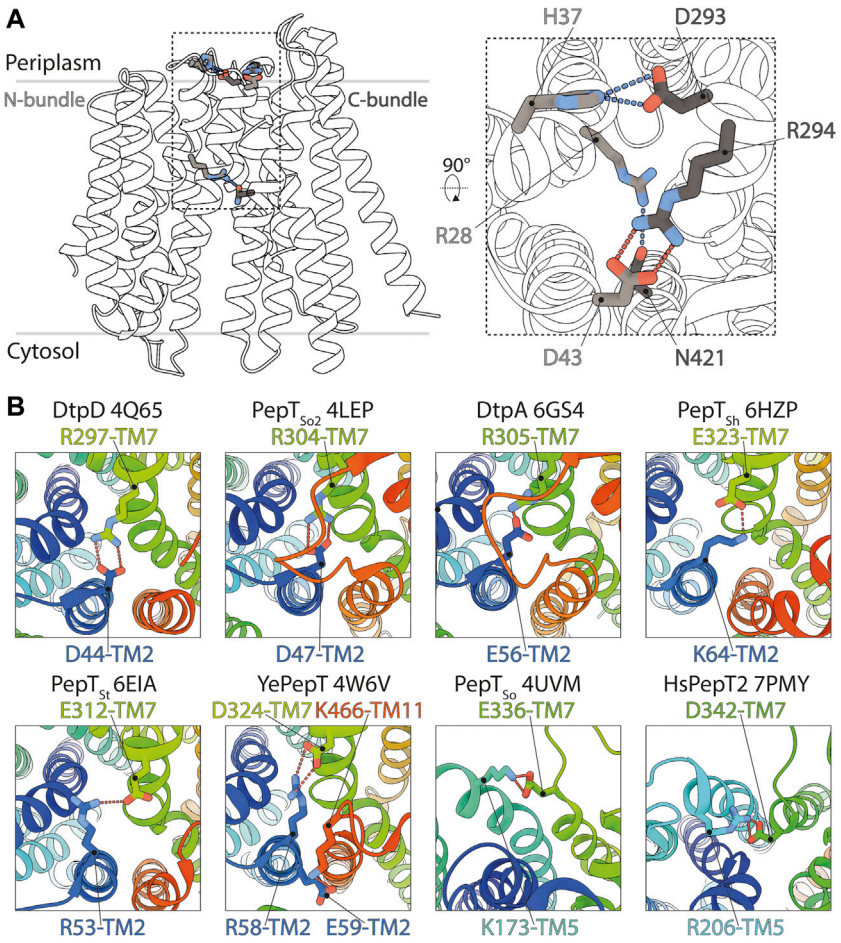

FIGURE 6 | Structural basis for the stabilization of the inward facing state in DtpC and other POT homologues. **(A)** The salt bridge and hydrogen bonds favoring closure of the two bundles on the periplasmic side of DtpC are respectively shown as red and blue dashes. **(B)** The structures of homologous POTs from *Escherichia coli* (DtpD, DtpA), *Shewanella oneidensis* (PepT$_{So2}$, PepT$_{So}$) *Staphylococcus hominis* (PepT$_{Sh}$), *Streptococcus thermophilus* (PepT$_{St}$), *Yersinia enterocolitica* (YePepT) and *Homo sapiens* (HsPepT2), were all previously captured in the IF state. Here they were analyzed to identify the strongest interaction stabilizing their common conformation. The structures are colored from blue to red, from their N- to C-termini, and the respective PDB accession numbers are indicated. Conserved salt bridges are labelled and highlighted by red dashed lines.

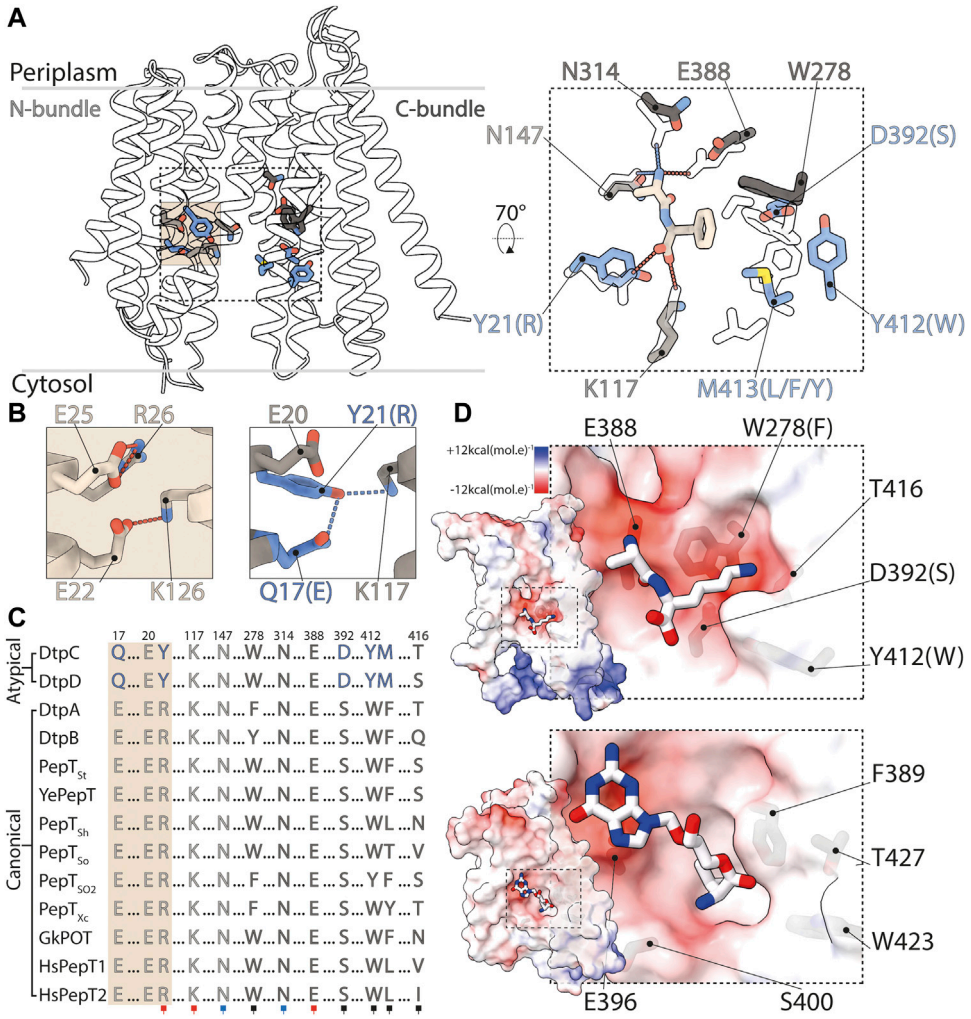

FIGURE 7 | Structural basis for ligand selectivity in DtpC and atypical POTs. **(A)** Key residues involved in substrate binding are colored and shown as sticks. In the close up view, an overlay of HsPepT2 (transparent residues) bound to the dipeptide Ala-Phe (beige) with DtpC is shown. Residues colored in grey are conserved while blue residues are exclusive to atypical POTs. **(B)** The arrangement of the E1XXE2R motif from PepT$_{St}$ is shown on the left panel, and the atypical Q1XXE2Y on the right. **(C)** The sequences of 13 POTs were aligned and residues involved in proton coupling and substrate binding are shown. The red squares mark residues strongly interacting with the charged termini of substrates peptides via salt bridges. The blue squares indicate two conserved asparagine residues stabilizing peptides through hydrogen bonds. The black squares point to residues constituting the side chain pocket of POTs, tuning ligand promiscuity or selectivity. **(D)** Surface representation colored by electrostatic potential, of the C-bundles of DtpC (top panel) and DtpA (bottom panel). A pose of the preferred substrate of DtpC, Ala-Lys, is proposed (top) and the co-crystallized valganciclovir drug hijacking canonical POTs is shown in DtpA (bottom). PDB accession codes of previously published work: HsPepT2 bound to Ala-Phe: 7PMY; PepT$_{St}$: 5OXO; DtpA bound to valganciclovir: 6GS4.

DtpC$_{1\text{-}475}$), and 10 residues (split sfGFP-DtpC$_{1\text{-}470}$), on the C-terminal side of DtpC.

*Hs*PepT1 was previously cloned into a pXLG vector containing an expression cassette composed of an N-terminal Twin-Streptavidin tag followed by the HRV-3C protease recognition sequence (Killer et al., 2021). Similarly, as for DtpC, the two self-assembling parts of split-sfGFP were first inserted into the N- and C-termini of the full-length version of *Hs*PepT1, and on two other versions with i) a C-terminal truncation of 36 residues (split sfGFP-HsPepT11-672), and ii) a C-terminal truncation of 36 residues and a N-terminal truncation of 10 residues (split sfGFP-HsPepT110-672) were cloned.

Recombinant DtpC, and the three split sfGFP-DtpC constructs were expressed in *E. coli* C41(DE3) cells grown in terrific broth (TB) media supplemented with 30 μg/ml kanamycin according to established procedures (Löw et al., 2012; Löw et al., 2013). Cultures were grown at 37°C and protein expression was induced with 0.2 mM IPTG at an $OD_{600\ nm}$ of 0.6–0.8. After induction, culture growth continued at 18°C for 16-18 h. Cells were harvested by centrifugation (10,000 × g, 15 min, 4°C), and the pellet was stored at -20°C until further use. Cell pellets were resuspended in lysis buffer (20 mM NaPi at pH 7.5, 300 mM NaCl, 5% (v/ v) glycerol, 15 mM imidazole, with 3 ml of lysis buffer per Gram of wet weight pellet), supplemented with lysozyme, DNase and 0.5 mM tris(2-carboxyethyl)phosphine (TCEP). The cells were lysed by three cycles using an Avestin Emulsiflex homogenizer at 10,000–15,000 psi. Recovered material

was centrifuged to remove non-lysed cells (10,000 × *g*, 15 min, 4°C) and the supernatant was subjected to ultracentrifugation to separate the membrane fraction (100,000 × *g*, 1 h, 4°C using an Optima XE-90, Beckman Coulter centrifuge). Membranes were resuspended in lysis buffer supplemented with cOmplete EDTA-free protease inhibitors (Roche), and solubilized by adding 1% n-Dodecyl-β-D-Maltoside (DDM) detergent (Anatrace). The sample was centrifuged for 50 min at 90,000 × *g*, and the supernatant was applied to Ni-NTA beads for immobilized-metal affinity chromatography (IMAC) on a gravity column. The beads were pre-equilibrated in lysis buffer and incubated with the solubilized membrane proteins for one hour at 4°C on a rotating wheel. Loaded beads were washed with buffer with increasing imidazole concentrations (20 mM NaPi at pH 7.5, 300 mM NaCl, 5% glycerol, 15-30 mM imidazole, 0.5 mM TCEP, 0.03% DDM). The proteins were eluted from the column with a buffer containing high imidazole concentration (20 mM NaPi at pH 7.5, 150 mM NaCl, 5% glycerol, 250 mM imidazole, 0.5 mM TCEP, 0.03% DDM) and combined with 1 mg of TEV protease to perform the His-tag cleavage during dialysis overnight at 4°C. The dialysis buffer contained 20 mM HEPES at pH 7.5, 150 mM NaCl, 5% glycerol, 0.5 mM TCEP, 0.03% DDM. The cleaved protein was recovered by negative IMAC, concentrated to 4 ml using a 50 kDa concentrator (Corning® Spin-X® UF concentrators) and run on an ÄKTA Pure system (GE Healthcare Life Sciences), using a HiLoad 16/ 600 Superdex 200 column for DtpC, and a Superdex 200 Increase 10/300 column for the split sfGFP-DtpC constructs. Fractions containing the protein were pooled, concentrated, flash frozen and stored at -80°C until further use.

For the split sfGFP-*Hs*PepT1 constructs, expression was done in mammalian cells as described previously (Pieprzyk et al., 2018; Killer et al., 2021). Briefly, HEK293F cells were collected 48 h after transient transfection, and stored at −80°C until further use. Frozen cell pellets were resuspended in 300 mM NaCl, 20 mM NaPi (pH 7.5), 0.5 mM TCEP, and 5% glycerol, supplemented with cOmplete EDTA-free protease inhibitors, and were disrupted using an Avestin Emulsiflex homogenizer at 10,000–15,000 psi. The lysate was centrifuged for 10 min at 10,000 × g, 4°C, and the supernatant was centrifuged for 90 min at 100,000 × g, 4°C. The pellet containing the membrane fraction was solubilized in 1% N-Dodecyl-β-D-Maltopyranoside (DDM) and 0.1% cholesteryl hemisuccinate (CHS; Tris Salt, Anatrace) for 1 h at 4°C. The sample was centrifuged for 50 min at 90,000 × *g*, and the supernatant was applied to Strep-TactinXT beads (IBA). After 20 min of incubation on a rotating wheel, the suspension was transferred to a gravity column. Following two wash steps with 300 mM NaCl, 20 mM HEPES (pH 7.5), 0.03% DDM, and 0.003% CHS, split sfGFP-*Hs*PepT1comnstructs were eluted with 0.03% DDM, 0.003% CHS, 150 mM NaCl, 20 mM HEPES (pH 7.5), and 10 mM desthiobiotin (Sigma-Aldrich).

3.2 Selection, Expression and Purification of Nanobodies Against DtpC

To generate DtpC specific nanobodies, two non-inbred llamas were injected six times at weekly intervals with a mixture of 94 different proteins including DtpC purified in the detergent DDM (50 μg of each antigen weekly). After 6 weeks of immunization, two separate phage display libraries were constructed, one from each animal, in the pMESy2 vector, which is a derivative of pMESy4 that contain a C-terminal EPEA-tag for affinity purification. After pooling both libraries, nanobodies were selected against individual antigens in two rounds of parallel panning in 96-well plates containing one immobilized antigen in each well. After two selection rounds on DtpC, 60 clones were picked for sequence analysis, 13 clones encoded antigen-specific nanobodies as tested in ELISA, grouping them in 5 different sequence families. A nanobody family is defined as a group of nanobodies with a high similarity in their CDR3 sequence (identical length and >80% sequence identity). Nanobodies from the same family derive from the same B-cell lineage and likely bind to the same epitope on the target. Immunizations, library construction, selection by panning and nanobody characterization were performed according to standard procedures (Pardon et al., 2014). Five nanobodies were further characterized.

The nanobodies were expressed in *E. coli* WK6 cells and purified following standard procedures. Specifically, the cell pellet was resuspended in TES buffer (0.2 M TRIS, pH 8, 0.5 mM EDTA, 0.5 M sucrose) supplemented with one protease inhibitor tablet (Roche). Osmotic shock was performed by the addition of diluted TES buffer to release the periplasmic proteins. The solution was first centrifuged for 20 min at 10,000 × *g* and additionally for 30 min at 100,000 × *g*. The supernatant was applied to CaptureSelect beads (Thermo Fisher Scientific), which were equilibrated with wash buffer (20 mM NaPi, pH 7.5, 20 mM NaCl). After three column volumes of washing, the nanobody was eluted with 20 mM HEPES, pH 7.5, 1.5 M $MgCl_2$. The nanobodies were further purified on a HiLoad 16/600 Superdex 75 pg column in 20 mM HEPES, pH 7.5, 150 mM NaCl, 5% glycerol, concentrated with a 5 kDa cut-off concentrator, flash-frozen and stored at -80°C until further use.

3.3 Expression and Purification of Macrobody 26

The nanobody 26 (Nb26) was first inserted into a pBXNPH3 vector containing a C-terminal penta-histidine tag preceded of a HRV-3C protease recognition sequence. The maltose binding protein (MBP) was then inserted in frame with the 3' end of the nanobody, with two proline residues as a linker between the two genes similar as described in (Botte et al., 2021). The resulting Pro-macrobody 26 (Mb26) was expressed in *E. coli* WK6 cells as above. The cell pellet was resuspended in TES buffer (0.2 M TRIS, pH 8, 0.5 mM EDTA, 0.5 M sucrose) supplemented with one protease inhibitor tablet (Roche). Osmotic shock was performed by the addition of diluted TES buffer to release the periplasmic proteins. The solution was first centrifuged for 20 min at 10,000 × *g* and additionally for 30 min at 142,000 × *g*. The supernatant was further purified by immobilized-metal affinity chromatography (IMAC) on a gravity column. The beads were pre-equilibrated in 20 mM NaPi at pH 7.5, 300 mM NaCl, 5% glycerol, 15-30 mM

imidazole, 0.5 mM TCEP and incubated. Loaded beads were washed with increasing imidazole concentrations (20 mM NaPi at pH 7.5, 300 mM NaCl, 5% glycerol, 15-30 mM imidazole, 0.5 mM TCEP, 0.03% DDM). The proteins were eluted from the column with a buffer containing high imidazole concentration (20 mM NaPi at pH 7.5, 150 mM NaCl, 5% glycerol, 250 mM imidazole, 0.5 mM TCEP, 0.03% DDM) and combined with 1 mg of 3C protease to perform the His-tag cleavage. The cleaved protein was recovered by negative IMAC, concentrated to 0.5 ml using a 30 kDa concentrator (Corning® Spin-X® UF concentrators) and run on an ÄKTA Pure system (GE Healthcare Life Sciences), using a Superdex 75 Increase 10/300 column. Fractions containing the protein were pooled, concentrated, flash frozen and stored at -80°C until further use.

3.4 Thermal Stability Measurements

The differential scanning fluorimetry method was used to follow the thermal unfolding event (Kotov et al., 2019) of Nb17, Nb26, Nb38, DtpC, DtpC-Nb17, DtpC-Nb26, DtpC-Nb38, Mb26, DtpC-Mb26, and split sfGFP-DtpC$_{1\text{-}475}$-Nb26 with a Prometheus NT.48 device (NanoTemper Technologies, Munich, Germany). The purified proteins were diluted to 16 μM, and the complexes were formed using a 1:1.5 M ratio of membrane protein: fiducial. The fluorescence at 330 and 350 nm was recorded over a temperature gradient scan from 15° to 95°C and processed in GraphPad Prism 9.0 (GraphPad Software).

3.5 AlphaFold2 Predictions

Structures with the following sequences were used as input for AlphaFold2 structure prediction (Jumper et al., 2021), and AMBER relaxation. The best ranked models were used for visualization.

3.5.1 Split sfGFP-DtpC$_{1\text{-}475}$

MSKGEELFTGVVPILVELDGDVNGHKFSVRGEGEGDATNG
KLTLKFICTTGKLPVPWPTLVTTLTYGVQCFSRYPDHMKR
HDFFKSAMPEGYVQERTISFKDDGTYKTRAEVKFEGDTLV
NRIELKGIDFKEDGNILGHKLEYNKTPSQPRAIYYIVAIQIWE
YFSFYGMRALLILYLTHQLGFDDNHAISLFSAYASLVYVTPI
LGGWLADRLLGNRTAVIAGALLMTLGHVVLGIDTNSTFSL
YLALAIIICGYGLFKSNISCLLGELYDENDHRRDGGFSLLYA
AGNIGSIAAPIACGLAAQWYGWHVGFALAGGGMFIGLLIF
LSGHRHFQSTRSMDKKALTSVKFALPVWSWLVVMLCLA
PVFFTLLLENDWSGYLLAIVCLIAAQIIARMMIKFPEHRRAL
WQIVLLMFVGTLFWVLAQQGGSTISLFIDRFVNRQAFNIEV
PTALFQSVNAIAVMLAGVVLAWLASPESRGNSTLRVWLKF
AFGLLLMACGFMLLAFDARHAAADGQASMGVMISGLAL
MGFAELFIDPVAIAQITRLKMSGVLTGIYMLATGAVANW
LAGVVAQQTTESQISGMAIAAYQRFFSQMGEWTLACVAI
IVVLAFATRFLFSTPNSHNVYITADKQKNGIKANFKIRHNV
EDGSVQLADHYQQNTPIGDGPVLLPDNHYLSTQSVLSKD
PNEKRDHMVLLEFVTAAGITHGMDELYK.

3.5.2 Split sfGFP-DtpC$_{FL}$

MSKGEELFTGVVPILVELDGDVNGHKFSVRGEGEGDATN
GKLTLKFICTTGKLPVPWPTLVTTLTYGVQCFSRYPDHMK
RHDFFKSAMPEGYVQERTISFKDDGTYKTRAEVKFEGDT
LVNRIELKGIDFKEDGNILGHKLEYNKTPSQPRAIYYIVAIQ
IWEYFSFYGMRALLILYLTHQLGFDDNHAISLFSAYASLVY
VTPILGGWLADRLLGNRTAVIAGALLMTLGHVVLGIDTNS
TFSLYLALAIIICGYGLFKSNISCLLGELYDENDHRRDGGFS
LLYAAGNIGSIAAPIACGLAAQWYGWHVGFALAGGGMFIG
LLIFLSGHRHFQSTRSMDKKALTSVKFALPVWSWLVVML
CLAPVFFTLLLENDWSGYLLAIVCLIAAQIIARMMIKFPEHR
RALWQIVLLMFVGTLFWVLAQQGGSTISLFIDRFVNRQAF
NIEVPTALFQSVNAIAVMLAGVVLAWLASPESRGNSTLR
VWLKFAFGLLLMACGFMLLAFDARHAAADGQASMGVMI
SGLALMGFAELFIDPVAIAQITRLKMSGVLTGIYMLATGAV
ANWLAGVVAQQTTESQISGMAIAAYQRFFSQMGEWTL
ACVAIIVVLAFATRFLFSTPTNMIQESNDNSHNVYITADKQ
KNGIKANFKIRHNVEDGSVQLADHYQQNTPIGDGPVLLP
DNHYLSTQSVLSKDPNEKRDHMVLLEFVTAAGITHGMDE
LYK.

3.5.3 Split sfGFP-DtpC$_{+5Gly}$

MSKGEELFTGVVPILVELDGDVNGHKFSVRGEGEGDATN
GKLTLKFICTTGKLPVPWPTLVTTLTYGVQCFSRYPDHMK
RHDFFKSAMPEGYVQERTISFKDDGTYKTRAEVKFEGDT
LVNRIELKGIDFKEDGNILGHKLEYNKTPSQPRAIYYIVAIQI
WEYFSFYGMRALLILYLTHQLGFDDNHAISLFSAYASLVYV
TPILGGWLADRLLGNRTAVIAGALLMTLGHVVLGIDTNST
FSLYLALAIIICGYGLFKSNISCLLGELYDENDHRRDGGFSLL
YAAGNIGSIAAPIACGLAAQWYGWHVGFALAGGGMFIGLL
IFLSGHRHFQSTRSMDKKALTSVKFALPVWSWLVVMLC
LAPVFFTLLLENDWSGYLLAIVCLIAAQIIARMMIKFPEHRR
ALWQIVLLMFVGTLFWVLAQQGGSTISLFIDRFVNRQA
FNIEVPTALFQSVNAIAVMLAGVVLAWLASPESRGNSTLR
VWLKFAFGLLLMACGFMLLAFDARHAAADGQASMGVMI
SGLALMGFAELFIDPVAIAQITRLKMSGVLTGIYMLATGAV
ANWLAGVVAQQTTESQISGMAIAAYQRFFSQMGEWTL
ACVAIIVVLAFATRFLFSTPTNMIQESNDGGGGGNSHNVY
ITADKQKNGIKANFKIRHNVEDGSVQLADHYQQNTPIGDG
PVLLPDNHYLSTQSVLSKDPNEKRDHMVLLEFVTAAGITH
GMDELYK.

3.6 Cryo-EM Sample Preparation, Data Collection, Image Analysis, and Atomic Modelling

One hour before vitrification, the purified protein complexes were thawed on ice and run on a Superdex Increase 200 5/150 column in 0.015% DDM, 100 mM NaCl, 10 mM HEPES (pH 7.5), 0.5 mM TCEP in order to remove the excess of empty detergent micelles earlier generated upon sample concentration. The top fraction reached a concentration ranging between 3 and 6 mg/ml, and for each sample, 3.6 μl were applied to glow-discharged gold holey carbon 2/1 300-mesh grids (Quantifoil). Grids were blotted for 4 s at 0 force and 1-s wait time before being vitrified in liquid propane using a Mark IV Vitrobot (Thermo Fisher Scientific). The blotting chamber was maintained at 4°C and 100% humidity during freezing.

All movies were collected using a Titan Krios (Thermo Fisher Scientific) outfitted with a K3 camera and BioQuantum energy

filter (Gatan) set to 10 eV. Automated data acquisitions were set using EPU (Thermo Fisher Scientific). The applied defocus ranged between -0.9 µm and -1.8 µm in all datasets.

For DtpC-Nb26 and DtpC-Mb26, movies were collected at a nominal magnification of ×105,000 and a physical pixel size of 0.85 Å, with a 70-µm C2 aperture and 100-µm objective aperture at a dose rate of 19.5 e−/pixel per second. A total dose of 75 e−/Å^2 was used with 2.8 s exposure time, fractionated in 50 frames. For split sfGFP-DtpC$_{1\text{-}475}$-Nb26, movies were collected at a nominal magnification of ×,130,000 and a physical pixel size of 0.67 Å, with a 50-µm C2 aperture and 100-µm objective aperture at a dose rate of 19.0 e−/pixel per second. A total dose of 57 e−/Å^2 was used with 3 s exposure time fractionated in 40 frames.

All movies were motion-corrected using Relion-3.1 (Scheres, 2012; Zivanov et al., 2018) own implementation of MotionCor2 (Zheng et al., 2017). Contrast transfer function parameters were calculated using CTFFIND4 (Rohou and Grigorieff, 2015) and putative particle coordinates were initially defined using CrYOLO (Wagner et al., 2019).

For DtpC-Mb26, 13,257 movies were collected, 3,062,337 coordinates were picked and used for 2D averaging and clustering. For split sfGFP-DtpC$_{1\text{-}475}$-Nb26, 7602 movies were collected, 1,049,399 coordinates were picked and used for 2D averaging and clustering. For DtpC-Nb26, 24,333 movies were collected, 6,464,070 coordinates were picked and used for 2D averaging and clustering, and 878,428 particles were used in the final 3D reconstruction. Briefly, DtpC-Nb26 dimeric population was clustered using 3D class averaging in Relion3.1 (Scheres, 2012). Particle trajectories and cumulative beam damage were further corrected by Bayesian polishing in Relion3.1 (Zivanov et al., 2019), and the resulting shiny particles were exported to cryoSPARCv3 (Punjani et al., 2017) for further 3D clustering via successive heterogeneous refinement cycles using "bad" and "good" volumes as references to denoise the dataset. Non uniform refinement (Punjani et al., 2020), followed by a local refinement using a soft mask around one transporter unit resulted in a 2.7 Å reconstruction of DtpC. The overall resolution was estimated in CryoSPARCv3 using the FSC = 0.143 cutoff. Local resolution estimations were also calculated in CryoSPARCv3 using the 0.5 FSC cutoff. The two half maps were used as inputs to assess various post-processing strategies such as the CryoSPARC's sharpening tool, DeepEMhancer (Sanchez-Garcia et al., 2021), and Resolve_cryo-em (Terwilliger et al., 2020). The latter led to a slightly better defined contour of the atoms, and was subsequently used for the last atomic-model refinement of DtpC. The initial models of DtpC and Nb26 were generated using AlphaFold2, and refined against the experimental maps; first in Isolde (Croll, 2018), and last in Phenix (Afonine et al., 2018), principally to refine atomic displacement parameters (B-factors) and perform a slight energy minimization while keeping restrains from Isolde's reference model. Half-maps, and postprocessed maps of the dimeric arrangement and of the focused refinement, as well as the atomic model of DtpC were deposited in the PDB and EMDB as deposition numbers 7ZC2, and EMD-14618. The atomic model of the dimeric DtpC-Nb26 is available upon request.

3.7 Small-Angle X-Ray Scattering Data Collection and Analysis

Synchrotron SAXS data from solutions of DtpC-Nb26 in β-DDM micelles (SEC-SAXS) were collected on the EMBL P12 (Blanchet et al., 2015) beamline at the PETRA III storage ring (Hamburg, Germany), in a buffer consisting of 0.015% DDM, 100 mM NaCl, 10 mM HEPES (pH 7.5), and 0.5 mM TCEP. Sample (10 mg/ml) was injected onto a Superdex Increase 200 10/300 column (Cytiva) and run at 0.5 ml/min at 20°C. 3000 successive 1 s frames were collected using a Pilatus 2M detector at a sample-detector distance of 3.1 m and at a wavelength of $\lambda = 0.124$ nm (I(s) vs. s, where $s = 4\pi\sin\theta/\lambda$, and 2θ is the scattering angle). The data were normalized to the intensity of the transmitted beam and radially averaged; the scattering of the solvent-blank was subtracted using CHROMIXS (Panjkovich and Svergun, 2018). Cryo-EM volume maps of DtpC-Nb26 were fit to the scattering data across the low-angle range (shape region only) using EM2DAM (Franke et al., 2017) at a density threshold of 0.1.

3.8 Data Visualization

Graphs were generated using GraphPad Prism 9.0 (GraphPad Software). Molecular graphics and analyses performed with UCSF ChimeraX-1.2.5 (Pettersen et al., 2021). Figures were prepared in Adobe Illustrator 2021.

DATA AVAILABILITY STATEMENT

The datasets presented in this study can be found in online repositories. The names of the repository/repositories and accession number(s) can be found below: http://www.wwpdb.org/, 7ZC2 https://www.ebi.ac.uk/pdbe/emdb/, EMD-14618.

AUTHOR CONTRIBUTIONS

Conceptualization: MK, CL. Methodology: MK, GF, HM, EP. Investigation: MK, GF, HM, EP. Visualization: MK, HM. Funding acquisition: DS, JS, CL. Project administration: CL. Supervision: DS, JS, CL. Writing—original draft: MK, CL. Writing—review and editing: MK, GF, HM, DS, EP, JS, CL.

FUNDING

This work was supported by a grant from the BMBF (grant number: 05K18YEA). Part of this work was performed at the CryoEM Facility at CSSB, supported by the UHH and DFG grant numbers (INST 152/772–1|152/774–1|152/775–1|152/776–1|152/777–1 FUGG).

ACKNOWLEDGMENTS

We thank the Sample Preparation and Characterization facility of EMBL Hamburg for support in this project and the beamlines P13 and P14 at EMBL Hamburg for regular access. We acknowledge Instruct-ERIC and the FWO for their support to the Nb discovery and Saif Saifuzzaman for the technical assistance during Nb discovery. All past and current group members are acknowledged for their input to this manuscript and their efforts to crystallize DtpC over the years.

SUPPLEMENTARY MATERIAL

The Supplementary Material for this article can be found online at: https://www.frontiersin.org/articles/10.3389/fmolb.2022.917725/full#supplementary-material

REFERENCES

Aduri, N. G., Prabhala, B. K., Ernst, H. A., Jørgensen, F. S., Olsen, L., and Mirza, O. (2015). Salt Bridge Swapping in the EXXERFXYY Motif of Proton-Coupled Oligopeptide Transporters. *J. Biol. Chem.* 290, 29931–29940. doi:10.1074/jbc.M115.675603

Afonine, P. V., Poon, B. K., Read, R. J., Sobolev, O. V., Terwilliger, T. C., Urzhumtsev, A., et al. (2018). Real-space Refinement inPHENIXfor Cryo-EM and Crystallography. *Acta Cryst. Sect. D. Struct. Biol.* 74, 531–544. doi:10.1107/S2059798318006551

Bartels, K., Lasitza-Male, T., Hofmann, H., and Löw, C. (2021). Single-Molecule FRET of Membrane Transport Proteins. *Chembiochem* 22, 2657–2671. doi:10.1002/cbic.202100106

Blanchet, C. E., Spilotros, A., Schwemmer, F., Graewert, M. A., Kikhney, A., Jeffries, C. M., et al. (2015). Versatile Sample Environments and Automation for Biological Solution X-Ray Scattering Experiments at the P12 Beamline (PETRA III, DESY). *J. Appl. Cryst.* 48, 431–443. doi:10.1107/S160057671500254X

Boggavarapu, R., Jeckelmann, J.-M., Harder, D., Ucurum, Z., and Fotiadis, D. (2015). Role of Electrostatic Interactions for Ligand Recognition and Specificity of Peptide Transporters. *BMC Biol.* 13, 58. doi:10.1186/s12915-015-0167-8

Botte, M., Ni, D., Schenck, S., Zimmermann, I., Chami, M., Bocquet, N., et al. (2022). Cryo-EM Structures of a LptDE Transporter in Complex with Pro-macrobodies Offer Insight into Lipopolysaccharide Translocation. *Nat. Commun.* 13, 1826. doi:10.1038/s41467-022-29459-2

Brandsch, M., Knütter, I., and Leibach, F. H. (2004). The Intestinal H+/peptide Symporter PEPT1: Structure-Affinity Relationships. *Eur. J. Pharm. Sci.* 21, 53–60. doi:10.1016/s0928-0987(03)00142-8

Brandsch, M. (2009). Transport of Drugs by Proton-Coupled Peptide Transporters: Pearls and Pitfalls. *Expert Opin. Drug Metabolism Toxicol.* 5, 887–905. doi:10.1517/17425250903042292

Brunner, J. D., Jakob, R. P., Schulze, T., Neldner, Y., Moroni, A., Thiel, G., et al. (2020). Structural Basis for Ion Selectivity in TMEM175 K+ Channels. *Elife* 9, e53683. doi:10.7554/eLife.53683

Chen, X.-Z., Steel, A., and Hediger, M. A. (2000). Functional Roles of Histidine and Tyrosine Residues in the H^+-Peptide Transporter PepT1. *Biochem. Biophysical Res. Commun.* 272, 726–730. doi:10.1006/bbrc.2000.2851

Colas, C., Masuda, M., Sugio, K., Miyauchi, S., Hu, Y., Smith, D. E., et al. (2017). Chemical Modulation of the Human Oligopeptide Transporter 1, hPepT1. *Mol. Pharm.* 14, 4685–4693. doi:10.1021/acs.molpharmaceut.7b00775

Croll, T. I. (2018). ISOLDE: a Physically Realistic Environment for Model Building into Low-Resolution Electron-Density Maps. *Acta Cryst. Sect. D. Struct. Biol.* 74, 519–530. doi:10.1107/S2059798318002425

Daniel, H. (2004). Molecular and Integrative Physiology of Intestinal Peptide Transport. *Annu. Rev. Physiol.* 66, 361–384. doi:10.1146/annurev.physiol.66.032102.144149

Daniel, H., Spanier, B., Kottra, G., and Weitz, D. (2006). From Bacteria to Man: Archaic Proton-dependent Peptide Transporters at Work. *Physiology* 21, 93–102. doi:10.1152/physiol.00054.2005

Doki, S., Kato, H. E., Solcan, N., Iwaki, M., Koyama, M., Hattori, M., et al. (2013). Structural Basis for Dynamic Mechanism of Proton-Coupled Symport by the Peptide Transporter POT. *Proc. Natl. Acad. Sci. U.S.A.* 110, 11343–11348. doi:10.1073/pnas.1301079110

Drew, D., and Boudker, O. (2016). Shared Molecular Mechanisms of Membrane Transporters. *Annu. Rev. Biochem.* 85, 543–572. doi:10.1146/annurev-biochem-060815-014520

Drew, D., North, R. A., Nagarathinam, K., and Tanabe, M. (2021). Structures and General Transport Mechanisms by the Major Facilitator Superfamily (MFS). *Chem. Rev.* 121, 5289–5335. doi:10.1021/acs.chemrev.0c00983

Ernst, H. A., Pham, A., Hald, H., Kastrup, J. S., Rahman, M., and Mirza, O. (2009). Ligand Binding Analyses of the Putative Peptide Transporter YjdL from *E. coli* Display a Significant Selectivity towards Dipeptides. *Biochem. Biophysical Res. Commun.* 389, 112–116. doi:10.1016/j.bbrc.2009.08.098

Foley, D., Rajamanickam, J., Bailey, P., and Meredith, D. (2010). Bioavailability through PepT1: the Role of Computer Modelling in Intelligent Drug Design. *Curr. Comput. Aided Drug Des.* 6, 68–78. doi:10.2174/157340910790980133

Franke, D., Petoukhov, M. V., Konarev, P. V., Panjkovich, A., Tuukkanen, A., Mertens, H. D. T., et al. (2017). ATSAS 2.8: a Comprehensive Data Analysis Suite for Small-Angle Scattering from Macromolecular Solutions. *J. Appl. Cryst.* 50, 1212–1225. doi:10.1107/S1600576717007786

Gabrielsen, M., Kroner, F., Black, I., Isaacs, N. W., Roe, A. J., and McLuskey, K. (2011). High-throughput Identification of Purification Conditions Leads to Preliminary Crystallization Conditions for Three Inner Membrane Proteins. *Mol. Membr. Biol.* 28, 445–453. doi:10.3109/09687688.2011.628954

Guettou, F., Quistgaard, E. M., Raba, M., Moberg, P., Löw, C., and Nordlund, P. (2014). Selectivity Mechanism of a Bacterial Homolog of the Human Drug-Peptide Transporters PepT1 and PepT2. *Nat. Struct. Mol. Biol.* 21, 728–731. doi:10.1038/nsmb.2860

Guettou, F., Quistgaard, E. M., Trésaugues, L., Moberg, P., Jegerschöld, C., Zhu, L., et al. (2013). Structural Insights into Substrate Recognition in Proton-dependent Oligopeptide Transporters. *EMBO Rep.* 14, 804–810. doi:10.1038/embor.2013.107

Harder, D., Stolz, J., Casagrande, F., Obrdlik, P., Weitz, D., Fotiadis, D., et al. (2008). DtpB (YhiP) and DtpA (TppB, YdgR) Are Prototypical Proton-dependent Peptide Transporters of *Escherichia coli*. *FEBS J.* 275, 3290–3298. doi:10.1111/j.1742-4658.2008.06477.x

Hediger, M. A., Clémençon, B., Burrier, R. E., and Bruford, E. A. (2013). The ABCs of Membrane Transporters in Health and Disease (SLC Series): Introduction. *Mol. Aspects Med.* 34, 95–107. doi:10.1016/j.mam.2012.12.009

Heinz, L. X., Lee, J., Kapoor, U., Kartnig, F., Sedlyarov, V., Papakostas, K., et al. (2020). TASL Is the SLC15A4-Associated Adaptor for IRF5 Activation by TLR7-9. *Nature* 581, 316–322. doi:10.1038/s41586-020-2282-0

Hillgren, K. M., Keppler, D., Zur, A. A., Giacomini, K. M., Stieger, B., Cass, C. E., et al. (2013). Emerging Transporters of Clinical Importance: an Update from the International Transporter Consortium. *Clin. Pharmacol. Ther.* 94, 52–63. doi:10.1038/clpt.2013.74

Ingersoll, S. A., Ayyadurai, S., Charania, M. A., Laroui, H., Yan, Y., and Merlin, D. (2012). The Role and Pathophysiological Relevance of Membrane Transporter PepT1 in Intestinal Inflammation and Inflammatory Bowel Disease. *Am. J. Physiology-Gastrointestinal Liver Physiology* 302, G484–G492. doi:10.1152/ajpgi.00477.2011

Jardetzky, O. (1966). Simple Allosteric Model for Membrane Pumps. *Nature* 211, 969–970. doi:10.1038/211969a0

Jensen, J. M., Aduri, N. G., Prabhala, B. K., Jahnsen, R., Franzyk, H., and Mirza, O. (2014). Critical Role of a Conserved Transmembrane Lysine in Substrate Recognition by the Proton-Coupled Oligopeptide Transporter YjdL. *Int. J. Biochem. Cell Biol.* 55, 311–317. doi:10.1016/j.biocel.2014.09.016

Jensen, J. M., Ernst, H., Wang, X., Hald, H., Ditta, A. C., Ismat, F., et al. (2012a). Functional Investigation of Conserved Membrane-Embedded Glutamate Residues in the Proton-Coupled Peptide Transporter YjdL. *Protein Pept. Lett.* 19, 282–287. doi:10.2174/092986612799363109

Jensen, J. M., Ismat, F., Szakonyi, G., Rahman, M., and Mirza, O. (2012b). Probing the Putative Active Site of YjdL: an Unusual Proton-Coupled Oligopeptide Transporter from *E. coli*. *PLoS One* 7, e47780. doi:10.1371/journal.pone.0047780

Jensen, J. M., Simonsen, F. C., Mastali, A., Hald, H., Lillebro, I., Diness, F., et al. (2012c). Biophysical Characterization of the Proton-Coupled Oligopeptide Transporter YjdL. *Peptides* 38, 89–93. doi:10.1016/j.peptides.2012.08.012

Jumper, J., Evans, R., Pritzel, A., Green, T., Figurnov, M., Ronneberger, O., et al. (2021). Highly Accurate Protein Structure Prediction with AlphaFold. *Nature* 596, 583–589. doi:10.1038/s41586-021-03819-2

Killer, M., Wald, J., Pieprzyk, J., Marlovits, T. C., and Löw, C. (2021). Structural Snapshots of Human PepT1 and PepT2 Reveal Mechanistic Insights into Substrate and Drug Transport across Epithelial Membranes. *Sci. Adv.* 7, eabk3259. doi:10.1126/sciadv.abk3259

Kotov, V., Bartels, K., Veith, K., Josts, I., Subhramanyam, U. K. T., Günther, C., et al. (2019). High-throughput Stability Screening for Detergent-Solubilized Membrane Proteins. *Sci. Rep.* 9, 10379. doi:10.1038/s41598-019-46686-8

Liu, S., Li, S., Krezel, A. M., and Li, W. (2022). Stabilization and Structure Determination of Integral Membrane Proteins by Termini Restraining. *Nat. Protoc.* 17, 540–565. doi:10.1038/s41596-021-00656-5

Liu, S., Li, S., Yang, Y., and Li, W. (2020). Termini Restraining of Small Membrane Proteins Enables Structure Determination at Near-Atomic Resolution. *Sci. Adv.* 6, eabe3717. doi:10.1126/sciadv.abe3717

Löw, C., Jegerschöld, C., Kovermann, M., Moberg, P., and Nordlund, P. (2012). Optimisation of Over-expression in *E. coli* and Biophysical Characterisation of Human Membrane Protein Synaptogyrin 1. *PLoS One* 7, e38244. doi:10.1371/journal.pone.0038244

Löw, C., Moberg, P., Quistgaard, E. M., Hedrén, M., Guettou, F., Frauenfeld, J., et al. (2013). High-throughput Analytical Gel Filtration Screening of Integral Membrane Proteins for Structural Studies. *Biochimica Biophysica Acta (BBA) - General Subj.* 1830, 3497–3508. doi:10.1016/j.bbagen.2013.02.001

Lyons, J. A., Parker, J. L., Solcan, N., Brinth, A., Li, D., Shah, S. T., et al. (2014). Structural Basis for Polyspecificity in the POT Family of Proton-coupled Oligopeptide Transporters. *EMBO Rep.* 15, 886–893. doi:10.15252/embr.201338403

Martinez Molledo, M., Quistgaard, E. M., Flayhan, A., Pieprzyk, J., and Löw, C. (2018a). Multispecific Substrate Recognition in a Proton-dependent Oligopeptide Transporter. *Structure* 26, 467–476. e4. doi:10.1016/j.str.2018.01.005

Martinez Molledo, M., Quistgaard, E. M., and Löw, C. (2018b). Tripeptide Binding in a Proton-dependent Oligopeptide Transporter. *FEBS Lett.* 592, 3239–3247. doi:10.1002/1873-3468.13246

Minhas, G. S., Bawdon, D., Herman, R., Rudden, M., Stone, A. P., James, A. G., et al. (2018). Structural Basis of Malodour Precursor Transport in the Human Axilla. *Elife* 7, e34995. doi:10.7554/eLife.34995

Nagamura, R., Fukuda, M., Kawamoto, A., Matoba, K., Dohmae, N., Ishitani, R., et al. (2019). Structural Basis for Oligomerization of the Prokaryotic Peptide Transporter PepTSo2. *Acta Cryst. Sect. F.* 75, 348–358. doi:10.1107/S2053230X19003546

Newstead, S., Drew, D., Cameron, A. D., Postis, V. L. G., Xia, X., Fowler, P. W., et al. (2011). Crystal Structure of a Prokaryotic Homologue of the Mammalian Oligopeptide-Proton Symporters, PepT1 and PepT2. *EMBO J.* 30, 417–426. doi:10.1038/emboj.2010.309

Panjkovich, A., and Svergun, D. I. (2018). CHROMIXS: Automatic and Interactive Analysis of Chromatography-Coupled Small-Angle X-Ray Scattering Data. *Bioinformatics* 34, 1944–1946. doi:10.1093/bioinformatics/btx846

Pardon, E., Laeremans, T., Triest, S., Rasmussen, S. G. F., Wohlkönig, A., Ruf, A., et al. (2014). A General Protocol for the Generation of Nanobodies for Structural Biology. *Nat. Protoc.* 9, 674–693. doi:10.1038/nprot.2014.039

Parker, J. L., Deme, J. C., Wu, Z., Kuteyi, G., Huo, J., Owens, R. J., et al. (2021). Cryo-EM Structure of PepT2 Reveals Structural Basis for Proton-Coupled Peptide and Prodrug Transport in Mammals. *Sci. Adv.* 7, eabh3355. doi:10.1126/sciadv.abh3355

Pettersen, E. F., Goddard, T. D., Huang, C. C., Meng, E. C., Couch, G. S., Croll, T. I., et al. (2021). UCSF ChimeraX : Structure Visualization for Researchers, Educators, and Developers. *Protein Sci.* 30, 70–82. doi:10.1002/pro.3943

Pieprzyk, J., Pazicky, S., and Löw, C. (2018). Transient Expression of Recombinant Membrane-eGFP Fusion Proteins in HEK293 Cells. *Methods Mol. Biol.* 1850, 17–31. doi:10.1007/978-1-4939-8730-6_2

Prabhala, B. K., Aduri, N. G., Iqbal, M., Rahman, M., Gajhede, M., Hansen, P. R., et al. (2017). Several hPepT1-Transported Drugs Are Substrates of the *Escherichia coli* Proton-Coupled Oligopeptide Transporter YdgR. *Res. Microbiol.* 168, 443–449. doi:10.1016/j.resmic.2017.01.005

Prabhala, B. K., Aduri, N. G., Jensen, J. M., Ernst, H. A., Iram, N., Rahman, M., et al. (2014). New Insights into the Substrate Specificities of Proton-Coupled Oligopeptide Transporters from *E. coli* by a pH Sensitive Assay. *FEBS Lett.* 588, 560–565. doi:10.1016/j.febslet.2014.01.004

Prabhala, B. K., Aduri, N. G., Sharma, N., Shaheen, A., Sharma, A., Iqbal, M., et al. (2018). The Prototypical Proton-Coupled Oligopeptide Transporter YdgR from *Escherichia coli* Facilitates Chloramphenicol Uptake into Bacterial Cells. *J. Biol. Chem.* 293, 1007–1017. doi:10.1074/jbc.M117.805960

Punjani, A., and Fleet, D. J. (2021). 3D Variability Analysis: Resolving Continuous Flexibility and Discrete Heterogeneity from Single Particle Cryo-EM. *J. Struct. Biol.* 213, 107702. doi:10.1016/j.jsb.2021.107702

Punjani, A., Rubinstein, J. L., Fleet, D. J., and Brubaker, M. A. (2017). cryoSPARC: Algorithms for Rapid Unsupervised Cryo-EM Structure Determination. *Nat. Methods* 14, 290–296. doi:10.1038/nmeth.4169

Punjani, A., Zhang, H., and Fleet, D. J. (2020). Non-uniform Refinement: Adaptive Regularization Improves Single-Particle Cryo-EM Reconstruction. *Nat. Methods* 17, 1214–1221. doi:10.1038/s41592-020-00990-8

Quistgaard, E. M., Löw, C., Guettou, F., and Nordlund, P. (2016). Understanding Transport by the Major Facilitator Superfamily (MFS): Structures Pave the Way. *Nat. Rev. Mol. Cell Biol.* 17, 123–132. doi:10.1038/nrm.2015.25

Quistgaard, E. M., Martinez Molledo, M., and Löw, C. (2017). Structure Determination of a Major Facilitator Peptide Transporter: Inward Facing PepTSt from Streptococcus Thermophilus Crystallized in Space Group P3121. *PLoS One* 12, e0173126. doi:10.1371/journal.pone.0173126

Rohou, A., and Grigorieff, N. (2015). CTFFIND4: Fast and Accurate Defocus Estimation from Electron Micrographs. *J. Struct. Biol.* 192, 216–221. doi:10.1016/j.jsb.2015.08.008

Sanchez-Garcia, R., Gomez-Blanco, J., Cuervo, A., Carazo, J., Sorzano, C., and Vargas, J. (2021). DeepEMhancer: a Deep Learning Solution for Cryo-EM Volume Post-processing. *Communications Biology*. doi:10.1038/s42003-021-02399-1

Scheres, S. H. W. (2012). RELION: Implementation of a Bayesian Approach to Cryo-EM Structure Determination. *J. Struct. Biol.* 180, 519–530. doi:10.1016/j.jsb.2012.09.006

Sharma, N., Aduri, N. G., Iqbal, A., Prabhala, B. K., and Mirza, O. (2016). Peptide Selectivity of the Proton-Coupled Oligopeptide Transporter from Neisseria Meningitidis. *J. Mol. Microbiol. Biotechnol.* 26, 312–319. doi:10.1159/000447129

Shen, J., Hu, M., Fan, X., Ren, Z., Portioli, C., Yan, X., et al. (2022). Extracellular Domain of PepT1 Interacts with TM1 to Facilitate Substrate Transport. *Structure*. S0969-2126(22)00138–1. doi:10.1016/j.str.2022.04.011

Smith, D. E., Clémençon, B., and Hediger, M. A. (2013). Proton-coupled Oligopeptide Transporter Family SLC15: Physiological, Pharmacological and Pathological Implications. *Mol. Aspects Med.* 34, 323–336. doi:10.1016/j.mam.2012.11.003

Solcan, N., Kwok, J., Fowler, P. W., Cameron, A. D., Drew, D., Iwata, S., et al. (2012). Alternating Access Mechanism in the POT Family of Oligopeptide Transporters. *EMBO J.* 31, 3411–3421. doi:10.1038/emboj.2012.157

Spanier, B., and Rohm, F. (2018). Proton Coupled Oligopeptide Transporter 1 (PepT1) Function, Regulation, and Influence on the Intestinal Homeostasis. *Compr. Physiol.* 8, 843–869. doi:10.1002/cphy.c170038

Stauffer, M., Jeckelmann, J.-M., Ilgü, H., Ucurum, Z., Boggavarapu, R., and Fotiadis, D. (2022). Peptide Transporter Structure Reveals Binding and Action Mechanism of a Potent PEPT1 and PEPT2 Inhibitor. *Commun. Chem.* 5, 23. doi:10.1038/s42004-022-00636-0

Terwilliger, T. C., Ludtke, S. J., Read, R. J., Adams, P. D., and Afonine, P. V. (2020). Improvement of Cryo-EM Maps by Density Modification. *Nat. Methods* 17, 923–927. doi:10.1038/s41592-020-0914-9

Thwaites, D. T., and Anderson, C. M. H. (2007). H+-coupled Nutrient, Micronutrient and Drug Transporters in the Mammalian Small Intestine. *Exp. Physiol.* 92, 603–619. doi:10.1113/expphysiol.2005.029959

Ural-Blimke, Y., Flayhan, A., Strauss, J., Rantos, V., Bartels, K., Nielsen, R., et al. (2019). Structure of Prototypic Peptide Transporter DtpA from *E. coli* in

Complex with Valganciclovir Provides Insights into Drug Binding of Human PepT1. *J. Am. Chem. Soc.* 141, 2404–2412. doi:10.1021/jacs.8b11343

Viennois, E., Pujada, A., Zen, J., and Merlin, D. (2018). Function, Regulation, and Pathophysiological Relevance of the POT Superfamily, Specifically PepT1 in Inflammatory Bowel Disease. *Compr. Physiol.* 8, 731–760. doi:10.1002/cphy.c170032

Wagner, T., Merino, F., Stabrin, M., Moriya, T., Antoni, C., Apelbaum, A., et al. (2019). SPHIRE-crYOLO Is a Fast and Accurate Fully Automated Particle Picker for Cryo-EM. *Commun. Biol.* 2, 218. doi:10.1038/s42003-019-0437-z

Yan, N. (2015). Structural Biology of the Major Facilitator Superfamily Transporters. *Annu. Rev. Biophys.* 44, 257–283. doi:10.1146/annurev-biophys-060414-033901

Zhang, Y., Zhang, Y., Sun, K., Meng, Z., and Chen, L. (2019). The SLC Transporter in Nutrient and Metabolic Sensing, Regulation, and Drug Development. *J. Mol. Cell Biol.* 11, 1–13. doi:10.1093/jmcb/mjy052

Zhao, Y., Mao, G., Liu, M., Zhang, L., Wang, X., and Zhang, X. C. (2014). Crystal Structure of the *E. coli* Peptide Transporter YbgH. *Structure* 22, 1152–1160. doi:10.1016/j.str.2014.06.008

Zheng, S. Q., Palovcak, E., Armache, J.-P., Verba, K. A., Cheng, Y., and Agard, D. A. (2017). MotionCor2: Anisotropic Correction of Beam-Induced Motion for Improved Cryo-Electron Microscopy. *Nat. Methods* 14, 331–332. doi:10.1038/nmeth.4193

Zivanov, J., Nakane, T., Forsberg, B. O., Kimanius, D., Hagen, W. J., Lindahl, E., et al. (2018). New Tools for Automated High-Resolution Cryo-EM Structure Determination in RELION-3. *eLife* 7, e42166. doi:10.7554/eLife.42166

Zivanov, J., Nakane, T., and Scheres, S. H. W. (2019). A Bayesian Approach to Beam-Induced Motion Correction in Cryo-EM Single-Particle Analysis. *Int. Union Crystallogr. J.* 6, 5–17. doi:10.1107/S205225251801463X

Conflict of Interest: The authors declare that the research was conducted in the absence of any commercial or financial relationships that could be construed as a potential conflict of interest.

Publisher's Note: All claims expressed in this article are solely those of the authors and do not necessarily represent those of their affiliated organizations, or those of the publisher, the editors and the reviewers. Any product that may be evaluated in this article, or claim that may be made by its manufacturer, is not guaranteed or endorsed by the publisher.

frontiers | Frontiers in Molecular Biosciences

TYPE Original Research
PUBLISHED 05 August 2022
DOI 10.3389/fmolb.2022.945772

OPEN ACCESS

EDITED BY
James A. Garnett,
King's College London, United Kingdom

REVIEWED BY
Brent L. Nannenga,
Arizona State University, United States
Vidya Chandran Darbari,
Queen Mary University of London,
United Kingdom

*CORRESPONDENCE
Rebecca F. Thompson,
r.f.thompson@leeds.ac.uk
Stephen P. Muench,
s.p.muench@leeds.ac.uk

†These authors have contributed equally to this work

SPECIALTY SECTION
This article was submitted to Structural Biology,
a section of the journal
Frontiers in Molecular Biosciences

RECEIVED 16 May 2022
ACCEPTED 27 June 2022
PUBLISHED 05 August 2022

CITATION
Klebl DP, Wang Y, Sobott F, Thompson RF and Muench SP (2022), It started with a Cys: Spontaneous cysteine modification during cryo-EM grid preparation.
Front. Mol. Biosci. 9:945772.
doi: 10.3389/fmolb.2022.945772

It started with a Cys: Spontaneous cysteine modification during cryo-EM grid preparation

David P. Klebl[1†], Yiheng Wang[1†], Frank Sobott[2], Rebecca F. Thompson[2*] and Stephen P. Muench[1*]

[1]School of Biomedical Sciences, Faculty of Biological Sciences & Astbury Centre for Structural and Molecular Biology, University of Leeds, Leeds, United Kingdom, [2]School of Molecular and Cellular Biology, Faculty of Biological Sciences & Astbury Centre for Structural and Molecular Biology, University of Leeds, Leeds, United Kingdom

Advances in single particle cryo-EM data collection and processing have seen a significant rise in its use. However, the influences of the environment generated through grid preparation, by for example interactions of proteins with the air-water interface are poorly understood and can be a major hurdle in structure determination by cryo-EM. Initial interactions of proteins with the air-water interface occur quickly and proteins can adopt preferred orientation or partially unfold within hundreds of milliseconds. It has also been shown previously that thin-film layers create hydroxyl radicals. To investigate the potential this might have in cryo-EM sample preparation, we studied two proteins, HSPD1, and beta-galactosidase, and show that cysteine residues are modified in a time-dependent manner. In the case of both HSPD1 and beta-galactosidase, this putative oxidation is linked to partial protein unfolding, as well as more subtle structural changes. We show these modifications can be alleviated through increasing the speed of grid preparation, the addition of DTT, or by sequestering away from the AWI using continuous support films. We speculate that the modification is oxidation by reactive oxygen species which are formed and act at the air-water interface. Finally, we show grid preparation on a millisecond timescale outruns cysteine modification, showing that the reaction timescale is in the range of 100s to 1,000s milliseconds and offering an alternative approach to prevent spontaneous cysteine modification and its consequences during cryo-EM grid preparation.

KEYWORDS

single particle cryo-EM, sample preparation, air–water-interface, protein modification, structure determination

Introduction

In the past decade, cryo-EM has become one of the major techniques for protein structure determination with rapid improvements in microscope hardware and data processing software, recently reaching atomic resolution (Nakane et al., 2020; Yip et al., 2020). However, the physical and chemical processes impacting macromolecules during cryo-EM grid preparation are not yet fully understood and sample preparation for cryo-EM has increasingly become a bottleneck (Weissenberger et al., 2021). Conventional cryo-EM sample preparation is done by manually applying a small volume of sample (typically ~3 µl) to a grid. Excess liquid is then blotted away with filter paper in an automated fashion, leaving a thin liquid film suspended over the grid foil holes only 10s to 100s nm thick. After blotting, the grid with the thin film is plunged into liquid ethane, where the sample is vitrified. The blotting process usually takes seconds, as does the manual sample application process. While undeniably successful for many samples, this approach is not universally successful, in part due to problems arising from air–water interface (AWI) interactions.

The vast majority of proteins are thought to interact with the AWI, which for some samples may affect particle orientation (Noble et al., 2018a) and in some cases the integrity of the sample (D'Imprima et al., 2019). In sample films with suitable thickness for cryo-EM, local protein unfolding at the AWI can occur in 100s of milliseconds (Klebl et al., 2020) and can potentially be detrimental to accurate structure determination or interpretation. Effects of the AWI on orientation or resolution can be reduced by minimizing the time the sample spends in the thin film environment (Noble et al., 2018b; Levitz et al., 2021), and by other approaches for example the use of surfactants such as detergents (Chen et al., 2019). Solutions to preferred orientation or denaturation are often protein-specific, and there is no one solution that fits all (Drulyte et al., 2017). Charge and hydrophobicity have been identified as important factors that govern protein-AWI interactions (Glaeser, 2018; Li et al., 2021) but there may be other effects.

Properties of the AWI other than charge or hydrophobicity have received less attention in the cryo-EM field, but are likely to also influence the protein sample and have been studied for example in the fields of catalysis or atmospheric chemistry. Most research has been done using microdroplets but many factors also apply to the AWI of a thin film. The pH at or near the AWI is thought to be different from bulk solution (Buch et al., 2007; Wei et al., 2018) and it has also been suggested that a very large electric field exists that is present at the AWI, on the order of 10^8–10^{10} V/m^{-1} (Kathmann et al., 2008). This electric field may be sufficient to split water into OH radicals which would be able to modify the protein directly. Moreover, this environment has been shown to spontaneously produce H_2O_2 from pure water when atomizing into small droplets at an approximate concentration of 30 µM (Lee et al., 2019). The downstream effects that may result from the production of H_2O_2 in combination with other negative features of the AWI are poorly understood but those residues more sensitive to oxidation could become modified. Moreover, even more, complex reactions such as peptide bond formation have been shown to occur at the AWI (Griffith & Vaida, 2012) and some enzymes exhibit a dramatic increase in reaction rates in the presence of a large AWI (Zhong et al., 2020).

The present work examines cysteine residues and shows evidence for their modification during cryo-EM grid preparation, which is prevented either by adding reducing agents such as DTT, by sequestering away from the AWI, or by fast grid preparation. This suggests that the modification is dependent on exposure within the thin film and/or time at the AWI. Conformational changes are associated with cysteine modification and observed in both the model proteins used for this study, HSPD1, and β-gal, albeit to different degrees. We hypothesize that free cysteines are modified by hydroxyl radicals from the AWI before exposure of the sample to the electron beam and that this process may occur in many cases but has been overlooked because unambiguous identification requires high-resolution reconstructions and multiple datasets.

Materials and methods

HSPD1 was expressed and purified as previously described (Klebl et al., 2021). Briefly, 4 h after induction [250 µM IPTG (final concentration)], bacterial cells were harvested by centrifugation (10 min, 4,000 rpm). Cell pellets were resuspended in 20 ml lysis buffer (50 mM Tris, 500 mM NaCl, 10 mM imidazole pH 8), containing 1 mM PMSF and protease inhibitor cocktail (set V, Calbiochem). Sonication was performed after further resuspending the cells in a Dounce homogenizer, Centrifugation was used to clear lysate (30 min, 17,000 rpm) with the resultant supernatant applied to 3.5 ml Ni-NTA resin (equilibrated in lysis buffer). The resin was washed with 2 × 100 ml lysis buffer and 100 ml of 50 mM Tris, 300 mM NaCl, and 50 mM imidazole (pH 8). Elution was achieved using 10 ml of 50 mM Tris, 300 mM NaCl, and 300 mM imidazole (pH 8). Protein was cleaved with TEV protease (1.6 mg per 1 L of culture and 1 mM DTT) for 4 h at RT. The cleaved protein was subsequently dialyzed overnight into 50 mM Tris, 150 mM NaCl pH 7.5 (2 L) using 10 kDa molecular weight cutoff (MWCO) dialysis tubing with the resultant product incubated with 1.5 ml Ni-NTA resin (pre-equilibrated in lysis buffer) for 1 h. Flow-through was then concentrated to 20–30 mg/ml in a Sartorius, 10 kDa MWCO spin concentrator. For reconstitution into oligomers, monomeric HSPD1 was mixed with 100 µl KCl (1 M), 100 µl $Mg(OAc)_2$ (1 M), and 400 µl Mg-ATP (50 mM, pH 7) and incubated for 90 min at 30°C. The sample was then centrifuged at 13,000 rpm for 10 min at RT, with the resultant supernatant loaded onto a HiLoad 16/600 Superdex 200 gel

filtration column (GE Healthcare) in 50 mM Tris, 300 mM NaCl, 10 mM $MgCl_2$ (pH 7.7).

Concentrated HSPD1 was diluted to the target concentration in the desired buffer. β-gal was obtained from Sigma-Aldrich (G6008). As a final purification step before grid preparation, β-gal was purified by size-exclusion chromatography using a Superose 6 10/300 Increase column in 25 mM Tris, 50 mM NaCl, 2 mM $MgCl_2$ pH 8. The peak eluting at 14 ml was collected, concentrated to 4.4 mg/ml using a 30 kDa cut-off spin concentrator, and diluted to the target concentration in the desired buffer.

Conventional blotted grids of HSPD1 ("blotted," "5 mM Met," and "1 mM Asc") were prepared using a Vitrobot at > 90% humidity and 20–22°C temperature (blot force 6, blot time 6 s). Quantifoil 300 mesh Cu R1.2/1.3 grids were used after glow discharge in a Cressington 208 carbon coater with a glow discharge unit (10 mA, 30 s, 0.1 mbar). The final protein concentration was 2.3 mg/ml, the buffer was 25 mM Tris, 150 mM NaCl, 5 mM $MgCl_2$ pH 7.7. The "5 mM Met" sample additionally contained 5 mM L-methionine, and the "1 mM Asc" sample additionally contained 1 mM ascorbic acid.

Conventional blotted grids of β-gal ("blotted," "1 mM DTT," and "1 mM TCEP") were prepared using a Vitrobot at > 95% humidity and 4–6°C temperature (blot force 2, blot time 6 s). Quantifoil 300 mesh Cu R1.2/1.3 grids were used after glow discharge in a Cressington 208 carbon coater with a glow discharge unit (15 mA, 30 s, 0.1 mbar). The final protein concentration was 0.25 mg/ml for "blotted" β-gal and 1 mg/ml for "1 mM DTT"/"1 mM TCEP" β-gal. The buffer was in 25 mM Tris, 50 mM NaCl, and 2 mM $MgCl_2$ pH 8. The "1 mM DTT" sample additionally contained 1 mM DTT, and the "1 mM TCEP" sample additionally contained 1 mM TCEP.

"Fast" grids were prepared using an in-house device for fast grid preparation as previously described (Klebl et al., 2020). Briefly, this device works by depositing small- and high-velocity droplets of the sample onto a fast-moving grid which is subsequently plunged in liquid ethane to produce vitreous ice. By removing the traditional "blotting" stage the process from spray to vitrification can be achieved in >5 ms. Changes in the nozzle to grid distance, plunge speed, and liquid flow rate can be used to modify the speed of grid making. Self-wicking grids supplied by SPT Labtech were used, after glow discharge in a Cressington 208 carbon coater with a glow discharge unit (15 mA, 80 s, 0.1 mbar) to assist with droplet spreading on the grid. The spray nozzle/ethane distance was 2.2 cm, the nozzle/grid distance was 1.2 cm, and the spray gas pressure was 2 bar. For "fast" HSPD1, a liquid flow rate of 7.8 µl/s was used. The plunge speed was 1.5 m/s and a final protein concentration of 5 mg/ml was used in 25 mM Tris, 150 mM NaCl, and 5 mM $MgCl_2$ pH 7.7. For "fast" b-gal, a liquid flowrate of 5.2 µL/s was used. The plunge speed was 1.3 m/s and a final protein concentration of 4.4 mg/ml was used in 25 mM Tris, 50 mM NaCl, and 2 mM $MgCl_2$ pH 8.

The main parameters for data collection and processing are listed in Supplementary Tables S1, S2. All single-particle datasets were collected using a Titan Krios G2 microscope using Thermo Fisher Scientific EPU software (Thompson et al., 2019). The "5 mM Met" and "1 mM Asc" HSPD1 datasets were collected with a Falcon III detector in integrating mode. The "fast" β-gal dataset was collected with a Falcon IV detector in counting mode and a Selectris energy filter set to a width of 10 eV. All other datasets were collected with a Falcon IV detector in counting mode. Data processing pipelines for HSPD1 are shown in Supplementary Figures S2–S5. Data processing pipelines for β-gal are shown in Supplementary Figures S6–S10. Most processing steps were carried out using RELION 3.1, and in some cases, non-uniform refinement in cryoSPARC was used (Zivanov et al., 2018; Punjani, Zhang, & Fleet, 2020). The beam-induced motion was corrected using MotionCor2, in some cases with RELION's implementation, and CTF-estimation was done using gctf or CTFFIND (Rohou & Grigorieff, 2015; Zhang, 2016; Zheng et al., 2017).

Docking of atomic models and visualization of maps and models was done in Chimera or ChimeraX (Pettersen et al., 2004; Goddard et al., 2018). Small adjustments to docked models, where needed were done using Isolde within ChimeraX (Croll, 2018).

Results

Our previous structural studies of the mitochondrial chaperonin HSPD1 (Hsp60) (Klebl et al., 2021) included cryo-EM data collection in a range of buffers and using different grid-preparation approaches. As a part of this, we prepared cryo-EM grids of HSPD1 in 25 mM Tris, 150 mM NaCl, and 5 mM $MgCl_2$ pH 7.7 and obtained a reconstruction at 3.4Å resolution by standard single-particle data processing methods. In this cryo-EM map ("blotted" HSPD1), we noticed broken and weak density for a surface-exposed beta-hairpin near the ATP-binding site of the protein, suggesting that the region is disordered (residues 475–486, Figures 1A, B) while it is well resolved in cryo-EM structures of the bacterial homolog GroEL (Figure 1C) (Joseph et al., 2016). A more detailed inspection of this region of HSPD1 showed unexpected density for cysteine 416 near the disordered segment, suggesting that Cys416 may be chemically modified (Figure 1D). The map resolution was not sufficient to identify the modification but we noticed that the additional density of HSPD1 cysteine 416 would sterically clash with an intact beta-hairpin 475–486, so we concluded that Cys416 modification is linked to beta-hairpin 475–486 unfolding. The equivalent amino acid residue in GroEL is an alanine, which cannot undergo the same modifications and could explain why this region of GroEL shows different behavior.

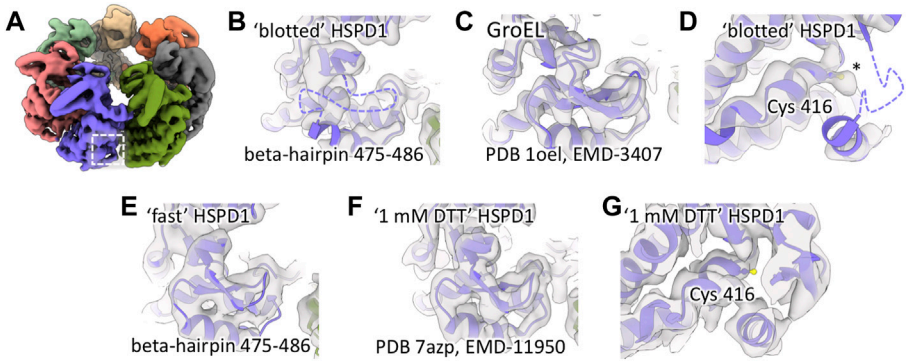

FIGURE 1
Local unfolding and additional density for Cys416 of HSPD1. **(A)** Reconstruction of "blotted" HSPD1 (determined to 3.4Å) with the region around beta-hairpin 475–486 highlighted by the box. **(B)** Beta-hairpin 475–486 is unfolded in "blotted" HSPD1, the unresolved region is indicated with a dashed purple line. **(C)** Equivalent region in GroEL (determined to 3.3Å), showing an intact beta-hairpin. **(D)** Additional density for Cys416 in "blotted" HSPD1, indicated by an asterisk. **(E)** "Fast" HSPD1 (determined to 6.8Å) has density indicating an intact beta-hairpin 475–486. **(F)** "1 mM DTT" HSPD1 (determined to 3.5Å) shows an intact beta-hairpin 475–486 and **(G)** no additional density for Cys416.

Using data from a previous study (Klebl et al., 2020), we compared our "blotted" HSPD1 to reconstructions from fast grid preparation with delays of less than 100 ms between sample application and vitrification. These reconstructions of HSPD1 (EMD-10883, EMD-10884, EMD-10885) in contrast to the blotted grids, did not show signs of beta-hairpin 475–486 unfolding. To confirm this, we prepared new grids of HSPD1 in the same buffer as 'blotted' HSPD1 using our in-house setup for fast grid preparation with a delay of 14 ms between sample application and vitrification. Cryo-EM data collection and processing gave a reconstruction at 6.8 Å resolution of "fast" HSPD1. This reconstruction, like previous cryo-EM maps from a fast grid preparation approach, showed density for beta-hairpin 475–486 and no sign of local unfolding (Figure 1E). Despite the limited resolution, we concluded that Cys416 was unmodified in "fast" HSPD1 because we expect the Cys416 modification to be incompatible with an intact beta-hairpin 475–486.

We hypothesized that Cys416 modification in "blotted" HSPD1 was oxidation, and that this was the cause for local unfolding. Consequently, the addition of a reducing agent should alleviate oxidation. We added 1 mM DTT to the buffer before conventionally blotting grids (Klebl et al., 2021). In line with our hypothesis, this "1 mM DTT" HSDP1 showed a well-resolved beta-hairpin 475–486 and no signs of modification of Cys416 (Figures 1F, G).

Together, the data show that with fast grid preparation or DTT added, HSPD1 beta-hairpin 475–486 is structurally ordered. When using conventional blotting in the absence of additives, however, Cys416 appears to be modified and beta-hairpin 475–486 disordered. We concluded that oxidation and unfolding occur during grid preparation in the thin-film environment at the air-water interface (AWI). We further reasoned that if exposure to the AWI is the cause for Cys416 oxidation, this spontaneous modification during grid preparation should not be specific to HSPD1 and surface-exposed cysteines in other proteins may also be affected.

To understand whether cysteine oxidation was a more general phenomenon during cryo-EM grid preparation, we searched the literature and electron microscopy database (EMDB) for unexpected cysteine modifications. Interestingly, we found cases that indicate modified cysteines in other cryo-EM density maps. In an atomic resolution reconstruction of human apoferritin, the authors identified a sulfenic acid group on Cys90 (Yip et al., 2020). We also found additional density for cysteine residues in published structures of beta-galactosidase (β-gal) (Bartesaghi et al., 2018; Saur et al., 2020), while there were no additional densities in a different structure when the buffer contained DTT (Figures 2A–C).

Encouraged by these findings, and given the relative amenability of β-gal to single-particle cryo-EM analysis we prepared grids by blotting, in the absence of additives (25 mM Tris, 50 mM NaCl, and 2 mM $MgCl_2$ pH 8) or with 1 mM DTT added to the buffer. Furthermore, β-gal grids were prepared by fast grid preparation with a time delay of 18 ms between sample application and vitrification. Striking differences between the grid-preparation conditions were apparent directly from raw images: In the absence of DTT, particles were visibly aggregated and the concentration had to be lowered to give useable cryo-EM images (0.25 mg/ml, Figure 3A). Grids prepared at high speeds generally require higher protein concentration, but most particles were well dispersed in the raw images (Figure 3B), suggesting that reduced exposure to the AWI reduced aggregation. With 1 mM DTT in the buffer, particles were well dispersed at high concentrations (1 mg/ml used for grid preparation, Figure 3C).

Data collection and processing for the three beta-galactosidase grids ("blotted", "fast", "1 mM DTT") resulted in reconstructions at 2.2, 2.4, and 2.1 Å, respectively. As expected,

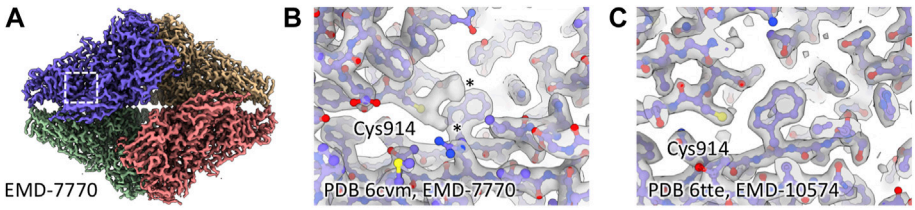

FIGURE 2
Additional cysteine density in published β-gal structures. **(A)** Region around Cys914 in EMD-7770. **(B)** Cys914 shows additional density in EMD-7770 (1 mM TCEP), marked with asterisks. **(C)** There is no additional density for Cys914 in EMD-10574 where 5 mM DTT was present during grid preparation.

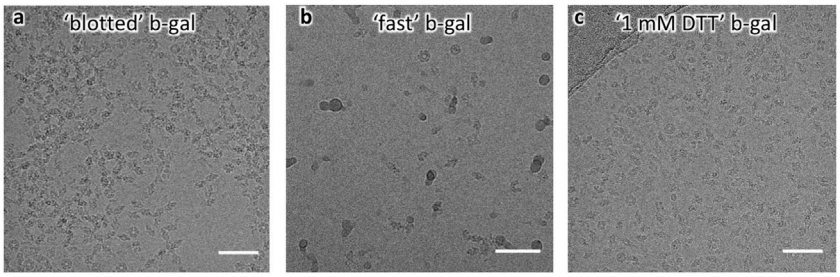

FIGURE 3
Raw micrographs of β-gal. **(A)** "Blotted" β-gal shows aggregated particles. **(B)** "Fast" β-gal shows lower apparent concentration and dispersed particles. **(C)** "1 mM DTT" β-gal shows well-dispersed particles at high concentration.

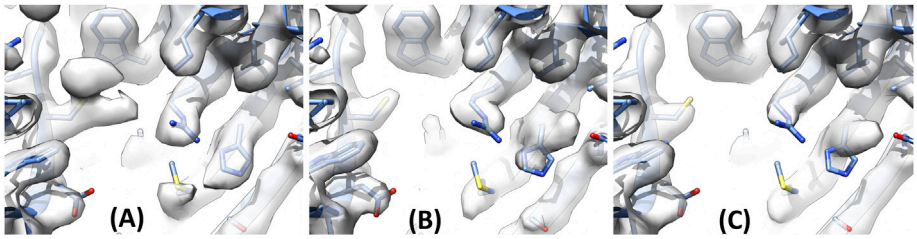

FIGURE 4
B-gal Cysteine 914 and Histidine 653 under different grid preparation conditions. **(A)** "Blotted" β-gal shows additional density for Cys914. **(B)** "Fast" β-gal and **(C)** "1 mM DTT" β-gal show no additional density for Cys914. His653 adopts a different rotamer in "blotted" β-gal **(A)** where a modification is seen on Cys914, compared to **(B)**,**(C)**.

the three reconstructions appeared very similar overall, with well-resolved side-chains. However, the density for Cys914 differed between "blotted" and "1 mM DTT"/"fast" β-gal (Figures 4A–C). There was clear additional density for Cys914 in "blotted" β-gal (Figure 4A) while in "fast" and "1 mM DTT" β-gal Cys914 showed no additional density. Interestingly, His653 which is located near Cys914 adopted a different rotamer in "blotted" β-gal than in "fast"/"1 mM DTT" β-gal (Figure 4). This may be caused by modification of Cys914, and by subtle changes propagated through the structure or solvent to His653. The bidentate shape of the density for Cys914 in "blotted" β-gal may be consistent with a sulfinic acid group, but the unambiguous assignment of the modification would require higher resolution. We also investigated if any other residues were modified in β-gal and found two further Cys residues (77 and 248), which also display a similar trend to that seen for 914 (Supplementary Figure S1). Other Cys residues remained unmodified, indicating that the

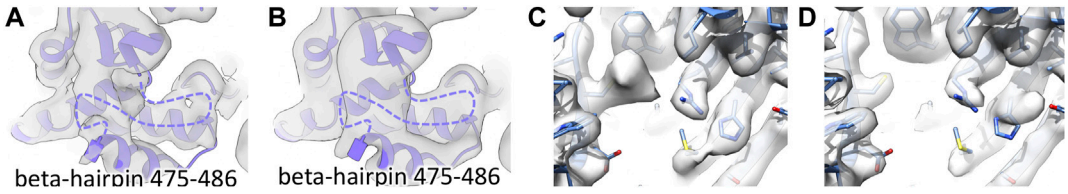

FIGURE 5
Effects of other radical scavengers and reducing agents. **(A)** Beta-hairpin 475–486 is disordered in "5 mM Met" HSPD1 as well as in "1 mM Asc" HSPD1 **(B)**. **(C)** Additional density for Cys914 in "1 mM TCEP" β-gal and His653 rotamer is the same for "blotted" β-gal. **(D)** Cys914 remains unmodified when prepared on a continuous support film and His653 adopts the same rotamer as seen for the "fast" prepared grid and DTT added (for clarity His653 is modeled in the same rotamer position in both **(C)** and **(D)**.

local environment and/or surface exposure may also play a role in the propensity for modification at the Cys residue.

The results for HSPD1 and β-gal suggested that some of the effects of prolonged exposure of proteins to the AWI or grid can be alleviated by the addition of DTT to the buffer. To better understand this observation, we tested other reducing agents which differ chemically from DTT. We prepared grids of HSPD1 by conventional blotting in the presence of 5 mM methionine or 1 mM ascorbic acid. These additives were chosen because both are known scavengers of hydroxyl radicals in aqueous solutions (Niu et al., 2015; Crosas et al., 2017). In addition, we prepared grids by conventional blotting of β-gal in the presence of 1 mM TCEP, a commonly used reducing agent which does not contain a thiol group such as DTT. We note that one of the published β-gal structures (Figure 2B) was also obtained from a sample containing TCEP (5 mM). Methionine and ascorbic acid at 5 and 1 mM, respectively, failed to protect the beta hairpin 475–486 in HSPD1 from unfolding (Figures 5A, B). The addition of 1 mM TCEP did not prevent additional density on Cys914 of β-gal (Figure 5C), and His653 adopted the same rotamer as in the modified "blotted" β-gal (Figure 5D). However, the additional density for Cys914 in 1 mM TCEP β-gal was less continuous and particles were visibly less aggregated in the raw micrographs, allowing data collection at 1 mg/ml concentration. This suggested that while relatively weak hydroxyl radical scavengers such as methionine or ascorbic acid do not protect from cysteine modification, alternative reducing agents such as TCEP might offer some protection against modification, although not as effectively as DTT did in the case of β-gal. The reasons for the difference seen between DTT and TCEP are not understood but we hope further investigations will shed further light on this observation.

To further investigate the role of the AWI we next prepared conventionally blotted grids of β-gal on grids with continuous carbon support, without reducing agent present. This produced grids with well-distributed particles showing little signs of aggregation (consistent with the rapid freezing and DTT grids). The data set provided a high-resolution structure at 2.4 Å. We saw no evidence for Cys modification for the continuous carbon grid suggesting that sequestering away from the AWI protects the cysteine residue, despite the seconds-long timescales involved in preparing the blotted grid. This suggests modification occurs at or in very close proximity to the AWI. All experimental parameters tested are shown in Table 1.

Discussion

While single-particle cryo-EM analysis relies on vitrifying proteins in a thin film, the full extent to which this environment impacts protein folding is yet to be fully understood. Here, we have observed spontaneous modification of cysteines during cryo-EM grid preparation, which can be prevented either by the addition of DTT, fast grid preparation, or sequestering away from the AWI. It has been proposed that in the harsh environment of the AWI, electric fields of sufficient strength are present to cause the formation of hydroxyl radicals. We speculate that hydroxyl radicals form at the AWI and react with surface-exposed cysteine residues on proteins which are located at, or close to the AWI. During the long time that the protein is exposed to the AWI in conventional blotting, this will result in the transformation of the cysteine thiol group to a sulfenic or sulfinic acid and potentially followed by additional reactions. While we think that hydroxyl radicals from the AWI are the most plausible explanation, more work is required to confirm this hypothesis. Moreover, by making a grid of continuous carbon that was also blotted we also show processes relating to the blotting paper itself are likely not responsible for the resulting cysteine modifications. It is also important to note that we observe modifications on specific cysteine residues, with others showing no modification in both β-gal and HSPD1. One explanation is that the local chemical environment of cysteine will influence its p*K*a and its sensitivity to modification. Features such as an electronegative local environment, hydrogen bond donors, and/or charged residues can lower the p*K*a significantly (Poole, 2014).

TABLE 1 Summary of the modifications seen in HSPD1 and β-gal and the different parameters tested. NT = not tested.

	Blotted	Fast (<50 ms)	DTT	TCEP	Carbon backed
HSPD1	Modified	No modification	No modification	Some modification	NT
β-gal	Modified	No modification	No modification	Some modification	No modification

In both proteins, HSPD1 and β-gal, cysteine modification occurs together with wider structural changes. In the case of HSPD1, most of the density for beta-hairpin 475–486 is lost suggesting that this region becomes locally unfolded. In the case of β-gal, we see more subtle structural changes such as changes in rotamers, as seen for His653. We cannot unambiguously say if these structural changes are caused by the cysteine modifications observed, or whether the structural change is caused by binding to the AWI and is separate from cysteine modification. However, the fact that neither structural change is observed in the presence of DTT nor when the protein is sequestered away from the AWI suggests that cysteine modification is the cause of the structural perturbation.

This work highlights that care should be taken when interpreting the oxidation state of cysteine residues from cryo-EM structures. In addition to beam-induced effects as previously shown (Kato et al., 2021), cysteines also appear to be affected by the harsh environment of the AWI with a potential impact on the surrounding protein structure. As demonstrated for β-gal and HSPD1, cysteine modification can be prevented by the addition of a reducing agent such as DTT. In cases where reducing agents cannot be used, for example for proteins with structurally relevant disulfide bonds, fast grid preparation can be used to avoid cysteine modification, along with continuous support films. It is also interesting to note that reducing agents such as DTT has also been shown to influence the surface tension and result in increased protein aggregation and degradation (Tihonov et al., 2016). The reduction in surface tension may also mirror the effect seen with detergents which can also form a protective layer at the AWI influencing factors such as preferred orientation (Chen et al., 2022). These studies illustrate the challenges of unpicking the varying physical and chemical processes that occur at the AWI.

The above results raise the question of how commonly cysteine modification occurs during cryo-EM grid preparation. We expect that in most cases, such modifications will remain unnoticed because of limited resolution, especially in the surface-exposed regions of proteins. However, in some cases, cysteine modifications could impact protein structure. If the observed cysteine modifications are indeed caused by hydroxyl radicals from the AWI, there may also be other reactions occurring during cryo-EM grid preparation and affecting protein structure.

More work is required to understand the precise chemical processes occurring in the thin film environment. While outside the scope of this work, we have noted that there is likely a role for grid support material, as a preliminary assessment of β-gal on an UltrAuFoil® grid show no modification of cysteine residues (data not shown). A future series of experiments are needed to untangle these relationships. We suggest that by understanding more precisely the impacts of the AWI on macromolecular complexes and more widely the chemistry, which is possible in the thin film environment, we will be better able to design universally successful strategies for cryo-EM sample preparation.

Data availability statement

The datasets presented in this study can be found in online repositories. All maps have been deposited within the EMDB with accession numbers; β-gal EMDB-14981 (blotted), EMDB-14982 (DTT), EMDB-14983 (TCEP), EMDB-14984 (Carbon support). HSPD1 EMDB-15178 (blotted), EMDB-15162 (fast), EMDB-11950 (blotted and DTT), EMDB-15167 (blotted with Methionine), EMDB-15176 (blotted with Ascorbate).

Author contributions

Conceptualisation and experimental design: DK, YW, FS, RT, and SM; Performed experiments DK, YW, and RT; Analysis of data DK, YW, RT, and SM. Discussed the data and wrote the manuscript: DK, YW, FS, RT, and SM all authors have read and agreed to the published version of the manuscript.

Funding

DK is a PhD student in the Wellcome Trust 4-years PhD program in The Astbury Center funded by The University of Leeds. The FEI Titan Krios microscopes were funded by the University of Leeds (UoL ABSL award) and Wellcome (108466/Z/15/Z), with Falcon 4 and Selectris Falcon4 direct electron

detector and microED packages (Q2 2021) upgrades funded by Wellcome 221524/Z/20/Z.

Acknowledgments

We would like to thank John Berriman for his insightful and useful discussions on the topic. We also thank Dr Louie Aspinall for preparing some of the B-gal grids.

Conflict of interest

The authors declare that the research was conducted in the absence of any commercial or financial relationships that could be construed as a potential conflict of interest.

Publisher's note

All claims expressed in this article are solely those of the authors and do not necessarily represent those of their affiliated organizations, or those of the publisher, the editors, and the reviewers. Any product that may be evaluated in this article, or claim that may be made by its manufacturer, is not guaranteed or endorsed by the publisher.

Supplementary material

The Supplementary Material for this article can be found online at: https://www.frontiersin.org/articles/10.3389/fmolb.2022.945772/full#supplementary-material

References

Bartesaghi, A., Aguerrebere, C., Falconieri, V., Banerjee, S., Earl, L. A., Zhu, X., et al. (2018). Atomic resolution cryo-EM structure of β-galactosidase. *Structure* 26 (6), 848–856. doi:10.1016/j.str.2018.04.004

Buch, V., Milet, A., Vácha, R., Jungwirth, P., and Devlin, J. P. (2007). Water surface is acidic. *Proc. Natl. Acad. Sci. U. S. A.* 104 (18), 7342–7347. doi:10.1073/pnas.0611285104

Chen, J., Noble, A. J., Kang, J. Y., and Darst, S. A. (2019). Eliminating effects of particle adsorption to the air/water interface in single-particle cryo-electron microscopy: Bacterial RNA polymerase and CHAPSO. *J. Struct. Biol. X* 1, 100005. doi:10.1016/j.yjsbx.2019.100005

Chen, S., Li, J., Vinothkumar, K. R., and Henderson, R. (2022). Interaction of human erythrocyte catalase with air-water interface in cryoEM. *Microscopy* 71 (S1), i51–i59. doi:10.1093/jmicro/dfab037

Croll, T. I. (2018). Isolde: A physically realistic environment for model building into low-resolution electron-density maps. *Acta Crystallogr. D. Struct. Biol.* 74 (6), 519–530. doi:10.1107/S2059798318002425

Crosas, E., Castellvi, A., Crespo, I., Fulla, D., Gil-Ortiz, F., Fuertes, G., et al. (2017). Uridine as a new scavenger for synchrotron-based structural biology techniques. *J. Synchrotron Radiat.* 24 (1), 53–62. doi:10.1107/S1600577516018452

D'Imprima, E., Floris, D., Joppe, M., Sánchez, R., Grininger, M., Kühlbrandt, W., et al. (2019). Protein denaturation at the air-water interface and how to prevent it. *Elife* 8, e42747. doi:10.7554/eLife.42747

Drulyte, I., Johnson, R. M., Hesketh, E. L., Hurdiss, D. L., Scarff, C. A., Porav, S. A., et al. (2017). Approaches to altering particle distributions in cryo-electron microscopy sample preparation. *Acta Crystallogr. D. Struct. Biol.* D74, 560–571. doi:10.1107/S2059798318006496

Glaeser, R. M. (2018). Proteins, interfaces, and cryo-EM grids. *Curr. Opin. Colloid Interface Sci.* 34, 1–8. doi:10.1016/j.cocis.2017.12.009

Goddard, T. D., Huang, C. C., Meng, E. C., Pettersen, E. F., Couch, G. S., Morris, J. H., et al. (2018). UCSF ChimeraX: Meeting modern challenges in visualization and analysis. *Protein Sci.* 27 (1), 14–25. doi:10.1002/pro.3235

Griffith, E. C., and Vaida, V. (2012). *In situ* observation of peptide bond formation at the water–air interface. *Proc. Natl. Acad. Sci. U. S. A.* 109 (39), 15697–15701. doi:10.1073/pnas.1210029109

Joseph, A. P., Malhotra, S., Burnley, T., Wood, C., Clare, D. K., Winn, M., et al. (2016). Refinement of atomic models in high resolution EM reconstructions using Flex-EM and local assessment. *Methods* 100, 42–49. doi:10.1016/j.ymeth.2016.03.007

Kathmann, S. M., Kuo, I.-F. W., and Mundy, C. J. (2008). Electronic effects on the surface potential at the vapor– liquid interface of water. *J. Am. Chem. Soc.* 130 (49), 16556–16561. doi:10.1021/ja802851w

Kato, K., Miyazaki, N., Hamaguchi, T., Nakajima, Y., Akita, F., Yonekura, K., et al. (2021). High-resolution cryo-EM structure of photosystem II reveals damage from high-dose electron beams. *Commun. Biol.* 4 (1), 382. doi:10.1038/s42003-021-01919-3

Klebl, D. P., Feasey, M. C., Hesketh, E. L., Ranson, N. A., Wurdak, H., Sobott, F., et al. (2021). Cryo-EM structure of human mitochondrial HSPD1. *Iscience* 24 (1), 102022. doi:10.1016/j.isci.2020.102022

Klebl, D. P., Gravett, M. S., Kontziampasis, D., Wright, D. J., Bon, R. S., Monteiro, D., et al. (2020). Need for speed: Examining protein behavior during CryoEM grid preparation at different timescales. *Structure* 28 (11), 1238–1248. doi:10.1016/j.str.2020.07.018

Lee, J. K., Walker, K. L., Han, H. S., Kang, J., Prinz, F. B., Waymouth, R. M., et al. (2019). Spontaneous generation of hydrogen peroxide from aqueous microdroplets. *Proc. Natl. Acad. Sci. U. S. A.* 116 (39), 19294–19298. doi:10.1073/pnas.1911883116

Levitz, T. S., Brignole, E. J., Fong, I., Darrow, M. C., and Drennan, C. L. (202110782). Effects of chameleon dispense-to-plunge speed on particle concentration, complex formation, and final resolution: A case study using the Neisseria gonorrhoeae ribonucleotide reductase inactive complex. *J. Struct. Biol.* 214. doi:10.1016/j.jsb.2021.107825

Li, B., Zhu, D., Shi, H., and Zhang, X. (2021). Effect of charge on protein preferred orientation at the air–water interface in cryo-electron microscopy. *J. Struct. Biol.* 213 (4), 107783. doi:10.1016/j.jsb.2021.107783

Nakane, T., Kotecha, A., Sente, A., McMullan, G., Masiulis, S., Brown, P. M., et al. (2020). Single-particle cryo-EM at atomic resolution. *Nature* 587 (7832), 152–156. doi:10.1038/s41586-020-2829-0

Niu, B., Zhang, H., Giblin, D., Rempel, D. L., and Gross, M. L. (2015). Dosimetry determines the initial OH radical concentration in fast photochemical oxidation of proteins (FPOP). *J. Am. Soc. Mass Spectrom.* 26 (5), 843–846. doi:10.1007/s13361-015-1087-0

Noble, A. J., Dandey, V. P., Wei, H., Brasch, J., Chase, J., Acharya, P., et al. (2018a). Routine single particle CryoEM sample and grid characterization by tomography. *Elife* 7, e34257. doi:10.7554/eLife.34257

Noble, A. J., Wei, H., Dandey, V. P., Zhang, Z., Tan, Y. Z., Potter, C. S., et al. (2018b). Reducing effects of particle adsorption to the air–water interface in cryo-EM. *Nat. Methods* 15 (10), 793–795. doi:10.1038/s41592-018-0139-3

Pettersen, E. F., Goddard, T. D., Huang, C. C., Couch, G. S., Greenblatt, D. M., Meng, E. C., et al. (2004). UCSF Chimera—A visualization system for exploratory research and analysis. *J. Comput. Chem.* 25 (13), 1605–1612. doi:10.1002/jcc.20084

Poole, L. B. (2014). The basics of thiols and cysteines in redox biology and chemistry. *Free Radic. Biol. Med.* 0, 148–157. doi:10.1016/j.freeradbiomed.2014.11.013

Punjani, A., Zhang, H., and Fleet, D. J. (2020). Non-uniform refinement: Adaptive regularization improves single-particle cryo-EM reconstruction. *Nat. Methods* 17 (12), 1214–1221. doi:10.1038/s41592-020-00990-8

Rohou, A., and Grigorieff, N. (2015). CTFFIND4: Fast and accurate defocus estimation from electron micrographs. *J. Struct. Biol.* 192 (2), 216–221. doi:10.1016/j.jsb.2015.08.008

Saur, M., Hartshorn, M. J., Dong, J., Reeks, J., Bunkoczi, G., Jhoti, H., et al. (2020). Fragment-based drug discovery using cryo-EM. *Drug Discov. Today* 25 (3), 485–490. doi:10.1016/j.drudis.2019.12.006

Thompson, R. F., Iadanza, M. G., Hesketh, E. L., Rawson, S., and Ranson, N. A. (2019). Collection, pre-processing and on-the-fly analysis of data for high-resolution, single-particle cryo-electron microscopy. *Nat. Protoc.* 14, 100–118. doi:10.1038/s41596-018-0084-8

Tihonov, M. M., Kim, V. V., and Noskov, B. A. (2016). Impact of a reducing agent on the dynamic surface properties of lysozyme solutions. *J. Oleo Sci.* 65 (5), 413–418. doi:10.5650/jos.ess15247

Wei, H., Vejerano, E. P., Leng, W., Huang, Q., Willner, M. R., Marr, L. C., et al. (2018). Aerosol microdroplets exhibit a stable pH gradient. *Proc. Natl. Acad. Sci. U. S. A.* 115 (28), 7272–7277. doi:10.1073/pnas.1720488115

Weissenberger, G., Henderikx, R. J., and Peters, P. J. (2021). Understanding the invisible hands of sample preparation for cryo-EM. *Nat. Methods* 18 (5), 463–471. doi:10.1038/s41592-021-01130-6

Yip, K. M., Fischer, N., Paknia, E., Chari, A., and Stark, H. (2020). Atomic-resolution protein structure determination by cryo-EM. *Nature* 587 (7832), 157–161. doi:10.1038/s41586-020-2833-4

Zhang, K. (2016). Gctf: Real-time CTF determination and correction. *J. Struct. Biol.* 193 (1), 1–12. doi:10.1016/j.jsb.2015.11.003

Zheng, S. Q., Palovcak, E., Armache, J.-P., Verba, K. A., Cheng, Y., Agard, D. A., et al. (2017). MotionCor2: Anisotropic correction of beam-induced motion for improved cryo-electron microscopy. *Nat. Methods* 14 (4), 331–332. doi:10.1038/nmeth.4193

Zhong, X., Chen, H., and Zare, R. N. (2020). Ultrafast enzymatic digestion of proteins by microdroplet mass spectrometry. *Nat. Commun.* 11 (1), 1049. doi:10.1038/s41467-020-14877-x

Zivanov, J., Nakane, T., Forsberg, B. O., Kimanius, D., Hagen, W. J., Lindahl, E., et al. (2018). New tools for automated high-resolution cryo-EM structure determination in RELION-3. *Elife* 7, e42166. doi:10.7554/eLife.42166

frontiers | Frontiers in Molecular Biosciences

TYPE Brief Research Report
PUBLISHED 18 August 2022
DOI 10.3389/fmolb.2022.910218

OPEN ACCESS

EDITED BY
Felix Weis,
European Molecular Biology Laboratory
Heidelberg, Germany

REVIEWED BY
Sarah Schneider,
European Molecular Biology Laboratory
Grenoble, France
Armel Bezault,
Institut Pasteur, France

*CORRESPONDENCE
Pierre-Damien Coureux,
pierre-damien.coureux@
polytechnique.edu

SPECIALTY SECTION
This article was submitted to Structural Biology,
a section of the journal
Frontiers in Molecular Biosciences

RECEIVED 01 April 2022
ACCEPTED 12 July 2022
PUBLISHED 18 August 2022

CITATION
Kazan R, Bourgeois G, Carisetti D, Florea I, Larquet E, Maurice J-L, Mechulam Y, Ozanam F, Schmitt E and Coureux P-D (2022), Grid batch-dependent tuning of glow discharge parameters.
Front. Mol. Biosci. 9:910218.
doi: 10.3389/fmolb.2022.910218

Grid batch-dependent tuning of glow discharge parameters

Ramy Kazan[1], Gabrielle Bourgeois[1], Dominique Carisetti[2], Ileana Florea[3], Eric Larquet[4], Jean-Luc Maurice[3], Yves Mechulam[1], François Ozanam[4], Emmanuelle Schmitt[1] and Pierre-Damien Coureux[1]*

[1]Laboratoire de Biologie Structurale de la Cellule, BIOC, Ecole Polytechnique, CNRS-UMR7654, IP Paris, Palaiseau, France, [2]Thales Research and Technology, Palaiseau, France, [3]Laboratoire de Physique des Interfaces et Couches Minces (LPICM), CNRS-UMR 7647, Ecole Polytechnique, IP Paris, Palaiseau, France, [4]Laboratoire de Physique de la Matière Condensée, Ecole Polytechnique, CNRS, IP Paris, Palaiseau, France

Sample preparation on cryo-EM grids can give various results, from very thin ice and homogeneous particle distribution (ideal case) to unwanted behavior such as particles around the "holes" or complexes that do not entirely correspond to the one in solution (real life). We recently run into such a case and finally found out that variations in the 3D reconstructions were systematically correlated with the grid batches that were used. We report the use of several techniques to investigate the grids' characteristics, namely TEM, SEM, Auger spectroscopy and Infrared Interferometry. This allowed us to diagnose the origin of grid preparation problems and to adjust glow discharge parameters. The methods used for each approach are described and the results obtained on a common specific case are reported.

KEYWORDS

cryo-EM, sample preparation, glow discharge, quantifoil, continuous carbon

Introduction

Electron microscopy of frozen hydrated samples (cryo-EM) is a powerful structural technique that allows the direct observation at a high resolution of functional macromolecular complexes in their near-physiological environment. To obtain high-resolution images, one needs first to vitrify a thin layer (ideally between 50 and 150 nm thickness) of a sample of interest. This task is not that straightforward, and many trials and errors are needed to obtain an optimal ice thickness (Cho et al., 2013). Sample buffer, sample concentration, temperature and humidity chamber, type of grids (Quantifoil, C-flat, and Holey), grid sample support (holey carbon, gold, nickel, and graphene), with or without an extra continuous carbon layer, glow discharge conditions, blotting time, and blotting force are parameters that are usually screened (Passmore and Russo, 2016) to improve grid preparation. Finally, the air–water interface diffusion also needs to be taken into account (Glaeser, 2018) as it also influences particle orientation and stability (Noble et al., 2018; Jahagirdar et al., 2020).

Recently, we observed that the same biological sample spotted onto similar grids coming from different batches led to dissimilar results. The biological sample is

TABLE 1 Grid batch usage for each biophysical approach. Batches #1, #2, and #3 are copper Quantifoil R2/1 grids with a 2 nm extra continuous thin carbon layer. Batch #4 is copper Quantifoil R2/1 grids with 3 nm extra continuous thin carbon layer. Each batch was used (represented by an "x" sign) or not used (empty box) for some approaches mentioned in the first column. The infrared spectroscopy analysis was not performed on grid batches (explained by the n.d. (not determined) abbreviation) as a Si prism was used.

	Batch #1	Batch #2	Batch #3	Batch #4
Cryo-EM	x	x	x	
SEM	x	x		x
Auger spectroscopy	x	x		x
EELS	x	x		x
Infrared spectroscopy	n.d.	n.d.	n.d.	n.d.
ET	x			

a ribosomal translation initiation complex (IC) from *Pyrococcus abyssi* containing two initiation factors aIF1A and aIF5B. The grid preparation was performed with this IC complex using Quantifoil R2/1 grids with 2 nm extra continuous thin carbon layer (TCL) as previously described (Coureux et al., 2016; Coureux et al., 2020). Ribosomal particles were clearly visible within all data collections. After data processing, the two factors of the IC complex were only visible in some cases. After addressing sample preparation/stability, grid preparation conditions, data collection parameters, or data processing strategy, we realized that the differences observed were linked to the batch of grids after our glow discharge conditions (−25 mA during 30 s). Those conditions were the same we used for previous batches of grids that led us to publish our cryo-EM results (Coureux et al., 2016; Coureux et al., 2020) and are consistent with the conditions widely used in the cryo-EM community. After further investigation, we hypothesized that, for some grid batches, the TCL was damaged during the glow discharge step (Lu et al., 2016) in our standard conditions (see Materials and Methods): the extra carbon layer seems of good integrity before glow discharge while it was completely sheared after. This observation was not the case for previous grid batches.

Glow discharge is an empirical method for rendering the carbon support film hydrophilic and, hence, facilitates the adsorption of biological material (Aebi and Pollard, 1987; Russo and Passmore, 2016). In brief, the grid is placed between two electrodes in a reduced atmosphere, usually of air. A high voltage is then applied to cause a glow discharge that generates an air plasma containing ions and radicals that, in turn, react with the carbon surface to reduce its hydrophobicity.

To further investigate the different behaviors of grids during glow discharge, several approaches have been used: overall grid quality was checked using Scanning Electron Microscopy (SEM). Carbon membrane thickness and composition were studied using electron energy loss spectroscopy (EELS) and Auger spectroscopy. Analysis of the surface chemical composition of the carbon membrane over time was performed on a study model using infrared spectroscopy. Local grid quality was also assessed using electron tomography (ET). Each technique, briefly presented, has its own limitations but can give simple and valuable information when one needs to better rationalize the quality of the thin extra continuous carbon membrane.

The first aim of this article is to report a case study where variations between grid batches were observed. The analysis of our cryo-EM experiments (data collection and processing) combined with the approaches mentioned earlier confirmed the importance of glow discharge adjustment depending on the grid batch to keep intact TCLs. The second aim of this article is to describe physical methods useful for cryo-EM grid characterization.

Materials and methods

Cryo-EM–Cryo-electron microscopy

Complex preparation

Translation initiation complexes from *Pyrococcus abyssi* (*Pab*) were prepared using a strategy similar to that previously described (Coureux et al., 2016; Coureux et al., 2020; Kazan et al., 2022)). In brief, the different partners of the complex were independently purified. The 30S *Pab* ribosomal subunits were extracted and purified from archaeal cells, and the initiation factors (aIF1A and aIF5B) and $tRNA_i^{Met}$ were over-expressed and purified from *E. coli*. The $tRNA_i^{Met}$ was then methionylated *in vitro* as previously described (Mechulam et al., 2007). mRNA was commercially synthesized. The full complex (called Initiation Complex 3 or IC3) was formed *in vitro* and purified. An excess of initiation factors (5x) was added, then the sample was incubated with the crosslinker BS^3 (1 mM final concentration) for 10 min at 51°C just before spotting onto grids to favor complex formation (Querido et al., 2020). The final concentration of the full complex was 120 nM. After IC3 *in vitro* assembly, the sample was kept at 51°C shortly prior to grid preparation.

Grid preparation

In our study, we used three different batches of copper Quantifoil grids 300 mesh R2/1 grids with 2 nm TCL, named batches #1, #2, and #3. One batch of copper Quantifoil grids 300 mesh R2/1 with 3 nm TCL (called batch#4) was also used in this study. Each grid coming from batch#1, #2, or #3 was first glow-discharged (GD) with a Pelco Easiglow device set up at −25 mA for 30 s as routinely used (Coureux et al., 2020). The grid was then transferred within minutes into the LEICA EM-GP grid plunger. The chamber was set to 20°C and 90% humidity. Liquid ethane was maintained at −182°C and the preblot, blot, and postblot parameters for grid preparation were set to 10 s, 1.2 s with auto-sensor, and 0 s, respectively. 3.4 µL of the IC3 complex was applied onto the grid prior to the preblot. As a control for biophysical approaches, grids from batch#4 were also glow-discharged using the same preparation conditions. The summary of usage for each grid batch with the corresponding biophysical approach used is summarized in Table 1.

Data collection and processing

Cryo-EM data were recorded either on the in-house TFS Titan Themis (X-FEG operating at 300 kV) microscope equipped with a Falcon 3 camera and a Gatan ELSA holder at the CIMEX facility at Ecole polytechnique or on the TFS Titan Krios (X-FEG operating at 300 kV) microscope equipped with an energy filter (Bioquantum) and a Gatan K3 camera at Pasteur Institute in Paris. Total exposure of 40 $e^{-}/Å^{2}$ was applied to the sample and distributed on 39 or 40 frames on the corresponding camera. The final pixel sizes were 1.12 Å/pixel and 0.86 Å/pixel for the Themis and Krios data collection, respectively. Data processing of Single Particle Analysis (SPA) data was carried out with Relion 3.1 (Scheres, 2012) from raw images to the 3D structure. A motion correction of the frames recorded was performed using Relion's own implementation of Motioncor2 (Zheng et al., 2017). CTF estimation, resolution limit, and astigmatism were estimated using gCTF (Zhang, 2016). Several rounds of 2D classification, 3D refinement, 3D classification, and final 3D refinement of the best-resolved 3D classes were performed with the Relion suite. In each case, the 3D classes with density corresponding to the IC3 complex were selected for further processing.

Scanning electron microscopy

Scanning electron microscopy was performed with an S4800 Hitachi FESEM for the observation of the surface topography of the carbon foil from the Quantifoil grids with 2 or 3 nm extra continuous carbon layer. This microscope was a cold field emission gun high-resolution scanning electron microscope (Accelerating Voltage from 0.5 to 30 kV), which is mainly based upon the detection of secondary electrons emerging from the surface under the impact of a very fine beam of primary electrons that scans the surface observed. The first interest of this type of microscope is its large range of magnification from X20 to X800K. The combined use of the super ExB filter with the first upper detector allows filtering and collecting secondary electrons and backscattering signal energies of interest, thereby suppressing charging artifacts and showing topographical details. In our case, all observations and images were made at 1 kV using the upper detector that guarantees a spatial resolution of 2 nm in conventional conditions.

Electron energy loss spectroscopy

The membrane thickness of Quantifoil grids with 2 or 3 nm extra continuous carbon layer was measured using EELS. No glow discharge was performed to prevent shearing the extra carbon layer. The microscope used was a transmission electron microscope (Jeol 2010F) equipped with a Gatan TRIDIEM imaging filter allowing for electron energy loss spectroscopy (EELS) and the recording of filtered images. The accelerating voltage was set to 200 kV. The thickness measurement was performed using the so-called log-ratio method, by comparing the intensity in an image recorded with all the transmitted electrons (the integral of the EEL spectrum, including elastic and inelastic electrons) with one recorded with only elastic electrons (the integral of the zero-loss peak). See Supplementary Figure S1 for details.

Let us call I_0 the latter and I_{tot} the former; the ratio of the two depends exponentially on the sample thickness t through the following expressions:

$$I_{tot}/I_0 = \exp(t/\lambda), \quad (1)$$

where λ is the inelastic mean free path in amorphous carbon. Thus, the sample thickness is simply

$$t = \lambda \, \mathrm{Log}(I_{tot}/I_0). \quad (2)$$

The inelastic mean free path λ depends on the material and measurement parameters (Malis et al., 1988; Iakoubovskii et al., 2008a; Egerton, 2009). The latter is the kinetic energy of the incident electrons and the convergence angle of the beam and the acceptance angle of the detector. However here, we recorded t/λ maps in imaging mode at an energy of 200 keV, using the software installed in Gatan Digital Micrograph. In this mode, the acceptance angle is so large that the whole scattered intensity can be considered collected (Iakoubovskii et al., 2008a; Iakoubovskii et al., 2008b). In such conditions, the inelastic mean free path in carbon is well documented in the literature (Malis et al., 1988; Iakoubovskii et al., 2008a; Iakoubovskii et al., 2008b; Egerton, 2009). It is for a thickness range close to the mean free path (70–150 nm), where the main energy loss mechanism is that of bulk plasmons, and the second one is that of the 1s core level ionization. Here, surface plasmons, which can be neglected in the reference configuration, dominate the other contributions.

Supplementary Figure S1 shows the comparison of a reference spectrum, recorded in the nearby thicker area (made of the Holey carbon membrane and the 2 or 3 nm extra continuous carbon layer) to a spectrum recorded on the TCL (made of the 2 or 3 nm extra continuous carbon layer only). Note the bulk plasmon peak at 24 eV (Berger et al., 1988) in the reference spectrum, is not visible in the TCL spectrum. The plasmon maximum appears to shift towards low energy in the latter case by more than 5 eV; which denotes the influence of surface plasmons, the energy of which has been positioned between 14 and 20 eV by X-ray photoelectron energy loss spectroscopy (Godet et al., 2009).

Quite counterintuitively, the total energy loss is proportionally larger for the present very thin films, as the energy loss mechanisms at work in thicker samples are not suppressed, and must add up to surface plasmons to make the total loss. Thus the actual inelastic mean free path must be significantly shorter in those very thin films. As developing a model taking the surface plasmons into account is out of the scope of the present work, we used the mean free path measured in diamond in the same conditions as the present ones by Iakoubovskii *et al.* (λ = 112 nm) (Iakoubovskii et al., 2008b), to which we applied a correction to take into account the change of density between diamond and amorphous carbon. For the dependence of λ upon density ρ, we used the expression in $\rho^{-0.3}$ given by the same authors (Iakoubovskii et al., 2008a), and for the density of amorphous carbon, we took that measured by Iwaki (2.15 ± 0.15 gcm^{-3}) (Iwaki, 2002). With a density of diamond at 3.5 gcm^{-3}, it gives $\lambda_{aC,\ 200kV}$ = 130 nm. In this way, we got over-estimated values, which still can give useful indications.

Infrared spectroscopy

The sensitivity of infrared spectroscopy is too limited for the direct investigation of a carbon membrane deposited on a TEM grid. Therefore, a geometry of attenuated total reflection (ATR) has been used. For that purpose, a thin (1 nm) carbon film has been deposited on a ~15 × 20 mm^2 Si prism. The film mimics the TEM membranes with a much larger surface area. The prism was cut from a 0.5 mm thick Si wafer (FZ-purified, ~10 Ω cm Si crystal). The two long parallel edges were polished at 45° using first abrasive papers of successive grades (from 240 to 1,200), then diamond pastes of successive grades down to 1 µm. The obtained prism finally provided 14 to 15 useful internal reflections for the infrared beam on the large face of the prism. Before use, final cleaning of the sample was performed by immersion for 15 min in a hot "piranha" solution (1: 3 volumes of H_2O_2:H_2SO_4), leaving a clean thin oxide at the surface of the prism.

A thin carbon film was evaporated on the large face of the prism using a Cressington 208C. Two pulses of 6 s at 4.6 A gave a carbon thickness that corresponds to the perforated carbon deposited on copper grids.

The infrared spectra were recorded using a Bomem MB100 Fourier-transform infrared spectrometer coupled to an external homemade ATR compartment. After mounting the sample, the compartment was purged with N_2 for 1 h before recording the data, in order to minimize the contribution of atmosphere water and carbon dioxide in the spectra. Each spectrum corresponded to the average of 400 acquisitions at a resolution of 4 cm^{-1}. The infrared beam was polarized by passing through a wire-grid polarizer, and spectra in p and s polarizations were successively recorded without breaking the purge. Spectra are displayed in terms of absorbance scaled to one reflection. Absorbance was computed from the natural logarithm of the ratio of the considered spectrum intensity to that of a reference spectrum. Unless otherwise indicated, the reference spectrum is that of the sample prior to the application of the glow-discharge treatment.

Glow discharge of the Si prism was made with a Pelco EasiGlow device, using -25 mA for 30 s at 0.39 mbar. New infrared spectra were recorded at 1 and 4 h after glow-discharging to assess the evolution of the charges on the Si prism surface.

Electron tomography

For the tomography studies, unidirectional acquisition of the tilt series was performed in the classical Bright-Field (BF) mode of a Titan-Themis 300 microscope, using the serialEM (Mastronarde, 2005) acquisition software and a 4096 × 4096 pixels cooled CMOS Ceta camera. The data collection of the ET series was performed on Quantifoil grids with 2 nm TCL (batch#1). The same batch grids with or without glow discharge were analyzed twice for each condition. The tomography software allows an automatic variation of the tilt angle step by step, a correction of the focus of the image, and the preservation of the object under study within the field of view. The tilt angle was varied in a range from −60° to +50°, with an image recorded every 1° giving a total of 111 images with a total acquisition time of about 15 min. The data treatment of the tilt series for the preliminary image processing procedure was performed using the IMOD software (Mastronarde, 1997). The volume reconstruction was obtained using 50 iterations of the algebraic reconstruction technique algorithm (ART) (Gordon et al., 1970) implemented in the 2.8 version of the TomoJ software (MessaoudiI et al., 2007).

Results

Cryo-EM–3D reconstructions of different datasets were performed to assess the *Pab* IC3 complex integrity. Depending on the dataset, the 3D reconstructions showed either the studied full complex IC3 or the IC3 complex lacking the initiation factors aIF1A and aIF5B. The resolution limits obtained in the different datasets varied around 3 Å (see FSCs in Supplementary Figure

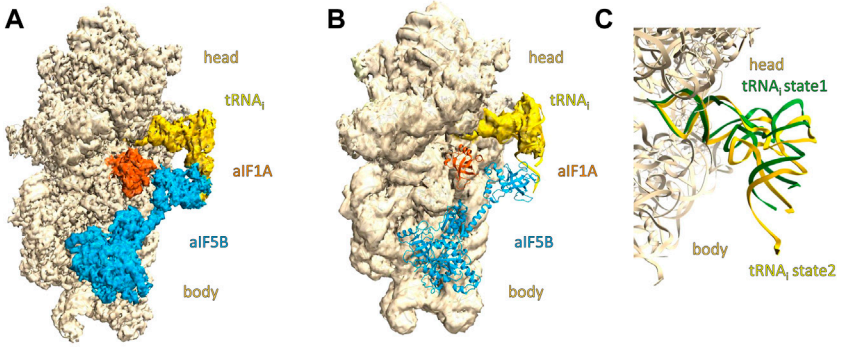

FIGURE 1
Overall view of cryo-EM maps of IC3 complexes prepared on grids coming from batch#3 and batch#1. The small ribosomal subunit 30S (made of the head and body parts) is colored in wheat, the tRNA is colored in yellow, aIF1A in orange, and aIF5B in cyan. 1A/3D density and corresponding model in the density of the IC3 complex containing the translation initiation factors aIF1A and aIF5B. 1B/3D density of the IC3 complex and corresponding model lacking density for translation initiation factors aIF1A and aIF5B. 1C/Close-up showing the $tRNA_i$ conformations observed in structures 1A and 1B. The view was obtained after superimposition of the tRNAi conformation of the two structures. The model for aIF1A and aIF5B have been omitted for better clarity. The $tRNA_i$ corresponding to the structure obtained in the IC3 complex lacking the translation initiation factors aIF1A and aIF5B is colored in green. The $tRNA_i$ corresponding to the structure obtained in the full IC3 complex is colored in yellow. The tRNA in green is in an upper position compared to the tRNA colored in yellow.

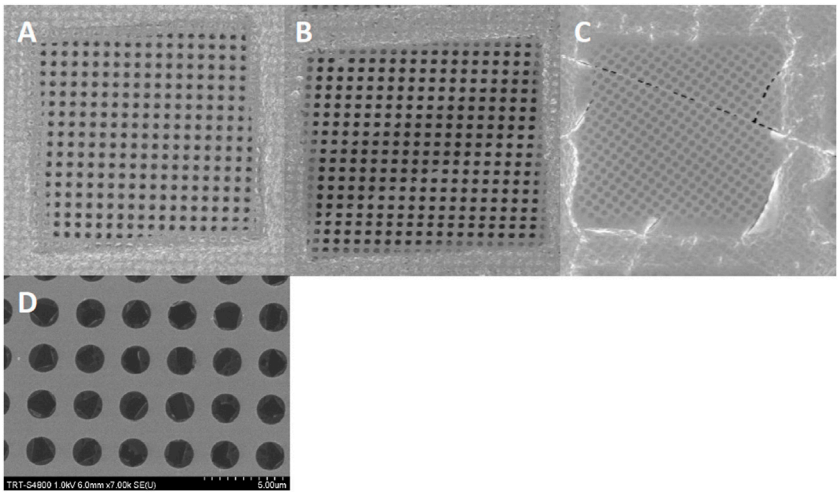

FIGURE 2
SEM images of a Quantifoil 300 mesh carbon grid with a 2 nm continuous carbon layer. A quick look at the grid with simple binoculars or SEM at low magnification (x700) doesn't show clear defects in the grid (Figure 2A). A more careful analysis of the grid displays patches where the extra carbon layer is sometimes missing (Figure 2B) or contains irregular holes (Figure 2C). At higher magnification (x7000), the extra carbon layer is disrupted in each hole. (Figure 2D).

S2) and were sufficient to conclude the presence or absence of translation initiation factors, even at low thresholds.

Processed data from batch#3 (2 grids in total) gave 3D reconstructions where the potential map was clearly visible for the two initiation factors (Figure 1A). Processed data from batches #1 and #2 (5 grids in total), using the same sample and preparing the grids in the same experimental conditions, gave systematically stripped complexes without any density in the 3D reconstructions for the initiation factors (Figure 1B). Any further 3D classification did not help to identify a subset of particles showing the IC3 full complex. Comparing the experimental details we used for grid preparation, we noted a systematic correlation between the grid batch and the 3D reconstruction: the sample preparation and the grid preparation were as much as possible the same (see Materials and Methods).

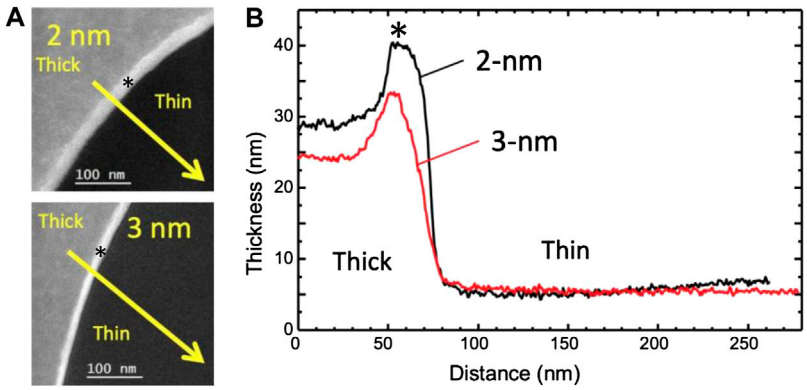

FIGURE 3
Thickness maps of Quantifoil 300 mesh carbon grid with 2 or 3 nm continuous carbon layer **(A)** Thickness maps were recorded as explained in the text, in a region such as that squared in Supplementary Figure S1A, on a 2 nm membrane (A1) and a 3 nm membrane (A2). **(B)** Thickness profiles were recorded along the yellow arrows in **(A)**, where the inelastic mean free path λ has been set to 130 nm: 2 nm nominal thickness in black, and 3 nm in red. The thickness maximum at both thick part edges is partly an artifact due to the presence of a Fresnel fringe (represented by the sign *).

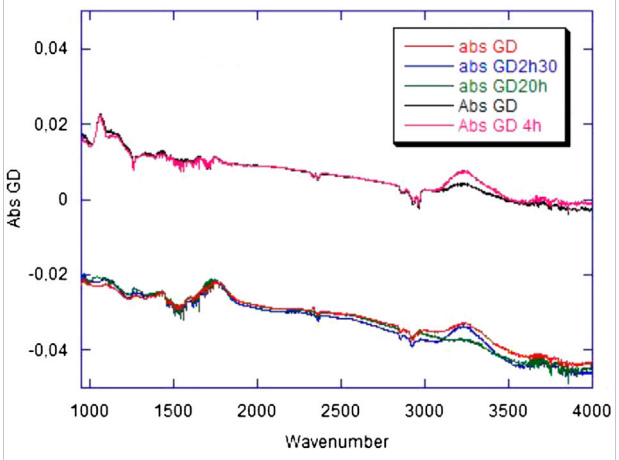

FIGURE 4
Infrared spectra of bare and carbon-covered Si prism. The red, blue, and green spectra (group in the lower part of the frame) correspond to the Si prism covered with a continuous carbon layer to simulate a classic Quantifoil grid; they have been recorded 1 h, 2 h 30 min, and 20 h after glow discharge, respectively. The black and pink spectra (upper part of the frame) correspond to the bare Si prism. Spectra have been recorded 1 and 4 h after glow discharge. All spectra have been recorded for an s-polarized infrared beam. In each case, the reference spectrum has been recorded prior to the GD treatment. The spectra are plotted as absorbances computed using a natural logarithm and correspond to 14 useful reflections in internal-reflection geometry.

When comparing the potential maps obtained, the major difference is obviously the presence or absence of aIF1A and aIF5B as well as $tRNA_i$ conformations (Figure 1C). The position of the $tRNA_i$ in the P site of the small ribosomal subunit in the stripped complex is rather in an upper position compared to the full IC3 complex.

To further investigate these results, different biophysical approaches were used to better characterize the different grid batches. Batch#4 was used as a control as grids from this batch did not show any morphological difference before and after glow discharge, and because we ran out of grids for batch#3.

SEM–Bare grids from batches #1, #2, and #4 were used for SEM analysis. Each grid, with or without glow discharge, was carefully checked using conventional SEM imaging. For the nonglow discharged grids, at low magnification (×700), looking at whole grid squares, the carbon membranes seemed to be of good quality (Figure 2A). Some grid squares contained sheared regions where the extra thin continuous carbon layer was absent (Figures 2B, C). Going to higher magnification (7000x), for the glow discharged grids from batches #1 and #2, it became obvious that the TCL was broken, at least at the level of the holes of the perforated carbon layer (Figure 2D). This was not the case for the grids coming from batch#4, with or without glow discharge. Furthermore, Auger electron spectroscopy was also performed on nonglow discharged grids from batches #1, #2, and #4 to prevent the carbon layer on top of the perforated carbon to break. This analysis did not show a significant difference in chemical composition (Supplementary Figures S3, S4).

EELS–Bare grids from batches #1, #2, and #4 were also used for EELS analysis. We measured the thickness of two TCLs with respective nominal thicknesses of 2 and 3 nm. The measurements were performed in five different areas in either case, taking 130-nm as the value of the inelastic mean free path λ. The raw data is available in Supplementary Table S1. The geometry of the measurements and the local thickness variations are shown in Figure 3.

If we assume that the differences with the nominal values are entirely due to the error on the mean free path, the actual inelastic mean free path would be shorter than the one used by respectively 58 and 44% for the 2 and 3 nm cases, which is consistent indeed with surface plasmons playing a lower role in the thicker samples.

Finally, given the specificity of the plasmon losses in thin membranes, we thus estimate that the measured values may be compatible with the nominal values of 2 and 3 nm. However, even if its average thickness is close to the nominal value, the 2 nm membrane presents more thickness variations than the 3 nm membrane.

Infrared spectroscopy–Figure 4 shows the absorbance changes induced by the GD treatment on the carbon film, about 1 hour after the treatment and at later times. As a reference, the absorbance changes observed for a bare Si prism submitted to the same treatment are plotted on the same figure. The plots represent the difference spectra taking the nonglow discharge material as the reference. Absorbance spectra exhibit vibrational peaks, positive when they result from the generation of chemical species by the treatment, and negative when they result from the removal of chemical species by the treatment. They also exhibit a baseline that, in the case of a bare Si prism, is characteristic of free-carrier absorption. It results from the change of the surface charge which affects the band bending in silicon close to the surface (Rao et al., 1986). The positive background of the spectra refers to a decrease in the space-charge region in silicon, corresponding to a positive charging of the surface. In the bare Si case, vibrational features evidence 1) the removal of adventitious carbon contamination (νCH_2 and νCH_3 modes around 2,900 cm^{-1} and δCH_3 at 1,260 cm^{-1}); a slight increase in the silicon oxide thickness (νSiOSi modes at 1,075 and tail in the 1,100–1,200 cm^{-1} range); 3) a hydroxylation of the silicon oxide surface (νOH mode around 3,250 cm^{-1}). The first two features are expected phenomena upon treatment in an oxidative plasma. The third one reveals that the oxide surface tends to be covered by an increased amount of SiOH groups, plausibly resulting from the breaking of Si-O bonds upon plasma exposure, with the capture of protons coming either from water physisorbed at the surface or from atmospheric water in the plasma.

In the case of the carbon film, the baseline is of the opposite sign and exhibits a spectral shape distinct from classical free-carrier absorption (Drude-type absorption). These features suggest that the baseline can be tentatively assigned to a change in the charge of the surface, like for bare silicon, but which mostly affects the carbon film and not the underlying silicon oxide. This assignment is consistent with the absence of modification in the silicon oxide thickness (absence of the characteristic bands in the 1,050–1,200 cm^{-1} wavenumber range). However, the amplitude of the baseline appears to vary from experiment to experiment and may become null. Therefore, no reproducible specific charging of the carbon film can be detected. Two specific vibrational features appear and remain stable after the GD treatment: a broad asymmetric peak in the 1750 cm^{-1} range and a weaker one at ~1,450 cm^{-1}. The former evidences the combined formation of heavily oxidized carbon species (ketones, carboxylic acids, esters) and C=C bonds. Local aromatization could account for the presence of the 1,450 cm^{-1} peak. These peaks witness the irreversible changes induced by the GD treatment: breaking of C-C bonds and strong oxidation of the carbon film surface. A set of three other peaks are also induced by the treatment (a broad band centered at ~3,250 cm^{-1}, a relatively narrow peak at ~1,290 cm^{-1}, and a broader one around ~1,100 cm^{-1}), but they are seen to evolve on a time scale of several hours after the treatment. They all increase in the first hours after the treatment; at subsequent times, the 3,250 cm^{-1} band decreases, and the other ones keep growing. The 3,250 cm^{-1} band is assigned to the νOH mode of carboxylic-acid and alcohol type species. The bands at 1,290 and 1,100 cm^{-1} could mostly come from ester-type species.

An emergent picture consistent with the experimental observation is the following. The GD treatment induces the breaking of C-C bonds in the carbon film. The oxidative character of the plasma induces the irreversible formation of oxidized species and C=C bonds. However, some of the plasma-induced species remain unrelaxed and slowly evolve, inducing an increase in the population of surface species like alcohols and carboxylic acids. In a later stage, the layer relaxes, resulting in the formation of ester-type species resulting from the reaction of carboxylic acid sites with neighboring alcohol ones. Obviously, this picture remains schematic, and further specific mechanisms likely contribute to the phenomena. But whatever the detailed picture is, the slow evolution of the vibrational peaks after the end of the GD treatment points out that reactive species are induced by the exposure to the plasma, and that these species slowly relax on a several-hour time scale, affecting the reactivity of the carbon film surface. As a final remark, one may notice that a similar phenomenon (slow post-treatment evolution of the νOH band) takes place on the bare Si prism. Of course, in that case, carbon-specific species are not generated and detected, and the picture is likely simpler than for the carbon film. Here, the oxide surface deactivation corresponding to the slow evolution is ascribed to the formation of SiOH bonds arising from the H capture by non-bridging SiO species, a picture consistent with the decrease of a small peak at the low-energy side of the spectrum assigned to non-bridging SiO species.

Electron tomography

In order to reveal the structure of the Quantifoil membrane with respect to the initial structure and to confirm the assumptions made from the 2D-SEM and EELS observations as illustrated in Figures 2, 3, electron tomography (ET) analyses

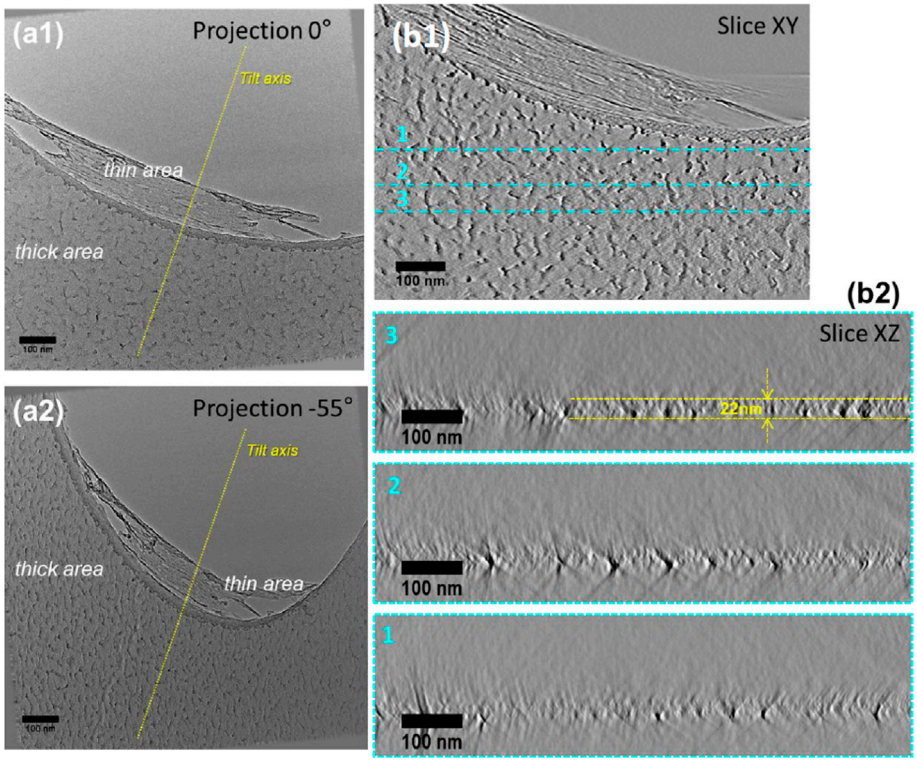

FIGURE 5
Electron tomography analyses of an area of the Quantifoil membrane containing a thick and thin area. **(A1)** and **(A2)** Projections acquired at two different tilt angles (−55° and +0°) from the tilt series used to calculate the reconstruction. **(B1)** and **(B2)**. Transversal and longitudinal slices were acquired at different depths and orientations through the reconstructed volume, illustrating the roughness of the Quantifoil membrane.

were performed on several areas within the membrane having undergone the same treatment as those illustrated in Figures 2, 3. Figure 5a1a2 displays two representative 2D-TEM micrographs of the analyzed area extracted from the tilt series used to reconstruct the volume, on which one can easily identify two different contrast regions corresponding to the thick and thin areas, respectively, with a marked apparent roughness. As a control (Figure 5a3), the same procedure was performed on a nonglow discharged grid. The ET analysis was performed twice on grids coming from batch#1 with and without glow discharge (Supplementary Figure S5): the pattern found on the grids from batch#1 with (thin area sheared) or without glow discharge (intact thin area) was identical. Also, the power spectrum of thick or thin areas was calculated to confirm the presence or absence of a carbon layer (Supplementary Figure S6).

By analyzing the projection series recorded one can easily observe that the structure of the thick area exhibits a marked difference at high tilt angles with respect to that at low tilt angles. A more detailed analysis of the projections recorded at low tilt angles, on which the presence of the two contrasts is clearly visible, allows us to unambiguously conclude, that the membrane has some granular species on both sides with different sizes that can be estimated to be about 7–10 nm. Representative sections through the volume of the reconstructed area are presented in Figure 5B. A quick visualization of the volume slice by slice clearly points out a rough structure of the membrane. This important observation is even more obvious when the volume is visualized in the direction perpendicular to the membrane axis (slices XZ1, XZ2, XZ3). We can clearly observe that the membrane is not perfectly flat, as is suggested by the 2D projections. Also, very importantly, the thickness of the membrane can vary between 20 and 25 nm. Regarding the thin part inside the hole, the ET analysis revealed that this part of the membrane is completely altered after glow discharge and falls back on the hole walls.

This ET study highlights the irregular structure of the Quantifoil membrane as well as its external roughness. A similar study is presented in the Supporting Information part on a larger area evidencing the same features of the membrane. A closer analysis of the thin area from the reconstructed volume of the series presented in Supplementary Figure S6 allowed us to estimate its thickness which is about 3 nm (for grids coming from batch#1).

Discussion

The analysis of the different 3D reconstructions obtained from the same biological sample strongly suggested that grid batches can be an issue when performing cryo-EM experiments. The sensitivity of the 2 nm carbon layer to glow discharge was shown to vary between grid batches. Grids coming from batch#3 contain an intact 2 nm TCL after our usual glow discharge conditions, whereas grids from batches #1 and #2 systematically showed a broken TCL. This sensitivity was not observed on previous grid batches that were used in the same conditions. The analysis by SEM and ET clearly demonstrates the sheared state of the TCL of grids coming from batch#1 or #2 whereas no grid integrity problem, before glow discharge, could be suspected. The systematic correlation of the 3D reconstructions of glow discharge grids coming from batch#1 and their corresponding analysis by ET on grids coming from the same batch emphasizes the importance of the glow discharge parameter. The same analyses were done with nonglow discharged grids: the continuous carbon layer did not show strong defects (data not shown). As a consequence of the 2 nm TCL damage, ribosomal particles, during grid preparation, could have remained for a long time near the air-water interface which most likely explains the removal of factors (Glaeser, 2018).

The comparison between cryo-EM results from batch#3 (2 nm TCL) and other batches (2 or 3 nm TCL) suggested that the presence of an intact TCL is required for intact biological ribosomal complexes. It is worth noting that the presence of an intact TCL on batch#3 grids could not be checked as no more spare grids from batch#3 were available; this assumption was only derived from previous studies before running into the glow discharge problems and complex integrity. The other approaches used in this study could not directly correlate the TCL and the ribosomal complexes integrities.

EELS and ET estimated the thickness of the continuous carbon layer and the results obtained were in the same range as that indicated by the supplier. As demonstrated, these two techniques can quickly give some valuable checks when one needs to confirm the membrane thickness. Characterization of carbon thickness of Quantifoil grids without any extra TCL using EELS reported in previous studies (Cho et al., 2013) mentioned a thickness of 49.11 ± 8.5 nm. This is a 2-fold difference from our studies, suggesting a possible change in grid preparation. This information was not confirmed by the grid manufacturer.

Using infrared spectroscopy, the chemical evolution of the membrane could have been studied. A model (Si prism with deposited carbon) had to replace a bare grid due to signal weakness. The charge distribution and its evolution over time on a cryo-EM grid before or after glow discharge appears to be weak and poorly reproducible at the scale of the experimental sensitivity accessible in our measurements. However, it has been possible to draw a consistent picture of the chemical activation of the membrane surface and its evolution during a grid preparation time course.

Overall, we describe several approaches that can be used by cryo-EM researchers to characterize the quality of the TCL of cryo-EM grids. The variability between grid batches should always stay in mind, even though it is not an easy criterion to assess. The glow discharge parameters need also to be adapted for each batch of grids to avoid breakage of the TCL. To tackle this grid batch issue, the glow discharge parameters were lowered down to only −5 mA for 30 s for grids of batches#1 and #2 as a higher intensity above this value and time limit did still break the thin layer of carbon.

Data availability statement

The raw data supporting the conclusions of this article will be made available by the authors, without undue reservation.

Author contributions

RK performed the IC3 data processing, GB performed the IC3 purification, DC performed the SEM and AES analysis, IF and EL performed the ET analysis, JLM performed the EELS analysis, and FO performed the infrared spectroscopy analysis. YM, ES, and PDC designed research. All the authors equally contributed to the writing of the manuscript.

Funding

This work was supported by grants from the Centre National de la Recherche Scientifique and Ecole polytechnique to Unité Mixte de Recherche n°7654 and by a grant from the Agence Nationale de la Recherche (ANR-17-CE11–0037). Cryo-EM data benefited from access to the following facilities: eBIC, Diamond Light Source, United Kingdom; ESRF, Grenoble; Pasteur Institute, Paris; and the Interdisciplinary Center for Electron Microscopy of Ecole Polytechnique (CIMEX). We also thank Célia Plisson-Chastang (CBI, Toulouse) and Magali Blaud (CiTCom, Paris) for their kind gifts of cryo-EM grids at critical stages of this work.

Conflict of interest

The authors declare that the research was conducted in the absence of any commercial or financial relationships that could be construed as a potential conflict of interest.

Publisher's note

All claims expressed in this article are solely those of the authors and do not necessarily represent those of

their affiliated organizations, or those of the publisher, the editors, and the reviewers. Any product that may be evaluated in this article, or claim that may be made by its manufacturer, is not guaranteed or endorsed by the publisher.

Supplementary material

The Supplementary Material for this article can be found online at: https://www.frontiersin.org/articles/10.3389/fmolb.2022.910218/full#supplementary-material

References

Aebi, U., and Pollard, T. D. (1987). A glow discharge unit to render electron microscope grids and other surfaces H ydrop hilic. *J. Electron Microsc. Tech.* 7–29.

Berger, S. D., McKenzie, D. R., and Martin, P. J. (1988). Eels analysis of vacuum arc-deposited diamond-like films. *Philos. Mag. Lett.* 57, 285–290. doi:10.1080/09500838808214715

Cho, H.-J., Hyun, J-K., Kim, J-G., Jeong, H. S., Park, H. N., You, D-J., et al. (2013). Measurement of ice thickness on vitreous ice embedded cryo-EM grids: Investigation of optimizing condition for visualizing macromolecules. *J. Anal. Sci. Technol.* 4, 7.

Coureux, P.-D., Lazennec-Schurdevin, C., Monestier, A., Larquet, E., Cladiere, L., Klaholz, B. P., et al. (2016). Cryo-EM study of start codon selection during archaeal translation initiation. *Nat. Commun.* 7, 13366. doi:10.1038/ncomms13366

Coureux, P. D., Lazennec-Schurdevin, C., Bourcier, S., Mechulam, Y., and Schmitt, E. (2020). Cryo-EM study of an archaeal 30S initiation complex gives insights into evolution of translation initiation. *Commun. Biol.* 3, 58. doi:10.1038/s42003-020-0780-0

Egerton, R. F. (2009). Electron energy-loss spectroscopy in the TEM. *Rep. Prog. Phys.* 72, 016502. doi:10.1088/0034-4885/72/1/016502

Glaeser, R. M. (2018). Proteins, interfaces, and cryo-EM grids. *Curr. Opin. Colloid Interface Sci.* 34, 1–8. doi:10.1016/j.cocis.2017.12.009

Godet, C., David, D., Sabbah, H., Ababou-Girard, S., and Solal, F. (2009). Bulk and surface plasmon excitations in amorphous carbon measured by core-level photoelectron spectroscopy. *Appl. Surf. Sci.* 255, 6598–6606. doi:10.1016/j.apsusc.2009.02.050

Gordon, R., Bender, R., and Herman, G. T. (1970). Algebraic Reconstruction Techniques (ART) for three-dimensional electron microscopy and X-ray photography. *J. Theor. Biol.* 29, 471–481. doi:10.1016/0022-5193(70)90109-8

Iakoubovskii, K., Mitsuishi, K., Nakayama, Y., and Furuya, K. (2008). Mean free path of inelastic electron scattering in elemental solids and oxides using transmission electron microscopy: Atomic number dependent oscillatory behavior. *Phys. Rev. B* 77, 104102. doi:10.1103/physrevb.77.104102

Iakoubovskii, K., Mitsuishi, K., Nakayama, Y., and Furuya, K. (2008). Thickness measurements with electron energy loss spectroscopy. *Microsc. Res. Tech.* 71, 626–631. doi:10.1002/jemt.20597

Iwaki, M. (2002). Estimation of the atomic density of amorphous carbon using ion implantation, SIMS and RBS. *Surf. Coat. Technol.* 158–159, 377–381. doi:10.1016/s0257-8972(02)00247-5

Jahagirdar, D., Jha, V., Basu, K., Gomez-Blanco, J., Vargas, J., and Ortega, J. (2020). Alternative conformations and motions adopted by 30S ribosomal subunits visualized by cryo-electron microscopy. *Rna* 26, 2017–2030. doi:10.1261/rna.075846.120

Kazan, R., Bourgeois, B., Lazennec-Schurdevin, C., Larquet, E., Mechulam, Y., Coureux, P-D., et al. (2022). Role of aIF5B in archaeal translation initiation. *Nucleic Acids Res.* 50 (11), 6532–6548. doi:10.1093/nar/gkac490

Lu, X., Naidis, G., Laroussi, M., Reuter, S., Graves, D., and Ostrikov, K. (2016). Reactive species in non-equilibrium atmospheric-pressure plasmas: Generation, transport, and biological effects. *Phys. Rep.* 630, 1–84. doi:10.1016/j.physrep.2016.03.003

Malis, T., Cheng, S. C., and Egerton, R. F. (1988). EELS log-ratio technique for specimen-thickness measurement in the TEM. *J. Electron Microsc. Tech.* 8, 193–200. doi:10.1002/jemt.1060080206

Mastronarde, D. N. (2005). Automated electron microscope tomography using robust prediction of specimen movements. *J. Struct. Biol.* 152, 36–51. doi:10.1016/j.jsb.2005.07.007

Mastronarde, D. N. (1997). Dual-axis tomography: An approach with alignment methods that preserve resolution. *J. Struct. Biol.* 120, 343–352. doi:10.1006/jsbi.1997.3919

Mechulam, Y., Guillon, L., Yatime, L., Blanquet, S., and Schmitt, E. (2007). Protection-based assays to measure aminoacyl-tRNA binding to translation initiation factors. *Methods Enzymol.* 430, 265–281. doi:10.1016/S0076-6879(07)30011-6

MessaoudiI, C., Boudier, T., Sorzano, C. O. S., and Marco, S. TomoJ. (2007). Tomography software for three-dimensional reconstruction in transmission electron microscopy. *BMC Bioinforma.* 8, 1–9.

Noble, A. J., Dandey, V. P., Wei, H., Brasch, J., Chase, J., Acharya, P., et al. (2018). Routine single particle CryoEM sample and grid characterization by tomography. *Elife* 7, e34257. doi:10.7554/eLife.34257

Passmore, L. A., and Russo, C. J. (2016). Specimen preparation for high-resolution cryo-EM. *Methods Enzym.* 579, 51–86. doi:10.1016/bs.mie.2016.04.011

Querido, J. B., Sokabe, M., Kraatz, S., Gordiyenko, Y., Skehel, J. M., Fraser, C. S., et al. (2020). Structure of a human 48S translational initiation complex. *Science* 369, 1220–1227. doi:10.1126/science.aba4904

Rao, A. V., Chazalviel, J.-N., and Ozanam, F. (1986). *In situ* characterization of the n-Si/acetonitrile interface by electromodulated infrared internal-reflection spectroscopy. *J. Appl. Phys.* 60, 696–706. doi:10.1063/1.337417

Russo, C. J., and Passmore, L. A. (2016). Progress towards an optimal specimen support for electron cryomicroscopy. *Curr. Opin. Struct. Biol.* 37, 81–89. doi:10.1016/j.sbi.2015.12.007

Scheres, S. H. W. R. E. L. I. O. N. (2012). Relion: Implementation of a bayesian approach to cryo-EM structure determination. *J. Struct. Biol.* 180, 519–530. doi:10.1016/j.jsb.2012.09.006

Zhang, K. Gctf (2016). Gctf: Real-time CTF determination and correction. *J. Struct. Biol.* 193, 1–12. doi:10.1016/j.jsb.2015.11.003

Zheng, S. Q., Palovcak, E., Armache, J. P., Verba, K. A., Cheng, Y., and Agard, D. A. (2017). MotionCor2: Anisotropic correction of beam-induced motion for improved cryo-electron microscopy. *Nat. Methods* 14, 331–332. doi:10.1038/nmeth.4193

frontiers | Frontiers in Molecular Biosciences

TYPE Original Research
PUBLISHED 17 October 2022
DOI 10.3389/fmolb.2022.912072

OPEN ACCESS

EDITED BY
Felix Weis,
European Molecular Biology Laboratory
Heidelberg, Germany

REVIEWED BY
Pierre-Damien Coureux,
École Polytechnique, France
Zhao Wang,
Baylor College of Medicine,
United States
Simon Arnold Mortensen,
European Molecular Biology Laboratory
Hamburg, Germany

*CORRESPONDENCE
Dominika Borek,
Dominika.Borek@UTSouthwestern.edu
Zbyszek Otwinowski,
Zbyszek.Otwinowski@UTSouthwestern.edu

SPECIALTY SECTION
This article was submitted to Structural Biology,
a section of the journal
Frontiers in Molecular Biosciences

RECEIVED 03 April 2022
ACCEPTED 19 August 2022
PUBLISHED 17 October 2022

CITATION
Bromberg R, Cai K, Guo Y, Plymire D, Emde T, Puzio M, Borek D and Otwinowski Z (2022), The His-tag as a decoy modulating preferred orientation in cryoEM.
Front. Mol. Biosci. 9:912072.
doi: 10.3389/fmolb.2022.912072

The His-tag as a decoy modulating preferred orientation in cryoEM

Raquel Bromberg[1,2], Kai Cai[1], Yirui Guo[2], Daniel Plymire[1,2], Tabitha Emde[1], Maciej Puzio[1], Dominika Borek[1,3,4]* and Zbyszek Otwinowski[1,3,4]*

[1]Department of Biophysics, The University of Texas Southwestern Medical Center, Dallas, TX, United States, [2]Ligo Analytics, Dallas, TX, United States, [3]Department of Biochemistry, The University of Texas Southwestern Medical Center, Dallas, TX, United States, [4]Center for Structural Genomics of Infectious Diseases, Dallas, TX, United States

The His-tag is a widely used affinity tag that facilitates purification by means of affinity chromatography of recombinant proteins for functional and structural studies. We show here that His-tag presence affects how coproheme decarboxylase interacts with the air-water interface during grid preparation for cryoEM. Depending on His-tag presence or absence, we observe significant changes in patterns of preferred orientation. Our analysis of particle orientations suggests that His-tag presence can mask the hydrophobic and hydrophilic patches on a protein's surface that mediate the interactions with the air-water interface, while the hydrophobic linker between a His-tag and the coding sequence of the protein may enhance other interactions with the air-water interface. Our observations suggest that tagging, including rational design of the linkers between an affinity tag and a protein of interest, offer a promising approach to modulating interactions with the air-water interface.

KEYWORDS

cryo-electron microscopy single particle reconstruction, cryoEM SPR, air-water interface, AWI, His-tag, preferred orientation, visualization

1 Introduction

Cryogenic electron microscopy single particle reconstruction (cryoEM SPR) datasets consist of images of macromolecular particles dispersed in a thin layer of amorphous ice formed over a thin supporting material that is attached to a metal grid. In recent years, there have been several studies on the angular and positional orientations of particles within the ice layer in cryoEM SPR and on the interactions of particles with the air-water interface (AWI) during cryo-cooling. In these studies, the kinetic parameters, variations in mechanical support, and chemical modifications to the support were explored. A number of strategies helping to keep biological samples in their optimal state have been proposed (D'Imprima et al., 2019; Glaeser, 2018; Noble et al., 2018a; Drulyte et al., 2018).

The AWI has been shown (D'Imprima et al., 2019; Noble et al., 2018b; Chen et al., 2019) to have a damaging influence due to the extremely high hydrophobicity of air (van Oss et al., 2005). Many macromolecular particles have on their surface hydrophobic

patches which are strongly attracted to the AWI (Taylor and Glaeser, 2008; Glaeser and Han, 2017), and diffusion allows particles to reach the interface within milliseconds, with partial or full unfolding frequently following initial binding (D'Imprima et al., 2019; Noble et al., 2018b; Glaeser and Han, 2017). Even if molecules do not unfold, they may become preferentially oriented (Han et al., 2012; Tan et al., 2017; Noble et al., 2018b; Chen et al., 2019). The binding to the AWI has also a significant advantage in reducing particle exclusion from thin ice, which is highly preferred for obtaining high quality data. Therefore, interactions between particles and the AWI have a complex impact upon experimental results.

Preferred orientation hinders cryoEM SPR reconstruction in two ways (Radermacher, 1988). Firstly, the preferred orientation results in a systematic lack of information regarding some orientations through the so-called missing cone effect, which leads to uneven coverage of reciprocal space and thus can be considered analogous to anisotropic diffraction in X-ray crystallography. In addition, the lack of a large group of orientations affects the convergence of the computational procedures used in 3D reconstruction for cryoEM SPR. Particularly for macromolecular systems having molecular mass lower than ~150 kDa, systematic misalignment of particles will result in introducing bias and artifacts to the reconstruction (Radermacher, 1988; Barth et al., 1989; Naydenova and Russo, 2017; Tan et al., 2017; Noble et al., 2018b).

Several approaches have been proposed to alleviate the problem of damage induced by the AWI or of the preferred orientation induced by it. They include using surfactants (Frederik et al., 1989; Glaeser et al., 2016; Chen et al., 2019) to saturate the surface at the AWI or the surface of the support (Russo and Passmore, 2014), and graphene oxide or graphene supports to prevent interactions of particles with the AWI (Pantelic et al., 2010; Pantelic et al., 2011; Wang et al., 2020a; Wang et al., 2020b). These supports may also be chemically modified to promote specific, high-affinity interactions with particles (Crucifix et al., 2004; Kelly et al., 2008; Kelly et al., 2010a; Kelly et al., 2010b; Han et al., 2012; Llaguno et al., 2014; Benjamin et al., 2016a; Benjamin et al., 2016b; Wang et al., 2020a; Wang et al., 2020b; Yeates et al., 2020). Finally, fast new approaches for depositing samples on a grid have been developed (Arnold et al., 2017; Dandey et al., 2018; Schmidli et al., 2018; Wei et al., 2018; Ravelli et al., 2019; Dandey et al., 2020). One of the strategies for changing interactions of macromolecules with a support, and with the AWI, is to chemically modify the molecule itself without changing the chemical properties of the support. Affinity tags chemically modify a protein and have been used in sample preparation for cryoEM in the context of affinity purification (Benjamin et al., 2016a; Benjamin et al., 2016b; Wang et al., 2020a; Wang et al., 2020b), but as we observed, tag presence can modify interactions with the AWI even without the use of affinity grids.

The His-tag is an affinity tag used widely to facilitate purification of recombinant proteins to homogeneity (Hochuli et al., 1988). Such proteins, with 6–10 consecutive histidine residues inside the tag which is introduced at their N- or C-termini, are overexpressed, with the tag facilitating purification by immobilized metal ion affinity chromatography (IMAC) (Wong et al., 1991). After purification, the His-tag is usually cleaved with a protease that recognizes the specific amino acid sequence motif—a cleavage site. Several proteolytic enzymes are used for this purpose, e.g. thrombin, factor Xa, Tobacco Etch Virus (TEV)-protease, and carboxypeptidase A. TEV-protease is a common choice because its classical cleavage site ENLYFQ(G/S) is very specific; the cleavage is performed after a glutamine residue, with TEV cleavage generating only a single amino acid addition if the His-tag was used at the N-terminal end of the expressed protein. When used for this purpose, TEV protease is usually expressed with an uncleavable His-tag (Raran-Kurussi et al., 2017). After the first round of purification, when a His-tagged protein of interest is separated from untagged proteins using IMAC, His-tag labelled TEV protease is added to the protein of interest. TEV protease cleaves His-tags from the protein of interest, and this cleavage is followed by a second round of IMAC to capture both the His-tag labelled TEV protease and also molecules with uncleaved His-tags, while the His-tag free protein is collected in the flow-through fractions. This procedure is frequently followed by an additional chromatography step, e.g. size exclusion chromatography, to assure that the protein is properly folded and in its proper oligomeric state.

The presence of the His-tag in crystallization is considered an obstacle, as the His-tag is usually connected to the protein of interest by a flexible linker and the increased flexibility may interfere with crystallization success (Majorek et al., 2014). However, in the case of cryoEM SPR, this does not necessarily pose a problem as the requirements for conformational homogeneity for a cryoEM sample are less stringent than for crystallization. With multiple possible conformations of flexible sequence extensions, forming a crystal lattice may be a challenge, and a well-packed crystal lattice is necessary for high-resolution diffraction. In cryoEM SPR, flexible sequence extensions will not contribute to the alignment of particles if they are truly flexible and will produce the 3D reconstructions with the flexible parts averaged out. However, such flexible extension may sometimes contribute to aggregation in the case of a cryoEM sample or may have higher propensity to unfolding at the AWI in comparison with more compact structures. Here we show and discuss how the His-tag affects interactions between labelled proteins and the AWI, which results in the modulation of particle preferred orientations.

2 Materials and methods

2.1 Protein expression and purification

Coproheme decarboxylase from *Geobacillus stearothermophilus* (HemQ) is encoded by the

GYMC52_3505 plasmid which is available from the DNASU Plasmid Repository (https://dnasu.org/). The open reading frame of the protein is cloned in the pMCSG7 vector containing Tobacco Etch Virus (TEV) cleavable N-terminal His6-tag (Stols et al., 2002).

His-tagged Tobacco Etch Virus (TEV) protease encoded by the pMHTDelta238 plasmid is available from the DNASU Plasmid Repository (https://dnasu.org/). It expresses a mutated and truncated form of the TEV protease as an N-terminal fusion to MBP-His7 (Raran-Kurussi et al., 2017), in which the MBP fusion is removed *in vivo* by autocleavage, leaving His7-TEV.

Our protein expression and purification followed a previously established protocol (Kim et al., 2011) with modifications that we describe here in detail.

The GYMC52_3505 and pMHTDelta238 plasmids were transformed to Rosetta2 (DE3)pLysS competent cells (Cat. No. 71401–3, EMD Millipore). Transformation reactions were spread on LB plates with ampicillin (Amp) at 200 μg/ml and chloramphenicol (Cam) at 37 μg/ml for GYMC52_3505, and with kanamycin (Kan) at 25 μg/ml and Cam at 37 μg/ml for pMHTDelta238. Single colonies grown on selective LB plates were used to initiate 3 ml or 25 ml liquid media cultures of Luria Broth medium (LB) with 200 μg/ml Amp and 37 μg/ml Cam for coproheme decarboxylase, and with 50 μg/ml Kan and 37 μg/ml Cam for TEV. All cultures were grown overnight in an incubated shaker (225 rpm, 37°C). The next morning, these cultures were used to seed larger volume cultures at the ratio 1: 1000. 1 L or 6 L LB cultures, with appropriate antibiotics, were grown at 37°C with 225 rpm shaking until OD_{600} of ~1.0, when the expression was induced by adding Isopropyl β-d-1-thiogalactopyranoside (IPTG) to the final concentration of 1 mM. The temperature in the shaker was decreased to 28°C for coproheme decarboxylase and 20°C for TEV, and cultures were grown overnight at these temperatures with shaking at 225 rpm. The cultures were centrifuged, and pellets were further processed and purified with slightly different protocols.

The bacterial pellets were resuspended in the lysis buffer (50 mM sodium phosphate pH 7.5, 300 mM NaCl buffer) at ~5 ml of the buffer per 1 g of the bacterial pellet. One tablet of cOmplete™ Protease Inhibitor Cocktail (Roche) was added to lysate. The bacterial suspension was then sonicated on ice for 15 min [30 × (30/30 s on/off), at 50% amplitude]. The lysate was centrifuged at 45,000×g for 30 min. The supernatant was retained and clarified by filtration through the 0.8 μm filter Millex-AA Syringe Filter Uni (MCE/blue colour). The clarified lysate was applied onto the column containing 3–4 ml of Talon resin preequilibrated with a binding buffer consisting of 50 mM sodium phosphate pH 7.5 and 300 mM NaCl. After the lysate flowed gravitationally through the column, ~100 ml of the binding buffer was applied to remove non-specifically bound proteins. The protein was eluted from the column in 1.5–2 ml fractions by applying ~15 ml of the elution buffer consisting of 50 mM sodium phosphate pH 7.5, 300 mM NaCl, and 150 mM imidazole. The aliquot of lysate as well as aliquots of the flow-through fraction, a fraction from the wash with binding buffer and a fraction from the wash with wash buffer, and each of the elution fractions were analyzed with the SDS-PAGE (Supplementary Figure S1). The fractions containing coproheme decarboxylase or TEV proteins were pooled. Purified according to the above protocol, His-tagged TEV protease (~1 mg) was added to pooled fractions of coproheme decarboxylase proteins and dialyzed 24–48 h against the binding buffer for HemQ preparations with completely or partially cleaved His-tag. Then, for samples with completely cleaved His-tag, dialysate was applied to 5 ml of Talon resin equilibrated with the binding buffer and flow-through was collected. The samples with partially cleaved His-tag were not subjected to the second Talon column. The dialysate for samples with the His-tag partially cleaved, or flow-through from either first or second round of affinity purification for samples with all His-tags cleaved or all His-tags present were concentrated to ~2 ml with Amicon® Ultra-15 Centrifugal Filter Unit with Ultracel® regenerated cellulose membrane and a 10 kDa molecular mass cutoff (Millipore), filtered through a 0.2 μm centrifugal filter and applied to a Superdex® 200 10/300 column run with an AKTA Pure system at a flow rate of 1 ml/min in 50 mM HEPES pH 7.5, 100 mM NaCl. Coproheme decarboxylase eluted at ~12 ml, in agreement with the molecular mass of a pentamer (~144–175 kDa depending on His-tag status) (Supplementary Figure S2). The fractions were collected, analyzed on the SDS-PAGE and concentrated with ~2 ml with Amicon® Ultra-15 Centrifugal Filter Unit with Ultracel® regenerated cellulose membrane and a 10 kDa molecular mass cutoff (Millipore) to the desired concentrations (20–30 mg/ml), which were assessed by measuring UV absorbance at 280 nm. In addition, centrifugal filtration was accompanied with buffer exchange to 50 mM HEPES pH 7.5, 100 mM NaCl. For partially cleaved and uncleaved batches of the protein, we did not use the second IMAC step, and instead applied the sample after TEV digestion directly to the gel filtration column, with the assumption that it contained a mixture of tagged states in the pentamer for a partially cleaved protein.

2.2 Preparation of grids, cryoEM data collection and data analysis

The purified coproheme decarboxylase samples were used to prepare grids. We used gold Quantifoil R 1.2/1.3 grids. The grids were glow discharged 90 s at 30 mA with a PELCO easiGlow™ Glow Discharge Cleaning System to obtain a hydrophilic surface. The glow-discharged grids were used to prepare vitrified samples with the Thermo Scientific Vitrobot Mark IV System. We applied 3 μl of purified protein to the glow-discharged surface of the grid at 4°C, 100% of humidity and blotted the solution for 5.5–6 s with blot force of either 19 or 20.

TABLE 1 Data collection and processing.

	HemQ-57K (no His-tag)	HemQ-45K-T (partial His-tag)	HemQ-45K-K (His-tag present)
Instrument	Talos 200 kV	Talos 200 kV	Krios 300 kV
Detector	K2	K2	K3
Energy filter	No	No	Yes
Objective aperture	No	No	No
Nominal magnification	57,000×	45,000×	105,000×
Data collection mode	Parallel beam; 1 hole per movie	Parallel beam; 1 hole per movie	Beam-image shift; 3×3 holes with beam tilt/astigmatism compensation
Frames per movie	100	200	100
Electron dose (e/A^2/frame)	0.9	0.9	0.78
Exposure time (s/frame)	0.4	0.4	0.07
Super-resolution mode	Yes	Yes	Yes
Detector pixel size (Å)	0.72	0.91	0.835
Data pixel size (Å)	0.36	0.455	0.417
Movies acquired	268	28	937
Movies used for processing	258	28	937
Molecular weight (kDa)	145	145	157
Reconstruction symmetry	C5/C1	C5/C1	C5/C1
Total picked particles	156,210	38,818	1,098,210
Particles after 2D averaging	145,966	38,818	1,041,821
Particles used in refinement	81,302	38,818	1,041,821
Resolution $FSC_{0.143}$ [C5/C1, Å]	2.32/2.93	2.53/~4.00	2.46/3.68

The data were acquired and analyzed as described before (Bromberg et al., 2020) (Table 1). Briefly, the cryoEM datasets for HemQ without His-tag (HemQ-57K), with His-tag partially present (HemQ-45K-T) were collected with a 200 kV Talos Arctica using a K2 Gatan camera run in super-resolution mode, with a physical pixel of 0.72 Å. A phase plate was not used and the objective aperture was not inserted. For HemQ-57K, 268 movies were collected with an exposure time of 40 s/movie. Each movie contains 100 frames with an exposure time of 0.4 s/frame and an electron dose of 90 e/Å^2 per movie. For HemQ-45K-T, 28 movies were collected with an exposure of 80 s/movie. Each movie contained 200 frames with an exposure time of 0.4 s/frame and an electron dose of 180 e/Å^2 per movie. The dataset for HemQ with His-tag present in all copies (HemQ-45K-K) was acquired with a 300 kV Titan Krios and K3 Gatan camera run in super-resolution mode, with a physical pixel of 0.835 Å. A phase plate was not used and the objective aperture was not inserted, the energy filter was used with slits set at 25 eV. For HemQ-45K-K, 937 movies were collected with an exposure of 7 s/movie. Each movie contained 100 frames with an exposure time of 0.07 s/frame and an electron dose of 78 e/Å^2 per movie.

We processed all datasets with cisTEM (Grant et al., 2018) with C5 symmetry applied. We modified the cisTEM pipeline by adding reference-based refinement of aberrations, including coma and trefoil, as in JSPR and Relion (Zivanov et al., 2018; Li et al., 2019). All the structures were solved with MOLREP (Vagin and Teplyakov, 2010) used within CCPEM (Wood et al., 2015; Burnley et al., 2017; Nicholls et al., 2018) with 6VSA.pdb used as a search model. Coot (Emsley and Cowtan, 2004; Emsley et al., 2010) was used to manually inspect the models and maps.

For reconstruction with C1 symmetry of the dataset with all His-tags included, we used cryoSPARC (Punjani et al., 2017). The particle stack (1,041,821 particles, box size 256) was exported from cisTEM into Relion format. The exported particle stack was imported to cryoSPARC using Import Particles job. An *ab initio* reconstruction job was then conducted in C1 symmetry with three *ab initio* classes to minimize biases. One out of three *ab initio* classes (consisting of 616,955 particles) showed appropriate representation of all views of the protein and was selected for the next processing step. One round of homogeneous refinement in C1 symmetry using the selected *ab initio* model and all particles (1,041,821 particles) resulted in a map with 3.68 Å resolution.

For tomographic reconstruction, IMOD software (Kremer et al., 1996) was used to align the tilt serial images and to reconstruct the tomograms by the weighted back-projection (WBP) approach. Ice thickness measurements were performed as previously described (Noble et al., 2018b). Briefly, after orienting the tomograms in IMOD to make the AWI parallel

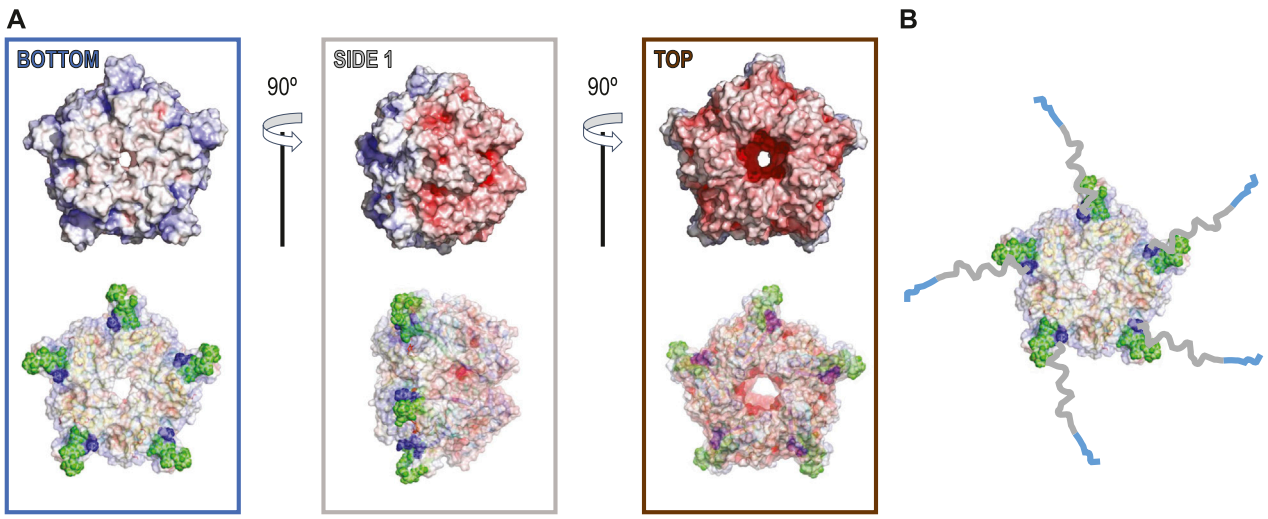

FIGURE 1
(A) The electrostatic potential map for 6VSA.pdb, which represents the cryoEM reconstruction of the cleaved version of coproheme decarboxylase. Three different orientations that stress a highly polarized charge distribution for this protein that explains observed patterns of preferred orientation (top). In the bottom row, each orientation of the electrostatic potential map is shown with 40% of transparency to show the orientations of the hydrophobic loop between residues 110–120 (green spheres) based on 1T0T.pdb and its proximity to the N-terminus (dark blue speres). **(B)** The model with the His-tags and their linkers added to show how they can extend from the surface of the protein up to ~60–65 Å.

to the field of view, two adsorbed particle layers were identified and used to locate the two AWIs, and the distance between the two interfaces was measured as the ice thickness.

Figures were prepared with PYMOL (The PyMOL Molecular Graphics System, Version 2.3.2, Schrödinger, LLC.), Excel (Microsoft Office 365 ProPlus, Microsoft), and Adobe Illustrator (Adobe Illustrator 2020; Version 24.0.1, Adobe Inc.). PYMOL includes an APBS electrostatic plugin (Baker et al., 2001), which we used with default values an input generated with 6VSA.pdb. Electrostatic surfaces are displayed at ± 10 k_BT/e^- at full color saturation.

3 Results and discussion

Coproheme decarboxylase (formerly HemQ) from *Geobacillus stearothermophilus* was one of the targets of the Midwest Center for Structural Genomics (MCSG; target APC35880). We solved its X-ray crystallographic structure in 2004 (PDB code: 1T0T.pdb) (Stols et al., 2002; Kim et al., 2011), while others determined its function later. We recently characterized this protein using cryoEM SPR (EMPIAR-10363, EMD-21373 and EMPIAR-10362, EMD-21376) (Grant et al., 2018; Bromberg et al., 2020) and noticed during cryoEM experiments that batches of the protein purified at different times showed different patterns of preferred orientation during cryoEM SPR data collection (Figure 1-3, Supplementary Figure S3). This observation prompted the analysis presented here. In the process of analyzing these datasets, we acquired additional cryoEM SPR datasets (Table 1).

Our data processing and analysis indicate that His-tag presence and occupancy greatly change preferred orientation patterns (Figures 2A–C) of 5-fold symmetric coproheme decarboxylase particles. Without the His-tag, these particles show very strong preferred orientation, with most (~40%) having their 5-fold axis oriented along the electron beam and perpendicular to both AWIs. However, out of two possible polarities (Figure 2A and Figure 3A), one is preferred (30% *vs.* 10%). With the His-tag partially cleaved, more particles are rotated on their side, which significantly changes the patterns of preferred orientation; ~78% of the particles have their 5-fold axes oriented at ~116° or equivalently, at ~64° (if the opposite orientation of the symmetry axis is used) to the AWI (Figures 2B, 3B). Finally, when the His-tag is present in all monomers of the particle, particles have also very strong preferred orientation with ~55% of particles having their 5-fold axis oriented roughly parallel to the beam again but with the reversed polarity in comparison with the dataset where all particles have His-tag cleaved (Figures 2C, 3C).

We present these data using a new graphical representation for preferred orientation of particles with n-fold symmetry (Figure 2), in addition to standard angular plots (Figure 3). 2D orientation plots of different types are not straightforward to interpret quantitatively. For this reason, we projected them on

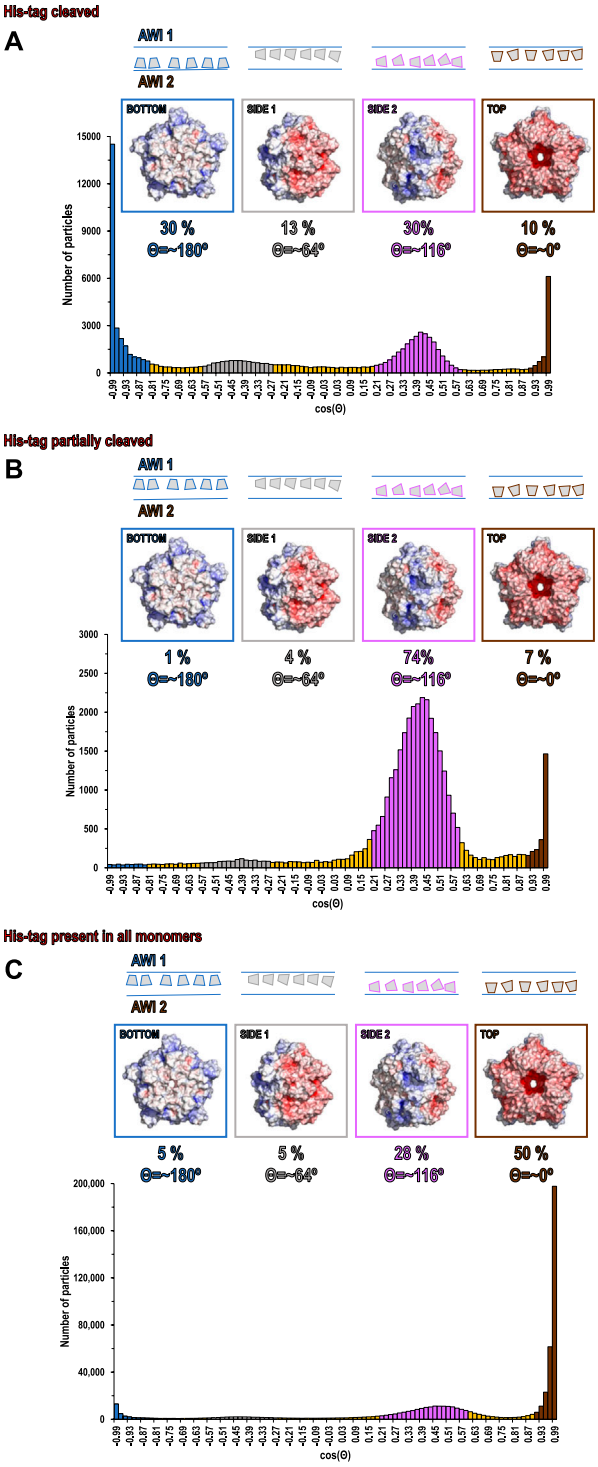

FIGURE 2
Histograms of distributions for particles of coproheme decarboxylase with His-tag cleaved **(A)**, His-tag partially cleaved **(B)**, and His-tag uncleaved **(C)**. The histograms show the number of particles as the function of cosine Θ, where Θ is the angle between the 5-fold axis of the particle and the direction of the beam. The map of the electrostatic potential for each orientation is shown above the specific peaks corresponding to the most frequent orientations.

a single axis, which is the angle between the electron beam and symmetry axis (Θ). Because particles of coproheme decarboxylase are polar, we can differentiate between parallel and anti-parallel orientations. The choice regarding which orientations are considered parallel is arbitrary, but we kept it consistent in our figures to facilitate comparisons. For such 1D orientation plots, uniform angular sampling would result in a sine modulation. We compensated for it by presenting the plots in uniform steps of cos(Θ). A random angular distribution will be flat in such a representation. The extremes in the range of cos(Θ) represent parallel and antiparallel to the beam orientation of particles. This representation is natural for particles with n-fold symmetry, but there is no natural choice of Θ for particles without symmetry.

The data show only the orientation with respect to the beam, including the polarity aspect. However, if we are interested in polarity of orientation with respect to the AWI, we need to consider the possibility of particles that bound to both AWIs in a thin layer to be cryo-cooled. The strong polarity pattern, i.e. the observed asymmetry (Figures 3A,C), indicates that the frequency of binding to these two interfaces is very different. Precisely establishing the apolar binding pattern for a single AWI would require tomographic reconstruction to isolate data arising from each interface. We performed such reconstruction for one of our datasets for a sample with His-tag uncleaved (Figure 5) and the observed asymmetry of binding agrees with quantitative data presented on Figure 2C and Figure 3C for the same type of the sample. Past tomographic reconstruction of particles trapped in a thin ice layer established that typically there is strong asymmetry in binding to the top and bottom (relative to the beam direction) interfaces (Tan et al., 2014; Noble et al., 2018b; Klebl et al., 2020), and this is also fully consistent with our data.

For polar particles, an advantage of our method of presenting data is that it provides a quick and convenient characterization of asymmetry between two surfaces, and it also allows for retrospective analysis of cryoEM SPR data. The width of the peaks in our histogram (Figure 2) results not only from the range of the angles between particles and the AWI, but also from variations in the tilt between the AWI and the beam. For typical grids, this is on the order of a few degrees (Noble et al., 2018b) when data are acquired at a zero-tilt angle. In addition to traditional 2D frequency plots, we also calculated 2D plots for two opposing polarities, to emphasize the significance of the asymmetry of binding to the AWI in two opposing directions (Figure 3).

The direction of preferred orientation can strongly influence 3D reconstruction; if it is aligned with the symmetry axis, as it is for datasets with the His-tag cleaved in all copies or the His-tag present in all copies, it generates only one back projection orientation, while if it is at a high angle to the symmetry axis as it happens for His-tag partially cleaved, it generates a number of back projections equal to the symmetry

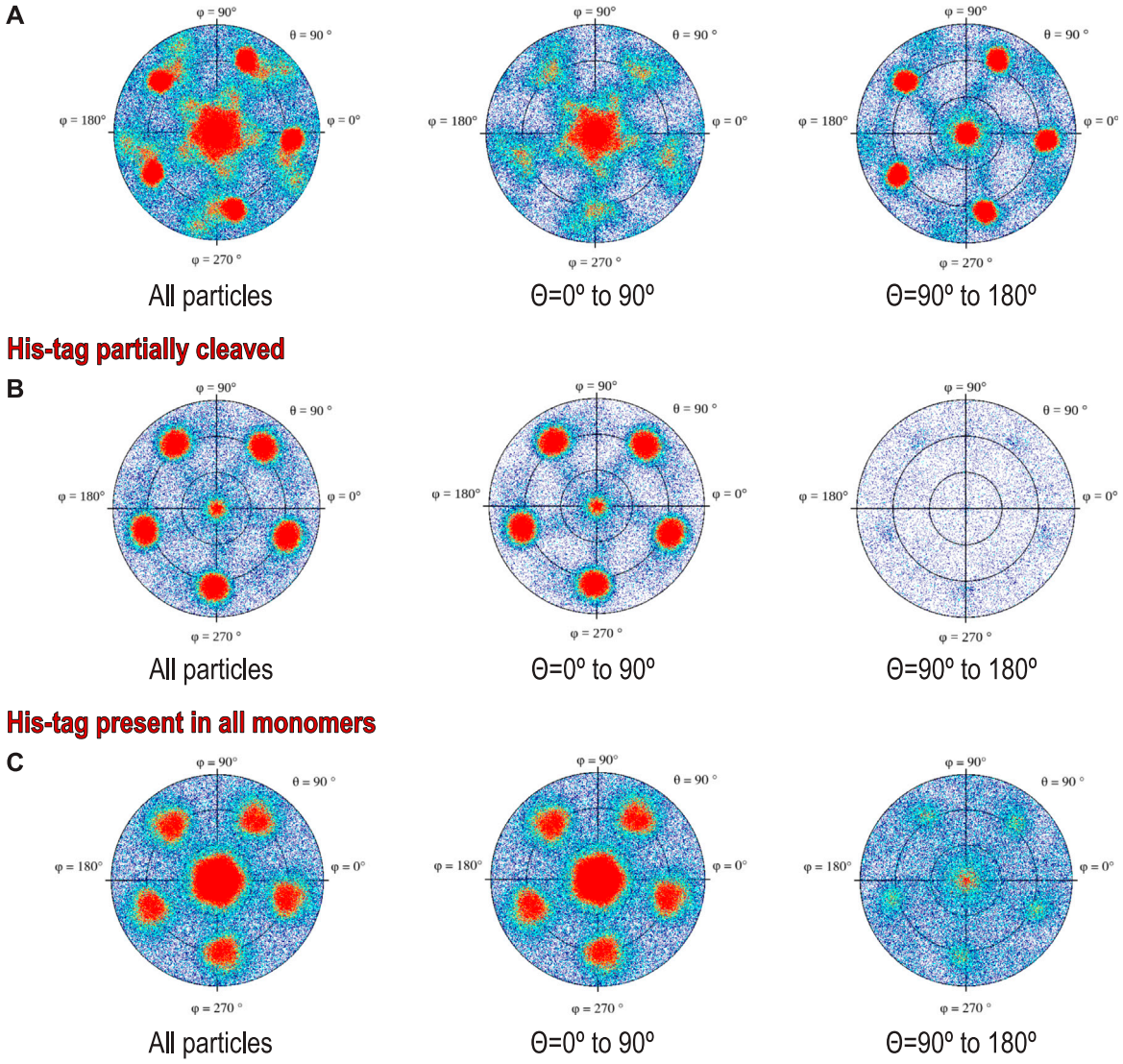

FIGURE 3
Preferred orientations (heat plots) shown in polar coordinates for protein with: **(A)** His-tag cleaved protein, **(B)** His-tag partially cleaved, and **(C)** His-tag uncleaved. To stress the difference in the polarity of the particles, we show on the left traditional plots for all particles, while the middle and right figures show (+) and (-) polarities (particles tilted away from or toward the beam). The different polarities result from different angles of interactions with the AWI, but also may result from interactions with two separate AWIs, which would symmetrize the histogram, as the cosine of the angle between the particle and the beam changes sign for the same geometric interaction with the AWI. We do not directly know how much these two effects contribute to our data.

factor (5 in this case), all contributing to the 3D reconstruction. Therefore, the change from one pattern of preferred orientation to another can have high impact, even if the orientations are not uniformly sampled.

The significant change in patterns of preferred orientation between a protein with and without a His-tag prompted us to analyze 6VSA.pdb (cryoEM data without His-tag) and 1T0T.pdb (X-ray data without His-tag) to identify possible reasons for the observed rearrangements.

The coproheme decarboxylase molecule is a compact structure which has a strikingly asymmetric charge distribution, with only a small number of possible hydrophobic patches that would be attracted by the AWI (Figure 1A). One of the patches is located at the bottom of the pentamer (Figure 1A) and this patch most likely facilitates preferred orientation for proteins without His-tags (Figure 2A). However, monomers retaining the His-tag had their N-termini extended by the sequence, HHHHHHSSGVDLGTENLYFQSNA, 23 amino acids in length,

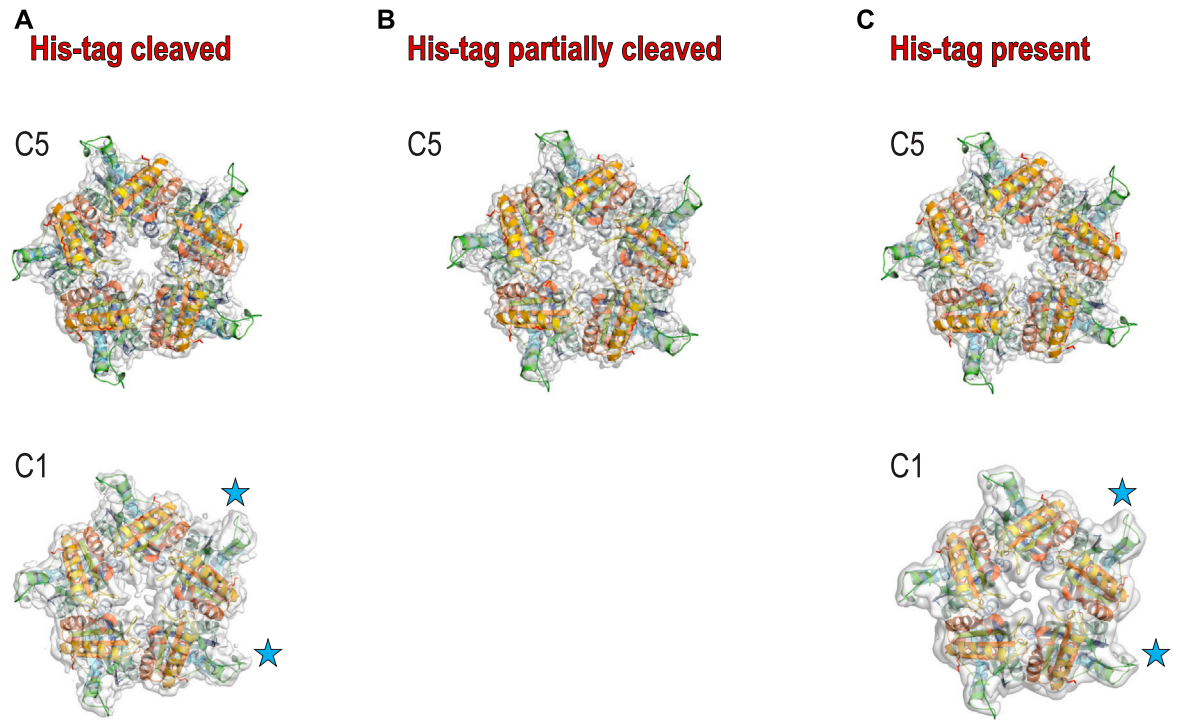

FIGURE 4
3D reconstructions for three samples. **(A)** 3D reconstruction with C5 (top) and C1 (bottom) symmetries for the sample with His-tag cleaved; **(B)** 3D reconstruction with C5 symmetry for the sample with His-tag partially cleaved. The reconstruction with C1 symmetry did not provide the interpretable density. **(C)** 3D reconstruction with C5 (top) and C1 (bottom) symmetries for the sample with His-tag uncleaved. The blue stars denote the 2 loops that have the best density in C1 reconstructions.

and originating from the MCSG7 vector. This part of the structure had no reconstructed density in our reconstructions performed with C5 symmetry, as expected for parts of the chain that are disordered. This disordered sequence can extend up to ~3.25 Å per amino acid residue, so it can extend up to ~60–65 Å, which is more than the radius of the reconstructed part of the protein structure. The N-terminal tail containing His-tag may dynamically bind the flat, hydrophobic patch at the bottom of the pentameric assembly, and so prevent binding of this hydrophobic patch to the AWI. It may bind directly to the AWI as its parts have hydrophobic character. The stretch of histidine residues in the His-tag can balance highly negative charges on the other side of the molecule, and form a new neutral/hydrophobic surface that may preferentially interact with the AWI. Finally, the N-terminal tail with the His-tag and its linker may interact with the hydrophobic loop discussed below and enhance its interactions with the AWI.

The second hydrophobic patch is located at a highly hydrophobic surface loop between amino acids 110 and 120 (PAYSYVSVVEL) (Figure 1). This region was ordered in the X-ray structure (1T0T.pdb) due to stabilizing interactions provided by the crystal lattice and a polyethylene glycol molecule present in crystallization solution, but in the cryoEM reconstructions obtained in C5 symmetry in this study (with and without His-tag), it is not visible. This unstructured region in our reconstruction is likely to serve as the AWI anchor and thus becomes partially unfolded (D'Imprima et al., 2019; Glaeser and Han, 2017), while the compactness of the rest of the structure prevents further unfolding. If the region was only unfolded upon binding to the AWI, then only 2 out of 5 loops in the pentamer would be affected, with the remaining 3 providing a weak but unambiguously visible contribution. This loop seems to direct the orientation with respect to the AWI both for fully His-tagged particles and those with the His-tag entirely cleaved with similar frequency (Figures 2A,C). The N-termini of each monomer are also close to this surface loop. The much stronger presence of the side orientation in datasets with partially cleaved His-tag (Figure 2B) may be due to the AWI interacting synergistically with both the hydrophobic part of the His-tag and the surface loop. We could not test these hypotheses for reconstructions performed with C5 symmetry and all datasets were reconstructed with C5 symmetry because we expected that the reconstruction in C1 would be severely affected by very strong preferred orientation. However, the observed differences in patterns of preferred orientation, in particular the reversal of polarity for the dataset with His-tag entirely uncleaved, prompted us to attempt reconstruction in C1. We succeeded in finding the self-consistent group of orientations for particles in all three datasets, i.e. particles aligned to each other in 2D. However, the 3D

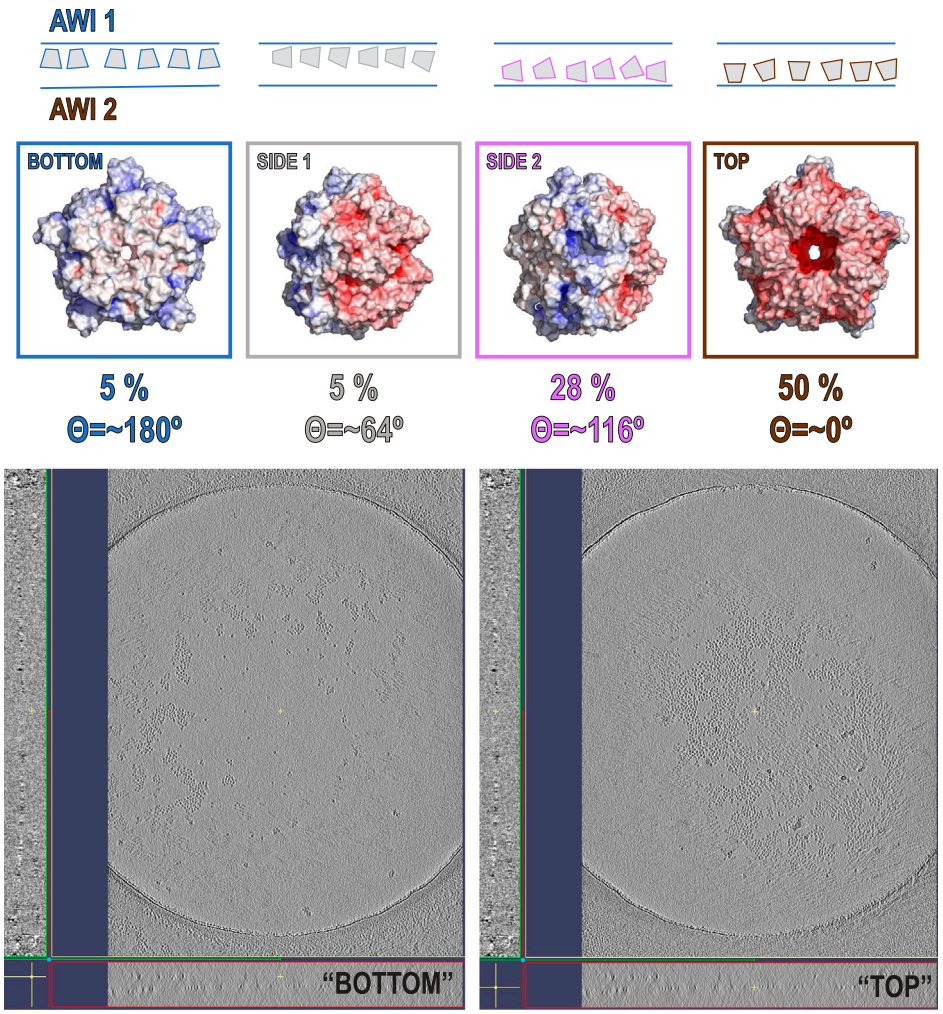

FIGURE 5
Tomographic reconstruction of the sample with His-tag present in all copies. The upper part of the figure shows the distribution of orientations for that sample, while the two panels at the bottom part of the figure represent the patterns on two different AWIs. One of the AWIs (left) shows very few particles in comparison with the second AWI (right). This is consistent with the results of our data analysis performed on a different subset of particles from the same type of sample. The particles in the sample are also forming "groups" that are not present in the sample with His-tags cleaved (Supplementary Figure S3A–C).

reconstruction produced interpretable maps only for the dataset without the His-tag and with the His-tag present in all subunits, with resulting resolution of reconstructions of 2.93 and 3.68 Å (by $FSC_{0.143}$ criterion), respectively (Table 1). Although we successfully performed classification for the dataset with partially cleaved His-tag, we were unable to obtain 3D reconstruction, despite the $FSC_{0.143}$ indicating a resolution of ~4 Å. The resolution of the reconstructions in C1 is lower than for reconstructions in C5, as expected, but we can analyze structural differences. The His-tag is not visible in the reconstruction from the sample with all monomers containing His-tags. The partially ordered loops in the reconstructions for the sample with His-tags and the sample without His-tag assume conformations similar to the conformations observed in the X-ray crystal structure (1T0T.pdb) (Figure 4). We believe that reconstructions in C1 are partially symmetrized, i.e. have approximately C5 symmetry due to particles having strong preferred orientation, with properties facilitating such symmetrization. HemQ is a pentamer and all three datasets we analyzed show preferred orientation. In two datasets, the 5-fold axis of HemQ is roughly parallel to the beam direction for most of the particles, with groups of particles having opposite polarities (Figures 2A, 3A and Figures 2C, 3C). For the third dataset, for particles with His-tag partially cleaved, the 5-fold axis is oriented ~116° with respect to the beam direction for most of the particles (Figures 2B, 3B). These patterns of preferred orientations have specific consequences depending on the symmetry used in reconstruction. The preferred

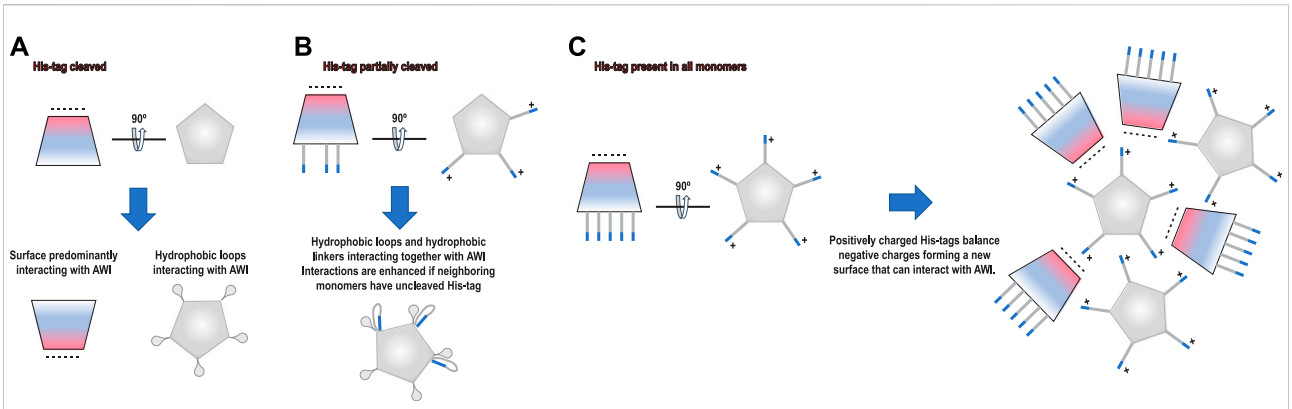

FIGURE 6
Proposed models of interactions with the AWI for each sample. **(A)** Particles with His-tag cleaved interact with the AWI using predominantly a hydrophobic "bottom" surface. **(B)** Particles with His-tag partially cleaved interact with the AWI using a hydrophobic loop with interactions most likely enhanced by the hydrophobic linker between the N-terminus of the protein and the His-tag. **(C)** Particles with His-tag present in all monomers interact with the AWI using the predominantly negatively charged side of the molecule. This can be achieved if the positively charged His-tag compensates the negative charge on the other surface, forming a new interface that can interact with the AWI.

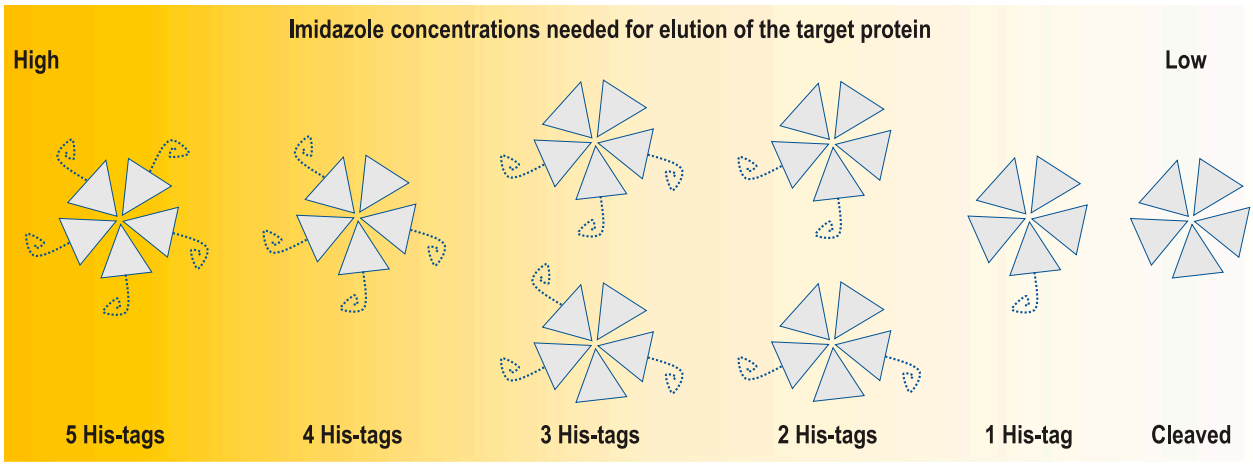

FIGURE 7
Schematic representation of an incomplete cleavage problem for a pentameric protein such as coproheme decarboxylase. The incomplete cleavage may make partially labelled particles escape binding to the affinity column and flow through together with oligomers having all His-tags cleaved. This is why for multimeric proteins, it is worth performing detailed analysis of the applicable ranges of eluting agent concentrations.

orientation with the 5-fold symmetry axis parallel to the beam direction is detrimental because little new information is generated after C5 symmetry expansion is applied to particle orientations. For the preferred orientation with 5-fold symmetry at a ~116° angle to the beam direction, the C5 symmetry expansion results in new orientations, so the reconstruction in C5 works well, even though the preferred orientation was much stronger for this dataset, and we also had a limited number of particles (Table 1).

The success of reconstruction in C1 for particles having their 5-fold axis oriented along the beam depends on the signal strength of the features differentiating monomers. The differences between the monomers must be significant enough so that the particles can align asymmetrically, otherwise the reconstruction in C1 will be averaged in an approximate C5 symmetry even though this symmetry has not been explicitly applied. We believe that although we successfully reconstructed two datasets in C1, the symmetrization took place in both cases due to the very low mass of features we tried to discern (1–2 kDa). Nevertheless, we observe that three out of five hydrophobic loops show density that is much better ordered than the density for the remaining two loops (Figure 4). This is consistent with the hypothesis that these two less

ordered loops interact with the AWI for datasets both with and without His-tag.

What would then cause the reversed polarity between the datasets with the His-tag in all monomers and with the His-tag entirely cleaved? Our initial hypothesis was that His-tag presence may obscure the hydrophobic surface on one of the sides of HemQ (Figure 1A). However, the datasets with the His-tag entirely uncleaved suggests a different model. The particles in this dataset (Figure 5 and Supplementary Figure S3) group together but do not aggregate and the reversed polarity of their preferred orientation (Figures 2C, 3C) indicates that the highly charged end of the molecule interacts with the AWI. A possible explanation for such interactions is that the positively charged end of the His-tag compensates the negative charges on the surface of the molecule. The grouping that we observe (Figure 5 and Supplementary Figure S3) is consistent with this hypothesis, as the His-tag with its linker in its extended conformation is long enough (~5–6 nm) to capture and interact with the negatively charged surface of the same particle but can also interact with the surfaces of other particles. Such interactions would generate the "grouping" we observed in Figure 5.

The His-tag may act as a decoy compensating for the charge at one end of the particle to form a new surface interacting with the AWI or as a decoy obscuring the more hydrophobic, flat surface perpendicular to the 5-fold axis of the particle to prevent interactions with the AWI. The linker between the N-terminus of the protein and the His-tag may enhance the hydrophobicity of the already hydrophobic loop. These effects together are likely creating the observed distributions (Figures 5, 6). There is no doubt that the interactions with the AWI have been also affected by our attempts to obtain as thin an ice layer as possible. However, for particles having limited molecular mass, thin ice is required to achieve a high resolution reconstruction. Particles are suspended at different z values, i.e. they will have different defocus in thicker ice and so one of the steps in refinement needs to include per particle defocus refinement. Unfortunately, for particles that have lower molecular mass, the signal-to-noise ratio (SNR) is too low for this step to succeed and without this refinement reconstruction to high resolution is not possible. Thin ice results in more uniform defocus per particle and an SNR that is higher, so per-particle defocus refinement becomes feasible for a higher number of projects.

In the case of homo-polymeric particles, multiple enzymatic reactions must happen before His-tags are removed from all monomers (Figure 7). An incomplete cleavage of the His-tag for multimeric proteins may be difficult to mitigate by size exclusion chromatography. The second round of IMAC should retain both TEV protease and particles partially labelled with His-tag. However, IMAC purification conditions are frequently optimized for fully labelled proteins, e.g. binding buffers contain some level of imidazole to minimize non-specific binding, and even such low levels of chelators may be sufficient for escape of partially labelled multimers in flow-through fractions during the second round of IMAC. The size exclusion step that follows the second IMAC usually cannot separate species that differ only by the mass of the His-tag and its linker for macromolecular assemblies having larger masses than 100 kDa. This is an additional factor that should be considered when one analyzes His-tag interactions with the AWI.

If retaining the His-tag allows for more general modulations of preferred orientation, then this suggests additional biochemical strategies for modulating interactions with the AWI and modulating the preferred orientation that is driven by these interactions: for example, modifying the length and the nature of the linker between the His-tag or other affinity tags, mixing tagged and untagged proteins, attaching other decoy molecules, e.g. pegylation, or using reductive methylation of lysine residues (Means and Feeney, 1990; Rypniewski et al., 1993), to name just a few. Reductive methylation was used to change the pattern of hydrophobicity on the surface of proteins to promote their crystallization (Kim et al., 2008; Tan et al., 2014). One can expect that reductive methylation will have a similar impact on interactions with supports used in cryoEM SPR. Finally, one can also use a simple additive (e.g. 0.2 mM Ni_2SO_4) to adjust the state of His-tags in a labelled protein. This strategy was already successfully used in the case of membrane proteins, to change their associations with micelles (Rasmussen et al., 2019) and consequently change their aggregative properties. The Supplementary Figure S3 shows also another protein, for which we observed a dramatic change of the preferred orientation between sample with and without a His-tag.

Using tags as anchors and decoys to modify interactions with the AWI and consequently modulate patterns of preferred orientation offers an additional strategy to improve sample handling for cryoEM.

Data availability statement

The original contributions presented in the study are included in the text of the article and in the Supplementary Materials. The datasets analyzed in this study can be found in EMPIAR (deposits EMPIAR-10363, EMD-21373 and EMPIAR-10362, EMD-21376). https://www.ebi.ac.uk/empiar/EMPIAR-10363/, https://www.ebi.ac.uk/empiar/EMPIAR-10362/,https://www.emdataresource.org/EMD-21373/, https://www.emdataresource.org/EMD-21376. Further inquiries about data can be directed to the corresponding authors.

Author contributions

RB, KC, YG, DP, TE, MP, DB and ZO generated data; RB, KC, YG, DB and ZO analyzed data; RB, KC, YG, DP, TE, MP, DB, YG, and ZO wrote manuscript.

Funding

The National Institute of Allergy and Infectious Diseases (NIAID), National Institutes of Health, Department of Health

and Human Services (contract No. HHSN272201700060C to Zbyszek Otwinowski); The National Institute of General Medical Sciences (NIGMS), National Institutes of Health (grant No. R21GM126406 to Dominika Borek; grant No. R01GM117080 to Zbyszek Otwinowski; grant No. R01GM118619 to Zbyszek Otwinowski; grant No. R43GM137671 to Yirui Guo); Department of Energy (grant No. DESC0019600 to Yirui Guo); The National Institute of Allergy and Infectious Diseases (NIAID), National Institutes of Health (grant No. P01AI120943 to Dominika Borek, Zbyszek Otwinowski).

Acknowledgments

We thank the Cryo-Electron Microscopy Facility (CEMF) at UT Southwestern Medical Center which is supported by grant RP170644 from the Cancer Prevention and Research Institute of Texas (CPRIT).

Conflict of interest

RB, YG, DB, and ZO are co-founders of Ligo Analytics, a company that develops software for cryogenic electron microscopy. YG serves as the CEO of Ligo Analytics, RB is currently employed by Ligo Analytics, while DP was employed by Ligo Analytics and UT Southwestern in the past. ZO is a co-founder of HKL Research, a company that develops and distributes software for X-ray crystallography.

The remaining authors declare that the research was conducted in the absence of any commercial or financial relationships that could be construed as a potential conflict of interest.

Publisher's note

Supplementary material

The Supplementary Material for this article can be found online at: https://www.frontiersin.org/articles/10.3389/fmolb.2022.912072/full#supplementary-material

References

Arnold, S. A., Albiez, S., Bieri, A., Syntychaki, A., Adaixo, R., McLeod, R. A., et al. (2017). Blotting-free and lossless cryo-electron microscopy grid preparation from nanoliter-sized protein samples and single-cell extracts. *J. Struct. Biol.* 197 (3), 220–226. doi:10.1016/j.jsb.2016.11.002

Baker, N. A., Sept, D., Joseph, S., Holst, M. J., and McCammon, J. A. (2001). Electrostatics of nanosystems: Application to microtubules and the ribosome. *Proc. Natl. Acad. Sci. U. S. A.* 98 (18), 10037–10041. doi:10.1073/pnas.181342398

Barth, M., Bryan, R. K., and Hegerl, R. (1989). Approximation of missing-cone data in 3d electron-microscopy. *Ultramicroscopy* 31 (4), 365–378. doi:10.1016/0304-3991(89)90335-5

Benjamin, C. J., Wright, K. J., Bolton, S. C., Hyun, S. H., Krynski, K., Grover, M., et al. (2016). Selective capture of histidine-tagged proteins from cell lysates using TEM grids modified with NTA-graphene oxide. *Sci. Rep.* 6, 32500. doi:10.1038/srep32500

Benjamin, C. J., Wright, K. J., Hyun, S. H., Krynski, K., Yu, G., Bajaj, R., et al. (2016). Nonfouling NTA-PEG-based TEM grid coatings for selective capture of histidine-tagged protein targets from cell lysates. *Langmuir* 32 (2), 551–559. doi:10.1021/acs.langmuir.5b03445

Bromberg, R., Guo, Y., Borek, D., and Otwinowski, Z. (2020). High-resolution cryo-EM reconstructions in the presence of substantial aberrations. *IUCrJ* 7 (3), 445–452. doi:10.1107/S2052252520002444

Burnley, T., Palmer, C. M., and Winn, M. (2017). Recent developments in the CCP-EM software suite. *Acta Crystallogr. D. Struct. Biol.* 73 (6), 469–477. doi:10.1107/S2059798317007859

Chen, J., Noble, A. J., Kang, J. Y., and Darst, S. A. (2019). Eliminating effects of particle adsorption to the air/water interface in single-particle cryo-electron microscopy: Bacterial RNA polymerase and CHAPSO. *J. Struct. Biol. X* 1, 100005. doi:10.1016/j.yjsbx.2019.100005

Crucifix, C., Uhring, M., and Schultz, P. (2004). Immobilization of biotinylated DNA on 2-D streptavidin crystals. *J. Struct. Biol.* 146 (3), 441–451. doi:10.1016/j.jsb.2004.02.001

D'Imprima, E., Floris, D., Joppe, M., Sanchez, R., Grininger, M., and Kuhlbrandt, W. (2019). Protein denaturation at the air-water interface and how to prevent it. *Elife* 8, e42747. doi:10.7554/eLife.42747

Dandey, V. P., Budell, W. C., Wei, H., Bobe, D., Maruthi, K., Kopylov, M., et al. (2020). Time-resolved cryo-EM using Spotiton. *Nat. Methods* 17 (9), 897–900. doi:10.1038/s41592-020-0925-6

Dandey, V. P., Wei, H., Zhang, Z., Tan, Y. Z., Acharya, P., Eng, E. T., et al. (2018). Spotiton: New features and applications. *J. Struct. Biol.* 202 (2), 161–169. doi:10.1016/j.jsb.2018.01.002

Drulyte, I., Johnson, R. M., Hesketh, E. L., Hurdiss, D. L., Scarff, C. A., Porav, S. A., et al. (2018). Approaches to altering particle distributions in cryo-electron microscopy sample preparation. *Acta Crystallogr. D. Struct. Biol.* 74 (6), 560–571. doi:10.1107/S2059798318006496

Emsley, P., and Cowtan, K. (2004). Coot: Model-building tools for molecular graphics. *Acta Crystallogr. D. Biol. Crystallogr.* 60 (1), 2126–2132. doi:10.1107/S0907444904019158

Emsley, P., Lohkamp, B., Scott, W. G., and Cowtan, K. (2010). Features and development of coot. *Acta Crystallogr. D. Biol. Crystallogr.* 66 (4), 486–501. doi:10.1107/S0907444910007493

Frederik, P. M., Stuart, M. C., Bomans, P. H., and Busing, W. M. (1989). Phospholipid, nature's own slide and cover slip for cryo-electron microscopy. *J. Microsc.* 153 (1), 81–92. doi:10.1111/j.1365-2818.1989.tb01469.x

Glaeser, R. M., Han, B. G., Csencsits, R., Killilea, A., Pulk, A., and Cate, J. H. (2016). Factors that influence the formation and stability of thin, cryo-EM specimens. *Biophys. J.* 110 (4), 749–755. doi:10.1016/j.bpj.2015.07.050

Glaeser, R. M., and Han, B. G. (2017). Opinion: Hazards faced by macromolecules when confined to thin aqueous films. *Biophys. Rep.* 3 (1), 1–7. doi:10.1007/s41048-016-0026-3

Glaeser, R. M. (2018). Proteins, interfaces, and cryo-em grids. *Curr. Opin. Colloid Interface Sci.* 34, 1–8. doi:10.1016/j.cocis.2017.12.009

Grant, T., Rohou, A., and Grigorieff, N. (2018). cisTEM, user-friendly software for single-particle image processing. *Elife* 7, e35383. doi:10.7554/eLife.35383

Han, B. G., Walton, R. W., Song, A., Hwu, P., Stubbs, M. T., Yannone, S. M., et al. (2012). Electron microscopy of biotinylated protein complexes bound to streptavidin monolayer crystals. *J. Struct. Biol.* 180 (1), 249–253. doi:10.1016/j.jsb.2012.04.025

Hochuli, E., Bannwarth, W., Dobeli, H., Gentz, R., and Stuber, D. (1988). Genetic approach to facilitate purification of recombinant proteins with a novel metal chelate adsorbent. *Nat. Biotechnol.* 6 (11), 1321–1325. doi:10.1038/nbt1188-1321

Kelly, D. F., Abeyrathne, P. D., Dukovski, D., and Walz, T. (2008). The affinity grid: A pre-fabricated EM grid for monolayer purification. *J. Mol. Biol.* 382 (2), 423–433. doi:10.1016/j.jmb.2008.07.023

Kelly, D. F., Dukovski, D., and Walz, T. (2010). A practical guide to the use of monolayer purification and affinity grids. *Methods Enzymol.* 481, 83–107. doi:10.1016/S0076-6879(10)81004-3

Kelly, D. F., Dukovski, D., and Walz, T. (2010). Strategy for the use of affinity grids to prepare non-His-tagged macromolecular complexes for single-particle electron microscopy. *J. Mol. Biol.* 400 (4), 675–681. doi:10.1016/j.jmb.2010.05.045

Kim, Y., Babnigg, G., Jedrzejczak, R., Eschenfeldt, W. H., Li, H., Maltseva, N., et al. (2011). High-throughput protein purification and quality assessment for crystallization. *Methods* 55 (1), 12–28. doi:10.1016/j.ymeth.2011.07.010

Kim, Y., Quartey, P., Li, H., Volkart, L., Hatzos, C., Chang, C., et al. (2008). Large-scale evaluation of protein reductive methylation for improving protein crystallization. *Nat. Methods* 5 (10), 853–854. doi:10.1038/nmeth1008-853

Klebl, D. P., Gravett, M. S. C., Kontziampasis, D., Wright, D. J., Bon, R. S., Monteiro, D. C. F., et al. (2020). Need for speed: Examining protein behavior during CryoEM grid preparation at different timescales. *Structure*. 28(11):1238–1248.e4. doi:10.1016/j.str.2020.07.018

Kremer, J. R., Mastronarde, D. N., and McIntosh, J. R. (1996). Computer visualization of three-dimensional image data using IMOD. *J. Struct. Biol.* 116 (1), 71–76. doi:10.1006/jsbi.1996.0013

Li, K., Sun, C., Klose, T., Irimia-Dominguez, J., Vago, F. S., Vidal, R., et al. (2019). Sub-3A apoferritin structure determined with full range of phase shifts using a single position of volta phase plate. *J. Struct. Biol.* 206 (2), 225–232. doi:10.1016/j.jsb.2019.03.007

Llaguno, M. C., Xu, H., Shi, L., Huang, N., Zhang, H., Liu, Q., et al. (2014). Chemically functionalized carbon films for single molecule imaging. *J. Struct. Biol.* 185 (3), 405–417. doi:10.1016/j.jsb.2014.01.006

Majorek, K. A., Kuhn, M. L., Chruszcz, M., Anderson, W. F., and Minor, W. (2014). Double trouble-Buffer selection and His-tag presence may be responsible for nonreproducibility of biomedical experiments. *Protein Sci.* 23 (10), 1359–1368. doi:10.1002/pro.2520

Means, G. E., and Feeney, R. E. (1990). Chemical modifications of proteins: History and applications. *Bioconjug. Chem.* 1 (1), 2–12. doi:10.1021/bc00001a001

Naydenova, K., and Russo, C. J. (2017). Measuring the effects of particle orientation to improve the efficiency of electron cryomicroscopy. *Nat. Commun.* 8 (1), 629. doi:10.1038/s41467-017-00782-3

Nicholls, R. A., Tykac, M., Kovalevskiy, O., and Murshudov, G. N. (2018). Current approaches for the fitting and refinement of atomic models into cryo-EM maps using CCP-EM. *Acta Crystallogr. D. Struct. Biol.* 74 (6), 492–505. doi:10.1107/S2059798318007313

Noble, A. J., Dandey, V. P., Wei, H., Brasch, J., Chase, J., Acharya, P., et al. (2018). Routine single particle CryoEM sample and grid characterization by tomography. *Elife* 7, e34257. doi:10.7554/eLife.34257

Noble, A. J., Wei, H., Dandey, V. P., Zhang, Z., Tan, Y. Z., Potter, C. S., et al. (2018). Reducing effects of particle adsorption to the air-water interface in cryo-EM. *Nat. Methods* 15 (10), 793–795. doi:10.1038/s41592-018-0139-3

Punjani, A., Rubinstein, J. L., Fleet, D. J., and Brubaker, M. A (2017). cryoSPARC: Algorithms for rapid unsupervised cryo-EM structure determination. 14, 290–296.

Pantelic, R. S., Meyer, J. C., Kaiser, U., Baumeister, W., and Plitzko, J. M. (2010). Graphene oxide: A substrate for optimizing preparations of frozen-hydrated samples. *J. Struct. Biol.* 170 (1), 152–156. doi:10.1016/j.jsb.2009.12.020

Pantelic, R. S., Suk, J. W., Magnuson, C. W., Meyer, J. C., Wachsmuth, P., Kaiser, U., et al. (2011). Graphene: Substrate preparation and introduction. *J. Struct. Biol.* 174 (1), 234–238. doi:10.1016/j.jsb.2010.10.002

Radermacher, M. (1988). Three-dimensional reconstruction of single particles from random and nonrandom tilt series. *J. Electron Microsc. Tech.* 9 (4), 359–394. doi:10.1002/jemt.1060090405

Raran-Kurussi, S., Cherry, S., Zhang, D., and Waugh, D. S. (2017). Removal of affinity tags with TEV protease. *Methods Mol. Biol.* 1586, 221–230. doi:10.1007/978-1-4939-6887-9_14

Rasmussen, T., Flegler, V. J., Rasmussen, A., and Bottcher, B. (2019). Structure of the mechanosensitive channel MscS embedded in the membrane bilayer. *J. Mol. Biol.* 431 (17), 3081–3090. doi:10.1016/j.jmb.2019.07.006

Ravelli, R. B. G., Nijpels, F. J. T., Henderikx, R. J. M., Weissenberger, G., Thewessem, S., Gijsbers, A., et al. (2019). Automated cryo-EM sample preparation by pin-printing and jet vitrification. *bioRxiv*, 651208.

Russo, C. J., and Passmore, L. A. (2014). Electron microscopy: Ultrastable gold substrates for electron cryomicroscopy. *Science* 346 (6215), 1377–1380. doi:10.1126/science.1259530

Rypniewski, W. R., Holden, H. M., and Rayment, I. (1993). Structural consequences of reductive methylation of lysine residues in hen egg white lysozyme: An X-ray analysis at 1.8-A resolution. *Biochemistry* 32 (37), 9851–9858. doi:10.1021/bi00088a041

Schmidli, C., Rima, L., Arnold, S. A., Stohler, T., Syntychaki, A., Bieri, A., et al. (2018). Miniaturized sample preparation for transmission electron microscopy. *J. Vis. Exp.* 137. doi:10.3791/57310

Stols, L., Gu, M., Dieckman, L., Raffen, R., Collart, F. R., and Donnelly, M. I. (2002). A new vector for high-throughput, ligation-independent cloning encoding a tobacco etch virus protease cleavage site. *Protein Expr. Purif.* 25 (1), 8–15. doi:10.1006/prep.2001.1603

Tan, K., Kim, Y., Hatzos-Skintges, C., Chang, C., Cuff, M., Chhor, G., et al. (2014). Salvage of failed protein targets by reductive alkylation. *Methods Mol. Biol.* 1140, 189–200. doi:10.1007/978-1-4939-0354-2_15

Tan, Y. Z., Baldwin, P. R., Davis, J. H., Williamson, J. R., Potter, C. S., Carragher, B., et al. (2017). Addressing preferred specimen orientation in single-particle cryo-EM through tilting. *Nat. Methods* 14 (8), 793–796. doi:10.1038/nmeth.4347

Taylor, K. A., and Glaeser, R. M. (2008). Retrospective on the early development of cryoelectron microscopy of macromolecules and a prospective on opportunities for the future. *J. Struct. Biol.* 163 (3), 214–223. doi:10.1016/j.jsb.2008.06.004

Vagin, A., and Teplyakov, A. (2010). Molecular replacement with MOLREP. *Acta Crystallogr. D. Biol. Crystallogr.* 66 (1), 22–25. doi:10.1107/S0907444909042589

van Oss, C. J., Giese, R. F., and Docoslis, A. (2005). Hyperhydrophobicity of the water-air interface. *J. Dispers. Sci. Technol.* 26 (5), 585–590. doi:10.1081/dis-200057645

Wang, F., Liu, Y., Yu, Z., Li, S., Feng, S., Cheng, Y., et al. (2020). General and robust covalently linked graphene oxide affinity grids for high-resolution cryo-EM. *Proc. Natl. Acad. Sci. U. S. A.* 117, 24269–24273. doi:10.1073/pnas.2009707117

Wang, F., Yu, Z., Betegon, M., Campbell, M. G., Aksel, T., Zhao, J., et al. (2020). Amino and PEG-amino graphene oxide grids enrich and protect samples for high-resolution single particle cryo-electron microscopy. *J. Struct. Biol.* 209 (2), 107437. doi:10.1016/j.jsb.2019.107437

Wei, H., Dandey, V. P., Zhang, Z., Raczkowski, A., Rice, W. J., Carragher, B., et al. (2018). Optimizing "self-wicking" nanowire grids. *J. Struct. Biol.* 202 (2), 170–174. doi:10.1016/j.jsb.2018.01.001

Wong, J. W., Albright, R. L., and Wang, N. H. L. (1991). Immobilized metal-ion affinity-chromatography (imac) chemistry and bioseparation applications. *Sep. Purif. Methods* 20 (1), 49–106. doi:10.1080/03602549108021408

Wood, C., Burnley, T., Patwardhan, A., Scheres, S., Topf, M., Roseman, A., et al. (2015). Collaborative computational project for electron cryo-microscopy. *Acta Crystallogr. D. Biol. Crystallogr.* 71 (1), 123–126. doi:10.1107/S1399004714018070

Yeates, T. O., Agdanowski, M. P., and Liu, Y. (2020). Development of imaging scaffolds for cryo-electron microscopy. *Curr. Opin. Struct. Biol.* 60, 142–149. doi:10.1016/j.sbi.2020.01.012

Zivanov, J., Nakane, T., Forsberg, B. O., Kimanius, D., Hagen, W. J., Lindahl, E., et al. (2018). New tools for automated high-resolution cryo-EM structure determination in RELION-3. *Elife* 7, e42166. doi:10.7554/eLife.42166

Advantages of publishing in Frontiers

OPEN ACCESS
Articles are free to read for greatest visibility and readership

FAST PUBLICATION
Around 90 days from submission to decision

HIGH QUALITY PEER-REVIEW
Rigorous, collaborative, and constructive peer-review

TRANSPARENT PEER-REVIEW
Editors and reviewers acknowledged by name on published articles

Frontiers
Avenue du Tribunal-Fédéral 34
1005 Lausanne | Switzerland

Visit us: www.frontiersin.org
Contact us: frontiersin.org/about/contact

REPRODUCIBILITY OF RESEARCH
Support open data and methods to enhance research reproducibility

DIGITAL PUBLISHING
Articles designed for optimal readership across devices

FOLLOW US
@frontiersin

IMPACT METRICS
Advanced article metrics track visibility across digital media

EXTENSIVE PROMOTION
Marketing and promotion of impactful research

LOOP RESEARCH NETWORK
Our network increases your article's readership